



Universiteit
Leiden
The Netherlands

Molecular imaging of pancreatic and rectal cancer: on a path towards optimized detection and response prediction

Vuijk, F.A.

Citation

Vuijk, F. A. (2024, January 10). *Molecular imaging of pancreatic and rectal cancer: on a path towards optimized detection and response prediction*. Retrieved from <https://hdl.handle.net/1887/3677368>

Version: Publisher's Version

License: [Licence agreement concerning inclusion of doctoral thesis in the Institutional Repository of the University of Leiden](#)

Downloaded from: <https://hdl.handle.net/1887/3677368>

Note: To cite this publication please use the final published version (if applicable).

MOLECULAR IMAGING OF PANCREATIC AND RECTAL CANCER

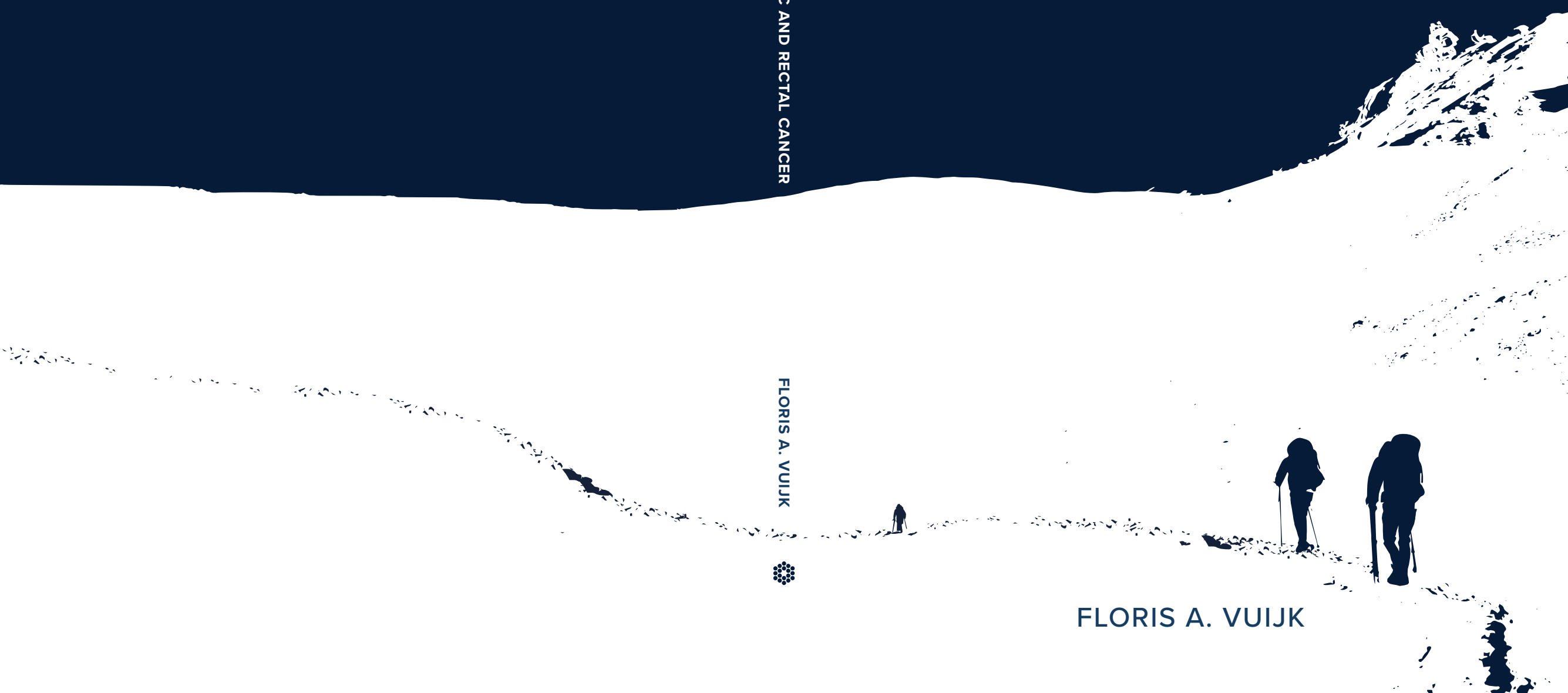
ON A PATH TOWARDS OPTIMIZED
DETECTION AND RESPONSE PREDICTION

MOLECULAR IMAGING OF PANCREATIC AND RECTAL CANCER

FLORIS A. VUIJK



FLORIS A. VUIJK



Molecular imaging of pancreatic and rectal cancer

On a path towards optimized detection and response prediction

Floris A. Vuijk

Molecular imaging of pancreatic and rectal cancer

On a path towards optimized detection and response prediction

Proefschrift

ter verkrijging van
de graad van doctor aan de Universiteit Leiden,
op gezag van rector magnificus prof. dr. ir. H. Bijl,
volgens besluit van het college voor promoties
te verdedigen op woensdag 10 januari 2024
klokke 16.15 uur

door

Floris Adriaan Vuijk

geboren te 's-Gravenhage
in 1996

© F.A. Vuijk 2024

ISBN: 978-94-6473-331-0

Cover: Tessa van Henten and Ilse Modder, www.ilsemodder.nl

Lay-out: Ilse Modder, www.ilsemodder.nl

Printed by proefschriften.nl

All rights reserved. No parts of this thesis may be reproduced, distributed, stored in a retrieval system or transmitted in any form or by any means, without prior written permission of the author.

The research in this thesis was financially supported by the Dutch Cancer Society, the Leiden University Fund, the European Research Council, and Horizon2020.

Financial support by Fluoptics/Tiniest.solutions, Curium Netherlands B.V., Viatrix B.V., Mobula IGM B.V., Raadsheren B.V., KARL STORZ Endoscopie Nederland B.V., Chipsoft B.V., ABN Amro Bank N.V. and the Leiden University Medical Center for the printing of this thesis is gratefully acknowledged.

Promotor:	Prof. dr. L.F. de Geus-Oei
Co-promotores:	Dr. D.E. Hilling Dr. A.L. Vahrmeijer
Promotiecommissie	Prof. dr. J. Burggraaf Prof. dr. R. Beets-Tan, NKI-AVL Dr. D.E. Oprea-Lager, Amsterdam UMC Dr. R.J. Swijnenburg, Amsterdam UMC

TABLE OF CONTENTS

Chapter 1	Introduction and thesis outline	9
Section I	Pancreatic cancer	19
Chapter 2	Molecular targeted PET imaging and radionuclide therapy of pancreatic ductal adenocarcinoma	21
Chapter 3	Molecular imaging of the tumor stroma and beyond	41
Chapter 4	Molecular targets for diagnostic and intraoperative imaging of pancreatic ductal adenocarcinoma after neoadjuvant FOLFIRINOX treatment	73
Chapter 5	Prostate-specific membrane antigen targeted PET/CT imaging in patients with colon, gastric and pancreatic cancer	93
Section II	Rectal cancer	111
Chapter 6	Accuracy of magnetic resonance imaging in primary staging and restaging after neoadjuvant therapy in rectal cancer patients	113
Chapter 7	[¹⁸ F]FDG PET/CT in treatment response monitoring: colorectal cancer	129
Chapter 8	Baseline and early digital [¹⁸ F]FDG PET/CT and multiparametric MRI show promise in predicting response to neoadjuvant therapy in locally advanced rectal cancer patients: a pilot study	157
Chapter 9	Intra-tumoral genomic heterogeneity in rectal cancer: mutational status is dependent on preoperative biopsy depth and location	177
Section III	Conclusions	195
Chapter 10	Summary and future perspectives	197
Chapter 11	Nederlandse samenvatting	211
Appendices	List of publications	220
	Curriculum Vitae	223
	Dankwoord	224

Introduction

1

GENERAL INTRODUCTION

The field of cancer diagnosis and treatment is a rapidly evolving field of medicine and has for years now been the most well-funded field of medical research. Due to the vast amount of research performed in this field, there is a wide array of treatments available for cancer patients. However, selecting the best treatment for the individual patient is often a difficult challenge. To be able to predict whether an individual patient will benefit from a specific therapy, there is a need for predictive (imaging) biomarkers. First, determination of the local tumor status and detection of possible local and/or distant (micro)metastasis is of paramount importance to decide on the possibility and effectiveness of surgical resection of the primary tumor. Second, when considering non-surgical treatments, biological tumor characteristics (such as mutational or receptor status) on which the effect of treatments will depend are important.

Clinical problems pancreatic cancer

Pancreatic cancer is currently the twelfth most prevalent cancer worldwide, with 2900 new patients diagnosed in 2021 in the Netherlands alone². As this disease is characterised by its asymptomatic progression in early stages, most pancreatic cancers are only detected when they are already in advanced stages when symptoms occur. As a result, pancreatic cancer has a dismal five year survival rate of only 7-9%⁷. Surgical resection combined with systemic treatment offers the only chance for cure, however, only 15-25% of patients are eligible for surgical resection^{8,9}. Despite careful patient selection and stratification by means of CT, magnetic resonance imaging, and endoscopic retrograde cholangiopancreatography (ERCP), resection with positive tumor margins (R1) occurs in a substantial proportion of patients (up to 75%)^{8,10,11}. Moreover, early recurrences (within six months) after pancreatic resection are reported in 28% of patients, likely due to the presence of (invisible) microscopic tumor deposits at the time of surgery¹¹. The clinical relevance of a microscopically radical (R0) resection is further underlined by the two-fold increase in survival time after R0 versus R1 resection¹¹⁻¹⁴.

To improve survival and facilitate improved radical resection rates, neoadjuvant chemotherapy has been implemented with results being evaluated in several clinical trials. However, current imaging modalities struggle to distinguish between vital tumor cells and tumor associated pancreatitis (TAP), therapy induced fibrosis (TIF) and necrosis after neoadjuvant therapy. This fact was demonstrated by a study in which the pre- and post neoadjuvant therapy CT scans were retrospectively evaluated by a radiologist blinded to the imaging time point (before or after neoadjuvant therapy) in pancreatic cancer patients after neoadjuvant chemotherapy. The results show that 92% of patients deemed unresectable at the post neoadjuvant therapy CT scan actually turned out to have had an R0 resection¹⁶, thus underlining the difficulty of determining resectability

on current CT scans.

With increasing use of potent neoadjuvant therapy, it is of great importance to accurately monitor tumor response to therapy and evaluate surgical resectability after neoadjuvant therapy. This is important in order to avoid missing the chance of an R0 resection in patients deemed unresectable at the imaging studies, and to prevent futile surgical procedures in unresectable patients who seem resectable.

Clinical problems rectal cancer

Colorectal cancer (CRC) is currently the third most prevalent cancer worldwide, with rectal cancer accounting for one third of CRC patients¹. In 2021, 3500 patients were diagnosed with rectal cancer in the Netherlands with a five year survival rate varying from 93% in stage I cancers to 13% in stage IV cancers². Currently, initial diagnosis is performed using colonoscopy and magnetic resonance imaging (MRI), whereas computed tomography (CT) is used to detect possible distant metastases. Curative treatment almost always includes surgical resection, either immediately after diagnosis or after neoadjuvant chemo- and/or radiotherapy treatment. The decision which therapy is most suited to the individual patient is based on relatively straightforward parameters such as the TNM stage and involvement of the mesorectal fascia. Neoadjuvant therapy for rectal cancer patients can consist of either radiotherapy or a combination of radio- and chemotherapy. This select combination of neoadjuvant therapy is used prior to surgical resection in order to downstage and downsize the primary tumor to enable surgical resection and prevent local recurrence of the tumor. Tumor response is most clearly seen after combined chemoradiotherapy, as a radiosensitizer (chemotherapy) is added to the treatment regimen during radiation and a waiting period is introduced before progressing to surgical resection. In most patients, a partial response of the tumor is seen. However, in 15-28% of patients, the use of neoadjuvant chemoradiotherapy even results in a pathological complete response of the primary tumor and tumor-positive lymph nodes (no tumor cells remaining after neoadjuvant therapy)³⁻⁵. Unfortunately, a substantial group of patients shows no response to neoadjuvant therapy, but does suffer from the associated side effects and delayed surgery⁶.

Diagnosis, response monitoring and prediction

For both rectal and pancreatic cancer, initial diagnosis of the primary tumor and possible metastases is performed using a combination of various imaging modalities (discussed in the next paragraph) and blood tests. Depending on the characteristics and location of the primary tumor or metastases, one of these various imaging modalities is most suited. In case of (neoadjuvant) treatment, the effect on the tumor can be monitored by for example sequential imaging or follow up of blood biomarkers. Currently, response monitoring is performed using CT (pancreatic cancer) or MRI (rectal cancer). In addition

to this, [¹⁸F]fluorodeoxyglucose (FDG) positron emission tomography combined with CT (PET/CT) can be used to visualize metabolic activity. Using these modalities, treatment inefficacy could be early detected and ineffective therapy could be terminated or altered to effective treatment regimen. Furthermore, effective treatment could be continued or (if useful) prolonged. Upfront prediction of treatment response, before initiation of treatment is even one step further, and could improve patient selection, to prevent patients from ineffective treatments and their associated side effects or complications.

Imaging modalities

Various imaging modalities have been investigated in this thesis. These include MRI, CT, PET/CT, and NIR fluorescent imaging. All modalities, except for NIR fluorescent imaging, provide a three-dimensional anatomical image of the human body.

MRI imaging employs a powerful magnetic field which forces protons in the human body to align with its field direction. Next, the protons are stimulated by a radiofrequent current, which causes the protons to spin out of this forced direction. When the radiofrequency is turned off, the MRI scanner is able to detect the energy released by the protons in order to regain alignment with the magnetic field direction. After computer processing, these data result in the images used in clinical practice. **CT imaging** uses x-rays which pass through the human body after which they hit a detector. Due to the differences in tissue density, the amount of x-rays absorbed differs, resulting in the image. **PET/CT** detects radiation emitted by a radioactive tracer, which is injected into the bloodstream of the patient before imaging. Depending on the specific tracer used, it binds or metabolizes in the body and accumulates at certain areas. Next, this image of accumulation throughout the body is projected over the CT scan made before, thus enabling specific localization in the human body.

NIR fluorescent imaging is a different imaging technique, which uses NIR fluorescent tracers injected in the tumor or bloodstream¹⁷. As these tracers bind or accumulate at the designated area, they can be excited using a light source and emitted NIR light can be captured. As NIR light is invisible to the naked eye, a dedicated camera system is needed for visualization and can project the NIR light signal over the image that is visible to the naked eye. In contrast to CT and PET/CT, NIR fluorescent imaging does not use ionizing radiation but only NIR light (harmless). Due to the limited penetration depth of NIR light (up to 1cm), the use of this technique is only feasible for superficial tumors or for intraoperative use.

THESIS OUTLINE

This thesis consists of three sections. In Section I, (pre)clinical research investigating novel targets for pre- and intraoperative molecular imaging of pancreatic cancer are discussed. In Section II, various studies are described which lay the groundwork for

further investigation into response monitoring and prediction in rectal cancer using various imaging modalities. Section III contains the summary, future perspectives and appendices.

As mentioned before, response monitoring of (neo)adjuvant treatment is challenging in pancreatic cancer. This is mostly due to the presence of therapy induced fibrosis, inflammation and edema which hamper clear distinction between vital tumor cells and fibrosis or necrosis. To gain insight into the current state of affairs of molecular imaging possibilities in pancreatic cancer, **Chapter 2** provides a narrative review of the currently available or investigated PET/CT tracers and radionuclide therapy tracers for use in pancreatic cancer. Unfortunately, only few molecular imaging tracers are currently available for this purpose. As pancreatic cancer is known for its high stromal content, targeting the tumor microenvironment (TME) for imaging or therapeutic purposes is promising. **Chapter 3** discusses the available literature regarding the molecular imaging of the components of the TME to provide guidance for future research into possible imaging and therapeutic targets of pancreatic cancer. In **Chapter 4**, these learnings are put into practice and various novel imaging targets for molecular imaging of pancreatic cancer after neoadjuvant therapy are investigated using immunohistochemistry in order to find suitable targets which could help distinguish vital tumor cells from therapy induced fibrosis. Following the promising results in **Chapter 4** of targeting the prostate specific membrane antigen (PSMA), **Chapter 5** discusses the clinical repurposing of a PSMA targeted PET/CT tracer ([¹⁸F]DCFPyL, known for its application in prostate cancer) to detect colon, gastric and pancreatic cancer.

Following these chapters, Section II focuses on rectal cancer. As with pancreatic cancer, evaluating response after neoadjuvant treatment in rectal cancer is very challenging. MRI is currently used for primary staging and restaging after neoadjuvant therapy, but lacks sensitivity at primary diagnosis and in discriminating vital tumor cells from fibrosis after neoadjuvant therapy. To provide insight into the diagnostic performance of MRI, a retrospective regional study investigating the accuracy of MRI at primary diagnosis and restaging after neoadjuvant therapy is described in **Chapter 6**. In this study, the clinical consequence (wrong treatment choice) of incorrect staging by MRI is also analysed. Knowing that response to neoadjuvant chemoradiotherapy varies extensively among patients, predicting response before or early during chemoradiotherapy could provide the opportunity to adjust (optimize) treatment regimens. Currently, no response prediction is performed and no accurate methods have yet been developed. Previous research has looked at various possibilities including using MRI and [¹⁸F]FDG PET/CT to predict this response. Using currently available data and clinical practice, **Chapter 7** reviews 20 educational cases which display a wide array of optional uses for [¹⁸F]FDG PET/CT imaging in the response evaluation of colorectal cancer. Following these

encouraging possibilities, **Chapter 8** describes a clinical pilot study which investigates the feasibility of using multiparametric MRI and [¹⁸F]FDG PET/CT before, during and after neoadjuvant therapy to predict and monitor response to neoadjuvant therapy in rectal cancer patients. Last, **Chapter 9** focuses on a different approach to response prediction. As we know from clinical experience, specific genomic mutations in tumor cells can predict sensibility to certain systemic treatments. An example of this is the high predictive value of the *KRAS* mutation on the efficacy of EGFR targeted therapy in colorectal cancers. Analysis of mutational status in colorectal cancer is generally performed on biopsy material obtained during colonoscopy. Although highly promising, tumor heterogeneity might greatly influence the results of mutational analysis from the biopsy samples. As samples are only taken from the luminal side of the tumor, other mutations might be found at different locations within this tumor. **Chapter 9** describes research investigating the possible influence of this tumor heterogeneity by comparing mutations found in tumor samples from various locations within rectal tumors.

REFERENCES

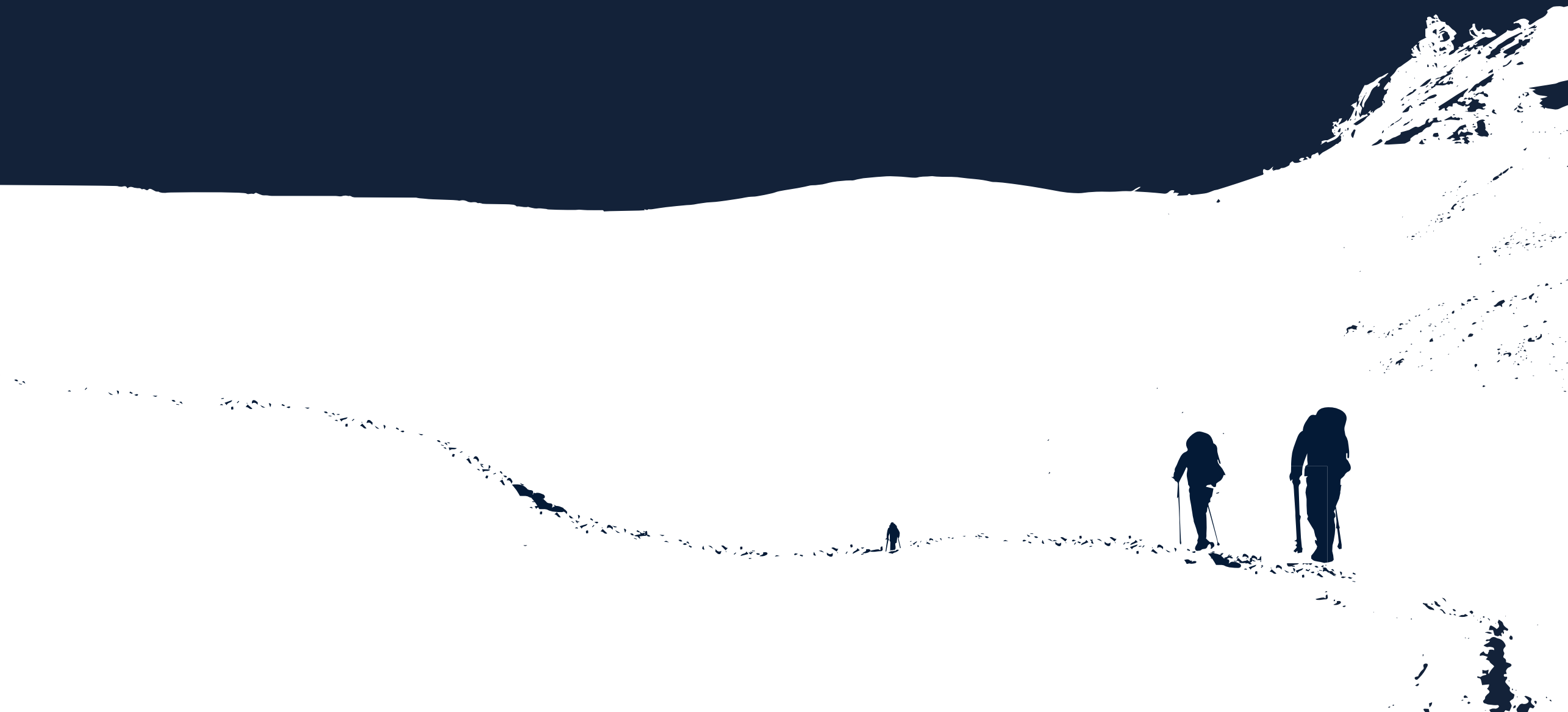
1. Ferlay J, Ervik M, Lam F, et al. Global cancer observatory: cancer today. Lyon, France: International Agency for Research on Cancer. 2020. Available from: <https://gco.iarc.fr.today>. Accessed February 9, 2022.
2. Dutch Cancer Registry (Nederlandse Kankerregistratie (NKR), IKNL). Available from: iknl.nl/nkr-cijfers. Accessed February 14, 2022.
3. Maas M, Nelemans PJ, Valentini V, et al. Long-term outcome in patients with a pathological complete response after chemoradiation for rectal cancer: a pooled analysis of individual patient data. *Lancet Oncol*. 2010;11:835–844.
4. van der Valk MJM, Hilling DE, Bastiaannet E, et al. Long-term outcomes of clinical complete responders after neoadjuvant treatment for rectal cancer in the International Watch & Wait Database (IWWD): an international multicentre registry study. *Lancet Lond Engl*. 2018;391:2537–2545.
5. Bahadoer RR, Dijkstra EA, van Etten B, et al. Short-course radiotherapy followed by chemotherapy before total mesorectal excision (TME) versus preoperative chemoradiotherapy, TME, and optional adjuvant chemotherapy in locally advanced rectal cancer (RAPIDO): a randomised, open-label, phase 3 trial. *Lancet Oncol*. 2021;22:29–42.
6. Park J-S, Baek J-H, Lee W-S, et al. Long-term oncologic outcomes in pathologic tumor response after neoadjuvant chemoradiation for locally advanced rectal cancer. *Korean J Clin Oncol*. 2018;14:37–42.
7. Latenstein AEJ, van der Geest LGM, Bonsing BA, et al. Nationwide trends in incidence, treatment and survival of pancreatic ductal adenocarcinoma. *Eur J Cancer Oxf Engl 1990*. 2020;125:83–93.
8. Barugola G, Partelli S, Marcucci S, et al. Resectable pancreatic cancer: who really benefits from resection? *Ann Surg Oncol*. 2009;16:3316–3322.
9. Stathis A, Moore MJ. Advanced pancreatic carcinoma: current treatment and future challenges. *Nat Rev Clin Oncol*. 2010;7:163–172.
10. Verbeke CS. Resection margins in pancreatic cancer. *Surg Clin North Am*. 2013;93:647–662.
11. Tummers WS, Groen JV, Sibinga Mulder BG, et al. Impact of resection margin status on recurrence and survival in pancreatic cancer surgery. *Br J Surg*. . Epub ahead of print March 18, 2019. DOI: 10.1002/bjs.11115.
12. Neoptolemos JP, Palmer DH, Ghaneh P, et al. Comparison of adjuvant gemcitabine and capecitabine with gemcitabine monotherapy in patients with resected pancreatic cancer (ESPAC-4): a multicentre, open-label, randomised, phase 3 trial. *Lancet Lond Engl*. 2017;389:1011–1024.
13. Yeo CJ, Cameron JL, Lillemoe KD, et al. Pancreaticoduodenectomy for cancer of the head of the pancreas. 201 patients. *Ann Surg*. 1995;221:721–733.
14. Ghaneh P, Kleeff J, Halloran CM, et al. The Impact of Positive Resection Margins on Survival and Recurrence Following Resection and Adjuvant Chemotherapy for Pancreatic Ductal Adenocarcinoma. *Ann Surg*. 2019;269:520–529.
15. Gerritsen A, Molenaar IQ, Bollen TL, et al. Preoperative characteristics of patients with presumed pancreatic cancer but ultimately benign disease: a multicenter series of 344 pancreatoduodenectomies. *Ann Surg Oncol*. 2014;21:3999–4006.
16. Ferrone CR, Marchegiani G, Hong TS, et al. Radiological and surgical implications of neoadjuvant

treatment with FOLFIRINOX for locally advanced and borderline resectable pancreatic cancer. *Ann Surg.* 2015;261:12–17.

17. Vahrmeijer AL, Hutteman M, van der Vorst JR, et al. Image-guided cancer surgery using near-infrared fluorescence. *Nat Rev Clin Oncol.* 2013;10:507–518.

SECTION I

Pancreatic cancer



Molecular targeted positron emission tomography
imaging and radionuclide therapy of pancreatic
ductal adenocarcinoma

T.T. Poels, F.A. Vuijk, L.F. de Geus-Oei, A.L. Vahrmeijer, D.E. Oprea-Lager and
R.J. Swijnenburg.

Cancers (Basel) 2021

2

ABSTRACT

Pancreatic ductal adenocarcinoma (PDAC) has an inauspicious prognosis, mainly due to difficulty in early detection of the disease by current imaging modalities. Upcoming development of tumour specific tracers provide an alternative solution for more accurate diagnostic imaging techniques for staging and therapy response monitoring. The future goal to strive for, in a patient with PDAC, should definitely be first to receive a diagnostic dose of an antibody labelled with a radionuclide and to subsequently receive a therapeutic dose of the same labelled antibody with curative intent. In the first part of this paper we summarize the available evidence on tumour-targeted diagnostic tracers for molecular positron emission tomography (PET) imaging that have been tested in humans, together with their clinical indications. Tracers such as radiolabelled prostate-specific membrane antigen (PSMA), in particular ^{18}F -labelled PSMA, already validated and successfully implemented in clinical practice for prostate cancer, also seem promising for PDAC.

In the second part we discuss the theranostic applications of these tumour specific tracers. Although targeted radionuclide therapy is still in its infancy, lessons can already be learned from early publications focusing on dose fractioning and adding a radiosensitizer, such as gemcitabine.

INTRODUCTION

Pancreatic ductal adenocarcinoma (PDAC) is the most frequent type of all pancreatic cancers and has an inauspicious prognosis, with a five-year survival rate of less than 5%^{1,2}. This extremely low survival rate is mainly due to difficulty in early detection of the disease extent by current imaging modalities. Staging, and hence rational use of treatment, are highly dependent on information yielded from conventional imaging modalities (i.e., computed tomography (CT), magnetic resonance imaging (MRI) or endoscopic ultrasound (EUS)³. However, almost 50% of surgery is performed without patient benefit (i.e., due to benign diagnoses, undetected metastases, or rapid recurrence <6 months), indicating that these imaging modalities are lacking diagnostic precision and therapy response evaluation accuracy.

During surgery for PDAC, 10% of the patients already present with metastases at laparoscopy and approximately half of the patients undergoing a resection will have microscopically positive resection margins (R1), of whom 25% will develop disease recurrence within six months after surgery. Furthermore, the imaging in patients with borderline resectable or locally advanced PDAC who started chemotherapy is unreliable due to difficulty in distinguishing between fibrosis and stroma in PDAC⁴. Also, ^{18}F -fluorodeoxyglucose (^{18}F -FDG) PET-CT, the most commonly used tracer in oncology, has a variable and debatable role in the routine pancreatic work up, mainly due to the large number of false positive findings by also identifying pancreatitis, potentially resulting in futile resections of the pancreas. ^{18}F -FDG PET-CT is therefore only reserved on indication for the individual patient⁴.

Upcoming development of tumour specific tracers provide an alternative solution for more accurate diagnostic techniques, staging and therapy response monitoring. Targeted radionuclides such as radiolabelled peptides, which bind to the receptors overexpressed by cancer cells and radiolabelled antibodies to tumour-specific antigens can provide a more specific diagnosis⁵⁻⁷. Additionally, this development offers new possibilities to maximally capitalize the theranostic applicability, i.e. the possibility to use the tracer both for imaging purposes as well as a targeting binder for radionuclide therapy.

In the first part of this review we summarize the available evidence on tumour-targeted imaging tracers for molecular PET-CT imaging that have been tested in humans, together with their clinical indications, and in the second part we discuss the theranostic applications of these tumour specific tracers.

For this narrative review our search strategy for both the diagnostic and therapeutic section consisted of a general search of diagnostic and therapeutic tracers in pancreatic

cancer, followed by a search of specific tracers and finally reviewing the papers for leads to other – not yet included- tracers.

PART I: TUMOUR TARGETED TRACERS FOR THE DETECTION OF PANCREATIC CANCER

Early detection is important for the treatment of PDAC. It is believed there are two main precursors for PDAC; namely pancreatic intraepithelial neoplasia (PanIN) and intraductal papillary mucinous neoplasm (IPMN). Three grades can be distinguished in PanIN. PanIN-1 and PanIN-2 are commonly found in patients over the age of 40 or in chronic pancreatitis. PanIN-3 is more exclusively found in the pancreas with PDAC and is the stage prior to invasion⁸⁻¹⁰. IPMNs develop in the cells lining the pancreatic ducts and contribute to mucin production, cystic dilatation of the pancreatic ducts and intraductal papillary growth. IPMNs are at risk of developing into malignancy in 20% over a period of 10 years^{8,11-12}.

PanIN's are challenging to diagnose, as all types are under the resolution of conventional imaging, due to their limited size. EUS may help in detecting identifiable parenchymal changes such as acinar cell loss, proliferation of small ductular structures and fibrosis. These combination of changes, labelled as lobulocentric atrophy (LCA), however, are not specific for PanIN^{8,13}.

In diagnosing PDAC, an important challenge is to distinguish PDAC from pancreatitis, as both entities have abundant stroma. Also, neoadjuvant treatment such as FOLFIRINOX make it difficult to discriminate between viable tumour and chemoradiation-induced tumour necrosis and fibrosis¹⁴⁻¹⁶. Tumour-targeted molecular imaging could provide essential knowledge in these situations, by adding metabolic molecular imaging information to the anatomical changes.

¹⁸F-Fluorodeoxyglucose - ¹⁸F-FDG

PET imaging for the diagnosis of PDAC uses ¹⁸F-FDG, a radiolabelled glucose¹⁷. ¹⁸F-FDG PET imaging relies on the property that a normal pancreas tissue has low glucose usage compared to PDAC. In PDAC a KRAS mutation induces over-expression of hexokinase-2 and glucose cell membrane transporter, GLUT-1²⁰. ¹⁸F-FDG is accumulated by PDAC where it is phosphorylated and consequently goes into metabolic arrest¹⁷⁻¹⁸. (Figure 1.1, Table 1).

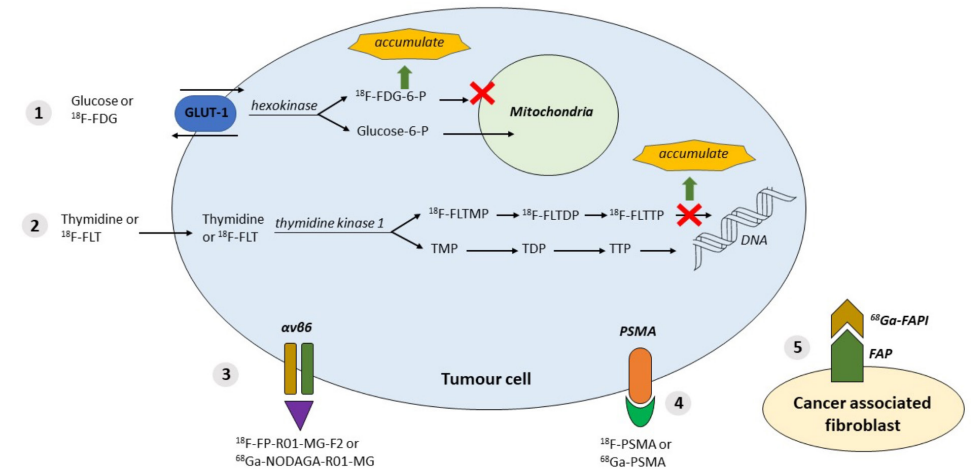


FIGURE 1. Available tracers and their properties

- ¹⁸F-FDG:** Tumour cells have the property of using glucose: GLUT-1 and hexokinase are upregulated in tumours. ¹⁸F labelled FDG accumulation
- ¹⁸F-FLT:** Cell proliferation in tumour cells: Thymidine kinase is upregulated. ¹⁸F labelled (FLT) → FLTTP accumulation
- $\alpha\text{v}\beta\text{6}$** overexpressed in tumour cells: targeted by labelled peptides: ¹⁸F-FP-R01-MG-F2 or ⁶⁸Ga-NODAGA-R01-MG
- PSMA** expressed in tumour cells: targeted by inhibitor molecules labelled with ¹⁸F or ⁶⁸Ga
- Expression of **FAP** (fibroblast activation protein) by CAF (cancer associated fibroblasts) targeted by FAPI (FAP inhibitor) labelled with ⁶⁸Ga or ¹⁸F

Abbreviations: $\alpha\text{v}\beta\text{6}$ = integrin $\alpha\text{v}\beta\text{6}$; DNA = Deoxyribonucleic acid; FAP= fibroblast activation protein; ¹⁸F = ¹⁸Fluorodeoxyglucose labelled; ¹⁸F-FDG = ¹⁸F-fluorodeoxyglucose; ¹⁸F-FDG-6-P = ¹⁸F-FDG-6-phosphate; ¹⁸F-FLT = ¹⁸F-fluorothymidine; ¹⁸F-FLTDP = ¹⁸F-FLT diphosphate; ¹⁸F-FLTMP = ¹⁸F-FLT monophosphate; ¹⁸F-FLTTP = ¹⁸F-FLT triphosphate; ¹⁸F-FP-R01-MG-F2 = ¹⁸F labelled integrin tracer; ¹⁸F-PSMA = ¹⁸F labelled PSMA; ⁶⁸Ga = ⁶⁸Gallium labelled; ⁶⁸Ga-FAPI = ⁶⁸Ga labelled fibroblast activation protein inhibitor; ⁶⁸Ga-NODAGA-R01-MG = ⁶⁸Ga labelled integrin tracer; ⁶⁸Ga-PSMA = ⁶⁸Ga labelled PSMA; Glucose-6-P = Glucose-6-Phosphate; GLUT-1 = glucose transporter type 1; PSMA= prostate-specific membrane antigen; TDP = thymidine diphosphate; TMP = thymidine monophosphate; TTP = thymidine triphosphate.

The average sensitivity and specificity for detecting PDAC by ¹⁸F-FDG is reported to be superior to CT, with sensitivity 94% and specificity 90% for ¹⁸F-FDG, compared to 82% and 75% respectively for CT^{14,19-20}.

A major limitation of PET imaging with ¹⁸F-FDG, is that glucose uptake can also be seen in inflammation, leading to similar appearance of pancreatitis and PDAC^{14,21}. However, when the diagnosis of PDAC is correct, the degree of ¹⁸F-FDG uptake can predict tumour aggressiveness and survival²²⁻²³.

In clinical practice differentiation between pancreatitis and PDAC is possible by performing a dual-phase PET scan. This method consists of performing a PET scan at two different time intervals after the injection of the tracer. Pancreatic masses on PET images in pancreatitis have lower standardized uptake values (SUV), which further decrease in the delayed phase. However, there can be overlap in SUV values between inflammation and PDAC. Furthermore, dual-phase ^{18}F -FDG PET imaging is very time consuming and therefore often not feasible in the daily practice^{17,24}.

The specificity of PET imaging for diagnosis of PDAC could be improved by using more disease-specific imaging agents compared to ^{18}F -FDG. Several other radiotracers have been used for the evaluation of PDAC^{17,25-26}. These include radiotracers such as ^{18}F -Fluorothymidine (^{18}F -FLT), ^{68}Ga labelled fibroblast activation protein inhibitor (^{68}Ga -FAP), ^{68}Ga labelled 1,4,7,10-tetraazacyclododecane-1,4,7,10-tetraacetic acid-FAPI-04 (^{68}Ga -DOTA-FAPI-04), ^{18}F Fluorodeoxyglucose labelled PSMA (^{18}F -PSMA), ^{68}Ga labelled PSMA (^{68}Ga -PSMA) and Integrin $\alpha\text{v}\beta\text{6}$ tracers. These tracers are amply discussed in the following part.

^{18}F -Fluorothymidine - ^{18}F -FLT

^{18}F -fluorothymidine is a marker of cell proliferation due to tracer accumulation in proliferating cells. Thymidine kinase activity is upregulated during proliferation, subsequently phosphorylating ^{18}F -FLT which gets trapped intracellularly. (Figure 1.2, Table 1)

^{18}F -FLT PET imaging has shown good correlation with histological Ki-67 expression, a marker of cell proliferation^{17,27}. Furthermore ^{18}F -FLT PET imaging is potentially superior to ^{18}F -FDG PET as ^{18}F -FLT uptake is not affected by inflammation or hyperglycaemia¹⁷.

Fibroblast Activation Protein Inhibitor - FAPI

In PDAC more than 90% of the tumour volume consists of cancer-associated fibroblasts (CAF). CAFs are associated with promotion of tumour growth, tissue invasion, metastasis developing and therapy resistance²⁸⁻³¹. CAFs express Fibroblast Activation Protein (FAP) on the cell surface, a type II membrane-bound glycoprotein³²⁻³³. FAP can be detected by performing a PET-CT with ^{68}Ga -labelled FAP-Inhibitors. (Figure 1.5, Table 1)

Röhrich et al. showed in a small study including 19 PDAC patients (7 primary and 12 progressive/recurrent) that ^{68}Ga -FAP PET-CT led to restaging in half of patients with PDAC and also in most patients with recurrent disease, compared to standard of care imaging. Differentiation from pancreatitis was challenging, but significantly improved with imaging at multiple time points after injection of ^{68}Ga -FAP²⁸.

Chen et al. compared the use of ^{68}Ga -DOTA-FAPI-04 to ^{18}F -FDG PET for the diagnosis of primary disease and metastatic lesions for various types of cancer. Four patients with pancreatic cancer were included. In one patient the pancreatic cancer was not visualised due to uptake throughout the pancreas caused by tumour-induced pancreatitis [34]. Identical findings of uptake of ^{68}Ga -DOTA-FAPI-04 in patients with Ig-G4 related disease have been reported by others³⁴⁻³⁸.

The study of Chen et al. did show a significantly lower uptake of ^{68}Ga -DOTA-FAPI-04 than ^{18}F -FDG, thus facilitating an improved detection of possible liver metastases³⁴.

TABLE 1. Available tracers and their properties for the diagnosis of primary disease.

Tracer	Properties	Localization	Main advantage	Main disadvantage
^{18}F -FDG	Marker of glucose consumption	Intracellular	High-glucose-use of malignant cells	High-glucose-using cells in inflammation
^{18}F -FLT	Marker of cell proliferation	Intracellular	Cell proliferation in malignancies	
^{68}Ga -FAP; ^{68}Ga -DOTA-FAPI-04;	Expression of FAP by CAF targeted by FAPI labelled with ^{68}Ga	Cell membrane of cancer associated fibroblast	After multiple time points, PDAC and pancreatitis show a trend for differential uptake kinetics.	Can be false positive in pancreatitis
^{18}F -FP-R01-MG-F2; ^{68}Ga -NODAGA-R01-MG; ^{68}Ga -Trivehexin	Labelled peptides targeting $\alpha\text{v}\beta\text{6}$ overexpressed in tumour cells	Cell membrane	Distinguishment between PDAC and pancreatitis. Also uptake in lymph node metastases	
Radiolabelled PSMA (i.e. ^{18}F -PSMA; ^{68}Ga -PSMA)	Inhibitor molecules labelled with ^{18}F or ^{68}Ga targeting PSMA expressed in tumour cells	Cell membrane	Very high diagnostic accuracy between PDAC and pancreatitis	

Abbreviations: $\alpha\text{v}\beta\text{6}$ = integrin $\alpha\text{v}\beta\text{6}$; CAF = cancer associated fibroblast; FAP = fibroblast activation protein; FAPI= FAP inhibitor; ^{18}F = ^{18}F Fluorodeoxyglucose labelled; ^{18}F -FDG = ^{18}F -fluorodeoxyglucose; ^{18}F -FLT = ^{18}F -fluorothymidine; ^{18}F -FP-R01-MG-F2 = ^{18}F labelled integrin tracer; ^{18}F -PSMA = ^{18}F labelled PSMA; ^{68}Ga = ^{68}Ga Gallium labelled; ^{68}Ga -DOTA-FAPI-04= ^{68}Ga labelled (macrocyclic chelator) 1,4,7,10-tetraazacyclododecane-1,4,7,10-tetraacetic acid-FAPI-04; ^{68}Ga -FAP = ^{68}Ga labelled fibroblast activation protein inhibitor; ^{68}Ga -NODAGA-R01-MG = ^{68}Ga labelled integrin tracer; ^{68}Ga -Trivehexin = ^{68}Ga labelled Trivehexin; ^{68}Ga -PSMA= ^{68}Ga labelled PSMA; PSMA= prostate-specific membrane antigen.

Integrin $\alpha\text{v}\beta\text{6}$

Integrins are proteins that facilitate adhesion of cells to extracellular matrix (ECM) of polypeptides. Integrins play a crucial role in the signalling pathway for the regulation of cell differentiation, migration, proliferation and apoptosis³⁹⁻⁴⁰. In many cancers the expression of specific integrins can become dysregulated, such as $\alpha\text{v}\beta\text{3}$ and $\alpha\text{v}\beta\text{6}$. Overexpression of $\alpha\text{v}\beta\text{3}$ results in over-promotion of the angiogenesis pathway^{39, 41}.

Integrin $\alpha\beta6$ promotes PDAC by modulating proliferation, survival, migration and invasion of both the cancer cells and its microenvironment⁴². Studies have shown higher expressions of $\alpha\beta6$ in PDAC compared to other type of cancers^{39,43-44}, also differentiation of PDAC from pancreatitis was possible⁴⁵. Additionally tumour positive lymph nodes also showed elevated levels of $\alpha\beta6$ ⁴⁵. As $\alpha\beta6$ seems to be an important integrin for the detection of PDAC and the distinguishment from pancreatitis, numerous research groups have been developing PET tracers⁴⁶⁻⁴⁸. Kimura et al. used ¹⁸F-FPR01-MG-F2 to target $\alpha\beta6$. (Figure 1.3, Table 1). The study group demonstrated that the targeting peptide was able to penetrate the pancreatic tumour rapidly and also showed an improved uptake compared to ¹⁸F-FDG, reflecting the difference in the peptide's target, namely glucose metabolism versus expression of ECM protein. In addition it was observed that uptake only occurred in the viable part of the tumour compared to parts of significant necrosis³⁹. A recent small study from Quigley et al. showed the first promising result for ⁶⁸Ga-labeled trimerized $\alpha\beta6$ -integrin selective nonapeptide (⁶⁸Ga-Trivehexin) enabled PET-CT imaging. One patient, out of a total of four, was included with PDAC, showing a high tracer uptake in the pancreatic tumour including multiple liver metastases⁴⁹.

Prostate-Specific Membrane Antigen targeted PET-CT imaging

Currently different types of radiolabelled-PSMA tracers exist (i.e. ¹⁸F-PSMA, ⁶⁸Ga-PSMA) with different biodistribution, as largely described in literature⁵⁰. Prostate-specific membrane antigen (PSMA) is a type II transmembrane glycoprotein highly expressed on the surface of prostate cancer cells. The expression of PSMA in tumour-associated (neo) vasculature of prostate cancer, breast cancer and primary gliomas have been reported, and has also proven to be high in PDAC⁵¹⁻⁵³. Immunohistochemical experiments from our group showed high expression of PSMA in 4 out of 5 patients with PDAC de novo, as well as in 32 out of 33 PDAC patients after neoadjuvant treatment (mean tumour H-score of 99 (maximum 300)). These experiments also showed no expression on adjacent normal and pancreatitis tissue (H-score 0), thus yielding high tumour contrast with the background and an improved tumour detection⁵⁴. Radiolabelled PSMA targeted PET-CT has proven highly successful for primary staging and restaging of prostate cancer patients and is currently being implemented worldwide⁵⁵⁻⁵⁶. PSMA expression can be imaged by labelling small inhibitor molecules, with PET radionuclides, i.e., ¹⁸F or ⁶⁸Ga⁵⁷. (Figure 1.4, Table 1)

¹⁸F labelled Prostate-Specific Membrane Antigen - ¹⁸F-PSMA

¹⁸F-radiolabelled PSMA PET has been recently technically validated and successfully implemented in clinical practice for prostate cancer^{54-55,58}. With one of the more commonly used variants the ¹⁸F-DCFpYL, a second generation ¹⁸F-fluorinated PSMA-ligand, has advantages over ⁶⁸Ga-labelled PSMA tracers. It provides namely a higher spatial resolution, along with a longer half-life, which may result in a more accurate

staging due to the detection of small local tumour deposits⁵⁹.

⁶⁸Ga labelled Prostate-specific Membrane Antigen - ⁶⁸Ga-PSMA

Krishnaraju et al. showed improved diagnostic accuracy with ⁶⁸Ga-PSMA compared to ¹⁸F-FDG in a study among 40 patients with pancreatic lesions - positive predictive value 90.5% vs. 65.4%, for ⁶⁸Ga-PSMA compared to ¹⁸F-FDG; accuracy 92.5% vs. 72.5%, respectively⁵⁷.

PART II: TARGETED RADIONUCLIDE THERAPY OF PANCREATIC DUCTAL ADENOCARCINOMA

Locally advanced and metastatic pancreatic cancer has a poor prognosis. Current standard of care treatment such as gemcitabine or FOLFIRINOX provides minimal survival benefit. Targeted radionuclide therapy may provide improved survival in addition to less systemic toxicity seen with current chemotherapy⁶⁰. In patients with cancer, the ultimate goal is first to identify the receptor expression (by using a diagnostic scan with a diagnostic tracer) and then, in case of an adequate expression of the receptor, to use the tracer, radiolabelled with alpha or beta-particles, for therapeutic purposes, with curative or sometimes palliative intent⁶¹.

In addition to therapy with radiolabelled antibodies, there is a possibility to add gemcitabine, serving as a radiosensitizer, which is generally well tolerated in combination with external radiotherapy⁶²⁻⁶⁶.

In this second part we discuss the theranostic applications of tumour specific tracers. To our knowledge, there have only been 2 different types of antibodies that have been reported on in humans as targeted radionuclide therapy of PDAC; ¹³¹I-KAb201 antibody and ⁹⁰Y-clivayuzumab tetraxetan antibody (⁹⁰Y-labelled hPAM4). Furthermore there is only one single study registered at popular databases that is currently recruiting patients and focusing on the theranostic pair of ⁶⁸Ga-DOTA-5G /¹⁷⁷Lu-DOTA-ABM-5G⁶⁷.

¹³¹I labelled KAb201 antibody - ¹³¹I-KAb201

Carcinoembryonic antigen (CEA) is expressed in most patients with pancreatic cancer and therefore serves as an interesting target for antibodies. One potential antibody is KAb201, an anti-CEA antibody labelled with ¹³¹Iodine⁶⁸.

Sultana et al. performed a randomised Phase I/II trial assessing the safety and efficacy of ¹³¹I-KAb201 in patients with inoperable PDAC. Patients were randomized to receive ¹³¹I-KAb201 via either the intra-arterial (gastroduodenal artery) or intravenous (standard

intravenous line) delivery route. The hypothesis of including an intra-arterial delivery route is expected higher concentration of the radiolabelled drug at the target site and thus increased effectiveness with reduced toxicity⁶⁸. In total nineteen patients were randomised (9 in the intravenous arm, 10 in the intra-arterial arm), of whom 1 patient was excluded from the intra-arterial arm as there was no uptake on the pre-therapy scan. The overall response rate was 6% (1 out of 18 patients). Dose limiting toxicity was only reached in the intra-arterial route (at 50 mCi). Both anti-chimeric antibodies (HACA) and anti-sheep antibodies (HASA) developed in the entire study population, thus limiting the possibility of repeat dosing as this could lead to either hypersensitivity reactions or to complexing with circulating antibodies, creating a challenge to maintain effective therapeutic levels⁶⁸⁻⁶⁹. Median overall survival was 5.2 months (95% CI = 3.3-9.0 months), with no significant difference between either delivery arm (log rank test $p = 0.79$)⁷⁰. Survival and efficacy data are comparable with a single agent therapy of gemcitabine⁷¹⁻⁷³. Future improvement can be found in the ability to predict the occurrence and type (I or II) of antibody response, thus aiding the possibility of repeat dosing. Also humanisation of the antibody may reduce the immunogenicity⁶⁸.

⁹⁰Y labelled clivazutumab tetraxetan antibody - ⁹⁰Y-hPAM4

Preclinical studies in nude mice have shown that ⁹⁰Y-labelled PAM4 decelerates tumour growth^{70,74}. PAM4 is a monoclonal antibody which binds to a mucin produced primarily in PDAC⁷⁵⁻⁷⁸. Gulec et al. performed a phase I single-dose escalation trial among 21 patients with PDAC (4 stage III- locally advanced; 17 stage IV- metastatic) with the primary aim to determine dose-limiting toxicity and the maximum tolerated dose. Patients first received ¹¹¹In-hPAM4 for diagnostic imaging and finally ⁹⁰Y-hPAM4 for therapy⁷⁹. Drug-related toxicities among the study group were grade 3/4 neutropenia and thrombocytopenia, which both increased with ⁹⁰Y dose. Fourteen patients progressed rapidly, however 7 patients remained progression-free for 2-6 months, with 3 patients showing partial response with tumour shrinkage. The combination with gemcitabine showed further improvements⁷⁹.

Fractionated dosing of ⁹⁰Y-hPAM4 (for increased total radiation dose) in combination with gemcitabine acting as a radiosensitizer (for increased potency of the radiation) could be a promising treatment regimen^{38,79}. Ocean et al. showed in a phase 1 trial among 38 untreated patients with pancreatic cancer (5 stage III- locally advanced, 33 stage IV- metastatic) that fractionated dosing of ⁹⁰Y-hPAM4 in combination with gemcitabine in repeated cycles (number of cycles varied among the patients) allowed for double the radioimmunotherapy dose⁸⁰.

Drug-related toxicities among the study group were grade 3/4 thrombocytopenia and neutropenia in 28 patients. Sixteen patients showed stabilization and 6 patients a

partial response. Median overall survival was 7.7 months for all patients, with improved survival up to 11.8 months with repeated cycles⁸⁰. An important terminated and unpublished study is the PANCRIT-1 trial. This was an international, multi-center, double-blind, randomized phase III trial of ⁹⁰Y-labelled hPAM4 in combination with gemcitabine versus placebo in combination with gemcitabine in patients with metastatic PDAC who had progressed despite receiving at least two prior therapies for metastatic disease. After enrolment of 334 patients, an interim analysis on overall survival was performed, showing that the treatment arm did not demonstrate a sufficient improvement in overall survival⁸¹. One major flaw of the study seems to be the lack of pre-treatment evaluation of receptor expression, thus not applying the theranostic concept.

⁶⁸Ga-DOTA-5G /¹⁷⁷Lu-DOTA-ABM-5G theranostic pair

(⁶⁸Gallium labelled- DOTA – 5G / ¹⁷⁷labelled Lutetium – DOTA–ABM-5G; DOTA=1,4,7,10-tetraazacyclododecane-1,4,7,10-tetraacetic acid)

The only study listed on a clinical study database (ClinicalTrials.gov) is from Sutcliffe et al. from the University of California. This is a phase I study evaluating the safety and efficacy of the theranostic pair of ⁶⁸Ga-DOTA-5G /¹⁷⁷Lu-DOTA-ABM-5G in patients with locally advanced or metastatic PDAC. Patients first receive a diagnostic ⁶⁸Ga-DOTA-5G PET scan, subsequently only the patients that show uptake receive ¹⁷⁷Lu-DOTA-ABM-5G as therapy.

The primary objective is to identify the dose limiting toxicity and the recommend phase 2 dose. The objective is to enrol 30 participants with an expected completion in 2023⁶⁷.

In summary, results from the study with ¹³¹I-KAb201 demonstrated the importance of further investigation into the type of antibody response and the ability to predict this adverse event for the possibility of repeat dosing. Future research will learn if humanisation of the antibody is able to reduce immunogenicity. Also, the route of delivery (intra-arterial versus intravenous) did not show any difference in survival benefit or reduction in toxicity. Studies using ⁹⁰Y-labelled hPAM4 proved that dose fractioning could be successful in increasing the total radiation dose without an increasing adverse events. In addition the combination with gemcitabine acting as a radiosensitizer can increase the potency of the radiation. Future research, including randomized controlled trials, will need to confirm these results.

We are looking forward to the first results from the ⁶⁸Ga-DOTA-5G /¹⁷⁷Lu-DOTA-ABM-5G theranostic pair, as evaluation of quantifiable antibody localization at the site of disease before administering a therapeutic dose seems to be the best tailored made medicine.

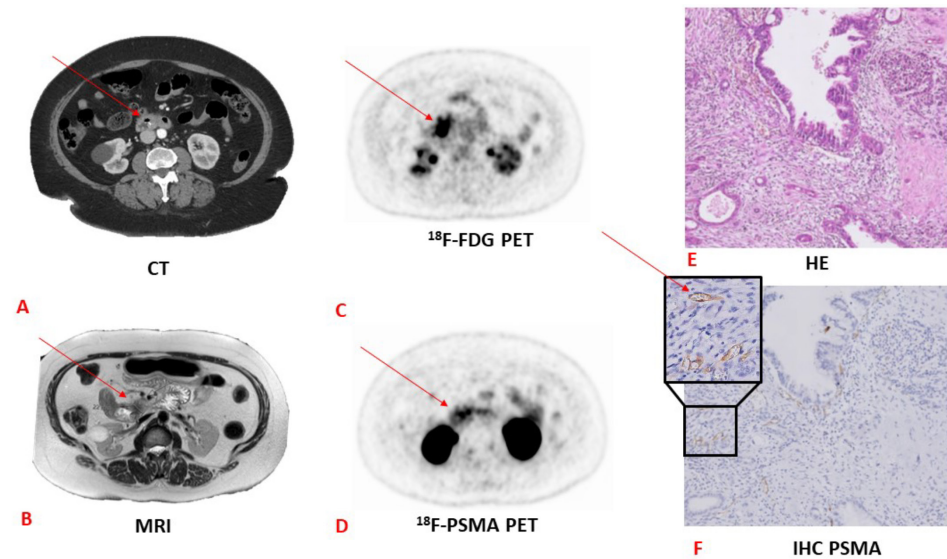


FIGURE 2. CT vs MRI vs ^{18}F -FDG vs ^{18}F -PSMA PET and corresponding pathology and HE and immunohistochemistry coupes in a patient with pancreatic adenocarcinoma

A: CT image with arrow pointing towards pancreatic lesion; B: MRI image with arrow pointing towards pancreatic lesion; C: ^{18}F -FDG PET image with arrow pointing towards pancreatic lesion; D: ^{18}F -PSMA PET image with arrow pointing towards pancreatic lesion. Note the more specific PSMA uptake compared to the ^{18}F -FDG PET scan; E: Hematoxylin and Eosin staining (HE) image. Adenocarcinoma is not visible on this staining; F: immunohistochemistry staining of PSMA. The arrow points towards stained PSMA. CT, computed tomography; MRI, magnetic resonance imaging; PET, positron emitting tomography; HE, hematoxylin eosin; IHC, immunohistochemistry.

(The "HE image" has previously been published by our study group⁸² and is licensed under a Creative Commons Attribution 4.0 International - <http://creativecommons.org/licenses/by/4.0>)

SUMMARY AND CHALLENGES FOR THE FUTURE

Impressive efforts have been made in improving tumour specific tracers for the detection of PDAC. In patients with PDAC, the ultimate goal is to firstly identify the radiolabelled peptide expression and then, in case of an adequate expression of the peptide, to use the tracer, radiolabelled with alpha or beta-particles, for therapeutic purposes, with curative or sometimes palliative intent. ^{18}F -FDG is a well-known radiotracer that already is being used in PDAC. An important limitation, however, is that increased glucose metabolism is not specific for malignant processes only, but can be also found in inflammatory and infectious disease sites. The specificity of PET imaging for the diagnosis of PDAC could be improved by a more disease specific imaging agent.

In general there are currently three types of tracers. Tracers that accumulate in the proliferating cell, such as ^{18}F -FLT. The second type of tracers target highly expressed integrin receptors or PSMA on the surface of cells in PDAC. In this group ^{18}F -PSMA is a

promising tracer (Figure 2) that already has been validated and successfully implemented in clinical practice for prostate cancer. The last type of tracer targets fibroblast activation protein (FAP inhibitor), which is expressed by CAF (cancer associated fibroblast).

Targeted radionuclide therapy is still in its infancy. The effectiveness of targeted radionuclide therapy has been limited by poor delivery to tumours. There have only been 2 different types of antibodies that have been reported on in humans as targeted radionuclide therapy of pancreatic ductal adenocarcinoma; ^{131}I -KAb201 antibody and ^{90}Y -clivayuzumab tetraxetan antibody (^{90}Y -labelled hPAM4). Besides selecting the correct radionuclide antibody, important contributing factors for successful therapy is dose fractioning and the addition of a radiosensitizer, such as gemcitabine.

These novel diagnostic and therapeutic approaches, in population often characterized by poor outcome and decreased quality of life, has the potential to add a new chapter to a patient's life.

REFERENCES

1. Vincent A, Herman J, Schulick R, Hruban RH, Goggins M. Pancreatic cancer. *Lancet*. 2011 Aug 13;378(9791):607-20.
2. Latenstein AEJ, van der Geest LGM, Bonsing BA, Groot Koerkamp B, Haj Mohammad N, de Hingh IHJT, et al.; Dutch Pancreatic Cancer Group. Nationwide trends in incidence, treatment and survival of pancreatic ductal adenocarcinoma. *Eur J Cancer*. 2020 Jan;125:83-93.
3. Gerritsen A, Molenaar IQ, Bollen TL, Nio CY, Dijkgraaf MG, van Santvoort HC, et al. Preoperative characteristics of patients with presumed pancreatic cancer but ultimately benign disease: a multicenter series of 344 pancreatoduodenectomies. *Ann Surg Oncol*. 2014 Nov;21(12):3999-4006.
4. van Veldhuisen E, van den Oord C, Brada LJ, Walma MS, Vogel JA, Wilmink JW, et al. Locally Advanced Pancreatic Cancer: Work-Up, Staging, and Local Intervention Strategies. *Cancers (Basel)*. 2019 Jul 12;11(7):976.
5. Orlando LA, Kulasingam SL, Matchar DB. Meta-analysis: the detection of pancreatic malignancy with positron emission tomography. *Aliment Pharmacol Ther*. 2004 Nov 15;20(10):1063-70.
6. Montemagno C, Cassim S, De Leiris N, Durivault J, Faraggi M, Pagès G. Pancreatic Ductal Adenocarcinoma: The Dawn of the Era of Nuclear Medicine? *Int J Mol Sci*. 2021 Jun 15;22(12):6413.
7. Ren H, Zhang H, Wang X, Liu J, Yuan Z, Hao J. Prostate-specific membrane antigen as a marker of pancreatic cancer cells. *Med Oncol*. 2014 Mar;31(3):857.
8. Petrone MC, Arcidiacono PG. New strategies for the early detection of pancreatic cancer. *Expert Rev Gastroenterol Hepatol*. 2016;10(2):157-9.
9. Canto MI, Goggins M, Hruban RH, Petersen GM, Giardiello FM, Yeo C, et al. Screening for early pancreatic neoplasia in high-risk individuals: a prospective controlled study. *Clin Gastroenterol Hepatol*. 2006 Jun;4(6):766-81; quiz 665.
10. Maire F, Couvelard A, Palazzo L, Aubert A, Vullierme MP, Rebours V, et al. Pancreatic intraepithelial neoplasia in patients with intraductal papillary mucinous neoplasms: the interest of endoscopic ultrasonography. *Pancreas*. 2013 Nov;42(8):1262-6.
11. Del Chiaro M, Verbeke C, Salvia R, Klöppel G, Werner J, McKay C, et al. European Study Group on Cystic Tumours of the Pancreas. European experts consensus statement on cystic tumours of the pancreas. *Dig Liver Dis*. 2013 Sep;45(9):703-11.
12. Tanaka M, Fernández-del Castillo C, Adsay V, Chari S, Falconi M, Jang JY, et al; International Association of Pancreatology. International consensus guidelines 2012 for the management of IPMN and MCN of the pancreas. *Pancreatology*. 2012 May-Jun;12(3):183-97.
13. Del Chiaro M, Segersvärd R, Lohr M, Verbeke C. Early detection and prevention of pancreatic cancer: is it really possible today? *World J Gastroenterol*. 2014 Sep 14;20(34):12118-31.
14. Tummers WS, Willmann JK, Bonsing BA, Vahrmeijer AL, Gambhir SS, Swijnenburg RJ. Advances in Diagnostic and Intraoperative Molecular Imaging of Pancreatic Cancer. *Pancreas*. 2018 Jul;47(6):675-689.
15. Conroy T, Desseigne F, Ychou M, Bouché O, Guimbaud R, Bécauarn Y, et al. FOLFIRINOX versus gemcitabine for metastatic pancreatic cancer. *N Engl J Med*. 2011 May 12;364(19):1817-25.
16. Ferrone CR, Marchegiani G, Hong TS, Ryan DP, Deshpande V, McDonnell EI, et al. Radiological and surgical implications of neoadjuvant treatment with FOLFIRINOX for locally advanced and borderline resectable pancreatic cancer. *Ann Surg*. 2015 Jan;261(1):12-7.
17. Panda A, Garg I, Johnson GB, Truty MJ, Halfdanarson TR, Goenka AH. Molecular radionuclide imaging of pancreatic neoplasms. *Lancet Gastroenterol Hepatol*. 2019 Jul;4(7):559-570.
18. Samuel N, Hudson TJ. The molecular and cellular heterogeneity of pancreatic ductal adenocarcinoma. *Nat Rev Gastroenterol Hepatol*. 2011 Dec 20;9(2):77-87.
19. Gambhir SS, Czernin J, Schwimmer J, Silverman DH, Coleman RE, Phelps ME. A tabulated summary of the FDG PET literature. *J Nucl Med*. 2001 May;42(5 Suppl):1S-93S.
20. Ghaneh P, Hanson R, Titman A, Lancaster G, Plumpton C, Lloyd-Williams H, et al. PET-PANC: multicentre prospective diagnostic accuracy and health economic analysis study of the impact of combined modality 18fluorine-2-fluoro-2-deoxy-d-glucose positron emission tomography with computed tomography scanning in the diagnosis and management of pancreatic cancer. *Health Technol Assess*. 2018 Feb;22(7):1-114.
21. Yokoyama Y, Nagino M, Hiromatsu T, Yuasa N, Oda K, Arai T, et al. Intense PET signal in the degenerative necrosis superimposed on chronic pancreatitis. *Pancreas*. 2005 Aug;31(2):192-4.
22. Epelbaum R, Frenkel A, Haddad R, Sikorski N, Strauss LG, Israel O, Dimitrakopoulou-Strauss A. Tumour aggressiveness and patient outcome in cancer of the pancreas assessed by dynamic 18F-FDG PET/CT. *J Nucl Med*. 2013 Jan;54(1):12-8.
23. Lee JW, Kang CM, Choi HJ, Lee WJ, Song SY, Lee JH, Lee JD. Prognostic Value of Metabolic Tumour Volume and Total Lesion Glycolysis on Preoperative 18F-FDG PET/CT in Patients with Pancreatic Cancer. *J Nucl Med*. 2014 Jun;55(6):898-904.
24. Kato K, Nihashi T, Ikeda M, Abe S, Iwano S, Itoh S, Shimamoto K, Naganawa S. Limited efficacy of (18)F-FDG PET/CT for differentiation between metastasis-free pancreatic cancer and mass-forming pancreatitis. *Clin Nucl Med*. 2013 Jun;38(6):417-21.
25. Sahani DV, Bonaffini PA, Catalano OA, Guimaraes AR, Blake MA. State-of-the-art PET/CT of the pancreas: current role and emerging indications. *Radiographics*. 2012 Jul-Aug;32(4):1133-58; discussion 1158-60.
26. Chang J, Schomer D, Dragovich T. Anatomical, Physiological, and Molecular Imaging for Pancreatic Cancer: Current Clinical Use and Future Implications. *Biomed Res Int*. 2015;2015:269641.
27. Chalkidou A, Landau DB, Odell EW, Cornelius VR, O'Doherty MJ, Marsden PK. Correlation between Ki-67 immunohistochemistry and 18F-fluorothymidine uptake in patients with cancer: A systematic review and meta-analysis. *Eur J Cancer*. 2012 Dec;48(18):3499-513.
28. Röhrich M, Naumann P, Giesel FL, Choyke PL, Staudinger F, Wefers A, et al. Impact of 68Ga-FAPI PET/CT Imaging on the Therapeutic Management of Primary and Recurrent Pancreatic Ductal Adenocarcinomas. *J Nucl Med*. 2021 Jun 1;62(6):779-786.
29. von Ahrens D, Bhagat TD, Nagrath D, Maitra A, Verma A. The role of stromal cancer-associated fibroblasts in pancreatic cancer. *J Hematol Oncol*. 2017 Mar 28;10(1):76.
30. Sun Q, Zhang B, Hu Q, Qin Y, Xu W, Liu W, Yu X, Xu J. The impact of cancer-associated fibroblasts on major hallmarks of pancreatic cancer. *Theranostics*. 2018 Oct 6;8(18):5072-5087.
31. Kalluri R. The biology and function of fibroblasts in cancer. *Nat Rev Cancer*. 2016 Aug 23;16(9):582-98.
32. Sahai E, Astsaturou I, Cukierman E, DeNardo DG, Egeblad M, Evans RM, et al. A framework for advancing

- our understanding of cancer-associated fibroblasts. *Nat Rev Cancer*. 2020 Mar;20(3):174-186.
33. McCarthy JB, El-Ashry D, Turley EA. Hyaluronan, Cancer-Associated Fibroblasts and the Tumor Microenvironment in Malignant Progression. *Front Cell Dev Biol*. 2018 May 8;6:48.
 34. Chen H, Pang Y, Wu J, Zhao L, Hao B, Wu J, et al. Comparison of [⁶⁸Ga]Ga-DOTA-FAPI-04 and [¹⁸F] FDG PET/CT for the diagnosis of primary and metastatic lesions in patients with various types of cancer. *Eur J Nucl Med Mol Imaging*. 2020 Jul;47(8):1820-1832.
 35. Luo Y, Pan Q, Zhang W, Li F. Intense FAPI Uptake in Inflammation May Mask the Tumor Activity of Pancreatic Cancer in 68Ga-FAPI PET/CT. *Clin Nucl Med*. 2020 Apr;45(4):310-311.
 36. Luo Y, Pan Q, Zhang W. IgG4-related disease revealed by ⁶⁸Ga-FAPI and ¹⁸F-FDG PET/CT. *Eur J Nucl Med Mol Imaging*. 2019 Nov;46(12):2625-2626.
 37. Pan Q, Luo Y, Zhang W. Recurrent Immunoglobulin G4-Related Disease Shown on 18F-FDG and 68Ga-FAPI PET/CT. *Clin Nucl Med*. 2020 Apr;45(4):312-313.
 38. Ocean AJ, Guarino MJ, Pennington KL, O'Neil BH, Rocha Lima CS, Bekaii-Saab TS, et al. Therapeutic effects of fractionated radioimmunotherapy (RAIT) with clivatuzumab tetraxetan combined with low-dose gemcitabine (Gem) in advanced pancreatic cancer (APC). *J Clin Oncol* 2010;28:75.
 39. Kimura RH, Wang L, Shen B, Huo L, Tummers W, Filipp FV, et al. Evaluation of integrin $\alpha\beta_6$ cystine knot PET tracers to detect cancer and idiopathic pulmonary fibrosis. *Nat Commun*. 2019 Oct 14;10(1):4673.
 40. Hynes RO. Integrins: bidirectional, allosteric signaling machines. *Cell*. 2002 Sep 20;110(6):673-87.
 41. Desgrosellier JS, Cheresh DA. Integrins in cancer: biological implications and therapeutic opportunities. *Nat Rev Cancer*. 2010 Jan;10(1):9-22.
 42. Reader CS, Vallath S, Steele CW, Haider S, Brentnall A, Desai A, et al. The integrin $\alpha\beta_6$ drives pancreatic cancer through diverse mechanisms and represents an effective target for therapy. *J Pathol*. 2019 Nov;249(3):332-342.
 43. Bandyopadhyay A, Raghavan S. Defining the role of integrin $\alpha\beta_6$ in cancer. *Curr Drug Targets*. 2009 Jul;10(7):645-52.
 44. Sipos B, Hahn D, Carceller A, Piulats J, Hedderich J, Kalthoff H, et al. Immunohistochemical screening for β_6 -integrin subunit expression in adenocarcinomas using a novel monoclonal antibody reveals strong up-regulation in pancreatic ductal adenocarcinomas in vivo and in vitro. *Histopathology*. 2004 Sep;45(3):226-36.
 45. Vachiranubhap B, Kim YH, Balci NC, Semelka RC. Magnetic resonance imaging of adenocarcinoma of the pancreas. *Top Magn Reson Imaging*. 2009 Feb;20(1):3-9.
 46. Hausner SH, DiCara D, Marik J, Marshall JF, Sutcliffe JL. Use of a peptide derived from foot-and-mouth disease virus for the noninvasive imaging of human cancer: generation and evaluation of 4-[¹⁸F] fluorobenzoyl A20FMDV2 for in vivo imaging of integrin $\alpha\beta_6$ expression with positron emission tomography. *Cancer Res*. 2007 Aug 15;67(16):7833-40.
 47. Kimura RH, Teed R, Hackel BJ, Pysz MA, Chuang CZ, Sathirachinda A, et al. Pharmacokinetically stabilized cystine knot peptides that bind $\alpha\beta_6$ integrin with single-digit nanomolar affinities for detection of pancreatic cancer. *Clin Cancer Res*. 2012 Feb 1;18(3):839-49.
 48. Altmann A, Sauter M, Roesch S, Mier W, Warta R, Debus J, et al. Identification of a Novel ITG $\alpha\beta_6$ -Binding Peptide Using Protein Separation and Phage Display. *Clin Cancer Res*. 2017 Aug 1;23(15):4170-4180.
 49. Quigley NG, Steiger K, Hoberück S, Czech N, Zierke MA, Kossatz S, et al. PET/CT imaging of head-and-neck and pancreatic cancer in humans by targeting the "Cancer Integrin" $\alpha\beta_6$ with Ga-68-Trivehexin. *Eur J Nucl Med Mol Imaging*. 2021 Sep 24:1–12.
 50. Ceci F, Oprea-Lager DE, Emmett L, Adam JA, Bomanji J, Czernin J, et al. E-PSMA: the EANM standardized reporting guidelines v1.0 for PSMA-PET. *Eur J Nucl Med Mol Imaging*. 2021 May;48(5):1626-1638.
 51. Stock K, Steinestel K, Wiesch R, Mikesch JH, Hansmeier A, Trautmann M, Bet al. Neovascular Prostate-Specific Membrane Antigen Expression Is Associated with Improved Overall Survival under Palliative Chemotherapy in Patients with Pancreatic Ductal Adenocarcinoma. *Biomed Res Int*. 2017;2017:2847303.
 52. Ren H, Zhang H, Wang X, Liu J, Yuan Z, Hao J. Prostate-specific membrane antigen as a marker of pancreatic cancer cells. *Med Oncol*. 2014 Mar;31(3):857.
 53. Sahbai S, Rieping P, Pfannenbergs C, la Fougère C, Reimold M. Pancreatic Ductal Adenocarcinoma With High Radiotracer Uptake in 68Ga-Prostate-Specific Membrane Antigen PET/CT. *Clin Nucl Med*. 2017 Sep;42(9):717-718.
 54. Vuijk FA, de Muynck LDAN, Franken LC, Busch OR, Wilmink JW, Besselink MG, et al. Molecular targets for diagnostic and intraoperative imaging of pancreatic ductal adenocarcinoma after neoadjuvant FOLFIRINOX treatment. *Sci Rep*. 2020 Oct 1;10(1):16211.
 55. Mottet N, van den Bergh RCN, Briers E, Van den Broeck T, Cumberbatch MG, De Santis M, et al. EAU-EANM-ESTRO-ESUR-SIOG Guidelines on Prostate Cancer-2020 Update. Part 1: Screening, Diagnosis, and Local Treatment with Curative Intent. *Eur Urol*. 2021 Feb;79(2):243-262.
 56. Jansen BHE, Cysouw MCF, Vis AN, van Moorselaar RJA, Voortman J, Bodar YJL, et al. Repeatability of Quantitative ¹⁸F-DCFPyL PET/CT Measurements in Metastatic Prostate Cancer. *J Nucl Med*. 2020 Sep;61(9):1320-1325.
 57. Krishnaraju VS, Kumar R, Mittal BR, Sharma V, Singh H, Nada R, et al. Differentiating benign and malignant pancreatic masses: Ga-68 PSMA PET/CT as a new diagnostic avenue. *Eur Radiol*. 2021 Apr;31(4):2199-2208.
 58. Jansen BHE, Yaqub M, Voortman J, Cysouw MCF, Windhorst AD, Schuit RC, et al. Simplified Methods for Quantification of ¹⁸F-DCFPyL Uptake in Patients with Prostate Cancer. *J Nucl Med*. 2019 Dec;60(12):1730-1735.
 59. Rowe SP, Gorin MA, Allaf ME, Pienta KJ, Tran PT, Pomper MG, et al. PET imaging of prostate-specific membrane antigen in prostate cancer: current state of the art and future challenges. *Prostate Cancer Prostatic Dis*. 2016 Sep;19(3):223-30.
 60. Aigner KR, Gailhofer S, Kopp S. Regional versus systemic chemotherapy for advanced pancreatic cancer: a randomized study. *Hepatogastroenterology*. 1998 Jul-Aug;45(22):1125-9.
 61. Shah M, Da Silva R, Gravekamp C, Libutti SK, Abraham T, Dadachova E. Targeted radionuclide therapies for pancreatic cancer. *Cancer Gene Ther*. 2015 Aug;22(8):375-9.
 62. Maitra A, Hruban RH. Pancreatic cancer. *Annu Rev Pathol*. 2008;3:157-88.
 63. Moore MJ, Goldstein D, Hamm J, Figier A, Hecht JR, Gallinger S, et al; National Cancer Institute of Canada Clinical Trials Group. Erlotinib plus gemcitabine compared with gemcitabine alone in patients with advanced pancreatic cancer: a phase III trial of the National Cancer Institute of Canada Clinical Trials Group. *J Clin Oncol*. 2007 May 20;25(15):1960-6.

64. Kulke MH, Blaszkowsky LS, Ryan DP, Clark JW, Meyerhardt JA, Zhu AX, et al. Capecitabine plus erlotinib in gemcitabine-refractory advanced pancreatic cancer. *J Clin Oncol*. 2007 Oct 20;25(30):4787-92.
65. Morgan MA, Parsels LA, Maybaum J, Lawrence TS. Improving gemcitabine-mediated radiosensitization using molecularly targeted therapy: a review. *Clin Cancer Res*. 2008 Nov 1;14(21):6744-50.
66. Pauwels B, Korst AE, Lardon F, Vermorken JB. Combined modality therapy of gemcitabine and radiation. *Oncologist*. 2005 Jan;10(1):34-51.
67. <https://clinicaltrials.gov/ct2/show/NCT04665947>
68. Sultana A, Shore S, Raraty MG, Vinjamuri S, Evans JE, Smith CT, et al. Randomised Phase I/II trial assessing the safety and efficacy of radiolabelled anti-carcinoembryonic antigen I(131) KAb201 antibodies given intra-arterially or intravenously in patients with unresectable pancreatic adenocarcinoma. *BMC Cancer*. 2009 Feb 25;9:66.
69. Adams GP, Weiner LM. Monoclonal antibody therapy of cancer. *Nat Biotechnol*. 2005 Sep;23(9):1147-57.
70. Cardillo TM, Ying Z, Gold DV. Therapeutic advantage of (90)yttrium- versus (131)iodine-labeled PAM4 antibody in experimental pancreatic cancer. *Clin Cancer Res*. 2001 Oct;7(10):3186-92.
71. Berlin JD, Catalano P, Thomas JP, Kugler JW, Haller DG, Benson AB 3rd. Phase III study of gemcitabine in combination with fluorouracil versus gemcitabine alone in patients with advanced pancreatic carcinoma: Eastern Cooperative Oncology Group Trial E2297. *J Clin Oncol*. 2002 Aug 1;20(15):3270-5.
72. Colucci G, Giuliani F, Gebbia V, Biglietto M, Rabitti P, Uomo G, et al. Gemcitabine alone or with cisplatin for the treatment of patients with locally advanced and/or metastatic pancreatic carcinoma: a prospective, randomized phase III study of the Gruppo Oncologia dell'Italia Meridionale. *Cancer*. 2002 Feb 15;94(4):902-10.
73. Burris HA 3rd, Moore MJ, Andersen J, Green MR, Rothenberg ML, Modiano MR, et al. Improvements in survival and clinical benefit with gemcitabine as first-line therapy for patients with advanced pancreas cancer: a randomized trial. *J Clin Oncol*. 1997 Jun;15(6):2403-13.
74. Gold DV, Cardillo T, Vardi Y, Blumenthal R. Radioimmunotherapy of experimental pancreatic cancer with 131I-labeled monoclonal antibody PAM4. *Int J Cancer*. 1997 May 16;71(4):660-7.
75. Gold DV, Karanjawala Z, Modrak DE, Goldenberg DM, Hruban RH. PAM4-reactive MUC1 is a biomarker for early pancreatic adenocarcinoma. *Clin Cancer Res*. 2007 Dec 15;13(24):7380-7.
76. Gold DV, Lew K, Maliniak R, Hernandez M, Cardillo T. Characterization of monoclonal antibody PAM4 reactive with a pancreatic cancer mucin. *Int J Cancer*. 1994 Apr 15;57(2):204-10.
77. Gold DV, Modrak DE, Ying Z, Cardillo TM, Sharkey RM, Goldenberg DM. New MUC1 serum immunoassay differentiates pancreatic cancer from pancreatitis. *J Clin Oncol*. 2006 Jan 10;24(2):252-8.
78. Gold DV, Goggins M, Modrak DE, Newsome G, Liu M, Shi C, Hruban RH, Goldenberg DM. Detection of early-stage pancreatic adenocarcinoma. *Cancer Epidemiol Biomarkers Prev*. 2010 Nov;19(11):2786-94.
79. Gulec SA, Cohen SJ, Pennington KL, Zuckier LS, Hauke RJ, Horne H, et al. Treatment of advanced pancreatic carcinoma with 90Y-Clivatuzumab Tetraxetan: a phase I single-dose escalation trial. *Clin Cancer Res*. 2011 Jun 15;17(12):4091-100.
80. Ocean AJ, Pennington KL, Guarino MJ, Sheikh A, Bekaii-Saab T, Serafini AN, et al. Fractionated radioimmunotherapy with (90)Y-clivatuzumab tetraxetan and low-dose gemcitabine is active in advanced pancreatic cancer: A phase 1 trial. *Cancer*. 2012 Nov 15;118(22):5497-506.
81. <https://clinicaltrials.gov/ct2/show/NCT01956812>
82. Vuijk FA, de Muynck LDAN, Franken LC, Busch OR, Wilmink JW, Besselink MG, et al. Molecular targets for diagnostic and intraoperative imaging of pancreatic ductal adenocarcinoma after neoadjuvant FOLFIRINOX treatment. *Sci Rep*. 2020 Oct 1;10(1):16211.

Molecular imaging of the tumor stroma and beyond

F.A. Vuijk, R. Hovast, V.M. Baart, C.J.H. van de Velde, A.L. Vahrmeijer, M. Slingerland,
L. de Geus-Oei, L.J.A.C. Hawinkels, and C.F.M Sier.

Bookchapter in The Tumor Stroma (2022)



INTRODUCTION

Over the last decades, development of anti-cancer therapy and imaging has primarily been focused on specifically targeting and/or eliminating cancerous cells. This approach has resulted in a tremendous development towards more effective cancer treatment, however, is still insufficient in several cancer types. One of the reasons for this might be the varying percentage of actual malignant cells within a tumor (others include for example tumor heterogeneity and resistance to therapy). Based on various recent studies and depending on cancer type, malignant cells account for approximately 30% of tumor mass, whereas fibroblasts account for 25%, immune cells for 20%, endothelial cells for 5% and macrophages for 5%¹⁻⁴. In recent years, the role and influence of the tumor microenvironment (TME) on tumor development and metastases has been studied extensively, and has resulted in a surge of new research initiatives in the field of TME targeting for both imaging as well as therapeutic purposes. It has been demonstrated that the components of the TME are prominently involved in tumor metabolism, proliferation, invasion, and metastases, and demonstrate a major influence on response to therapy⁵⁻¹⁸. In solid cancers the TME accounts for up to 90% of tumor volume, depending on the cancer type, indicating its importance and relevance as a target for imaging and therapy. Several TME components can be targeted, i.e. the tumor associated vasculature, immune cells like macrophages and T-lymphocytes, cancer-associated fibroblasts (CAF), and the extracellular matrix (ECM). These various components are depicted in **Figure 1**. In addition to imaging via the tumor cells, visualization of the TME might provide extra information about the potential aggressiveness (and size) of the tumor or the potential therapeutic efficacy of targeted therapy. Several imaging techniques have recently been deployed to specifically image the TME rather than the malignant cancer cells. These modalities include optical imaging (fluorescence imaging, optical coherence tomography, and photoacoustic imaging), magnetic resonance imaging (MRI), computed tomography (CT), positron emission tomography (PET), single photon emission computed tomography (SPECT), ultrasound (US) imaging, Cherenkov luminescence imaging, Raman spectroscopy, rapid evaporative ionization mass spectrometry and multispectral optoacoustic tomography¹⁹. The specificity and efficacy of these molecular imaging techniques are dependent on the contrast agents and the molecular TME targets they are focused on²⁰. This chapter will give an overview of the various cells and proteins within the TME, applicable as targets for molecular imaging, including cell types, extracellular matrix components, and alternative approaches.

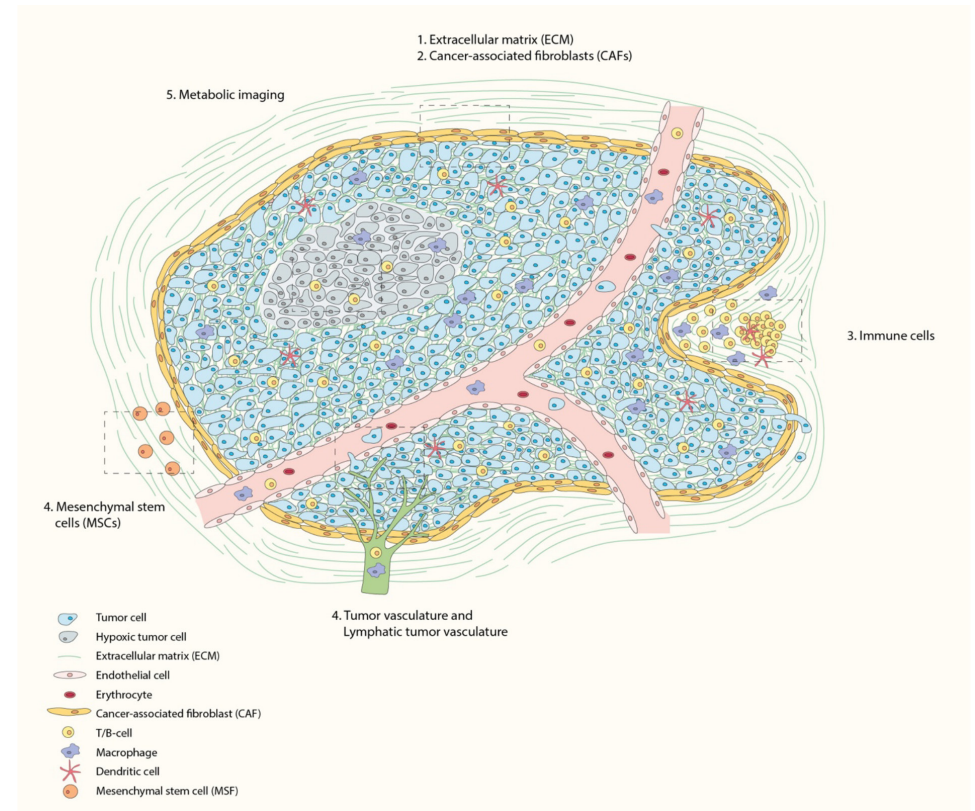


FIGURE 1. Overview of components of the tumor microenvironment.

TUMOR VASCULATURE

Historically, the concept of tumor neoangiogenesis was discovered by Ide, Algire and Chalkley in the first half of the 20th century^{21,22}. They found that growing malignancies continuously induce new capillaries from host tissue, and that specific factors released by the tumor can stimulate this process. Three decades later, Folkman and colleagues stated that tumor growth is neoangiogenesis dependent above a tumor size of 1-2 cm³, to supply nutrients and oxygen and to remove CO₂ and waste products²³. In addition, they reasoned that this process could be used for therapeutic targeting. In order to sustain and promote this process after the so-called 'angiogenic switch', tumor cells secrete pro-angiogenic factors, inducing large, abnormal, and ineffective blood vessels (Figure 1). These factors include for example vascular endothelial growth factor (VEGF), interleukin 8 (IL-8) and tumor growth factor β (TGF- β)²⁴.

Targeted vascular imaging

As there are various pathways involved in the process of neoangiogenesis, downstream proteins expressed within this process can be used for molecular imaging. An example of this is VEGF, inducing endothelial activation and subsequent sprouting of capillaries. The proangiogenic signal of VEGF is mainly mediated by its receptor tyrosine kinases VEGFR-1 and VEGFR-2. Overexpression of VEGFR-2 is seen in various solid tumor types, and is associated with worse prognosis^{25–28}. Various VEGF-axis targeting antibodies have been clinically translated and used in daily clinical practice, including ramucirumab (VEGFR-2) and bevacizumab (VEGF), or tested in clinical trials (tanibirumab (VEGFR-2))²⁹. For imaging purposes, the same antibodies as used for therapeutic purposes can be labeled with imaging probes such as a radioisotope for PET or SPECT imaging, or a fluorescent dye for fluorescent imaging. Various PET and SPECT tracers targeting VEGF and VEGFR's have been developed and clinically translated. Results demonstrated affinity for many different cancer types, and first results show a possible correlation to response to anti-angiogenic treatment^{30,31}. In addition to radiolabeled tracers, a near-infrared (NIR) fluorescent tracer, bevacizumab-IRDye800CW, enabled detection of breast cancer, colorectal cancer and peritoneal metastases either intraoperatively or during endoscopy in various clinical studies^{32–34}. Finally, preclinical research has shown the feasibility of VEGF targeted ultrasound (using microbubbles), and MRI imaging^{31,32,35,36}. In the future, radio-labeled VEGF targeted imaging might provide a tool for patient selection for antiangiogenic treatment.

In addition to VEGF/VEGFR, the integrin $\alpha\beta_3$ is highly expressed by neoangiogenic endothelial cells in tumor areas. Many tracers utilize the tri-peptide Arg-Gly-Asp (RGD) binding sequence, discovered by Ruoslahti and co-workers in 1984, as RGD has high affinity and specificity for several integrins, including $\alpha\beta_3$ ^{37–39}. As with VEGF, a therapeutic compound was developed, cilengitide, to target these integrins for therapeutic purposes⁴⁰.

Various RGD-based PET and SPECT tracers have been developed over the years since 1999 and demonstrate tumor detection of cancers of the lung, mediastinum, breast, head-and-neck, skeletal system and brain (reviewed by Assabella *et al.*⁴¹). An example of RGD based PET imaging of head and neck squamous cell carcinoma is displayed in **Figure 2**. Most recently, this concept has been clinically translated to near-infrared fluorescent imaging of colorectal tumors during surgery^{42,43}. Next to those endothelial cell targets, preclinical studies have evaluated targeted imaging of platelet-derived growth factor receptor (PDGFR)^{44–47}, vasculature cell adhesion molecule 1 (VCAM-1, or CD106)^{48–50} and tumor endothelial marker 1 (TEM-1, also known as endosialin and CD248)^{51,52}. Various endoglin (CD105) targeting microbubbles, MRI contrast agents, PET, SPECT and NIRF agents have been investigated in animal and *ex-vivo* human experiments, but have not been translated into the clinic yet^{53,54}.

In conclusion, as neoangiogenesis is required for growth and development of solid tumors, targeting this mechanism for both imaging and therapeutic purposes seems highly advantageous. In comparison to epithelial tumor targets, angiogenesis associated proteins are generally expressed by a wide variety of cancer types in the periphery and throughout the whole tumor. Epithelial markers mostly apply for a few selected tumor types and expression may vary heterogeneously between various tumor cell subsets. The applicability of angiogenic tracers for monitoring of cancer patients after antiangiogenic therapies or during wound healing seems fundamentally problematic.

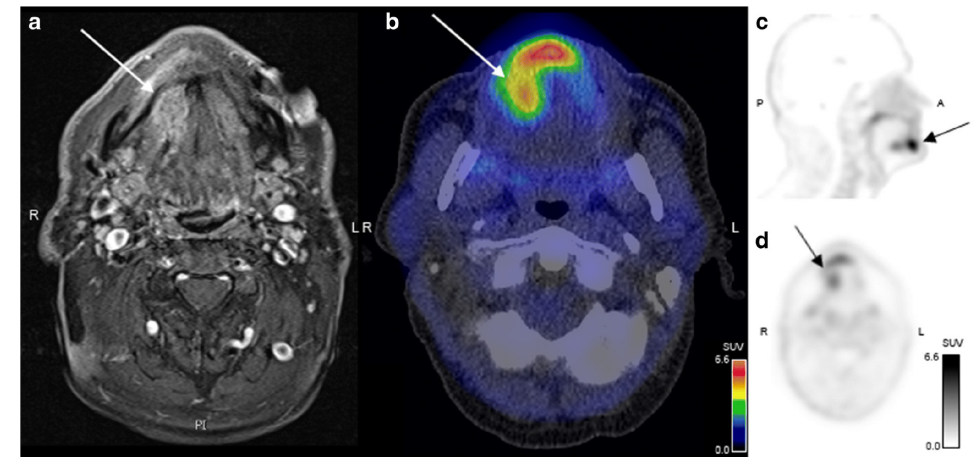


FIGURE 2. Imaging angiogenesis in a patient with head and neck squamous carcinoma by $[^{68}\text{Ga}]\text{Ga-DOTA-E-[c(RGDfk)]}_2$ PET/CT.

PET/CT after injection of 218 MBq ^{68}Ga -RGD in a patient with a moderately differentiated squamous cell carcinoma in the right oral cavity. **a** Transverse plane of magnetic resonance image. **b** Fused PET/CT of the oral cavity revealing a tumor lesion with SUV_{max} of 6.5. **c** and **d** Sagittal and axial PET images demonstrating a clearly visualized tumor in the oral cavity. Image from Lobeek *et al.*⁵⁵.

Lymphatic tumor vasculature

In recent years, the lymphatic tumor vasculature has gained increasing interest as a target for imaging and therapy. Various non-specific tracers have been used to image lymphatic flow in these vessels, known as lymphography or lymphangiography. By injecting a tracer into peripheral tissues, subsequent drainage through the lymphatic system and accumulation in sentinel lymph nodes can be visualized. This procedure can be performed using SPECT ($^{99\text{m}}\text{Tc}$ Technetium, lymphoscintigraphy) and fluorescence imaging (Patent blue, Direct blue, indocyanine green (ICG), and methylene blue)^{56,57}. Lymph node imaging is part of routine care during breast cancer and melanoma surgery, however, also has applications in several other solid tumor operations (including gynecologic, penile and head and neck cancers). Contrast-enhanced MRI has been used to assess vascular leakage and subsequent lymphatic drainage using intravenously

administered biotin-BSA0GGd-DTPA⁵⁸.

With respect to targeted imaging, proteins like lymphatic vessel endothelial hyaluronan receptor 1 (LYVE1), prospero homeobox protein 1 (Prox-1), and VEGFR3 seem overexpressed on tumor associated lymph vasculature and have been visualized using various fluorescent, PET, and SPECT tracers⁵⁷. Until now targeted imaging of lymphatic tumor vasculature has only been explored in preclinical studies and has yet to be translated into the clinic.

As mentioned above, several tracers are known to accumulate in draining lymph nodes after injection, due to the enhanced permeability and retention (EPR) effect. This concept was first described in 1986 by Matsumura and colleagues, and encompasses the entrapment of macromolecules in the tumor interstitium, due to the distinctive vasculature formed by neoangiogenesis and the production of vascular mediators^{59,60}. Tracers using this mechanism include ^{99m}Tc-technetium-nanocolloid (SPECT), ⁶⁸Ga-DOTA-albumin (PET), ICG, methylene blue (NIRF)^{61,62}, and the use of ultrasound⁶³⁻⁶⁵ and microbubbles^{66,67}. However, as this accumulation is a non-specific process based on the EPR effect and serves to identify the (first) draining lymph node(s), this process is not able to specifically differentiate between tumor-positive and tumor-negative lymph nodes and results must be interpreted with caution.

Functional (non-targeted) vascular imaging

Tumor vasculature associated features such as perfusion, permeability and density can be visualized using MRI, PET, CT, fluorescence molecular tomography (FMT), optical coherence tomography (OCT) and photoacoustic imaging. Tumor perfusion can be imaged using dynamic contrast enhanced MRI (DCE-MRI) and CT with or without contrast agents. Using PET/CT, tumor perfusion can be imaged using oxygen-15 labelled water (¹⁵O-H₂O)^{68,69}.

Hypoxia

Tumors are characterized by a highly heterogeneous microenvironment and poor vascularization, resulting in local hypoxia. Hypoxia has been imaged using PET, electron paramagnetic resonance (EPR) and ¹⁹F magnetic resonance spectroscopy (MRS). Several hypoxia-targeting PET, SPECT, and NIRF tracers have been developed. A frequently used marker for hypoxia in preclinical studies is the Hypoxyprobe™ (Hypoxyprobe, Inc., Burlington, Massachusetts, US). Clinically, carbonic anhydrase IX (CAIX) has been proposed as an attractive target⁷⁰⁻⁷⁴, and can be imaged using the PET tracer [⁸⁹Zr] Zr-DFO-girentuximab-PET/CT⁷⁵. The most studied clinical hypoxia tracer, however, is ¹⁸F-FMISO (reviewed by Xu et al.⁷⁶). Other hypoxia tracers include [¹⁸F]FAZA and [¹⁸F]HX4⁷⁷⁻⁷⁹. An example of [¹⁸F]FAZA imaging in lung cancer is displayed in **Figure 3**.

Also, several MRI techniques such as blood oxygen level dependent (BOLD)-, tissue oxygenation level dependent (TOLD)-, and dynamic contrast enhanced (DCE)-MRI have been studied to identify hypoxic areas or changes in tumors⁸⁰. All three methods are used clinically, but do not provide a real-time continuous indication of hypoxic areas. Alternatively, administration of the hypoxia-responsive NIR light emitting agent HyP-1 allowed clear real-time visualization of hypoxia *in vivo*, using bimodal high-resolution NIR/photoacoustic (PA) imaging⁸¹. Similarly, the hypoxia-activated tracers NR-azo and IR1038-MZ allowed bimodal NIR/PA imaging of tumors *in vivo*^{82,83}. However, as hypoxic areas are characterized by insufficient vessels and low perfusion, and thus limited drug delivery, the use of exogenous hypoxia targeting moieties is challenging.

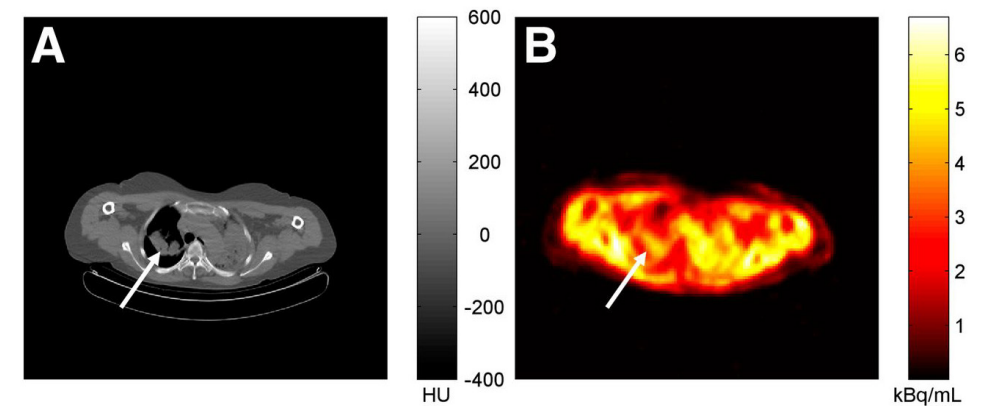


FIGURE 3. Axial images of typical patient diagnosed with non-small cell lung cancer.

(A) Low-dose CT. (B) ¹⁸F-FAZA averaged image for interval from 40 to 70 min after injection, illustrating tumor uptake. White arrow indicates location of tumor (tumor size, 76mL). HU = Hounsfield units. Image from Verwer *et al.*⁸⁴.

IMMUNE CELLS

In addition to endothelial cells, a wide variety of immune cells is present in the TME. Some are supporting tumor outgrowth, whereas other types have a tumor suppressive role. Research into the role and use of immune cells involved in oncogenesis has dramatically increased in the past few years and has led to the development of several variants of immunotherapy to treat various cancer types. Most of these affect tumor growth by increasing the influx and activity (checkpoint inhibition) of cytotoxic T-cells into tumor areas⁸⁵. To promote both the understanding and the possible utilization of immune cells in patients, various immune cell specific tracers have been developed to evaluate and predict tumor response to these immunotherapies. Moreover, abundant

presence of immune cells could also be used for diagnostic tumor imaging.

Three immune cell imaging methods can be distinguished: 1) targeting primary immune cells, 2) immune cell imaging through reporter genes, and 3) reinjection of ex vivo incubated of immune cells with imaging probe. These three methods are visualized in **Figure 4**. Examples of immune cell imaging are represented in **Figure 5**.

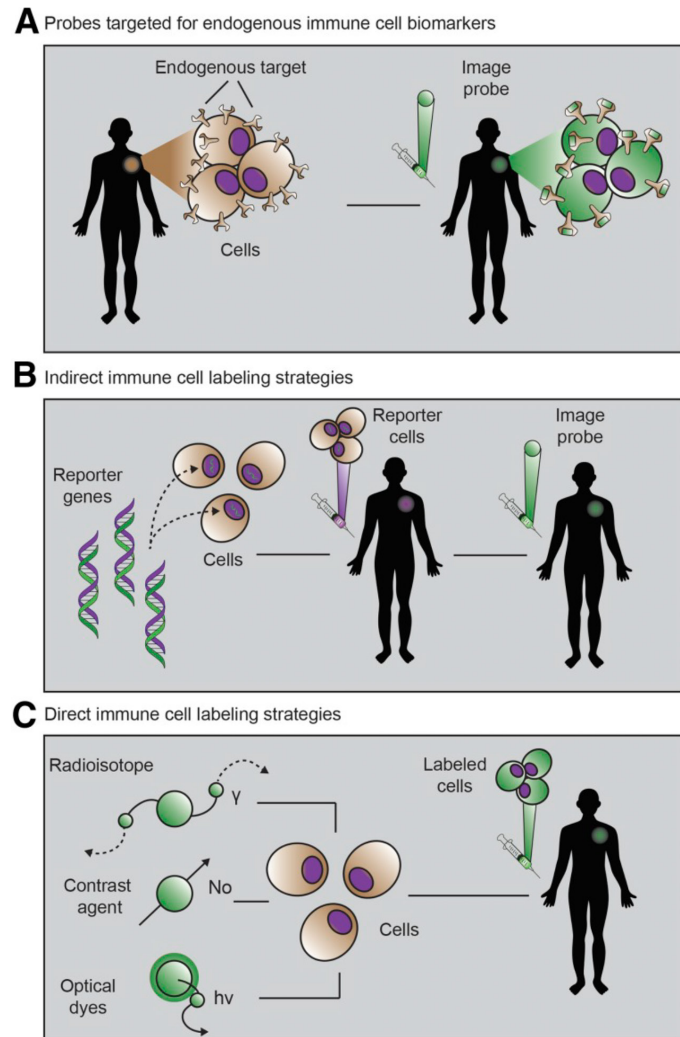


FIGURE 4. The three primary immunoimaging strategies.

(A) Imaging probe targeting natural immune cell receptor is injected. (B) Cells from patient are transduced with reporter gene, re-injected, and visualized via injection of reporter probe. (C) Cells from patient are incubated ex vivo with imaging probe, and labeled cells are injected into patient and monitored via imaging. Image from Mayer *et al.*⁸⁶.

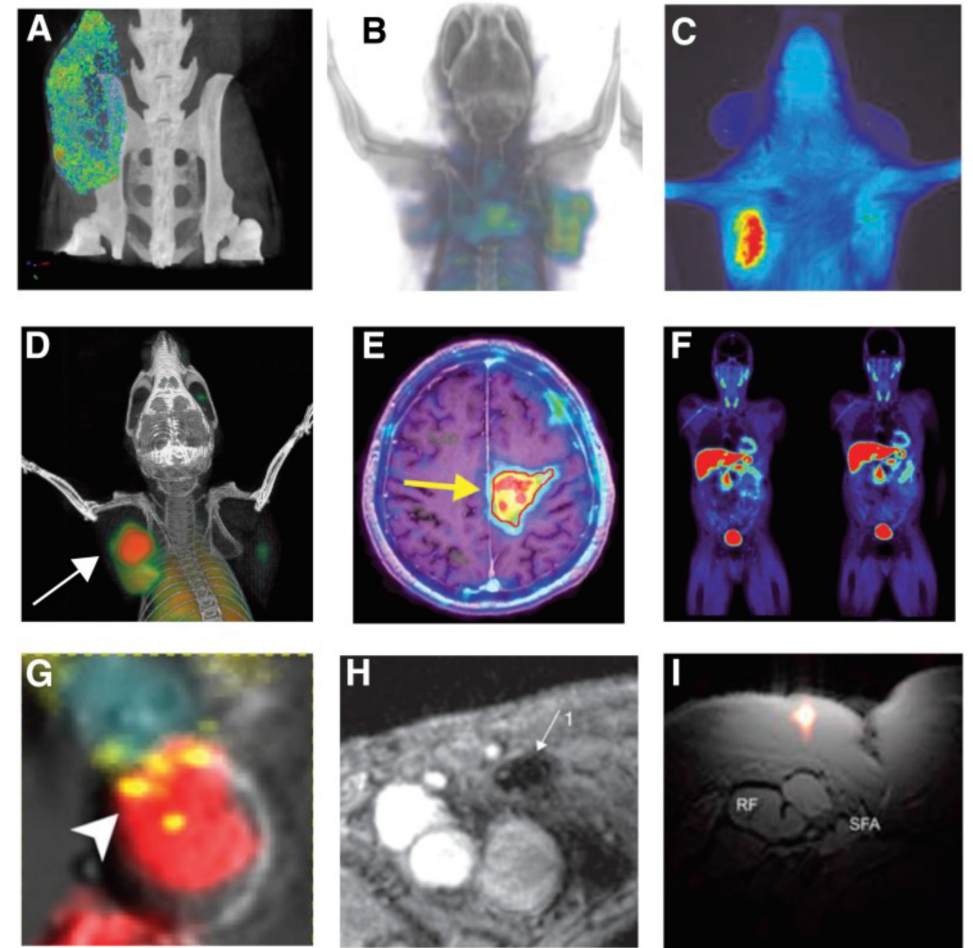


FIGURE 5. Immunoimaging examples.

(A–C) Imaging of PD-L1 immune checkpoint: CT using anti-PD-L1 gold nanoparticles (adapted from Meir *et al.*) (A); PET (B) and optical imaging (C) of humanized antibody to assess PD-L1 expression in tumors (adapted from Chatterjee *et al.*). (D–F) Imaging of activated T cells: PET of OX40 expressed on activated T cells after vaccine treatment within tumor (arrow) (adapted from Alam *et al.*) (D); reporter gene imaging of targeted T-cell immunotherapy in recurrent glioma (arrow) (adapted from Keu *et al.*) (E); PET of ¹⁸F-AraG to visualize activated T cells in acute graft-vs.-host disease (adapted from Ronald *et al.*) (F). (G–I) Imaging of myeloid cells: optical imaging revealing tumor-associated macrophage-mediated mechanism of resistance to anti-PD1 therapy (adapted from Arlauckas *et al.*; macrophage is in red, T cell in blue, and PD-1 in yellow) (G); MRI of dendritic cells labeled with superparamagnetic iron oxide (adapted from de Vries *et al.*; arrow indicates site of decreased signal in lymph node due to superparamagnetic iron oxide-labeled dendritic cell accumulation) (H); axial composite ¹⁹F/¹H MRI after intradermal dendritic cell administration into quadriceps of patient; RF = rectus femoris; SFA = superficial femoral artery) (I). Image from Mayer *et al.*⁸⁶.

T cells

Imaging and quantification of endogenously stimulated or adoptively transferred T-cells can help monitor the ongoing T-cell infiltration in tumor areas, thereby allowing clinicians to define and predict the success of immunotherapy at an early stage⁸⁷. T-cells can be imaged through several different targeting mechanisms, at various different time points during therapy, and has mostly been performed using PET and SPECT.

Early T-cell activation has been studied using SPECT and PET tracers targeting (amongst others) interleukin 2 (IL-2), C-X-C chemokine receptor 4 (CXCR4), and OX40 in clinical trials with varying results, and shows promise in providing evidence of successful immune induction⁸⁷. Unfortunately, the expression of the previously mentioned markers is variable throughout the span of the immune response which complicates the interpretation.

Upon activation, the metabolic activity of T-cells increases. This process can be imaged using tracers targeting T-cell specific metabolic pathways (such as the deoxyribonucleoside salvage pathway). These tracers include [¹⁸F]F-AraG, [¹⁸F]CFA, [¹⁸F]FACBC and [¹⁸F]FLT, which are all directed against different processes following T-cell activation and are currently developed in (pre)clinical trials. Also, several specific subpopulations of T-cells can be imaged by targeting various specific markers, including CD3, CD4, CD8, and CD19-4-1BBL.

After interaction of T-cells with tumor cells, the activity, proliferation and survival of T-cells decreases through PD-1/PD-L1 (programmed death ligand 1) interaction (programmed cell death protein). This process can be imaged using anti-PD-1 tracers, and can thereby select patients for such therapies, as is currently under extensive investigation (these tracers include [⁸⁹Zr]atezolizumab, [⁸⁹Zr]durvalumab)⁸⁸⁻⁹⁰.

After injection of T-cell-based immunotherapy, two methods are common to track these cells *in vivo*: direct labelling with contrast agents or indirect labeling by genetically engineering the cells to express specific reporter genes. The first method has been studied using [¹¹¹In]In-oxine, [⁸⁹Zr]Zr-Oxine, [^{99m}Tc]Tc-HMPAO, [⁸⁹Zr]Zr-DBN, [⁶⁴Cu]Cu-AU-NP, and [⁶⁴Cu]Cu-DOTA-K1 labeled to various cell types to track them *in vivo*. The second method of reporter gene imaging has been performed using various viral reporter genes such as the herpes simplex virus 1 thymidine kinase (HSV-1tk), which are imaged using tracers including [¹⁸F]FHBG and [¹⁸F]BF₄⁻⁹¹.

In the upcoming years, research will most likely focus on the further development and clinical validation of tracers targeting various clinically relevant targets such as PD-1/PD-L1, as these imaging methods could be used for therapy response prediction and improve patient selection for the optimal treatment regimen, and might enable the use

of futile treatment and related toxicity.

Dendritic cells

Dendritic cells are professional antigen presenting cells and needed for T-cell maturation, proliferation, and their cytotoxic effects. They are also involved in antigen transport from peripheral tissues to lymph nodes, and for T cell presentation. Results from a clinical trial show that superparamagnetic iron oxide or ¹¹¹In-labeled dendritic cells can be tracked by MRI or SPECT, respectively, to lymph nodes, and showed more dendritic cell positive lymph nodes than conventional scintigraphy⁹². Unfortunately, dendritic cells are not very prone for imaging due to their low numbers and widespread location, however imaging would be very relevant to predict response to cellular therapeutics such as dendritic cell vaccination.

Tumor associated macrophages

Tumor associated macrophages (TAM) stimulate or inhibit tumor growth by secretion of various agents and by modulating T-cell immunity. Anti-inflammatory and pro-tumor TAMs, currently called M2-(like) TAMs comprise 5-50% of tumor cell mass, whereas M1-(like) TAMs, which are pro-inflammatory and anti-tumor, are less abundant and therefore less appropriate for imaging⁹³. M2 TAMs promote tumor progression by enhancing for example VEGF availability and the production of cytokines (e.g. IL10, IL13, and TGF-β), chemokines, proteases and reactive oxygen species⁹⁴⁻⁹⁸. Non-invasive imaging of TAMs is mostly performed by targeted PET/CT or MRI, and could help stratify patients, as M2 like TAM presence is associated with poor prognosis, and enable individualized patient treatment by distinguishing these two different TAM types on non-invasive imaging⁹⁹. M2 like TAMs are known to secrete factors promoting angiogenesis (CXCL8, VEGF), tumor progression (EGF, FGF and PDGF), epithelial mesenchymal transition (EMT)(TGFβ), and matrix remodeling (MMPs, cathepsins and uPA)¹⁰⁰. Some of these factors are bound directly on the TAMs by specific receptors. Previous research has shown that some of those receptors, like mitochondrial translocator protein (TSPO), mannose receptor CD206, macrophage scavenger receptor CD163, uPAR, and the folate receptor β (FRβ) are distinctive markers for M2 type TAMs^{101,102}. Using TSPO specific PET tracers, tumor uptake was seen in gliomas, however it was uncertain this uptake was due to glioma cell or TAM uptake¹⁰³. Several preclinical studies have shown microglia and TAM uptake of TSPO specific radiotracers in mouse models, however not further specified the TAM type^{104,105}. Preclinical experiments have investigated the use of various CD206 targeting radiotracers, and show great promise for *in vivo* M2 like TAM imaging^{106,107}. FRβ macrophage specific imaging has only been studied in inflammatory disease^{108,109}, whereas FRβ fluorescent imaging has been clinically investigated in tumors expressing FR^{110,111}. Last, CD163 imaging using radiolabeled tracers has been studied in preclinical experiments, however little research has been published using animal models¹¹². In addition to the previously mentioned markers, other targets for macrophage imaging include SCL18B1,

uPAR, iNOS, system X_c, somatostatin receptor, CXCR4 and the cysteine cathepsins^{93,113}.

In addition to radioisotope imaging, magnetic resonance imaging using macrophage specific contrast agents have been investigated. Amongst many different tracers developed and tested in preclinical experiments, only super paramagnetic iron oxide (ferumoxytol) particles (SPIO) have been clinically translated. These SPIOs accumulate in the interstitium of malignant tumors, after which they are phagocytosed by TAMs. As this phagocytosis is a relatively slow process (24 hours), imaging is possible starting 24 hours post injection¹¹⁴. Recently, this concept has been clinically translated for macrophage detection in cancer patients, and might be used for patient stratification^{115,116}. However, anaphylactic reactions have been described following ferumoxytol injection, and limit the use of these agents.

Cancer associated fibroblasts

Compared to endothelial cells and immune cells, cancer associated fibroblasts (CAF) are the most abundant cells in the TME, even outnumbering malignant cells in various cancer types, as is depicted in Figure 1^{1,2}. In tumors with a low percentage of tumor cells, the CAF targeted imaging might provide a good alternative to [¹⁸F]FDG imaging which is suboptimal in these tumors. The origin of CAFs is not completely established yet, as they might develop from various progenitor lineages such as resident fibroblasts, endothelial cells, adipocytes, mesenchymal stromal cells (see next section) and bone marrow derived stem cells¹¹⁷. CAFs are activated during oncogenesis and are found in over 90% of epithelial cancers^{118,119}. In addition to TME, activated fibroblasts are also found in diseases associated with matrix remodeling such as healing wounds, inflammation, infarction and fibrosis, underlining their active role similar processes¹²⁰. Activation of CAFs leads to morphological and functional characteristics distinguishing them from normal fibroblasts, such as enhanced proliferation, and migration properties, associated with the capacity to remodel the extracellular matrix (ECM). The transformation is associated with the production of several CAF specific proteins implicated with either the structure or the function of these cells, like α -smooth muscle actin (α -SMA), vimentin, platelet derived growth factor β (PDGFR β), fibroblast activating protein α (FAP- α), and several matrix establishing or matrix degrading proteins, like collagens and matrix metalloproteinases.

FAP- α is expressed by many CAFs, particularly at the invasive front, and as a type 2 membrane bound glycoprotein (dipeptidyl peptidase 4 family) is particularly suitable for targeted imaging¹²¹. Both antibodies and inhibitor molecules have been evaluated, labelled with radioisotopes or fluorescent proteins^{122–124}. As early as 1994, hepatic metastases from colorectal carcinoma were detected by the anti-FAP antibody ¹³¹I-sibrotuzumab¹²⁵. More recently, several FAP inhibitors (FAPi) have been developed for both imaging and radionuclide therapy, demonstrating specific tumor uptake in

patients with metastasized epithelial carcinomas^{120,126–128}. An example of imaging with this tracer in various cancer types is displayed in **Figure 6**. In addition, an activatable NIRF tracer cleaved by FAP was developed and showed clear tumor uptake during *in vivo* experiments¹²², and recruitment of radiolabeled fibroblasts to tumor areas followed by fluorescence and MRI (using R2 mapping and biexponential resonance relaxometry) using the reporter gene h-ferritin^{129,130}.

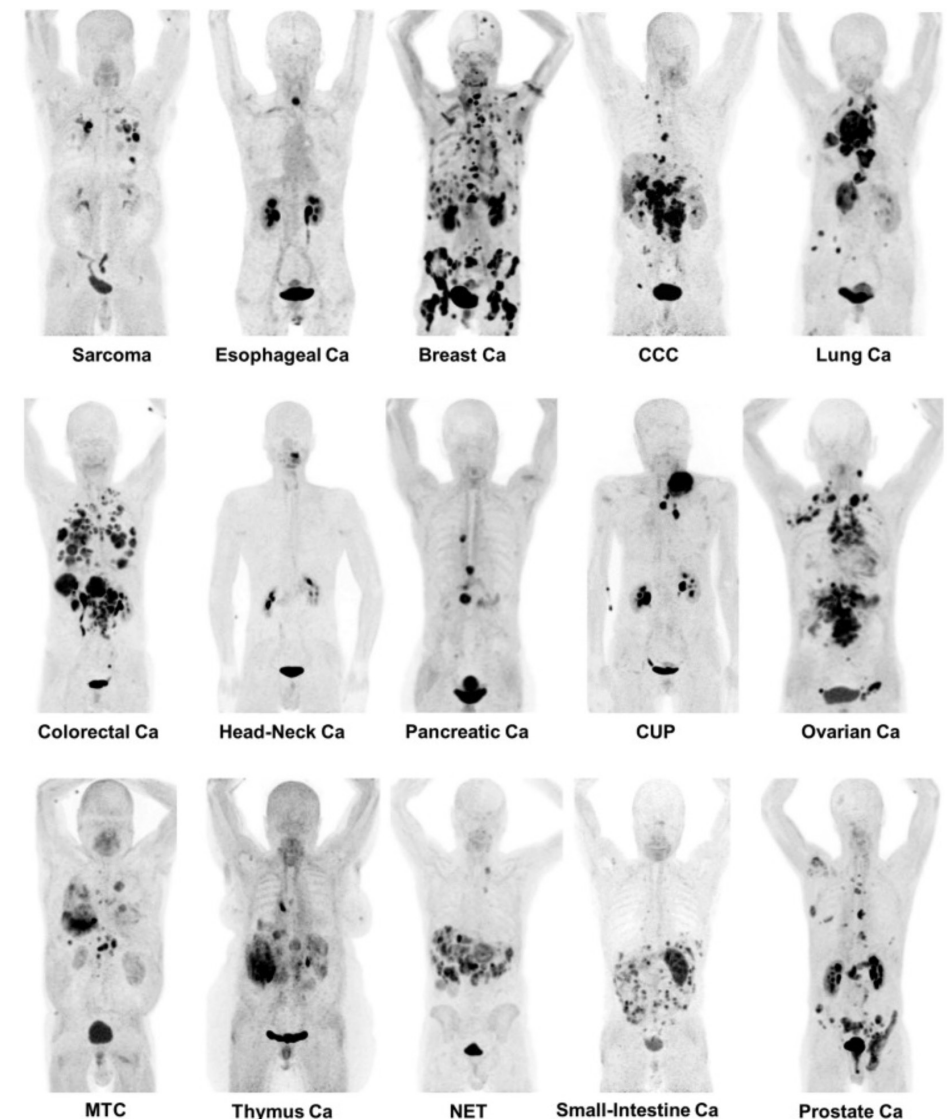


FIGURE 6. Maximum-intensity projections of ⁶⁸Ga-FAPi PET/CT in patients reflecting 15 different histologically proven tumor entities (sorted by uptake in descending order).

Ca = cancer; CCC = cholangiocellular carcinoma; CUP = carcinoma of unknown primary; MTC = medullary thyroid cancer; NET = neuroendocrine tumor. Image from Kratochwil *et al.*¹³⁵.

In addition to FAP targeting tracers, various PDGFR targeting PET and SPECT tracers have been developed and tested in animal experiments^{44–46,131,132}. Targeted PET and fluorescent tracers against MMP-14/MT1-MMP, expressed mainly by CAFs but also epithelial cells, endothelial cells and several immune cells within the tumor, have been developed and tested in animal experiments^{133,134}.

CAF-based tumor imaging might contribute to predicting therapy response and help in clinical decision making¹¹⁷. Recently several distinct CAF subtypes have been characterized, e.g. the matrix-producing contractile phenotype and the immunomodulating secretome, which could result in more specific tracer selection for particularly suitable CAF subtypes.

Mesenchymal stromal cells

As a CAF progenitor, mesenchymal stromal cells (MSC) are pluripotent cells found in many parts of the body (e.g. endothelium, bone marrow, and adipose tissue), fulfilling various functions, and are able to develop into a wide range of cells (including osteoblasts, adipocytes, chondrocytes and fibroblasts)¹³⁶. During oncogenesis, MSCs are involved in progression, angiogenesis and metastasis, but also influence immune reaction and are a suggested source of CAFs¹³⁷. MSC localization and function have been studied using MRI and bioluminescence imaging of prelabelled MSCs^{138–143}. To our knowledge, no reports on the evaluation of MSCs as targets for tumor imaging exist unfortunately, as these would be very relevant in the context of targeted cancer gene therapy using MSC (as they are able to migrate to sites of tumor growth).

Extracellular matrix (ECM)

All tissues and organs in the human body are constituted of cells and ECM, a three-dimensional extracellular network of structural proteins such as collagen, laminin, fibronectin, and, elastin, proteoglycans, and enzymes¹⁴⁴. The ECM provides structural support to cells, but also partakes in crucial biological pathways including tissue morphogenesis, differentiation and homeostasis. During oncogenesis, some of these processes and functions are disturbed, thereby facilitating tumor progression, growth, cell migration, invasion and angiogenesis⁵⁷. The tumor ECM is characterized by an altered deposition and rearrangement of structural proteins and soluble factors and proteinases by the implicated cell types, favoring extravasation and metastasis of malignant cells^{57,145}. During cancer development, the specific configuration of the ECM is continuously changed and can be targeted at different stages for non-invasive diagnosis, risk stratification, targeted therapy selection and therapeutic response monitoring.

Collagen

Collagen is the main constituent of the ECM and provides structure and resiliency to tissues¹⁴⁴. Up until now, twenty-eight different collagen subtypes have been described

¹⁴⁶. From these, collagen types 1, 3, 5, and 11A1 are mainly produced by fibroblasts, whereas collagen type 4 is generally expressed by epithelial and endothelial cells¹⁴⁷. Tumor-associated collagens have been shown to promote cell invasion, proliferation, differentiation and apoptosis, as well as induce chemoresistance and affect drug delivery to tumor cells by forming a physical barrier and changing the intratumoral pressure^{148,149}. Collagen imaging is most routinely performed using second-harmonic generation (also called frequency doubling) and has been studied in many animal models⁵⁷. Collagen deposition has been positively correlated with tumor stiffness. Using magnetic collagen elastography, a non-invasive technique for the imaging of collagen, collagen deposition and tumor stiffness could be quantified in meningioma patients, allowing preoperative determination of time quantification of collagen deposition and tumor stiffness¹⁵⁰. As both factors estimate penetrability of tissue, it is hypothesized that quantification of tumor stiffness may be an indicator of therapeutic efficacy of ECM-targeted drugs^{150,151}. Moreover, due to the multifactorial dependence, tumor stiffness may pose an overall ECM-marker, reflecting its general composition¹⁵⁰. Nevertheless, extensive preclinical and clinical validation of these concepts is required. Additionally, near-infrared (NIR) fluorescent collagen imaging was successfully performed *in vivo* using a collagen type IV targeting antibody and a collagen mimetic peptide targeting (degrading) collagen^{152–154}. Also, a collagen type 1 targeting PET tracer, ⁶⁸Ga-CBP8, was recently translated for human use in idiopathic pulmonary fibrosis patients, and showed increased uptake in diseased versus healthy lungs¹⁵⁵.

As collagen depositions form interstitial stromal barriers preventing drug diffusion into tumor tissue, pretreatment imaging of these depositions might provide guidance in predicting therapeutic success of anti-cancer treatments¹⁵⁶. In addition to oncologic diseases, collagen imaging would be relevant in a wide variety of collagen forming diseases such as chronic kidney disease or pulmonary fibrosis.

Laminins

Laminins are ECM glycoproteins located mostly in the basement membrane and are involved in various mechanisms, including cell attachment, migration, growth and angiogenesis. During tumor development, laminins might be involved by inducing proteolysis or upregulation of MMPs^{157,158}. Despite their pivotal role in tumor progression, *in vivo* imaging of laminins is still in its infancy⁸⁰. Several tracers allowing preclinical *in vivo* visualization of laminin expression or receptor activity have been tested and showed uptake in tumors of diverse origins^{159–163}. Up until now, no clinical translation of these has been described, and the role and clinical benefit of this is subject of discussion.

Fibronectin

Fibronectin (FN) is a multimer glycoprotein present in the ECM. It mediates various cellular interactions, is involved in cell migration, adhesion, growth and differentiation, and is crucial in early phase vertebrate development^{144,164}. Several isoforms of fibronectin are found in tissue remodeling (e.g. wound healing, tumorigenesis, angiogenesis). FN interacts with many cell surface integrins and ECM components, including the RGD binding domain, frequently used for tumor imaging¹⁶⁴. FN is known as a TGF- β target gene, and in turn can stimulate protein expression such as N-cadherin, snail, SLUG, vimentin and downregulation of E-cadherin. As FN expression is a marker of EMT, in which epithelial markers are lost and mesenchymal markers become expressed, it may be an alternative therapeutic and imaging target for drug-resistant tumors that lack common epithelial markers, such as EGFR, VEGF, EpCAM and HER2¹⁶⁵.

Several nuclear imaging tracers, such as ZD2-(68Ga-NOTA) and ¹²⁴I-L19SIP/¹³¹I-L19SIP, that target FN's extracellular domain B (EDB) have been presented in preclinical and clinical settings. These tracers consisted of either a radiolabeled monoclonal antibody or peptide and showed tumor-specific uptake^{165,166}. Moreover, MRI contrast agents targeting EDB or fibrin-fibronectin clots have been described and provided clear delineation of the tumor ECM in animal models¹⁶⁷. As fibronectin is overexpressed in a wide range of tumor types, it may form a potential pan-carcinoma target for imaging.

Hyaluronan (hyaluronic acid)

Hyaluronan is a linear polysaccharide involved in many signaling pathways, and the expression is frequently elevated during oncogenesis, leading to increased intratumoral interstitial fluid pressure¹⁶⁸. Hyaluronan is involved in cell adhesion, migration, and angiogenesis, partly via its interaction with the tumor-associated protein CD44.

As imaging of endogenous hyaluronan has proved challenging due to non-specific binding as a result of the high negative charge, exogenous hyaluronan is often used as a tracer for targeting its receptors⁵⁷. Both fluorescence and magnetic resonance imaging has successfully been performed using endogenously injected fluorescent or contrast labelled hyaluronan in CD44 positive tumors¹⁶⁹⁻¹⁷³. For instance, hyaluronan-derived nanoparticles were loaded with NIR dye indocyanine green and provided excellent tumor specificity in pancreatic cancer-bearing mice. As hyaluronan mimics the effects of polyethylene-glycol (PEG), long tracer half-life and low toxicity were observed¹⁷³.

Other proteoglycans

Heparin sulfate proteoglycans, such as glypicans and syndecans are heavily involved in integrin and growth factor signaling and regulation of Wnt and Hedgehog pathways, respectively. Syndecan-1 was targeted using a NIR dye-conjugated monoclonal antibody

for multispectral optoacoustic imaging (MSOT) and allowed high-contrast tumor imaging in animal models¹⁷⁴. Moreover, several studies developed and evaluated tracers directed against glypican-3, which has been established as a potent target for hepatocellular carcinoma imaging. In all studies using labeled peptide- or antibody (fragment)-based targeting moieties, tumors could be excellently delineated using PET, ultrasound, fluorescence and MRI in a preclinical setting¹⁷⁵⁻¹⁷⁹. As these proteoglycans are involved in various clinically relevant pathways, successful clinical imaging of these could prove to be very useful in clinical imaging.

MATRIX METALLOPROTEINASES

MMPs are a family of over 20 zinc-dependent endopeptidases, which fulfil crucial roles in various biological processes including tissue remodeling, organ development, regulation of inflammatory processes, and oncogenesis¹⁸⁰. Most MMPs are initially expressed in an enzymatically inactive state and are subsequently activated by the release/cleavage of the pro-domain. During oncogenesis, activated MMPs are involved in tumor progression, invasion, and angiogenesis¹⁸⁰. Being downstream effectors of essential signaling pathways, such as EGF and VEGF cascades, they pose an attractive therapeutic target¹⁸¹.

To visualize MMP distribution, several radiolabeled MMP inhibitors have been developed, which, however, demonstrated low and non-specific tumor uptake¹⁸²⁻¹⁸⁶. Using MMP proteolytic activity rather than protein expression, radiolabeled MMP-2 and MMP-14 substrates have shown tumor-specific accumulation *in vivo*^{134,187,188}. Moreover, activatable fluorescence imaging tracers specific for MMP-14, MMP-2, and MMP-7 showed clear delineation of tumors of different origins^{189,190}. Moreover, an MMP-1-specific ultrasound tracer allowed evaluation of MMP-1 expression, subsequently providing precise tumor delineation. Likewise, MMP-2 and MMP-7 activatable MRI contrast agents allowed clear tumor localization^{191,192}. Several MMP-targeting tracers that combine multiple imaging applications were developed and evaluated *in vivo*. For instance, a MMP-2 and MMP-9-cleavable peptide was developed for use as a NIR fluorescence and magnetic resonance contrast agent, and showed tumor-specific enhancement¹⁹³. Alternatively, cleavable radio- and fluorescence-labelled MMP-14 or MMP-7, -9, -12, -13 peptide substrates, allowed bimodal PET and near-infrared fluorescence imaging of gliomas and glioblastomas in animal models, respectively^{133,194}.

Hyaluronidase

Hyaluronidase is a protein involved in hyaluronan hydrolysis, and is used as addition to chemotherapy to improve drug delivery by remodeling of the ECM^{195,196}. The activity

of hyaluronidase was evaluated using MRI contrast agents conjugated to hyaluronan, which show increased relaxivity after degradation^{197,198}. Of note, PEGylated recombinant hyaluronidase PH20 (PEGPH20) has been co-administered with other therapeutic agents to enhance their delivery by remodeling the peritumoral ECM. A study applying this strategy to an imaging tracer reported a higher tumor-to-background ratio compared to administration of tracer only¹⁹⁹.

Transglutaminase

Transglutaminases are enzymes that catalyze modification of proteins²⁰⁰. By doing so, these enzymes promote ECM stiffness and oncogenesis. Transglutaminase substrates have been conjugated to magnetic resonance contrast agents and fluorescent dyes. After enzymatic cleavage, these molecules attach to the ECM and were imaged in xenografts^{201,202}. So far, no clinical applications have been described yet.

Metabolic imaging and alternative imaging methods

Metabolic reprogramming is a distinct feature found in cancers. Tumor cells undergo a metabolic adaptation in which glycolysis, lactate and proton production are elevated, referred to as the Warburg effect. In addition, the metabolism of amino acids and lipids is altered, allowing tumor cells to maintain growth and viability. As metabolic changes are present before anatomical differences are observed, metabolic changes can be monitored to predict treatment response.

Glucose metabolism

Increased glycolysis by tumor cells forms the foundation of [¹⁸F]FDG PET/CT imaging, which has become the standard-of-care imaging modality for many cancer types. This tracer is widely used for instance in diagnosis, staging, detection of residual or recurrent disease, treatment planning, prediction of prognosis and monitoring of therapeutic efficacy. However, as high glucose-consuming organ and inflammatory foci also show high uptake of ¹⁸F-FDG, detecting specificity may be reduced. Also, various organs are known to have a physiologically high uptake of [¹⁸F]FDG, including for example the brain, kidneys and bladder. Additionally, heterogeneity in GLUT-1 expression, the main glucose channel associated with [¹⁸F]FDG uptake, across different cancer types might mitigate the standard use of ¹⁸F-FDG as well. Several alternative or complementary tracers for imaging glucose metabolism have been described. For instance, lactate production can be imaged using hyperpolarized ¹³C-pyruvate MRI^{203,204}. Moreover, 5-¹³C-(2S)-glutamine and ¹⁸F-(2S,4R)4-fluoroglutamine may be used to monitor glutamine metabolism, which is, after glucose, the second most abundant nutrient in men²⁰⁵.

Choline-phospholipid metabolism

In cancer cells, the choline-phospholipid metabolism is dysregulated. Higher levels

of phosphatidylcholine, the most abundant phospholipid in men, are more observed in cancer tissue compared to normal tissue and this overexpression is associated with malignant transformation, invasion and metastatic potential²⁰⁶. Changes in this metabolism are studied using ³¹P or ¹H magnetic resonance spectroscopy or spectroscopic imaging, or ¹³C-choline, ¹⁸F-fluoro-choline, ¹⁸F-fluoroethyl-choline and ¹⁸F-phosphorylfluoro-choline PET imaging (reviewed by Haberkorn *et al.*⁸⁰).

pH

Due to the secretion of acidic metabolites, a lower pH is observed in tumors compared to normal tissues. The measurement of in- and extracellular pH has been extensively investigated using MRS, MRSI, MRI, optical imaging, PA imaging or a combination of methods⁸⁰ (reviewed by Anemone *et al.*²⁰⁷). In addition to this, pH-sensitive dyes, reporter genes, ratiometric PA imaging and EPR spectroscopy have been investigated⁸⁰. pH-activated dyes may not only assist in detection of acidic areas, but may, once conjugated to a tumor-specific targeting moiety, increase tumor-to-background (i.e. tumor vs. non-tumor) contrast. For instance, a pH-activatable fluorescent dye was conjugated to $\alpha\beta3$ integrin-targeting peptide cRGD and allowed clear detection of primary tumors and metastatic lesions in an orthotopic breast cancer mouse model²⁰⁸.

FUTURE PERSPECTIVES

This chapter has given an overview over potential targets and mechanisms for the imaging of various TME components. As the TME components frequently account for more than 50% of the tumor volume, the therapeutic implications of its presence are vast, and TME targeted therapies will be further developed in the near future to support anti-cancer treatment. To predict and monitor the success of such therapies, imaging of these component is crucial. In addition to non-invasive PET, SPECT, MRI and CT imaging methods, intraoperative imaging methods such as NIRF and PA imaging will become important to help guide surgeons during operations.

Due to the clinical interest in therapy response predicting techniques and the acknowledgement of the importance of TME components influencing this response, the interest in imaging TME components, such as immune cells, CAFs and macrophages is expected to increase greatly. The synergistic use of TME targeted tracers for therapy selection, tumor localization, response monitoring, radionuclide therapy and intraoperative guidance holds great promise and will greatly influence and improve current cancer therapy by providing stratification and prediction tools for therapeutic success.

REFERENCES

1. Puram SV, Tirosh I, Parikh AS, et al. Single-cell transcriptomic analysis of primary and metastatic tumor ecosystems in head and neck cancer. *Cell*. 2017;171:1611-1624.e24.
2. Yu X, Chen YA, Conejo-Garcia JR, et al. Estimation of immune cell content in tumor using single-cell RNA-seq reference data. *BMC Cancer*. 2019;19:715.
3. Smits AJJ, Kummer JA, de Bruin PC, et al. The estimation of tumor cell percentage for molecular testing by pathologists is not accurate. *Mod Pathol Off J U S Can Acad Pathol Inc*. 2014;27:168-174.
4. Lambrechts D, Wauters E, Boeckx B, et al. Phenotype molding of stromal cells in the lung tumor microenvironment. *Nat Med*. 2018;24:1277-1289.
5. Liotta LA, Kohn EC. The microenvironment of the tumour-host interface. *Nature*. 2001;411:375-379.
6. Xing Y, Zhao S, Zhou BP, et al. Metabolic reprogramming of the tumour microenvironment. *FEBS J*. 2015;282:3892-3898.
7. Polet F, Feron O. Endothelial cell metabolism and tumour angiogenesis: glucose and glutamine as essential fuels and lactate as the driving force. *J Intern Med*. 2013;273:156-165.
8. Hanahan D, Weinberg RA. Hallmarks of cancer: the next generation. *Cell*. 2011;144:646-674.
9. Park CC, Bissell MJ, Barcellos-Hoff MH. The influence of the microenvironment on the malignant phenotype. *Mol Med Today*. 2000;6:324-329.
10. Mahadevan D, Hoff DDV. Tumor-stroma interactions in pancreatic ductal adenocarcinoma. *Mol Cancer Ther*. 2007;6:1186-1197.
11. Kopfstein L, Christofori G. Metastasis: cell-autonomous mechanisms versus contributions by the tumor microenvironment. *Cell Mol Life Sci*. 2006;63:449-468.
12. Jodele S, Blavier L, Yoon JM, et al. Modifying the soil to affect the seed: role of stromal-derived matrix metalloproteinases in cancer progression. *Cancer Metastasis Rev*. 2006;25:35-43.
13. Prostate Stroma: Physiology - Farnsworth - 1999 - The Prostate - Wiley Online Library Available from: [https://onlinelibrary.wiley.com/doi/abs/10.1002/\(SICI\)1097-0045\(19990101\)38:1%3C60::AID-PROS8%3E3.0.CO;2-3](https://onlinelibrary.wiley.com/doi/abs/10.1002/(SICI)1097-0045(19990101)38:1%3C60::AID-PROS8%3E3.0.CO;2-3). Accessed March 8, 2020.
14. Romero IL, Mukherjee A, Kenny HA, et al. Molecular pathways: trafficking of metabolic resources in the tumor microenvironment. *Clin Cancer Res Off J Am Assoc Cancer Res*. 2015;21:680-686.
15. Martinez-Outschoorn UE, Pavlides S, Howell A, et al. Stromal-epithelial metabolic coupling in cancer: integrating autophagy and metabolism in the tumor microenvironment. *Int J Biochem Cell Biol*. 2011;43:1045-1051.
16. Ratnikov B, Jeon YJ, Smith JW, et al. Right on TARGET: glutamine metabolism in cancer. *Oncoscience*. 2015;2:681-683.
17. Lisanti MP, Martinez-Outschoorn UE, Sotgia F. Oncogenes induce the cancer-associated fibroblast phenotype: metabolic symbiosis and "fibroblast addiction" are new therapeutic targets for drug discovery. *Cell Cycle Georget Tex*. 2013;12:2723-2732.
18. Correia AL, Bissell MJ. The tumor microenvironment is a dominant force in multidrug resistance. *Drug Resist Updat Rev Comment Antimicrob Anticancer Chemother*. 2012;15:39-49.
19. Stammes MA, Bugby SL, Porta T, et al. Modalities for image- and molecular-guided cancer surgery. *Br J Surg*. 2018;105:e69-e83.
20. James ML, Gambhir SS. A molecular imaging primer: modalities, imaging agents, and applications. *Physiol Rev*. 2012;92:897-965.
21. IDE A. Vascularization of the Brown Pearce rabbit epithelioma transplant as seen in the transparent ear chamber. *AJR Am J Roentgenol*. 1939;42:891-899.
22. Algire GH, Chalkley HW, Earle WE, et al. Vascular reactions of normal and malignant tissues in vivo. III. Vascular reactions' of mice to fibroblasts treated in vitro with methylcholanthrene. *J Natl Cancer Inst*. 1950;11:555-580.
23. Ribatti D. Judah Folkman, a pioneer in the study of angiogenesis. *Angiogenesis*. 2008;11:3-10.
24. Heinzman JM, Brower SL, Bush JE. Comparison of angiogenesis-related factor expression in primary tumor cultures under normal and hypoxic growth conditions. *Cancer Cell Int*. 2008;8:11.
25. Hicklin DJ, Ellis LM. Role of the vascular endothelial growth factor pathway in tumor growth and angiogenesis. *J Clin Oncol Off J Am Soc Clin Oncol*. 2005;23:1011-1027.
26. Carmeliet P, Jain RK. Molecular mechanisms and clinical applications of angiogenesis. *Nature*. 2011;473:298-307.
27. Ferrara N. Vascular endothelial growth factor: basic science and clinical progress. *Endocr Rev*. 2004;25:581-611.
28. Rudlowski C, Pickart A-K, Fuhljan C, et al. Prognostic significance of vascular endothelial growth factor expression in ovarian cancer patients: a long-term follow-up. *Int J Gynecol Cancer Off J Int Gynecol Cancer Soc*. 2006;16 Suppl 1:183-189.
29. Zirlirk K, Duyster J. Anti-Angiogenics: Current Situation and Future Perspectives. *Oncol Res Treat*. 2018;41:166-171.
30. Oosting SF, Brouwers AH, van Es SC, et al. 89Zr-bevacizumab PET visualizes heterogeneous tracer accumulation in tumor lesions of renal cell carcinoma patients and differential effects of antiangiogenic treatment. *J Nucl Med Off Publ Soc Nucl Med*. 2015;56:63-69.
31. Taurone S, Galli F, Signore A, et al. VEGF in nuclear medicine: Clinical application in cancer and future perspectives (Review). *Int J Oncol*. 2016;49:437-447.
32. Lamberts LE, Koch M, de Jong JS, et al. Tumor-Specific Uptake of Fluorescent Bevacizumab-IRDye800CW Microdosing in Patients with Primary Breast Cancer: A Phase I Feasibility Study. *Clin Cancer Res Off J Am Assoc Cancer Res*. 2017;23:2730-2741.
33. de Jongh SJ, Tjalma JJJ, Koller M, et al. Back-table fluorescence-guided imaging for circumferential resection margin evaluation in locally advanced rectal cancer patients using bevacizumab-800CW. *J Nucl Med Off Publ Soc Nucl Med*. . Epub ahead of print October 18, 2019. DOI: 10.2967/jnumed.119.232355.
34. Harlaar NJ, Koller M, de Jongh SJ, et al. Molecular fluorescence-guided surgery of peritoneal carcinomatosis of colorectal origin: a single-centre feasibility study. *Lancet Gastroenterol Hepatol*. 2016;1:283-290.
35. Pillai R, Marinelli ER, Fan H, et al. A phospholipid-PEG2000 conjugate of a vascular endothelial growth factor receptor 2 (VEGFR2)-targeting heterodimer peptide for contrast-enhanced ultrasound imaging of angiogenesis. *Bioconjug Chem*. 2010;21:556-562.
36. Willmann JK, Paulmurugan R, Chen K, et al. US imaging of tumor angiogenesis with microbubbles

- targeted to vascular endothelial growth factor receptor type 2 in mice. *Radiology*. 2008;246:508–518.
37. Pierschbacher MD, Ruoslahti E. Cell attachment activity of fibronectin can be duplicated by small synthetic fragments of the molecule. *Nature*. 1984;309:30–33.
 38. Ruoslahti E, Pierschbacher MD. New perspectives in cell adhesion: RGD and integrins. *Science*. 1987;238:491–497.
 39. Ruoslahti E. The RGD story: a personal account. *Matrix Biol J Int Soc Matrix Biol*. 2003;22:459–465.
 40. Mas-Moruno C, Rechenmacher F, Kessler H. Cilengitide: The First Anti-Angiogenic Small Molecule Drug Candidate. Design, Synthesis and Clinical Evaluation. *Anticancer Agents Med Chem*. 2010;10:753–768.
 41. Niccoli Asabella A, Di Palo A, Altini C, et al. Multimodality Imaging in Tumor Angiogenesis: Present Status and Perspectives. *Int J Mol Sci*;18 . Epub ahead of print August 28, 2017. DOI: 10.3390/ijms18091864.
 42. Handgraaf HJM, Boonstra MC, Prevoo HAJM, et al. Real-time near-infrared fluorescence imaging using cRGD-ZW800-1 for intraoperative visualization of multiple cancer types. *Oncotarget*. 2017;8:21054–21066.
 43. Valk KS de, Deken MM, Handgraaf HJM, et al. First-in-Human Assessment of cRGD-ZW800-1, a Zwitterionic, Integrin-Targeted, Near-Infrared Fluorescent Peptide in Colon Carcinoma. *Clin Cancer Res*. . Epub ahead of print January 1, 2020. DOI: 10.1158/1078-0432.CCR-19-4156.
 44. Cai H, Shi Q, Tang Y, et al. Positron Emission Tomography Imaging of Platelet-Derived Growth Factor Receptor β in Colorectal Tumor Xenograft Using Zirconium-89 Labeled Dimeric Affibody Molecule. *Mol Pharm*. 2019;16:1950–1957.
 45. Tolmachev V, Varasteh Z, Honarvar H, et al. Imaging of Platelet-Derived Growth Factor Receptor β Expression in Glioblastoma Xenografts Using Affibody Molecule ^{111}In -DOTA-Z09591. *J Nucl Med*. 2014;55:294–300.
 46. Effendi N, Mishiro K, Takarada T, et al. Design, synthesis, and biological evaluation of radioiodinated benzo[d]imidazole-quinoline derivatives for platelet-derived growth factor receptor β (PDGFR β) imaging. *Bioorg Med Chem*. 2019;27:383–393.
 47. Camorani S, Hill BS, Collina F, et al. Targeted imaging and inhibition of triple-negative breast cancer metastases by a PDGFR β aptamer. *Theranostics*. 2018;8:5178–5199.
 48. Scalici JM, Thomas S, Harrer C, et al. Imaging VCAM-1 as an indicator of treatment efficacy in metastatic ovarian cancer. *J Nucl Med Off Publ Soc Nucl Med*. 2013;54:1883–1889.
 49. Zhang X, Liu C, Hu F, et al. PET Imaging of VCAM-1 Expression and Monitoring Therapy Response in Tumor with a ^{68}Ga -Labeled Single Chain Variable Fragment. *Mol Pharm*. 2018;15:609–618.
 50. Montemagno C, Dumas L, Cavallès P, et al. In Vivo Assessment of VCAM-1 Expression by SPECT/CT Imaging in Mice Models of Human Triple Negative Breast Cancer. *Cancers*;11 . Epub ahead of print July 23, 2019. DOI: 10.3390/cancers11071039.
 51. Li C, Wang J, Hu J, et al. Development, optimization, and validation of novel anti-TEM1/CD248 affinity agent for optical imaging in cancer. *Oncotarget*. 2014;5:6994–7012.
 52. Cicone F, Denoël T, Gnesin S, et al. Preclinical Evaluation and Dosimetry of [^{111}In]CHX-DTPA-scFv78-Fc Targeting Endosialin/Tumor Endothelial Marker 1 (TEM1). *Mol Imaging Biol*. . Epub ahead of print January 28, 2020. DOI: 10.1007/s11307-020-01479-8.
 53. Paauwe M, ten Dijke P, Hawinkels LJAC. Endoglin for tumor imaging and targeted cancer therapy. *Expert Opin Ther Targets*. 2013;17:421–435.
 54. Dai W, Zhong L, He J, et al. Targeting Endoglin for Cancer Diagnosis and Therapy: Current State and Future Promise. *Discov Med*. 2019;28:87–93.
 55. Lobeek D, Rijpkema M, Terry SYA, et al. Imaging angiogenesis in patients with head and neck squamous cell carcinomas by [^{68}Ga]Ga-DOTA-E-[c(RGDfK)] $_2$ PET/CT. *Eur J Nucl Med Mol Imaging*. 2020;47:2647–2655.
 56. Munn LL, Padera TP. Imaging the lymphatic system. *Microvasc Res*. 2014;0:55–63.
 57. Narunsky L, Oren R, Bochner F, et al. Imaging aspects of the tumor stroma with therapeutic implications. *Pharmacol Ther*. 2014;141:192–208.
 58. Dafni H, Israely T, Bhujwalla ZM, et al. Overexpression of vascular endothelial growth factor 165 drives peritumor interstitial convection and induces lymphatic drain: magnetic resonance imaging, confocal microscopy, and histological tracking of triple-labeled albumin. *Cancer Res*. 2002;62:6731–6739.
 59. Matsumura Y, Maeda H. A new concept for macromolecular therapeutics in cancer chemotherapy: mechanism of tumorotropic accumulation of proteins and the antitumor agent smancs. *Cancer Res*. 1986;46:6387–6392.
 60. Maeda H, Tsukigawa K, Fang J. A Retrospective 30 Years After Discovery of the Enhanced Permeability and Retention Effect of Solid Tumors: Next-Generation Chemotherapeutics and Photodynamic Therapy--Problems, Solutions, and Prospects. *Microcirc N Y N 1994*. 2016;23:173–182.
 61. Vahrmeijer AL, Hutteman M, van der Vorst JR, et al. Image-guided cancer surgery using near-infrared fluorescence. *Nat Rev Clin Oncol*. 2013;10:507–518.
 62. Hoffend J, Mier W, Schuhmacher J, et al. Gallium-68-DOTA-albumin as a PET blood-pool marker: experimental evaluation in vivo. *Nucl Med Biol*. 2005;32:287–292.
 63. Alcázar JL. Tumor angiogenesis assessed by three-dimensional power Doppler ultrasound in early, advanced and metastatic ovarian cancer: A preliminary study. *Ultrasound Obstet Gynecol Off J Int Soc Ultrasound Obstet Gynecol*. 2006;28:325–329.
 64. Fleischer AC, Wojcicki WE, Donnelly EF, et al. Quantified color Doppler sonography of tumor vascularity in an animal model. *J Ultrasound Med Off J Am Inst Ultrasound Med*. 1999;18:547–551.
 65. Yang WT, Tse GMK, Lam PKW, et al. Correlation between color power Doppler sonographic measurement of breast tumor vasculature and immunohistochemical analysis of microvessel density for the quantitation of angiogenesis. *J Ultrasound Med Off J Am Inst Ultrasound Med*. 2002;21:1227–1235.
 66. Deshpande N, Pysz MA, Willmann JK. Molecular ultrasound assessment of tumor angiogenesis. *Angiogenesis*. 2010;13:175–188.
 67. Postema M, Gilja OH. Contrast-enhanced and targeted ultrasound. *World J Gastroenterol*. 2011;17:28–41.
 68. Dimitrakopoulou-Strauss A, Strauss LG, Burger C. Quantitative PET studies in pretreated melanoma patients: a comparison of 6-[^{18}F]fluoro-L-dopa with ^{18}F -FDG and (^{15}O)-water using compartment and noncompartment analysis. *J Nucl Med Off Publ Soc Nucl Med*. 2001;42:248–256.
 69. Mullani null, Herbst null, Abbruzzese null, et al. 9:30-9:45. First Pass FDG Measured Blood Flow in Tumors: A Comparison with ^{15}O -Labeled Water Measured Blood Flow. *Clin Positron Imaging Off J Inst Clin PET*. 2000;3:153.

70. Lau J, Zhang Z, Jenni S, et al. PET Imaging of Carbonic Anhydrase IX Expression of HT-29 Tumor Xenograft Mice with ⁶⁸Ga-Labeled Benzenesulfonamides. *Mol Pharm*. 2016;13:1137–1146.
71. Lv P-C, Roy J, Putt KS, et al. Evaluation of a Carbonic Anhydrase IX-Targeted Near-Infrared Dye for Fluorescence-Guided Surgery of Hypoxic Tumors. *Mol Pharm*. 2016;13:1618–1625.
72. Lv P-C, Putt KS, Low PS. Evaluation of Nonpeptidic Ligand Conjugates for SPECT Imaging of Hypoxic and Carbonic Anhydrase IX-Expressing Cancers. *Bioconjug Chem*. 2016;27:1762–1769.
73. Zhou Y, Maiti M, Sharma A, et al. Azo-based small molecular hypoxia responsive theranostic for tumor-specific imaging and therapy. *J Controlled Release*. 2018;288:14–22.
74. Ruan Q, Zhang X, Lin X, et al. Novel ^{99m}Tc labelled complexes with 2-nitroimidazole isocyanide: design, synthesis and evaluation as potential tumor hypoxia imaging agents. *MedChemComm*. 2018;9:988–994.
75. Verhoeff SR, van Es SC, Boon E, et al. Lesion detection by [⁸⁹Zr]Zr-DFO-girentuximab and [¹⁸F]FDG-PET/CT in patients with newly diagnosed metastatic renal cell carcinoma. *Eur J Nucl Med Mol Imaging*. 2019;46:1931–1939.
76. Xu Z, Li X-F, Zou H, et al. ¹⁸F-Fluoromisonidazole in tumor hypoxia imaging. *Oncotarget*. 2017;8:94969–94979.
77. Mortensen LS, Johansen J, Kallehauge J, et al. FAZA PET/CT hypoxia imaging in patients with squamous cell carcinoma of the head and neck treated with radiotherapy: results from the DAHANCA 24 trial. *Radiother Oncol J Eur Soc Ther Radiol Oncol*. 2012;105:14–20.
78. Trinkaus ME, Blum R, Rischin D, et al. Imaging of hypoxia with ¹⁸F-FAZA PET in patients with locally advanced non-small cell lung cancer treated with definitive chemoradiotherapy. *J Med Imaging Radiat Oncol*. 2013;57:475–481.
79. Zegers CML, Hoebers FJP, van Elmpt W, et al. Evaluation of tumour hypoxia during radiotherapy using [¹⁸F]HX4 PET imaging and blood biomarkers in patients with head and neck cancer. *Eur J Nucl Med Mol Imaging*. 2016;43:2139–2146.
80. Ramamonjisoa N, Ackerstaff E. Characterization of the Tumor Microenvironment and Tumor–Stroma Interaction by Non-invasive Preclinical Imaging. *Front Oncol*;7 . Epub ahead of print January 31, 2017. DOI: 10.3389/fonc.2017.00003.
81. Knox HJ, Hedhli J, Kim TW, et al. A bio-reducible N -oxide-based probe for photoacoustic imaging of hypoxia. *Nat Commun*. 2017;8:1–9.
82. Huang J, Wu Y, Zeng F, et al. An Activatable Near-Infrared Chromophore for Multispectral Photoacoustic Imaging of Tumor Hypoxia and for Tumor Inhibition. *Theranostics*. 2019;9:7313–7324.
83. Meng X, Zhang J, Sun Z, et al. Hypoxia-triggered single molecule probe for high-contrast NIR II/PA tumor imaging and robust photothermal therapy. *Theranostics*. 2018;8:6025–6034.
84. Verwer EE, Bahce I, van Velden FHP, et al. Parametric methods for quantification of ¹⁸F-FAZA kinetics in non-small cell lung cancer patients. *J Nucl Med Off Publ Soc Nucl Med*. 2014;55:1772–1777.
85. Pardoll DM. The blockade of immune checkpoints in cancer immunotherapy. *Nat Rev Cancer*. 2012;12:252–264.
86. Mayer AT, Gambhir SS. The Immunoimaging Toolbox. *J Nucl Med Off Publ Soc Nucl Med*. 2018;59:1174–1182.
87. Krekorian M, Fruhwirth GO, Srinivas M, et al. Imaging of T-cells and their responses during anti-cancer immunotherapy. *Theranostics*. 2019;9:7924–7947.
88. Niemeijer AN, Leung D, Huisman MC, et al. Whole body PD-1 and PD-L1 positron emission tomography in patients with non-small-cell lung cancer. *Nat Commun*. 2018;9:4664.
89. Broos K, Lecocq Q, Raes G, et al. Noninvasive imaging of the PD-1:PD-L1 immune checkpoint: Embracing nuclear medicine for the benefit of personalized immunotherapy. *Theranostics*. 2018;8:3559–3570.
90. Lv G, Sun X, Qiu L, et al. PET Imaging of Tumor PD-L1 Expression with a Highly Specific Nonblocking Single-Domain Antibody. *J Nucl Med Off Publ Soc Nucl Med*. 2020;61:117–122.
91. Yaghoubi SS, Jensen MC, Satyamurthy N, et al. Noninvasive detection of therapeutic cytolytic T cells with ¹⁸F-FHBG PET in a patient with glioma. *Nat Clin Pract Oncol*. 2009;6:53–58.
92. de Vries IJM, Lesterhuis WJ, Barentsz JO, et al. Magnetic resonance tracking of dendritic cells in melanoma patients for monitoring of cellular therapy. *Nat Biotechnol*. 2005;23:1407–1413.
93. Mukherjee S, Sonanini D, Maurer A, et al. The yin and yang of imaging tumor associated macrophages with PET and MRI. *Theranostics*. 2019;9:7730–7748.
94. Lin Y, Xu J, Lan H. Tumor-associated macrophages in tumor metastasis: biological roles and clinical therapeutic applications. *J Hematol Oncol J Hematol Oncol*. 2019;12:76.
95. Balkwill F, Charles KA, Mantovani A. Smoldering and polarized inflammation in the initiation and promotion of malignant disease. *Cancer Cell*. 2005;7:211–217.
96. Salmaninejad A, Valilou SF, Soltani A, et al. Tumor-associated macrophages: role in cancer development and therapeutic implications. *Cell Oncol Dordr*. 2019;42:591–608.
97. Lin EY, Li J-F, Gnatovskiy L, et al. Macrophages regulate the angiogenic switch in a mouse model of breast cancer. *Cancer Res*. 2006;66:11238–11246.
98. Chen Y, Song Y, Du W, et al. Tumor-associated macrophages: an accomplice in solid tumor progression. *J Biomed Sci*. 2019;26:78.
99. Leek RD, Lewis CE, Whitehouse R, et al. Association of macrophage infiltration with angiogenesis and prognosis in invasive breast carcinoma. *Cancer Res*. 1996;56:4625–4629.
100. Anfray C, Ummarino A, Torres Andón F, et al. Current Strategies to Target Tumor-Associated-Macrophages to Improve Anti-Tumor Immune Responses. *Cells*;9 . Epub ahead of print December 23, 2019. DOI: 10.3390/cells9010046.
101. Vogel DYS, Glim JE, Stavenuiter AWD, et al. Human macrophage polarization in vitro: maturation and activation methods compared. *Immunobiology*. 2014;219:695–703.
102. Narayan N, Owen DR, Mandhair H, et al. Translocator Protein as an Imaging Marker of Macrophage and Stromal Activation in Rheumatoid Arthritis Pannus. *J Nucl Med Off Publ Soc Nucl Med*. 2018;59:1125–1132.
103. Albert NL, Unterrainer M, Fleischmann DF, et al. TSPO PET for glioma imaging using the novel ligand ¹⁸F-GE-180: first results in patients with glioblastoma. *Eur J Nucl Med Mol Imaging*. 2017;44:2230–2238.
104. Zinnhardt B, Pigeon H, Thézé B, et al. Combined PET Imaging of the Inflammatory Tumor Microenvironment Identifies Margins of Unique Radiotracer Uptake. *Cancer Res*. 2017;77:1831–1841.
105. Lanfranca MP, Lazarus J, Shao X, et al. Tracking Macrophage Infiltration in a Mouse Model of Pancreatic Cancer with the Positron Emission Tomography Tracer [¹¹C]PBR28. *J Surg Res*. 2018;232:570–577.
106. Movahedi K, Schoonoghe S, Laoui D, et al. Nanobody-based targeting of the macrophage mannose

- receptor for effective in vivo imaging of tumor-associated macrophages. *Cancer Res.* 2012;72:4165–4177.
107. Blykers A, Schoonooghe S, Xavier C, et al. PET Imaging of Macrophage Mannose Receptor-Expressing Macrophages in Tumor Stroma Using 18F-Radiolabeled Camelid Single-Domain Antibody Fragments. *J Nucl Med Off Publ Soc Nucl Med.* 2015;56:1265–1271.
 108. Verweij NJF, Yaqub M, Bruijnen STG, et al. First in man study of [18F]fluoro-PEG-folate PET: a novel macrophage imaging technique to visualize rheumatoid arthritis. *Sci Rep.*;10. Epub ahead of print January 23, 2020. DOI: 10.1038/s41598-020-57841-x.
 109. Schniering J, Benešová M, Brunner M, et al. 18F-AzaFol for Detection of Folate Receptor- β Positive Macrophages in Experimental Interstitial Lung Disease—A Proof-of-Concept Study. *Front Immunol.*;10. Epub ahead of print 2019. DOI: 10.3389/fimmu.2019.02724.
 110. Hoogstins CES, Tummers QRJG, Gaarenstroom KN, et al. A Novel Tumor-Specific Agent for Intraoperative Near-Infrared Fluorescence Imaging: A Translational Study in Healthy Volunteers and Patients with Ovarian Cancer. *Clin Cancer Res Off J Am Assoc Cancer Res.* 2016;22:2929–2938.
 111. Predina JD, Newton AD, Connolly C, et al. Identification of a Folate Receptor-Targeted Near-Infrared Molecular Contrast Agent to Localize Pulmonary Adenocarcinomas. *Mol Ther J Am Soc Gene Ther.* 2018;26:390–403.
 112. Eichendorff S, Svendsen P, Bender D, et al. Biodistribution and PET imaging of a novel [68Ga]-anti-CD163-antibody conjugate in rats with collagen-induced arthritis and in controls. *Mol Imaging Biol.* 2015;17:87–93.
 113. Skovgaard D, Persson M, Kjaer A. Imaging of prostate cancer using urokinase type plasminogen activator receptor PET. In: *Prostate cancer imaging and therapy.* Elsevier; 2017. p. 243-256.
 114. Hildebrandt IJ, Gambhir SS. Molecular imaging applications for immunology. *Clin Immunol Orlando Fla.* 2004;111:210–224.
 115. Iv M, Samghabadi P, Holdsworth S, et al. Quantification of Macrophages in High-Grade Gliomas by Using Ferumoxytol-enhanced MRI: A Pilot Study. *Radiology.* 2019;290:198–206.
 116. Aghighi M, Theruvath AJ, Pareek A, et al. Magnetic Resonance Imaging of Tumor-Associated Macrophages: Clinical Translation. *Clin Cancer Res Off J Am Assoc Cancer Res.* 2018;24:4110–4118.
 117. Sahai E, Astsaturov I, Cukierman E, et al. A framework for advancing our understanding of cancer-associated fibroblasts. *Nat Rev Cancer.* 2020;20:174–186.
 118. Rettig WJ, Garin-Chesa P, Beresford HR, et al. Cell-surface glycoproteins of human sarcomas: differential expression in normal and malignant tissues and cultured cells. *Proc Natl Acad Sci U S A.* 1988;85:3110–3114.
 119. Garin-Chesa P, Old LJ, Rettig WJ. Cell surface glycoprotein of reactive stromal fibroblasts as a potential antibody target in human epithelial cancers. *Proc Natl Acad Sci U S A.* 1990;87:7235–7239.
 120. Lindner T, Loktev A, Giesel F, et al. Targeting of activated fibroblasts for imaging and therapy. *EJNMMI Radiopharm Chem.* 2019;4:16.
 121. Sandberg TP, Stuart MPME, Oosting J, et al. Increased expression of cancer-associated fibroblast markers at the invasive front and its association with tumor-stroma ratio in colorectal cancer. *BMC Cancer.* 2019;19:284.
 122. Li J, Chen K, Liu H, et al. Activatable near-infrared fluorescent probe for in vivo imaging of fibroblast activation protein-alpha. *Bioconjug Chem.* 2012;23:1704–1711.
 123. Ruger R, Tansi FL, Rabenhold M, et al. In vivo near-infrared fluorescence imaging of FAP-expressing tumors with activatable FAP-targeted, single-chain Fv-immunoliposomes. *J Control Release Off J Control Release Soc.* 2014;186:1–10.
 124. Laverman P, van der Geest T, Terry SYA, et al. Immuno-PET and Immuno-SPECT of Rheumatoid Arthritis with Radiolabeled Anti-Fibroblast Activation Protein Antibody Correlates with Severity of Arthritis. *J Nucl Med Off Publ Soc Nucl Med.* 2015;56:778–783.
 125. Welt S, Divgi CR, Scott AM, et al. Antibody targeting in metastatic colon cancer: a phase I study of monoclonal antibody F19 against a cell-surface protein of reactive tumor stromal fibroblasts. *J Clin Oncol Off J Am Soc Clin Oncol.* 1994;12:1193–1203.
 126. Loktev A, Lindner T, Mier W, et al. A Tumor-Imaging Method Targeting Cancer-Associated Fibroblasts. *J Nucl Med Off Publ Soc Nucl Med.* 2018;59:1423–1429.
 127. Giesel FL, Hadaschik B, Cardinale J, et al. F-18 labelled PSMA-1007: biodistribution, radiation dosimetry and histopathological validation of tumor lesions in prostate cancer patients. *Eur J Nucl Med Mol Imaging.* 2017;44:678–688.
 128. Giesel FL, Heussel CP, Lindner T, et al. FAPI-PET/CT improves staging in a lung cancer patient with cerebral metastasis. *Eur J Nucl Med Mol Imaging.* 2019;46:1754–1755.
 129. Vandsburger MH, Radoul M, Addadi Y, et al. Ovarian carcinoma: quantitative biexponential MR imaging relaxometry reveals the dynamic recruitment of ferritin-expressing fibroblasts to the angiogenic rim of tumors. *Radiology.* 2013;268:790–801.
 130. Granot D, Addadi Y, Kalchenko V, et al. In vivo imaging of the systemic recruitment of fibroblasts to the angiogenic rim of ovarian carcinoma tumors. *Cancer Res.* 2007;67:9180–9189.
 131. Lindborg M, Cortez E, Hoiden-Guthenberg I, et al. Engineered high-affinity affibody molecules targeting platelet-derived growth factor receptor β in vivo. *J Mol Biol.* 2011;407:298–315.
 132. Strand J, Varasteh Z, Eriksson O, et al. Gallium-68-labeled affibody molecule for PET imaging of PDGFR β expression in vivo. *Mol Pharm.* 2014;11:3957–3964.
 133. Kasten BB, Jiang K, Cole D, et al. Targeting MMP-14 for dual PET and fluorescence imaging of glioma in preclinical models. *Eur J Nucl Med Mol Imaging.* . Epub ahead of print November 26, 2019. DOI: 10.1007/s00259-019-04607-x.
 134. Watkins GA, Jones EF, Scott Shell M, et al. Development of an optimized activatable MMP-14 targeted SPECT imaging probe. *Bioorg Med Chem.* 2009;17:653–659.
 135. Kratochwil C, Flechsig P, Lindner T, et al. 68Ga-FAPI PET/CT: Tracer Uptake in 28 Different Kinds of Cancer. *J Nucl Med Off Publ Soc Nucl Med.* 2019;60:801–805.
 136. Traktuev DO, Merfeld-Claus S, Li J, et al. A population of multipotent CD34-positive adipose stromal cells share pericyte and mesenchymal surface markers, reside in a periendothelial location, and stabilize endothelial networks. *Circ Res.* 2008;102:77–85.
 137. Droujinine IA, Eckert MA, Zhao W. To grab the stroma by the horns: from biology to cancer therapy with mesenchymal stem cells. *Oncotarget.* 2013;4:651–664.
 138. Loebinger MR, Kyrtatos PG, Turmaine M, et al. Magnetic resonance imaging of mesenchymal stem

- cells homing to pulmonary metastases using biocompatible magnetic nanoparticles. *Cancer Res.* 2009;69:8862–8867.
139. Sasportas LS, Kasmieh R, Wakimoto H, et al. Assessment of therapeutic efficacy and fate of engineered human mesenchymal stem cells for cancer therapy. *Proc Natl Acad Sci U S A.* 2009;106:4822–4827.
140. Uchibori R, Okada T, Ito T, et al. Retroviral vector-producing mesenchymal stem cells for targeted suicide cancer gene therapy. *J Gene Med.* 2009;11:373–381.
141. Jia X-H, Du Y, Mao D, et al. Zoledronic acid prevents the tumor-promoting effects of mesenchymal stem cells via MCP-1 dependent recruitment of macrophages. *Oncotarget.* 2015;6:26018–26028.
142. Av M, Ei C, Mv S, et al. Influence of mesenchymal stem cells on metastasis development in mice in vivo. *Stem Cell Res Ther.* 2015;6:15–15.
143. Willmann JK, Paulmurugan R, Rodriguez-Porcel M, et al. Imaging gene expression in human mesenchymal stem cells: from small to large animals. *Radiology.* 2009;252:117–127.
144. Mecham RP. Overview of extracellular matrix. *Curr Protoc Cell Biol.* 2001;Chapter 10:Unit 10.1.
145. Petrova V, Annicchiarico-Petruzzelli M, Melino G, et al. The hypoxic tumour microenvironment. *Oncogenesis.* 2018;7:1–13.
146. Ricard-Blum S. The collagen family. *Cold Spring Harb Perspect Biol.* 2011;3:a004978.
147. Vázquez-Villa F, García-Ocaña M, Galván JA, et al. COL11A1/(pro)collagen 11A1 expression is a remarkable biomarker of human invasive carcinoma-associated stromal cells and carcinoma progression. *Tumour Biol J Int Soc Oncodevelopmental Biol Med.* 2015;36:2213–2222.
148. Provenzano PP, Eliceiri KW, Campbell JM, et al. Collagen reorganization at the tumor-stromal interface facilitates local invasion. *BMC Med.* 2006;4:38.
149. Egeblad M, Rasch MG, Weaver VM. Dynamic interplay between the collagen scaffold and tumor evolution. *Curr Opin Cell Biol.* 2010;22:697–706.
150. Riegler J, Labyed Y, Rosenzweig S, et al. Tumor Elastography and Its Association with Collagen and the Tumor Microenvironment. *Clin Cancer Res.* 2018;24:4455–4467.
151. Brown E, McKee T, diTomaso E, et al. Dynamic imaging of collagen and its modulation in tumors in vivo using second-harmonic generation. *Nat Med.* 2003;9:796–800.
152. Yasunaga M, Manabe S, Tarin D, et al. Cancer-stroma targeting therapy by cytotoxic immunoconjugate bound to the collagen 4 network in the tumor tissue. *Bioconjug Chem.* 2011;22:1776–1783.
153. Li Y, Foss CA, Summerfield DD, et al. Targeting collagen strands by photo-triggered triple-helix hybridization. *Proc Natl Acad Sci U S A.* 2012;109:14767–14772.
154. Baues M, Klinkhammer BM, Ehling J, et al. A collagen-binding protein enables molecular imaging of kidney fibrosis in vivo. *Kidney Int.* 2020;97:609–614.
155. Montesi SB, Izquierdo-García D, Désogère P, et al. Type I Collagen-targeted Positron Emission Tomography Imaging in Idiopathic Pulmonary Fibrosis: First-in-Human Studies. *Am J Respir Crit Care Med.* 2019;200:258–261.
156. Liu L, Zhang SX, Liao W, et al. Mechanoresponsive stem cells to target cancer metastases through biophysical cues. *Sci Transl Med.*;9 . Epub ahead of print 26 2017. DOI: 10.1126/scitranslmed.aan2966.
157. Patarroyo M, Tryggvason K, Virtanen I. Laminin isoforms in tumor invasion, angiogenesis and metastasis. *Semin Cancer Biol.* 2002;12:197–207.
158. Pesapane A, Ragno P, Selleri C, et al. Recent Advances in the Function of the 67 kDa Laminin Receptor and its Targeting for Personalized Therapy in Cancer . Epub ahead of print 2017. DOI: info:doi/10.2174/1381612823666170710125332.
159. Cuesta ÁM, Sánchez-Martín D, Sanz L, et al. In Vivo Tumor Targeting and Imaging with Engineered Trivalent Antibody Fragments Containing Collagen-Derived Sequences. *PLOS ONE.* 2009;4:e5381.
160. Koliakos G, Trontzos C, Kouzi-Koliakos K, et al. Lung carcinoma imaging using a synthetic laminin derivative radioiodinated peptide YIGSR. *J Nucl Med Off Publ Soc Nucl Med.* 1997;38:1940–1944.
161. Fujita M, Lee B-S, Khazenzon NM, et al. Brain tumor tandem targeting using a combination of monoclonal antibodies attached to biopoly(beta-L-malic acid). *J Control Release Off J Control Release Soc.* 2007;122:356–363.
162. Stelter L, Tseng J-C, Torosjan A, et al. Tumor-specific targeting with modified Sindbis viral vectors: evaluation with optical imaging and positron emission tomography in vivo. *Mol Imaging Biol.* 2013;15:166–174.
163. Mokotoff M, Swanson DP, Jonnalagadda SS, et al. Evaluation of laminin peptide fragments labeled with indium-111 for the potential imaging of malignant tumors. *J Pept Res.* 1997;49:510–516.
164. Pankov R, Yamada KM. Fibronectin at a glance. *J Cell Sci.* 2002;115:3861–3863.
165. Han Z, Lu Z-R. Targeting fibronectin for cancer imaging and therapy. *J Mater Chem B.* 2017;5:639–654.
166. Gao S, Qin J, Sergeeva O, et al. Synthesis and assessment of ZD2-(68Ga-NOTA) specific to extradomain B fibronectin in tumor microenvironment for PET imaging of pancreatic cancer. *Am J Nucl Med Mol Imaging.* 2019;9:216–229.
167. Ayat NR, Vaidya A, Yeung GA, et al. Effective MR Molecular Imaging of Triple Negative Breast Cancer With an EDB-Fibronectin-Specific Contrast Agent at Reduced Doses. *Front Oncol.*;9 . Epub ahead of print 2019. DOI: 10.3389/fonc.2019.01351.
168. Provenzano PP, Cuevas C, Chang AE, et al. Enzymatic targeting of the stroma ablates physical barriers to treatment of pancreatic ductal adenocarcinoma. *Cancer Cell.* 2012;21:418–429.
169. Cho H-J, Yoon HY, Koo H, et al. Hyaluronic acid-ceramide-based optical/MR dual imaging nanoprobe for cancer diagnosis. *J Control Release Off J Control Release Soc.* 2012;162:111–118.
170. Lee T, Lim E-K, Lee J, et al. Efficient CD44-targeted magnetic resonance imaging (MRI) of breast cancer cells using hyaluronic acid (HA)-modified MnFe2O4 nanocrystals. *Nanoscale Res Lett.* 2013;8:149.
171. Yoon HY, Koo H, Choi KY, et al. Tumor-targeting hyaluronic acid nanoparticles for photodynamic imaging and therapy. *Biomaterials.* 2012;33:3980–3989.
172. Yang R-M, Fu C-P, Fang J-Z, et al. Hyaluronan-modified superparamagnetic iron oxide nanoparticles for bimodal breast cancer imaging and photothermal therapy. *Int J Nanomedicine.* 2016;12:197–206.
173. Qi B, Crawford AJ, Wojtynek NE, et al. Indocyanine green loaded hyaluronan-derived nanoparticles for fluorescence-enhanced surgical imaging of pancreatic cancer. *Nanomedicine Nanotechnol Biol Med.* 2018;14:769–780.
174. Kimbrough CW, Hudson S, Khanal A, et al. Orthotopic pancreatic tumors detected by optoacoustic tomography using Syndecan-1. *J Surg Res.* 2015;193:246–254.
175. Zhu D, Qin Y, Wang J, et al. Novel Glypican-3-Binding Peptide for in Vivo Hepatocellular Carcinoma Fluorescent Imaging. *Bioconjug Chem.* 2016;27:831–839.
176. Sham JG, Kievit FM, Grierson JR, et al. Glypican-3–Targeted 89Zr PET Imaging of Hepatocellular

- Carcinoma. *J Nucl Med Off Publ Soc Nucl Med*. 2014;55:799–804.
177. Sham JG, Kievit FM, Grierson JR, et al. Glypican-3–Targeting F(ab')₂ for 89Zr PET of Hepatocellular Carcinoma. *J Nucl Med Off Publ Soc Nucl Med*. 2014;55:2032–2037.
178. Li W, Xiao X, Li X, et al. Detecting GPC3-Expressing Hepatocellular Carcinoma with L5 Peptide-Guided Pretargeting Approach: In Vitro and In Vivo MR Imaging Experiments. *Contrast Media Mol Imaging*. 2018;2018:9169072.
179. Di Paola M, Quarta A, Conversano F, et al. Human Hepatocarcinoma Cell Targeting by Glypican-3 Ligand Peptide Functionalized Silica Nanoparticles: Implications for Ultrasound Molecular Imaging. *Langmuir ACS J Surf Colloids*. 2017;33:4490–4499.
180. Kessenbrock K, Plaks V, Werb Z. Matrix Metalloproteinases: Regulators of the Tumor Microenvironment. *Cell*. 2010;141:52–67.
181. Sternlicht MD, Bergers G. Matrix metalloproteinases as emerging targets in anticancer therapy: status and prospects. *Emerg Ther Targets*. 2000;4:609–633.
182. Medina OP, Kairemo K, Valtanen H, et al. Radionuclide imaging of tumor xenografts in mice using a gelatinase–targeting peptide. *Anticancer Res*. 2005;25:33–42.
183. Scherer RL, McIntyre JO, Matrisian LM. Imaging matrix metalloproteinases in cancer. *Cancer Metastasis Rev*. 2008;27:679–690.
184. Wagner S, Breyholz H-J, Law MP, et al. Novel fluorinated derivatives of the broad-spectrum MMP inhibitors N-hydroxy-2(R)-[[[4-methoxyphenyl)sulfonyl](benzyl)- and (3-picolyl)-amino]-3-methyl-butanamide as potential tools for the molecular imaging of activated MMPs with PET. *J Med Chem*. 2007;50:5752–5764.
185. Zheng Q-H, Fei X, DeGrado TR, et al. Synthesis, biodistribution and micro-PET imaging of a potential cancer biomarker carbon-11 labeled MMP inhibitor (2R)-2-[[4-(6-fluorohex-1-ynyl)phenyl]sulfonylamino]-3-methylbutyric acid [11C]methyl ester. *Nucl Med Biol*. 2003;30:753–760.
186. Zheng X, Zhao FF, Liu YM, et al. Synthesis and preliminary biological evaluation of chrysin derivatives as potential anticancer drugs. *Med Chem Shariqah United Arab Emir*. 2010;6:6–8.
187. Chuang C-H, Chuang K-H, Wang H-E, et al. In vivo positron emission tomography imaging of protease activity by generation of a hydrophobic product from a noninhibitory protease substrate. *Clin Cancer Res Off J Am Assoc Cancer Res*. 2012;18:238–247.
188. Morcillo MÁ, García de Lucas Á, Oteo M, et al. MT1-MMP as a PET Imaging Biomarker for Pancreas Cancer Management. *Contrast Media & Molecular Imaging*. 2018;2018:e8382148.
189. Zhao T, Harada H, Teramura Y, et al. A novel strategy to tag matrix metalloproteinases-positive cells for in vivo imaging of invasive and metastatic activity of tumor cells. *J Control Release Off J Control Release Soc*. 2010;144:109–114.
190. Bremer C, Bredow S, Mahmood U, et al. Optical imaging of matrix metalloproteinase-2 activity in tumors: feasibility study in a mouse model. *Radiology*. 2001;221:523–529.
191. Lepage M, Dow WC, Melchior M, et al. Noninvasive detection of matrix metalloproteinase activity in vivo using a novel magnetic resonance imaging contrast agent with a solubility switch. *Mol Imaging*. 2007;6:393–403.
192. Lebel R, Jastrzębska B, Therriault H, et al. Novel solubility-switchable MRI agent allows the noninvasive detection of matrix metalloproteinase-2 activity in vivo in a mouse model. *Magn Reson Med*. 2008;60:1056–1065.
193. Olson ES, Jiang T, Aguilera TA, et al. Activatable cell penetrating peptides linked to nanoparticles as dual probes for in vivo fluorescence and MR imaging of proteases. *Proc Natl Acad Sci*. 2010;107:4311–4316.
194. Huang C-W, Li Z, Conti PS. Radioactive smart probe for potential corrected matrix metalloproteinase imaging. *Bioconjug Chem*. 2012;23:2159–2167.
195. Csoka AB, Frost GI, Stern R. The six hyaluronidase-like genes in the human and mouse genomes. *Matrix Biol J Int Soc Matrix Biol*. 2001;20:499–508.
196. Whatcott CJ, Han H, Posner RG, et al. Targeting the tumor microenvironment in cancer: why hyaluronidase deserves a second look. *Cancer Discov*. 2011;1:291–296.
197. Shifftan L, Neeman M. Kinetic analysis of hyaluronidase activity using a bioactive MRI contrast agent. *Contrast Media Mol Imaging*. 2006;1:106–112.
198. Shifftan L, Israely T, Cohen M, et al. Magnetic resonance imaging visualization of hyaluronidase in ovarian carcinoma. *Cancer Res*. 2005;65:10316–10323.
199. Rainey J, Maffuid P, Scholz WW, et al. Abstract 3036: PEGylated hyaluronidase increases tumor uptake of 89Zr-DFO-HuMab-5B1 (MVT-2163) in a CA19-9 positive hyaluronan-accumulating pancreatic cancer model. *Cancer Res*. 2018;78:3036–3036.
200. Tabolacci C, De Martino A, Mischiati C, et al. The Role of Tissue Transglutaminase in Cancer Cell Initiation, Survival and Progression. *Med Sci*;7 . Epub ahead of print January 25, 2019. DOI: 10.3390/medsci7020019.
201. Mazoos G, Mehlman T, Lai T-S, et al. Development of magnetic resonance imaging contrast material for in vivo mapping of tissue transglutaminase activity. *Cancer Res*. 2005;65:1369–1375.
202. Tei L, Mazoos G, Shellef Y, et al. Novel MRI and fluorescent probes responsive to the Factor XIII transglutaminase activity. *Contrast Media Mol Imaging*. 2010;5:213–222.
203. Dafni H, Ronen SM. Dynamic nuclear polarization in metabolic imaging of metastasis: common sense, hypersense and compressed sensing. *Cancer Biomark Sect Dis Markers*. 2010;7:189–199.
204. Chen AP, Tropp J, Hurd RE, et al. In vivo hyperpolarized 13C MR spectroscopic imaging with 1H decoupling. *J Magn Reson San Diego Calif 1997*. 2009;197:100–106.
205. Zhu L, Ploessl K, Zhou R, et al. Metabolic Imaging of Glutamine in Cancer. *J Nucl Med*. 2017;58:533–537.
206. Mori N, Wildes F, Takagi T, et al. The Tumor Microenvironment Modulates Choline and Lipid Metabolism. *Front Oncol*;6 . Epub ahead of print 2016. DOI: 10.3389/fonc.2016.00262.
207. Anemone A, Consolino L, Arena F, et al. Imaging tumor acidosis: a survey of the available techniques for mapping in vivo tumor pH. *Cancer Metastasis Rev*. 2019;38:25–49.
208. Lee H, Akers W, Bhushan K, et al. Near-Infrared pH-Activatable Fluorescent Probes for Imaging Primary and Metastatic Breast Tumors . Epub ahead of print March 9, 2011. DOI: 10.1021/bc100584d.

Molecular targets for diagnostic and intraoperative imaging of pancreatic ductal adenocarcinoma after neoadjuvant FOLFIRINOX treatment

F.A. Vuijk, L.D.A.N. de Muynck, L.C. Franken, O.R. Busch, J.W. Wilmink, M.G. Besselink, B.A. Bonsing, S.S. Bhairosingh, P.J.K. Kuppen, J.S.D. Mieog, C.F.M. Sier, A.L. Vahrmeijer, J. Verheij, A. Fariña-Sarasqueta and R.J. Swijnenburg.

Scientific Reports (2020)



ABSTRACT

Neoadjuvant systemic treatment is increasingly being integrated in the standard treatment of pancreatic ductal adenocarcinoma (PDAC) patients to improve oncological outcomes. Current available imaging techniques remain unreliable in assessing response to therapies, as they cannot distinguish between (vital) tumor tissue and therapy induced fibrosis (TIF). Consequently, resections with tumor positive margins and subsequent early post-operative recurrences occur and patients eligible for potential radical resection could be missed. To optimize patient selection and monitor results of neoadjuvant treatment, PDAC-specific diagnostic and intraoperative molecular imaging methods are required. This study aims to evaluate molecular imaging targets for PDAC after neoadjuvant FOLFIRINOX treatment. Expression of integrin $\alpha_v\beta_6$, carcinoembryonic antigen cell adhesion molecule 5 (CEACAM5), mesothelin, prostate-specific membrane antigen (PSMA), urokinase-type plasminogen activator receptor, fibroblast activating receptor, integrin α_5 subunit and epidermal growth factor receptor was evaluated using immunohistochemistry. Immunoreactivity was determined using the semiquantitative H-score. Resection specimens from patients after neoadjuvant FOLFIRINOX treatment containing PDAC (n=32), tumor associated pancreatitis (TAP) and TIF (n=15), normal pancreas parenchyma (NPP) (n=32) and tumor positive (n=24) and negative (n=56) lymph nodes were included. Integrin $\alpha_v\beta_6$, CEACAM5, mesothelin and PSMA stainings showed significantly higher expression in PDAC compared to TAP and NPP. No expression of $\alpha_v\beta_6$, CEACAM5 and mesothelin was observed in TIF. Integrin $\alpha_v\beta_6$ and CEACAM5 allow for accurate metastatic lymph node detection. Targeting integrin $\alpha_v\beta_6$, CEA, mesothelin and PSMA has the potential to distinguish vital PDAC from fibrotic tissue after neoadjuvant FOLFIRINOX treatment. Integrin $\alpha_v\beta_6$ and CEACAM5 detect primary tumors and tumor positive lymph nodes.

INTRODUCTION

Pancreatic ductal adenocarcinoma (PDAC) is a devastating malignancy with a five year survival rate of merely 7-9%¹. This rate reflects the disease's asymptomatic progression, resulting in advanced-stage disease at the time of diagnosis for the vast majority of patients. Surgical resection combined with systemic treatment offers the only chance for cure. Unfortunately, only 15-25% of patients qualifies for resection^{2,3}. Despite careful patient selection and stratification by means of computed tomography (CT), magnetic resonance imaging, and endoscopic retrograde cholangiopancreatography, resection with positive tumor margins (R1) occurs in a substantial proportion of patients (up to 75%)^{2,4,5}. Moreover, early recurrences (within six months) after pancreatic resection are reported in 28% of patients, likely due to microscopic tumor deposits at the time of surgery⁵. The clinical relevance of a microscopically radical (R0) resection is further underlined by the two-fold increase in survival time after R0 compared to R1 resection⁵⁻⁸.

To improve patient survival and facilitate improved R0 resection rates, neoadjuvant chemotherapy is being implemented increasingly with results being evaluated in several clinical trials, including the Dutch PREOPANC-1 (NTR3709) and PREOPANC-2 trials (NTR7292). However, current imaging modalities struggle to distinguish between vital tumor cells and tumor associated pancreatitis (TAP), therapy induced fibrosis (TIF) and necrosis. As a consequence, 7-13% of pancreatic resections are currently performed for benign conditions⁹, and a large number of patients (up to 92%) is deemed unresectable after neoadjuvant FOLFIRINOX treatment based on conventional imaging have a R0 resection¹⁰.

With increasing use of potent neoadjuvant therapy, it is of great importance to accurately monitor tumor response to therapy and evaluate surgical resectability after neoadjuvant therapy in order to avoid futile surgical procedures. Both near-infrared fluorescence (NIRF) and positron emission tomography – computed tomography (PET-CT) imaging show promise in providing molecularly targeted imaging solutions to this problem. NIRF imaging is a relatively novel technique that can be used during surgery to discriminate malignant from benign tissue in real time¹¹, whereas tumor-specific PET-CT may contribute to improved surgical planning, stratification and diagnosis as well as therapy response monitoring after neoadjuvant treatment. Both modalities exploit tumor-specific tracers (either labeled with a fluorescent protein or radioisotope), targeting biomarkers abundantly present on tumor tissue and absent on (or minimally expressed by) benign or inflamed tissue.

Previous research has shown that [¹⁸F]FDG-PET/CT is able to influence clinical decision making, but unfortunately with a low specificity of 76% for the detection of PDAC¹².

To enable more specific tumor targeting, our previous immunohistochemical (IHC) studies found both integrin $\alpha_v\beta_6$ and carcinoembryonic antigen cell adhesion molecule 5 (CEACAM5) to be suitable targets to identify PDAC, distinguishing tumor tissue from TAP or normal pancreatic parenchyma, and also allowing sensitive and specific metastatic lymph node detection^{13,14}. Interestingly, after neoadjuvant chemotherapy, $\alpha_v\beta_6$ expression remained unchanged in vital tumor cells, whereas CEACAM5 expression was reduced¹⁴. From previous research, we know that not only tumor cells are of influence in cancer progression, the formation of metastases, and the varying response seen after neoadjuvant treatment. Cells of the tumor microenvironment (e.g. cancer-associated fibroblasts and immune cells) are of importance too, and could be considered for both imaging and therapeutic purposes^{15,16}. In addition to CEACAM5 and integrin $\alpha_v\beta_6$, the overexpression of mesothelin¹⁷⁻²³, prostate-specific membrane antigen (PSMA)²⁴⁻²⁸, urokinase-type plasminogen activator receptor (uPAR)^{13,29-31}, fibroblast activation protein alpha (FAP)³²⁻³⁴, integrin subunit α_5 (ITGA5)³⁵ and epidermal growth factor receptor (EGFR) has been described in PDAC tissue, suggesting their candidacy as imaging targets for PDAC.

This study aims to evaluate the immunohistochemical expression of potential molecular imaging targets integrin $\alpha_v\beta_6$, CEACAM5, mesothelin, PSMA, uPAR, FAP, ITGA5 and EGFR for the identification of vital residual PDAC and metastatic lymph nodes after neoadjuvant FOLFIRINOX treatment^{13,14,17-37}.

METHODS

Patient and Material selection

Patients admitted to the Amsterdam UMC (location AMC) diagnosed with PDAC and treated with neoadjuvant FOLFIRINOX treatment (consisting of folinic acid, 5'-fluorouracil, irinotecan, and oxaliplatin) were retrospectively included. After surgical resection, representative formalin-fixed paraffin-embedded (FFPE) tissue blocks containing tumor, normal pancreatic parenchyma, and TAP, as well as tumor positive and negative lymph nodes, were selected and obtained from the Department of Pathology (Amsterdam UMC, location AMC). Clinicopathologic characteristics were obtained from medical records. The need for ethical approval and individual consent was waived by the Institutional Medical Ethics Committee, and this study conducted in accordance with the Declaration of Helsinki.

Immunohistochemistry

FFPE tissue sections at four μm thickness were sliced and stained for integrin $\alpha_v\beta_6$, CEACAM5, mesothelin, PSMA, uPAR, FAP, ITGA5 and EGFR. After deparaffinization in

xylene and rehydration in a stepwise series of alcohol solutions, endogenous peroxidase activity was blocked with 0.3% hydrogen peroxide in water for 20 minutes. Antigen retrieval was performed as described in Supplementary Table 1. Following antigen retrieval, slides stained for FAP were incubated for 10 minutes with Protein Block (Dako, Glostrup, Denmark). All slides were incubated overnight at room temperature with primary antibodies (Supplementary Table 1). Slides were washed in phosphate-buffered saline (PBS) and incubated for 30 minutes at room temperature with an HRP-labelled secondary antibody (anti-mouse, anti-rabbit (Envision, Dako, Glostrup, Denmark) or anti-donkey (Invitrogen, Carlsbad, USA)). After being rinsed with PBS, immunoreactions were visualized using DAB substrate buffer (Dako, Glostrup, Denmark) for ten minutes and counterstained using Mayer's hematoxylin for 30 seconds. After dehydration at 37°C, the slides were mounted with PERTEX® (Leica Microsystems, Wetzlar, Germany).

Evaluation of immunoreactivity

Evaluation of immunoreactivity was performed by two independent pathologists in tandem (A.F.S. and J.V.) and was conducted using the semi-quantitative H-score^{38,39}. Consensus was reached for all patients. This score takes into account both staining intensity and percentage of cells stained and is used by multiplying the staining intensity (0, 1, 2, or 3) by the percentage of cells expressing the target at this intensity (0-100%), resulting in a score ranging from 0 to 300. As a result, higher H-scores indicate more intense staining in a higher percentage of cells.

To define the contrast that a molecular target provides in distinguishing PDAC from normal pancreatic parenchyma or TAP, the Tumor to Normal Ratio (TNR) was established. The TNR was calculated by dividing the Tumor H-score by the Normal H-score (average H-score of normal pancreatic parenchyma and TAP). The H-score for Normal was defined as 1 when no expression was seen in TAP or normal pancreatic parenchyma.

The lymph node detection potential was evaluated by calculating sensitivity, specificity, positive predictive value (PPV), and negative predictive value (NPV) of selected biomarkers to correctly identify tumor positive lymph nodes. Sensitivity was calculated by dividing the true positive lymph nodes (TPLN) by the sum of TPLN and the false-negative lymph nodes (FNLN). Specificity was calculated by dividing the true negative lymph nodes (TNLN) by the sum of the TNLN and false-positive lymph nodes (FPLN). PPV was calculated by dividing the TPLN by the sum of TPLN and FPLN. NPV was calculated by dividing the TNLN by the sum of the TNLN and FNLN.

Statistical analysis

Statistical analysis was performed using SPSS version 25 (IBM SPSS, Inc., Chicago, USA) and GraphPad Prism 8 (GraphPad Software, Inc., San Diego, USA). Continuous descriptive

data respecting a Gaussian distribution were displayed as mean (standard deviation), or median (interquartile range) when non-parametric. Categorical data were displayed as frequencies and percentages. H-scores were compared using the Kruskal Wallis one way ANOVA test with post hoc Bonferroni correction for multiple testing. Results were considered significant when $p < 0.05$.

RESULTS

Patient characteristics

FFPE tissue from resection specimens of 32 patients treated with neoadjuvant FOLFIRINOX was included. Tissue containing primary tumor and normal pancreatic parenchyma from 32 patients, tumor associated TAP from 16 of these patients, and 24 tumor-positive and 56 tumor-negative lymph nodes were included. Primary tumor and normal pancreatic parenchyma tissue were stained for all eight biomarkers. Tissue containing TAP and lymph nodes were stained only for the four best performing biomarkers ($\alpha_v\beta_6$, CEACAM5, mesothelin and PSMA), as described in the section below. Patient characteristics are summarized in **Table 1**.

TABLE 1. Patient characteristics

		N = 32
Age	Mean (SD)	64.3 (8.8)
Sex	Male	17 (53%)
	Female	15 (47%)
Cycles of neoadjuvant FOLFIRINOX	Median (IQR)	4.5 (2)
ypT	1	4 (13%)
	2	8 (25%)
	3	17 (53%)
	4	3 (9%)
ypN	0	12 (37%)
	1	20 (63%)
ypM	0	31 (97%)
	1	1 (3%)
Differentiation	Good	5 (16%)
	Moderate	16 (50%)
	Poor	8 (25%)
	Missing	3 (16%)
Tumor diameter (mm)	Median (IQR)	30 (23.3)
Total lymph nodes	Median (IQR)	16 (8.8)
Tumor positive lymph nodes	Median (IQR)	1.5 (3)

Abbreviations: SD, standard deviation; IRQ, interquartile range; ypT, pathological tumor stage after neoadjuvant therapy; ypN, pathological nodal stage after neoadjuvant therapy; ypM, pathological metastatic stage after neoadjuvant therapy.

Biomarker expression in primary tumor tissue

All biomarkers, except for ITGA5 and FAP (both mean H-score of 0), were expressed by either tumor- or stromal cells with a median and interquartile range (IQR) tumor H-score of 270 (IQR 50) for $\alpha_v\beta_6$, 135 (IQR 168) for CEACAM5, 240 (IQR 67) for mesothelin, 60 (IQR 115) for PSMA, and 30 (IQR 50) for uPAR. Integrin $\alpha_v\beta_6$, CEACAM5, and mesothelin demonstrated membrane-bound tumor cell expression. PSMA was expressed on the endothelium of tumor-associated neovasculature. EGFR showed equal expression in both tumor and normal pancreatic parenchyma. uPAR was expressed very weakly on a low percentage of stromal cells (fibroblasts), but showed high expression by pancreatic islets of Langerhans. Based on these results, uPAR, FAP, ITGA5, and EGFR were excluded from further analyses. Expression patterns of integrin $\alpha_v\beta_6$, CEACAM5, mesothelin and PSMA are depicted in **Figure 1**. Expression patterns of the excluded biomarkers uPAR, FAP, ITGA5 and EGFR are depicted in **Supplementary Figure 1**. Results from the immunohistochemical stainings are summarized in **Table 2**.

Tumor-to-Normal Ratio (TNR)

Integrin $\alpha_v\beta_6$, CEACAM5, mesothelin, and PSMA all exhibited significantly higher H-scores on PDAC tissue compared to normal pancreatic parenchyma and TAP ($P < 0.001$), as depicted in **Figure 1 and 2**. Further analysis of H-scores resulted in a TNR of 4.1 for integrin $\alpha_v\beta_6$, 28.5 for CEACAM5, 25.5 for mesothelin and 99.4 for PSMA.

Biomarker expression in (therapy induced) fibrosis

Integrin $\alpha_v\beta_6$, CEACAM5 and mesothelin showed no expression on (therapy induced) fibrotic tissue. PSMA was expressed by neoangiogenic endothelium in close proximity to cancer cells, however not by the cancer cells themselves. After neoadjuvant therapy, capillaries are still present and express PSMA. It is, however, impossible to determine whether these are neoangiogenic capillaries in a former tumor bed, or 'normal' capillaries that were never associated with cancer growth.

Lymph node detection potential

Examples of IHC stainings of tumor positive lymph nodes are depicted in **Figure 3**. IHC staining identified 24 true positive (TP) and 56 true negative (TN) lymph nodes when staining for integrin $\alpha_v\beta_6$, 20 TP and 60 TN lymph nodes for CEACAM5, 16 TP and 63 TN lymph nodes for mesothelin and 15 TP and 24 TN lymph nodes for PSMA. This resulted in a sensitivity and specificity of 100% and 100% for integrin $\alpha_v\beta_6$, 83% and 100% for CEACAM5, 67% and 100% for mesothelin and 65% and 32% for PSMA, respectively, as summarized in **Table 3**. PSMA staining was only expressed by lymph nodes germinal centers, not by metastatic tumor ducts. An overview of IHC analysis results is provided in **Table 3**.

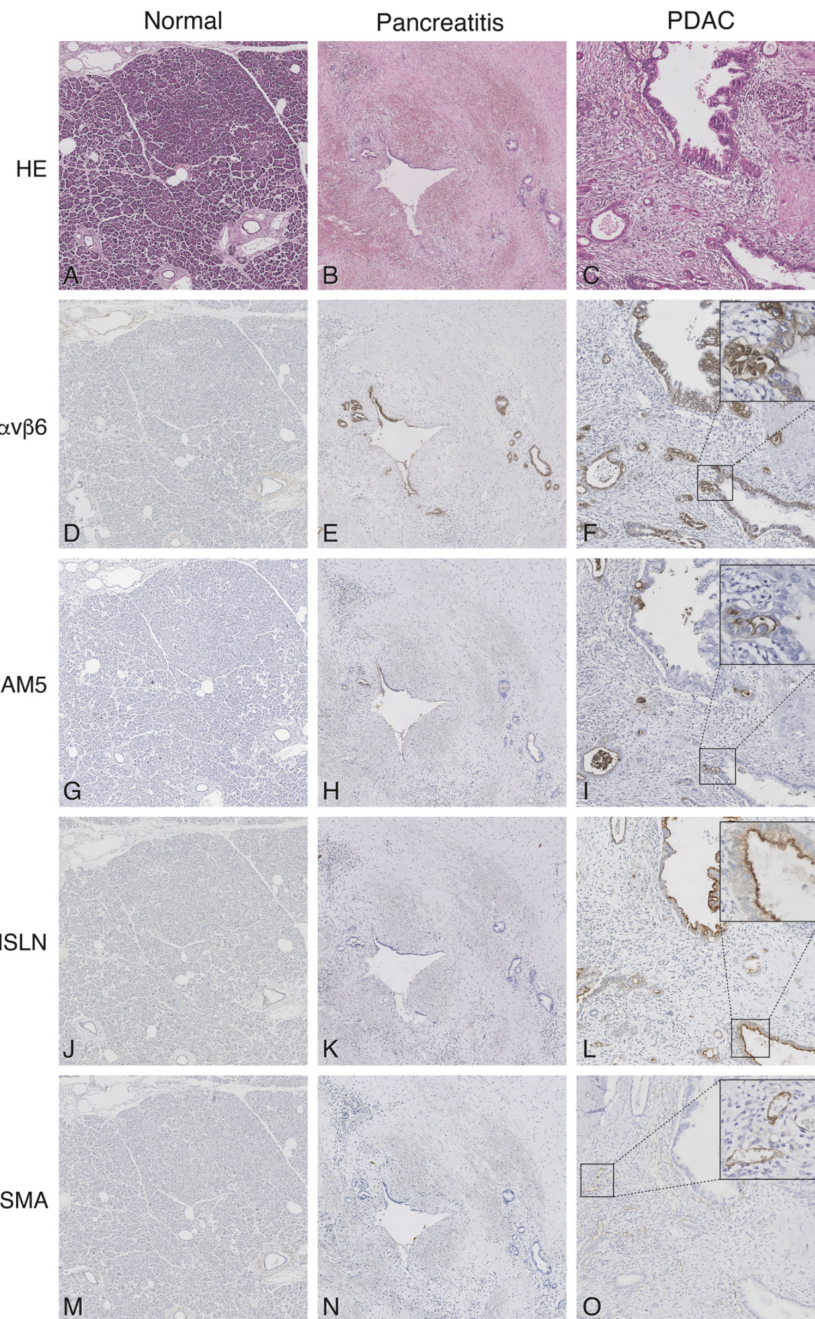


FIGURE 1. Overview of immunohistochemical staining

Representative images of HE (A-C), integrin $\alpha_v\beta_6$ (D-F), CEACAM5 (G-I), mesothelin (J-L) and PSMA (M-O) expression on normal pancreatic parenchyma, tumor induced pancreatitis and PDAC. All images are at 5x magnification, zoom images in C, F, I, L and O at 40x magnification. Abbreviations: HE, hematoxylin eosin; $\alpha_v\beta_6$, integrin $\alpha_v\beta_6$; CEACAM5, carcinoembryonic antigen cell adhesion molecule 5; MSLN, mesothelin; PSMA, prostate-specific membrane antigen.

TABLE 2. Overview of investigated molecular targets

Target	Previous research	TNR	Sensitivity lymph node metastases	Specificity lymph node metastases	Other structures expressing target
$\alpha_v\beta_6$	13,14,47,50	4.1	100	100	Duodenum, normal pancreatic parenchyma
CEACAM5	13,14,36,51,52	28.5	83	100	
Mesothelin	17–23	25.5	67	100	Mesothelium
PSMA	24–28	99.4	65	32	Duodenum, germ centers in lymph nodes
EGFR	13,37,53	N/A	N/A	N/A	Duodenum, normal pancreatic parenchyma
uPAR	13,29–31	N/A	N/A	N/A	Pancreatic islets, neuroendocrine cells, duodenum
FAP	32–34	N/A	N/A	N/A	Nerve, muscle, lymphocytes
ITGA5	35	N/A	N/A	N/A	Endothelium, duodenum, islet-progenitor acinar cells

Abbreviations: TNR, Tumor to Normal ratio (as described in methods); $\alpha_v\beta_6$, integrin $\alpha_v\beta_6$; CEACAM5, carcinoembryonic antigen cell adhesion molecule 5; PSMA, prostate-specific membrane antigen; EGFR, epidermal growth factor receptor; uPAR, urokinase-type plasminogen activator receptor; FAP, fibroblast activating protein; ITGA5, integrin α

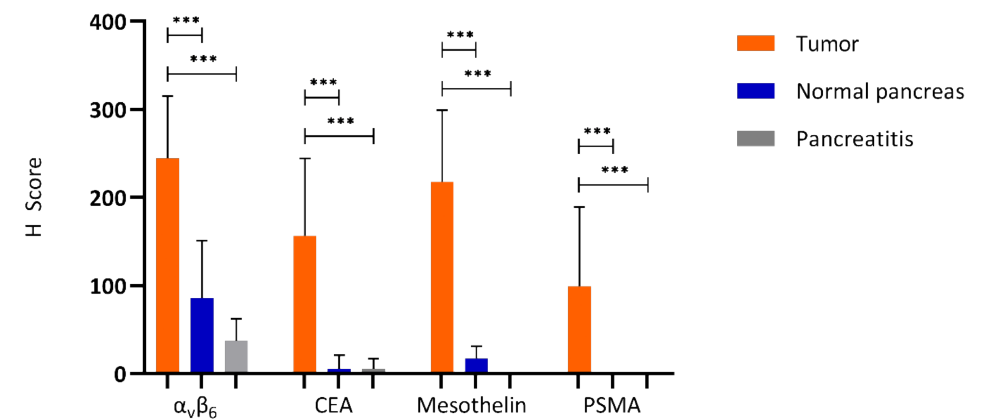


FIGURE 2. H-scores of selected molecular targets

Representative diagrams of H-scores of integrin $\alpha_v\beta_6$, CEACAM5, mesothelin and PSMA on tumor (PDAC), normal and tumor induced pancreatitis. H-scores were determined as described in Material and Methods. Abbreviations: CEACAM5, carcinoembryonic antigen cell adhesion molecule 5; PSMA, prostate-specific membrane antigen.

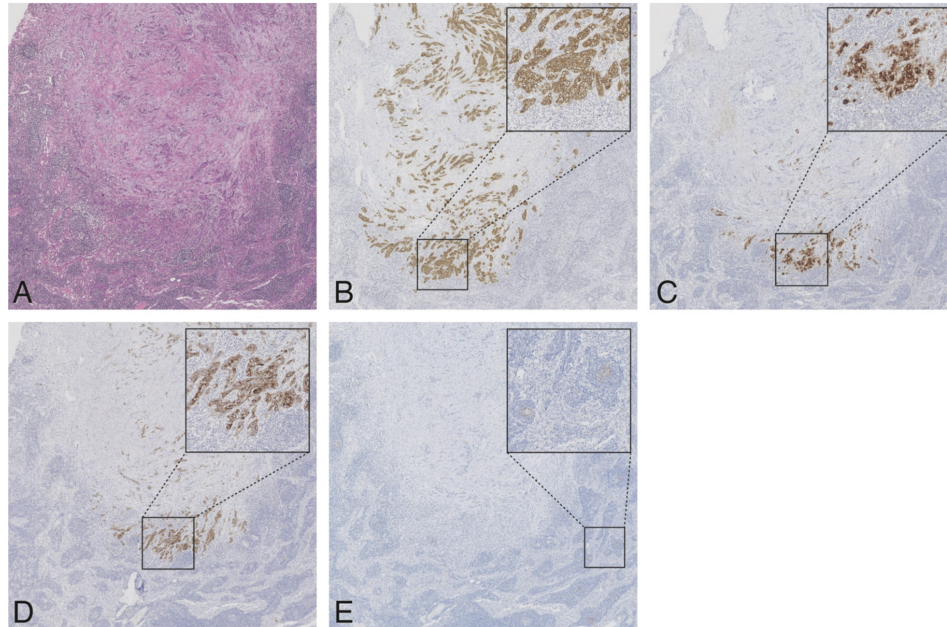


FIGURE 3. Overview of immunohistochemical stainings on a tumor positive lymph node
 Representative images of a metastatic lymph node stained for HE (A), integrin $\alpha_v\beta_6$ (B), CEACAM5 (C), mesothelin (D) and PSMA (E). All images are at 2x magnification, zoom images at 10x magnification. Abbreviations: CEACAM5, carcinoembryonic antigen cell adhesion molecule 5; PSMA, prostate-specific membrane antigen.

TABLE 3. Overview of lymph node detection potential of $\alpha_v\beta_6$, CEACAM5, mesothelin, and PSMA

	Sensitivity	Specificity	PPV	NPV
$\alpha_v\beta_6$	100	100	100	100
CEACAM5	83	100	100	94
Mesothelin	67	100	100	89
PSMA	65	32	33	75

Abbreviations: PPV, positive predictive value; NPV, negative predictive value; CEACAM5, carcinoembryonic antigen cell adhesion molecule 5; PSMA, prostate-specific membrane antigen.

DISCUSSION

Our results show significantly higher expression of integrin $\alpha_v\beta_6$, CEACAM5, mesothelin, and PSMA in PDAC tissue after neoadjuvant therapy as compared to both TAP and normal pancreatic parenchyma. No expression of integrin $\alpha_v\beta_6$, CEACAM5 and mesothelin was observed in fibrotic tissue, indicating these are potentially suitable targets for vital cancer cell identification after neoadjuvant therapy. In contrast to integrin $\alpha_v\beta_6$ and CEACAM5, which are also highly sensitive and specific in detecting metastatic lymph

nodes, mesothelin and PSMA seem less suitable for this second application.

In line with our previous results, a significant difference in expression of integrin $\alpha_v\beta_6$ was seen between PDAC tissue and both TAP and normal pancreatic parenchyma. However, in comparison to the other evaluated markers, a low Tumor to Normal Ratio was found due to moderate expression of $\alpha_v\beta_6$ on normal pancreatic ducts¹⁴. Moreover, we have previously described integrin $\alpha_v\beta_6$ expression after neoadjuvant therapy in PDAC as being twice as high in comparison to normal pancreatic parenchyma and four times higher in PDAC compared to TAP¹⁴. Results from the present study are similar, demonstrating integrin $\alpha_v\beta_6$ expression in PDAC to be almost three times higher compared to normal pancreatic parenchyma and 7.5 times higher compared to TAP. Before neoadjuvant treatment, CEACAM5 expression was absent in both normal and inflamed pancreatic parenchyma. Interestingly, our previous study described absence of CEACAM5 expression in 2/6 PDAC samples after neoadjuvant treatment¹⁴. Lack of CEACAM5 expression was seen in only 1/6 patient in this study. Two possible reasons for the reduced expression observed by Tummers *et al.* are tumor heterogeneity, in which CEACAM5 expression is selectively diminished by therapy in a subset of tumor cells, or a selective effect of therapy on the cell genome resulting in clonal evolution^{14,40–42}.

Although absolute PSMA expression was lower compared to other molecular targets, specificity for staining tumor associated vessels as well as the contrast seen between normal pancreatic parenchyma and TAP was high (TNR = 99.4). Considering the high sensitivity of both PET and fluorescence imaging (PET 10^{-11} to 10^{-12} M, NIRF 10^{-9} to 10^{-12} M)⁴³, the lower absolute expression might not pose a problem. However, considering the nature of targeting, i.e. neoangiogenic endothelial cells, the lack of expression in metastatic lymph nodes would be a limiting factor for PSMA-based targeting. A possible explanation for the absence of PSMA expression in lymph node metastases might lie in the biology of this receptor or lower density of neoangiogenic vessels. PSMA is a type II transmembrane protein upregulated in the neoangiogenesis pathway of solid tumors. Previous clinical and preclinical evidence suggest this pathway is highly activated in primary tumors, however metastatic lymph node development might rely on other pathways. This is demonstrated by the failure of antiangiogenic therapies to completely diminish (lymph node) metastases^{44,45}. Previous research shows sprouting angiogenesis is mostly involved in primary tumor angiogenesis, whereas mechanisms such as vessel co-option and intussusception have been implicated in the growth of various cancer metastases, and are possibly also more relevant in lymph node metastases development⁴⁶.

As reported by most studies investigating epithelial targets, the exact influence of patchy growth patterns on tracer accumulation and imaging results is uncertain. Although first results from tumor-specific pancreatic carcinoma PET-CT research look promising⁴⁷,

future clinical trials will have to provide more insight as to whether heterogenic tracer distribution throughout a larger tumor volume will provide sufficient imaging contrast. The high expression of integrin $\alpha_v\beta_6$, CAECAM5, mesothelin, and PSMA, might suggest a functional role of these proteins in the development of PDAC, through for example the β -catenin/wnt signaling pathway, as recently described by Argentiero *et al.*⁴⁸. In line with that, it could be speculated that by suppression of chemokine production by signalling of the previously mentioned proteins, T-cell infiltration can be halted and tumor progression is supported.

Depending on the purpose of imaging, optimal target selection can vary. Integrin $\alpha_v\beta_6$ and CEA might provide the most versatile imaging targets, offering both primary tumor detection as well as sensitive and specific lymph node imaging. Mesothelin and PSMA, however, are equally suitable for primary detection but lack accuracy in detecting metastatic lymph nodes. Results from previous work from our group demonstrate the feasibility of CEA-targeted imaging in pancreatic cancer patients. Results show tumor specific tracer accumulation and identified previously unseen tumor nodules³⁶. The present study shows that FAP, ITGA5 and EGFR are unsuitable targets for molecular imaging of PDAC as FAP and ITGA5 expression was minimal and EGFR was equally expressed by PDAC and normal pancreatic parenchyma. However, a recent study using a FAP targeted PET radioligand, [⁶⁸Ga]-FAPI, was able to detect 51/51 PDAC lesions (mean SUVmax of ~ 10)³², EGFR targeting cetuximab-IRDye800 was able to detect 7/7 pancreatic lesions using NIRF imaging³⁷, and a recent IHC study described strong ITGA5 expression in the tumor stroma of 66% out of 137 primary PDAC samples (without neoadjuvant treatment)³⁵. These results put the limited translational value of IHC studies in predicting clinical imaging results into perspective, and demonstrate that more than just receptor expression is involved in reaching successful tracer uptake in tumor tissue. Future animal studies will have to provide more information on the success of targeting these biomarkers for imaging.

Possible limitations of this study include a relatively small sample size, semi-quantitative analysis of IHC results and the lack of knowledge regarding biomarker expression in these patients before neoadjuvant therapy. Direct comparison before and after therapy was unfortunately not possible, as no pre-operative tissue was available. Nonetheless, due to previous work within our group and the fact that only targets with known overexpression were investigated in a substantial number of patients, we feel confident that expression levels in these tumors represent the general population and provide clinically relevant information.

In conclusion, integrin $\alpha_v\beta_6$, CEACAM5, mesothelin, and PSMA are potential suitable targets for both pre-operative as well as intraoperative molecular imaging before and

after neoadjuvant FOLFIRINOX treatment, as will have to be confirmed by future clinical imaging studies. Using PET-CT, NIRF, or other molecular imaging modalities, both integrin $\alpha_v\beta_6$ and CEACAM5 show most promise as molecular targets for the imaging of PDAC and metastatic lymph nodes, as is currently being further investigated in the PANSCAN trial and other clinical studies⁴⁹.

REFERENCES

1. Latenstein AEJ, van der Geest LGM, Bonsing BA, et al. Nationwide trends in incidence, treatment and survival of pancreatic ductal adenocarcinoma. *Eur J Cancer Oxf Engl 1990*. 2020;125:83–93.
2. Barugola G, Partelli S, Marcucci S, et al. Resectable pancreatic cancer: who really benefits from resection? *Ann Surg Oncol*. 2009;16:3316–3322.
3. Stathis A, Moore MJ. Advanced pancreatic carcinoma: current treatment and future challenges. *Nat Rev Clin Oncol*. 2010;7:163–172.
4. Verbeke CS. Resection margins in pancreatic cancer. *Surg Clin North Am*. 2013;93:647–662.
5. Tummers WS, Groen JV, Sibinga Mulder BG, et al. Impact of resection margin status on recurrence and survival in pancreatic cancer surgery. *Br J Surg*. . Epub ahead of print March 18, 2019. DOI: 10.1002/bjs.11115.
6. Neoptolemos JP, Palmer DH, Ghaneh P, et al. Comparison of adjuvant gemcitabine and capecitabine with gemcitabine monotherapy in patients with resected pancreatic cancer (ESPAC-4): a multicentre, open-label, randomised, phase 3 trial. *Lancet Lond Engl*. 2017;389:1011–1024.
7. Yeo CJ, Cameron JL, Lillemoie KD, et al. Pancreaticoduodenectomy for cancer of the head of the pancreas. 201 patients. *Ann Surg*. 1995;221:721–733.
8. Ghaneh P, Kleeff J, Halloran CM, et al. The Impact of Positive Resection Margins on Survival and Recurrence Following Resection and Adjuvant Chemotherapy for Pancreatic Ductal Adenocarcinoma. *Ann Surg*. 2019;269:520–529.
9. Gerritsen A, Molenaar IQ, Bollen TL, et al. Preoperative characteristics of patients with presumed pancreatic cancer but ultimately benign disease: a multicenter series of 344 pancreatoduodenectomies. *Ann Surg Oncol*. 2014;21:3999–4006.
10. Ferrone CR, Marchegiani G, Hong TS, et al. Radiological and surgical implications of neoadjuvant treatment with FOLFIRINOX for locally advanced and borderline resectable pancreatic cancer. *Ann Surg*. 2015;261:12–17.
11. Vahrmeijer AL, Hutteman M, van der Vorst JR, et al. Image-guided cancer surgery using near-infrared fluorescence. *Nat Rev Clin Oncol*. 2013;10:507–518.
12. Ghaneh P, Hanson R, Titman A, et al. PET-PANC: multicentre prospective diagnostic accuracy and health economic analysis study of the impact of combined modality 18fluorine-2-fluoro-2-deoxy-d-glucose positron emission tomography with computed tomography scanning in the diagnosis and management of pancreatic cancer. *Health Technol Assess Winch Engl*. 2018;22:1–114.
13. de Geus SWL, Boogerdt LSF, Swijnenburg R-J, et al. Selecting Tumor-Specific Molecular Targets in Pancreatic Adenocarcinoma: Paving the Way for Image-Guided Pancreatic Surgery. *Mol Imaging Biol MIB Off Publ Acad Mol Imaging*. 2016;18:807–819.
14. Tummers WS, Farina-Sarasqueta A, Boonstra MC, et al. Selection of optimal molecular targets for tumor-specific imaging in pancreatic ductal adenocarcinoma. *Oncotarget*. . Epub ahead of print 26 2017. DOI: 10.18632/oncotarget.18232.
15. Porcelli L, Iacobazzi RM, Di Fonte R, et al. CAFs and TGF- β Signaling Activation by Mast Cells Contribute to Resistance to Gemcitabine/Nabpaclitaxel in Pancreatic Cancer. *Cancers*.;11 . Epub ahead of print March 7, 2019. DOI: 10.3390/cancers11030330.
16. Ryzhov SV, Pickup MW, Chytil A, et al. Role of TGF- β signaling in generation of CD39+CD73+ myeloid cells in tumors. *J Immunol Baltim Md 1950*. 2014;193:3155–3164.
17. Argani P, Iacobuzio-Donahue C, Ryu B, et al. Mesothelin is overexpressed in the vast majority of ductal adenocarcinomas of the pancreas: identification of a new pancreatic cancer marker by serial analysis of gene expression (SAGE). *Clin Cancer Res Off J Am Assoc Cancer Res*. 2001;7:3862–3868.
18. Einama T, Kamachi H, Nishihara H, et al. Co-expression of mesothelin and CA125 correlates with unfavorable patient outcome in pancreatic ductal adenocarcinoma. *Pancreas*. 2011;40:1276–1282.
19. Hassan R, Laszik ZG, Lerner M, et al. Mesothelin is overexpressed in pancreaticobiliary adenocarcinomas but not in normal pancreas and chronic pancreatitis. *Am J Clin Pathol*. 2005;124:838–845.
20. Ordóñez NG. Application of mesothelin immunostaining in tumor diagnosis. *Am J Surg Pathol*. 2003;27:1418–1428.
21. Frank R, Li S, Ahmad NA, et al. Mesothelin expression in pancreatic mucinous cysts. *Am J Clin Pathol*. 2014;142:313–319.
22. Lin F, Chen ZE, Wang HL. Utility of immunohistochemistry in the pancreatobiliary tract. *Arch Pathol Lab Med*. 2015;139:24–38.
23. Lamberts LE, Menke-van der Houven van Oordt CW, ter Weele EJ, et al. ImmunoPET with Anti-Mesothelin Antibody in Patients with Pancreatic and Ovarian Cancer before Anti-Mesothelin Antibody-Drug Conjugate Treatment. *Clin Cancer Res Off J Am Assoc Cancer Res*. 2016;22:1642–1652.
24. Ren H, Zhang H, Wang X, et al. Prostate-specific membrane antigen as a marker of pancreatic cancer cells. *Med Oncol Northwood Lond Engl*. 2014;31:857.
25. Chang SS, Reuter VE, Heston WD, et al. Five different anti-prostate-specific membrane antigen (PSMA) antibodies confirm PSMA expression in tumor-associated neovasculature. *Cancer Res*. 1999;59:3192–3198.
26. Mhawech-Fauceglia P, Zhang S, Terracciano L, et al. Prostate-specific membrane antigen (PSMA) protein expression in normal and neoplastic tissues and its sensitivity and specificity in prostate adenocarcinoma: an immunohistochemical study using multiple tumour tissue microarray technique. *Histopathology*. 2007;50:472–483.
27. Milowsky MI, Nanus DM, Kostakoglu L, et al. Vascular targeted therapy with anti-prostate-specific membrane antigen monoclonal antibody J591 in advanced solid tumors. *J Clin Oncol Off J Am Soc Clin Oncol*. 2007;25:540–547.
28. Sahbai S, Rieping P, Pfannenbergl C, et al. Pancreatic Ductal Adenocarcinoma With High Radiotracer Uptake in 68Ga-Prostate-Specific Membrane Antigen PET/CT. *Clin Nucl Med*. 2017;42:717–718.
29. de Geus SW, Baart VM, Boonstra MC, et al. Prognostic Impact of Urokinase Plasminogen Activator Receptor Expression in Pancreatic Cancer: Malignant Versus Stromal Cells. *Biomark Insights*.;12 . Epub ahead of print June 22, 2017. DOI: 10.1177/1177271917715443.
30. Boonstra MC, Verspaget HW, Ganesh S, et al. Clinical applications of the urokinase receptor (uPAR) for cancer patients. *Curr Pharm Des*. 2011;17:1890–1910.
31. Hildenbrand R, Niedergethmann M, Marx A, et al. Amplification of the Urokinase-Type Plasminogen Activator Receptor (uPAR) Gene in Ductal Pancreatic Carcinomas Identifies a Clinically High-Risk Group.

- Am J Pathol.* 2009;174:2246–2253.
32. Kratochwil C, Flechsig P, Lindner T, et al. 68Ga-FAPI PET/CT: Tracer Uptake in 28 Different Kinds of Cancer. *J Nucl Med.* 2019;60:801–805.
 33. Shi M, Yu D-H, Chen Y, et al. Expression of fibroblast activation protein in human pancreatic adenocarcinoma and its clinicopathological significance. *World J Gastroenterol WJG.* 2012;18:840–846.
 34. Giesel FL, Kratochwil C, Lindner T, et al. 68Ga-FAPI PET/CT: Biodistribution and Preliminary Dosimetry Estimate of 2 DOTA-Containing FAP-Targeting Agents in Patients with Various Cancers. *J Nucl Med.* 2019;60:386–392.
 35. Kuninty PR, Bansal R, De Geus SWL, et al. ITGA5 inhibition in pancreatic stellate cells attenuates desmoplasia and potentiates efficacy of chemotherapy in pancreatic cancer. *Sci Adv.* 2019;5:eaax2770.
 36. Hoogstins CES, Boogerd LSF, Sibinga Mulder BG, et al. Image-Guided Surgery in Patients with Pancreatic Cancer: First Results of a Clinical Trial Using SGM-101, a Novel Carcinoembryonic Antigen-Targeting, Near-Infrared Fluorescent Agent. *Ann Surg Oncol.* 2018;25:3350–3357.
 37. Tummers WS, Miller SE, Teraphongphom NT, et al. Intraoperative Pancreatic Cancer Detection using Tumor-Specific Multimodality Molecular Imaging. *Ann Surg Oncol.* 2018;25:1880–1888.
 38. Hirsch FR, Varella-Garcia M, Bunn PA, et al. Epidermal growth factor receptor in non-small-cell lung carcinomas: correlation between gene copy number and protein expression and impact on prognosis. *J Clin Oncol Off J Am Soc Clin Oncol.* 2003;21:3798–3807.
 39. John T, Liu G, Tsao M-S. Overview of molecular testing in non-small-cell lung cancer: mutational analysis, gene copy number, protein expression and other biomarkers of EGFR for the prediction of response to tyrosine kinase inhibitors. *Oncogene.* 2009;28 Suppl 1:S14–23.
 40. Sahoo S, Lester SC. Pathology of breast carcinomas after neoadjuvant chemotherapy: an overview with recommendations on specimen processing and reporting. *Arch Pathol Lab Med.* 2009;133:633–642.
 41. Letai A. Cell Death and Cancer Therapy: Don't Forget to Kill the Cancer Cell! *Clin Cancer Res Off J Am Assoc Cancer Res.* 2015;21:5015–5020.
 42. Merlo LMF, Pepper JW, Reid BJ, et al. Cancer as an evolutionary and ecological process. *Nat Rev Cancer.* 2006;6:924–935.
 43. James ML, Gambhir SS. A molecular imaging primer: modalities, imaging agents, and applications. *Physiol Rev.* 2012;92:897–965.
 44. Jeong H-S, Jones D, Liao S, et al. Investigation of the Lack of Angiogenesis in the Formation of Lymph Node Metastases. *JNCI J Natl Cancer Inst.*;107 . Epub ahead of print June 10, 2015. DOI: 10.1093/jnci/djv155.
 45. Padera TP, Kuo AH, Hoshida T, et al. Differential response of primary tumor versus lymphatic metastasis to VEGFR-2 and VEGFR-3 kinase inhibitors cediranib and vandetanib. *Mol Cancer Ther.* 2008;7:2272–2279.
 46. Carmeliet P, Jain RK. Molecular mechanisms and clinical applications of angiogenesis. *Nature.* 2011;473:298–307.
 47. Kimura RH, Wang L, Shen B, et al. Evaluation of integrin $\alpha\beta 6$ cystine knot PET tracers to detect cancer and idiopathic pulmonary fibrosis. *Nat Commun.* 2019;10:4673.
 48. Argentiero A, De Summa S, Di Fonte R, et al. Gene Expression Comparison between the Lymph Node-Positive and -Negative Reveals a Peculiar Immune Microenvironment Signature and a Theranostic Role for WNT Targeting in Pancreatic Ductal Adenocarcinoma: A Pilot Study. *Cancers.*;11 . Epub ahead of print July 4, 2019. DOI: 10.3390/cancers11070942.
 49. Tummers WS, Willmann JK, Bonsing BA, et al. Advances in Diagnostic and Intraoperative Molecular Imaging of Pancreatic Cancer. *Pancreas.* 2018;47:675–689.
 50. Tummers WS, Kimura RH, Abou-Elkacem L, et al. Development and Preclinical Validation of a Cysteine Knottin Peptide Targeting Integrin $\alpha\beta 6$ for Near-infrared Fluorescent-guided Surgery in Pancreatic Cancer. *Clin Cancer Res.* 2018;24:1667–1676.
 51. Boonstra MC, Tolner B, Schaafsma BE, et al. Preclinical evaluation of a novel CEA-targeting near-infrared fluorescent tracer delineating colorectal and pancreatic tumors. *Int J Cancer.* 2015;137:1910–1920.
 52. Metildi CA, Kaushal S, Luiken GA, et al. Advantages of fluorescence-guided laparoscopic surgery of pancreatic cancer labeled with fluorescent anti-carcinoembryonic antigen antibodies in an orthotopic mouse model. *J Am Coll Surg.* 2014;219:132–141.
 53. Handra-Luca A, Hammel P, Sauvagnet A, et al. EGFR expression in pancreatic adenocarcinoma. Relationship to tumour morphology and cell adhesion proteins. *J Clin Pathol.* 2014;67:295–300.

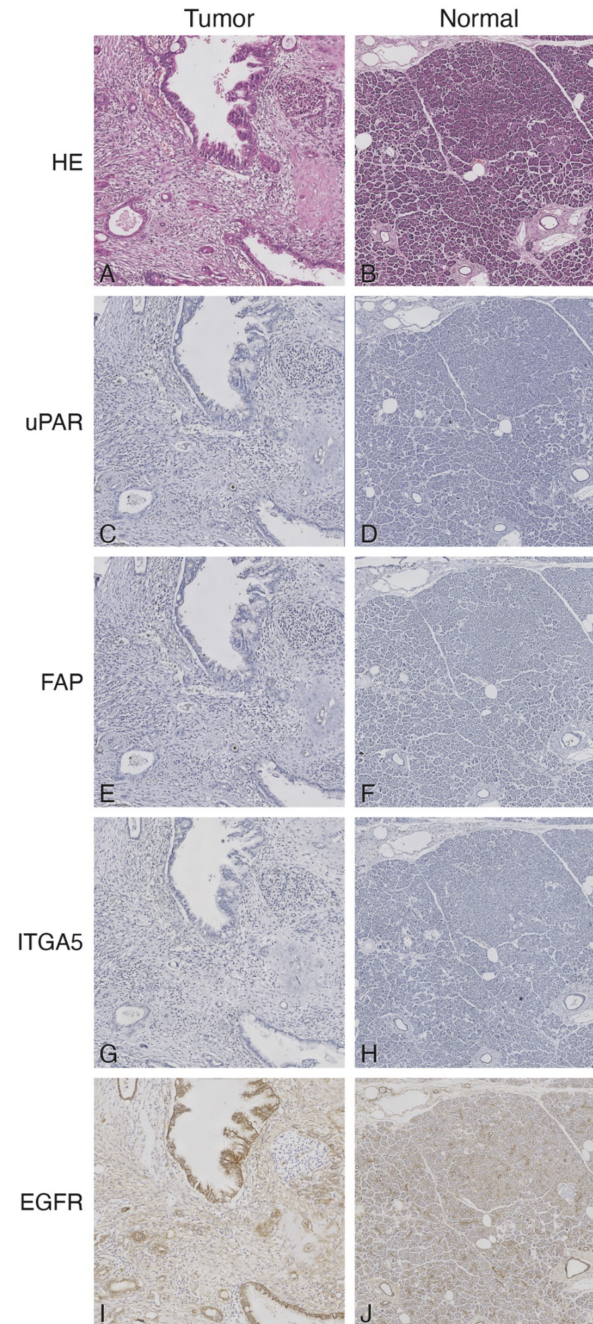
SUPPLEMENTARY

SUPPLEMENTARY TABLE 1. Monoclonal Antibody Selection and Immunohistochemical Protocol.

Antibody	Clone number	Host/isotype	Used concentration	Antigen retrieval	Vendor
$\alpha_5\beta_6$	6.2A1	Mouse	0.5 $\mu\text{g/ml}$	0.125% and 0.4% pepsin at 37°C	Biogen Idec MA Inc., Cambridge, USA.
CEACAM5	CI-P83-1	Mouse	0.2 $\mu\text{g/ml}$	Citrate buffer 95°C*	Santa Cruz Biotechnology, Inc., Dallas, USA
EGFR	E30	Mouse	2.86 $\mu\text{g/ml}$	0.4% pepsin and 1N HCl at 95°C	Dako, Glostrup, Denmark
uPAR	ATN-617	Mouse	1.2 $\mu\text{g/ml}$	Citrate buffer 95°C*	Kindly provided by prof. Andrew P. Mazar
FAP	AF3715	Donkey	2 $\mu\text{g/ml}$	Tris-EDTA buffer (pH 9.0) at 95°C	Invitrogen, Carlsbad, USA
ITGA5	HPA002642	Rabbit	0.2 $\mu\text{g/ml}$	Citrate buffer 95°C*	Atlas Antibodies, Bromma, Sweden
PSMA	3E6	Mouse	1.64 $\mu\text{g/L}$	Tris-EDTA buffer (pH 9.0) at 95°C	Dako, Glostrup, Denmark
Mesothelin	MN-1	Mouse	0.67 $\mu\text{g/ml}$	Tris-EDTA buffer (pH 9.0) at 95°C	Rockland Immunochemicals, Inc., Limerick, UK

Abbreviations: CEACAM5, carcinoembryonic antigen cell adhesion molecule 5; EGFR, epidermal growth factor receptor; uPAR, urokinase-type plasminogen activator receptor; FAP, fibroblast activating receptor; ITGA5, integrin α_5 ; PSMA, prostate-specific membrane antigen.

* In PT-Link module (Agilent, Santa Clara, USA).



SUPPLEMENTAL FIGURE 1. Overview of immunohistochemical staining of EGFR, uPAR, FAP and ITGA5.

Representative images of HE, EGFR, uPAR, FAP and ITGA5 expression on normal pancreatic parenchyma and PDAC. All images are at 10x magnification. Abbreviations: HE, hematoxylin eosin; EGFR, epidermal growth factor receptor; uPAR, urokinase-type plasminogen activator receptor; FAP, fibroblast activating protein alpha; ITGA5, integrin subtype α_5 .

Prostate-specific membrane antigen targeted PET/
CT imaging in patients with colon, gastric and
pancreatic cancer

F.A. Vuijk, F. Kleiburg, W.A. Noortman, L. Heijmen, S. Feshtali Shahbazi, F.H.P. van Velden, V.M. Baart, S.S. Bhairosingh, B.D. Windhorst, L.J.A.C. Hawinkels, P. Dibbets-Schneider, N. Bouwman, A.S.L.P. Crobach, A. Fariña-Sarasqueta, A.W.K.S. Marinelli, D.E. Oprea-Lager, R.J. Swijnenburg, F. Smit, A.L. Vahrmeijer, L.F. de Geus-Oei, D.E. Hilling and M. Slingerland.

Cancers (Basel) 2022



ABSTRACT

Current imaging modalities frequently misjudge disease stage in colorectal, gastric and pancreatic cancer. As treatment decisions are dependent on disease stage, incorrect staging has serious consequences. Previous preclinical research and case reports indicate that prostate-specific membrane antigen (PSMA) targeted PET/CT imaging might provide a solution to some of these challenges. This prospective clinical study aims to assess the feasibility of [¹⁸F]DCFPyL PET/CT imaging to target and visualize primary colon, gastric and pancreatic cancer. In this prospective clinical trial, patients with colon, gastric and pancreatic cancer were included and underwent both [¹⁸F]DCFPyL and [¹⁸F]FDG PET/CT scans prior to surgical resection or (for gastric cancer) neoadjuvant therapy. Semiquantitative analysis of immunohistochemical PSMA staining was performed on the surgical resection specimens, and results were correlated to imaging parameters. Results of this study demonstrate detection of the primary tumor by [¹⁸F]DCFPyL PET/CT in 7 out of 10 patients with colon, gastric and pancreatic cancer, with a mean tumor-to-bloodpool ratio (TBR) of 3.3 and mean SUV_{max} of 3.6. However, due to high surrounding uptake visual distinction of these tumours was difficult, and the SUV_{max} and TBR on [¹⁸F]FDG PET/CT were significantly higher than on [¹⁸F]DCFPyL PET/CT. In addition, no correlation between PSMA expression in the resection specimen and SUV_{max} on [¹⁸F]DCFPyL PET/CT was found. In conclusion, the detection of several gastrointestinal cancers using [¹⁸F]DCFPyL PET/CT is feasible. However, low tumor expression and high uptake physiologically in organs/background hamper clear distinction of the tumor. As a result, [¹⁸F]FDG PET/CT was superior in detecting colon, gastric and pancreatic cancers.

INTRODUCTION

Gastrointestinal cancers are among the most prevalent cancers worldwide, with colorectal cancer being the third, gastric cancer fifth and pancreatic cancer twelfth most common type of cancer, respectively¹. Currently, the diagnostic workup of suspected gastrointestinal tumors includes a combination of endoscopy, computed tomography (CT), magnetic resonance imaging (MRI), [¹⁸F]FDG positron emission tomography – computed tomography (PET/CT), ultrasound and even diagnostic laparoscopy, depending on the tumor type. Curative treatment for all three cancers still consists of surgical resection of the primary tumor and, if indicated, chemo(radio)therapy².

Although these imaging modalities are frequently used in the clinic, they lack sensitivity or specificity in specific diagnostic entities, leading to over- or undertreatment. In colon cancer, for example, imaging modalities (e.g. CT) are currently insufficient in determining nodal stage. As a result, early colorectal cancers with low risk for lymph node metastases (10-15%), might currently undergo unnecessary oncologic bowel resection, while in the majority of these patients (85-90%) local treatment would suffice. In gastric cancer, the sensitivity of CT to detect distant and peritoneal metastasis is 14-65% and 22-33%, respectively³⁻⁵. Recent results from the PLASTIC trial indicated a high detection rate for the primary tumor of 79%, however, found limited additional value of [¹⁸F]FDG PET/CT in gastric cancer staging⁶. Especially for signet cell, mucinous and poorly differentiated gastric carcinomas [¹⁸F]FDG PET/CT is difficult, as they tend to be less metabolically active⁷. Even more complicating is the physiological uptake of [¹⁸F]FDG in the stomach wall, frequently masking the primary tumor. This results in an underestimation of the tumor stage from which incorrect treatment choices are made. Finally, in pancreatic cancer, as much as 13% of Whipple procedures are currently being performed for benign disease⁸. Additionally, a high rate of early recurrence after resection is seen (28%)⁹, indicating the presence of micro-metastases at the time of resection. Possibly, molecular imaging such as PET/CT could provide information on tumor biology.

Prostate-specific membrane antigen (PSMA) targeted PET/CT imaging might provide a solution to some of these challenges. PSMA is a metallopeptidase that is expressed by prostate cells. Increased expression is found in prostate carcinoma, making it a well-established target for molecular imaging. PSMA targeted PET/CT imaging has quickly evolved in the past few years and is now being adopted into the standard-of-care in the primary staging and follow-up of prostate cancer.

Recently, PSMA expression was also reported in other cancer types, including colorectal, gastric and pancreatic cancer^{10,11}. PSMA expression is found on the endothelium of newly formed vasculature, which is essential for nutrient supply in all cancers.

By immunohistochemical analysis, approximately 85% of colorectal cancer, 66% of gastric cancer and 84% of pancreatic cancer patients demonstrated expression of PSMA in capillaries within the tumor bed, which can be selectively targeted by [¹⁸F] DCFPyL^{10,11}. In addition, our group demonstrated sustained PSMA expression after neoadjuvant treatment in pancreatic cancer using immunohistochemistry analysis¹². Three case reports in patients with synchronous prostate cancer and colorectal, gastric, or pancreatic cancer suggested the feasibility of PSMA targeted PET/CT for detection of the primary tumor and/or its metastases^{10,13–15}. Recently, a larger study including 19 pancreatic cancer patients demonstrated positive uptake in 18 of these, and allowed for the distinction of malignant from benign pancreatic lesions, with a sensitivity and specificity of 84.2% and 90.5%, respectively¹⁶. Aside from being a target for molecular imaging, PSMA could also serve as a target for theranostics¹⁷ ([¹⁷⁷Lu]Lu-PSMA, [²²⁵Ac] Ac-PSMA).

As a first step towards clinical use of PSMA targeted imaging in non-prostate cancer, this feasibility study aimed to assess the feasibility of [¹⁸F]DCFPyL PET/CT imaging to target and visualize primary colon, gastric and pancreatic cancer.

MATERIALS AND METHODS

Patient population

This is a bi-center, non-randomized prospective clinical trial. Patients admitted to the Leiden University Medical Center (Leiden, The Netherlands) and Haaglanden Medical Centrum (HMC, The Hague, The Netherlands), and diagnosed with (histologically proven) T3-4N0-2M0-1 colon, T3-4N0-2M0-1 gastric, or pancreatic cancer were included. No sample size calculation was possible due to the exploratory nature of this study. Gastric cancer patients received neoadjuvant therapy before surgery, consisting of 4 courses of fluorouracil, leucovorin, oxaliplatin and docetaxel. The other patients (colon and pancreatic cancer) underwent surgery without prior therapy. Clinical and pathological data were obtained from medical records. No follow-up was performed. The study was conducted in concordance with the Declaration of Helsinki, and the laws and regulations of the Netherlands. The study was approved by a certified medical ethics review board (Leiden Den Haag Delft) and the local review board of the HMC. All subjects provided written informed consent prior to any study-related activities. The study was registered in the Netherlands Trial Register (NL-8919). The goal was to include 30 patients. An early stopping rule was implemented in case interim analyses after 10 patients showed lower tumor accumulation on [¹⁸F]DCFPyL PET/CT than on [¹⁸F]FDG PET/CT (significant difference in average $SUV_{max}^{[18F]FDG}$ and [¹⁸F]DCFPyL).

Data acquisition and image reconstruction

As part of this trial, patients underwent both [¹⁸F]DCFPyL and [¹⁸F]FDG PET/CT prior to surgery (colon and pancreatic cancer patients) or start of neoadjuvant therapy (gastric cancer patients). There were ≥ 24 hours between scans. [¹⁸F]DCFPyL was chosen due to its favorable renal clearance. All PET/CT scans were acquired on a Vereos digital PET/CT scanner (Philips Healthcare, Best, The Netherlands), except one single [¹⁸F]DCFPyL PET/CT scan that was acquired on a GE Discovery MI 5-Ring digital PET/CT scanner (GE, Boston, MA, USA) (the other scan from this patient was acquired on the Vereos scanner). Both PET systems are EARL accredited. Patients underwent a low-dose CT scan (120 kV, 35 mA_{eff}) for attenuation correction purposes prior to the PET scan. Patients received an average dose of 198.9 ± 38.4 MBq [¹⁸F]DCFPyL and were scanned after an average of 120.8 ± 5.7 min post-injection^{18,19}. [¹⁸F]FDG was dosed using the quadratic formula with a factor of $379 \text{ MBq}\cdot\text{min}\cdot\text{bed}^{-1}\cdot\text{kg}^{-2}$, resulting in an average dose of 155.8 ± 93.5 MBq [¹⁸F]FDG and patients were scanned 63.4 ± 10.6 min post-injection. Before [¹⁸F]FDG PET/CT, patients fasted for 6 hours and were prehydrated with 1L of water. A blood glucose threshold of <11.0 mmol/L was set for patients undergoing [¹⁸F]FDG PET/CT. For both scans, a PET scan of the abdomen was performed in case of colon or pancreatic cancer, and a PET scan of the abdomen to skull base was performed in case of gastric cancer. As detection of distant metastases or staging was not the primary aim of this study, only partial body scans were performed to minimize radiation exposure. All scans were acquired for a duration of 5 min per bed position. [¹⁸F]DCFPyL and [¹⁸F]FDG PET/CT images were reconstructed in accordance with EANM guidelines for tumor [¹⁸F]FDG PET imaging version 2.0 with 4mm^3 voxel size²⁰.

Quantitative image analysis

PET/CT analysis was performed by two experienced, board-certified nuclear medicine physicians (L.G., L.H.) using Sectra IDS7 software (version 21.2; Sectra AB, Linköping, Sweden). The volumes of interest (VOI) were delineated using LIFEx (version 6.30; Inserm, Orsay, France)²¹. Various lesional body-weighted standardized uptake values (SUV), i.e. maximum (SUV_{max}), minimum (SUV_{min}), mean (SUV_{mean}) and peak (SUV_{peak}), as well as volumetric parameters tumor volume (TV_{DCFPyL} for [¹⁸F]DCFPyL or MTV for [¹⁸F]FDG) and total lesion uptake (TL_{DCFPyL} for [¹⁸F]DCFPyL or TLG for [¹⁸F]FDG), defined as $SUV_{mean} \times \text{tumor volume}$, were extracted for all patients from both scans²². TV_{DCFPyL} , TL_{DCFPyL} , MTV and TLG were determined with an isocontour set at 45% of the maximum uptake for [¹⁸F]DCFPyL PET/CT scans²² and 50% of the maximum uptake for [¹⁸F]FDG PET/CT scans²⁰. Uptake on both PET/CTs was considered positive when the $SUV_{max} \geq 2.5$. Tumors were considered detectable on PET/CT imaging when a tumor-to-blood pool ratio (TBR) ≥ 2 was observed. The blood pool was delineated using a 3×3 pixel region of interest (ROI) in the descending aorta (the ascending aorta was not in the field of view in colon or pancreatic cancer patients) on 5 consecutive slices of the CT scan, yielding the

blood pool activity used for the calculation of TBR²³. TBR was determined by dividing the SUV_{peak} of the tumor by the SUV_{peak} of the aortic blood pool.

Immunohistochemistry

PSMA expression in the resection specimens (after neoadjuvant therapy in gastric cancer) was visualized using immunohistochemistry on formalin-fixed paraffin-embedded tumor tissue sections (4 μm). Endoglin was used as the gold standard for identifying activated endothelial cells²⁴. After deparaffinization in xylene and rehydration, endogenous peroxidase activity was blocked with 0.3% H₂O₂ (20 min). Antigen retrieval was performed by boiling slides in Tris-EDTA buffer (pH 9.0) for PSMA and citrate buffer (pH 6.0) for endoglin at 95°C (10 minutes), followed by overnight incubation with the primary antibodies (mouse anti-PSMA (Dako, Clone 3E6, no. N1611, 1.64 μg/mL), or goat anti-endoglin (R&D systems, BAF1097, 1.0 μg/mL)). Next, slides were incubated for 30 min at room temperature with the secondary antibodies (anti-mouse, anti-goat (Envision, Dako, Glostrup, Denmark)). Last, immunoreactions were visualized using 3,3'-diaminobenzidine substrate buffer (Dako, Glostrup, Denmark) and counterstained using hematoxylin. Placental tissue was used as a positive control for endoglin staining, prostate cancer tissue was used as positive control for PSMA staining. Negative controls were included in the experiments.

Evaluation of PSMA expression was performed by an experienced, board-certified gastro-intestinal pathologist (S.C.) using the semi-quantitative H-score^{25,26}. This results in a score ranging from 0-300 and considers both staining intensity (0-3) as well as the percentage (0-100%) of target cells stained. The endoglin staining was used as the gold standard (100% staining) for neo-angiogenesis (pre-existing vasculature was excluded from the analyses by visual identification). Higher scores indicate more PSMA expression.

Statistical analysis

Statistical analysis and figure editing were performed using SPSS (version 25; IBM SPSS, Inc., Chicago, USA) and GraphPad Prism (version 8; GraphPad Software, Inc., San Diego, USA). Due to the small sample size, all data are displayed as mean ± standard deviation. Imaging parameters of patients between [¹⁸F]DCFPyL and [¹⁸F]FDG PET/CT were compared using the independent samples t-test. The correlation between [¹⁸F]DCFPyL SUV_{max} and H-score was evaluated using a logistic regression analysis, and displayed as the r² and concurrent p-value. A p-value <0.05 was considered significant.

RESULTS

Ten patients were included in this clinical trial in the period from August 2020 until May 2021. After interim analysis of 10 patients, low [¹⁸F]DCFPyL SUV_{max} values in primary tumors compared to surrounding organs were seen in all but one patient (in contrast to high [¹⁸F]FDG SUV_{max} values), and the study was prematurely terminated. Six women and four men were included, who were on average 65.3 ± 11.9 years old. All patients underwent both [¹⁸F]DCFPyL and [¹⁸F]FDG PET/CT, except one (patient 5) that did not undergo the [¹⁸F]FDG PET/CT as this was not part of standard-of-care diagnostics (cT2-3 gastric carcinoma). Of 10 included patients, four patients were diagnosed with colon cancer, three with gastric cancer, and three with pancreatic cancer. Two patients had a well-differentiated adenocarcinoma, three were scored as well/moderate, two as moderate and three as poor. Patient characteristics are further depicted in **Table 1**.

Quantitative analysis of PET/CT scans

Of the 9 [¹⁸F]FDG PET/CT scans, 100% demonstrated positive uptake (SUV_{max} ≥ 2.5) with a mean SUV_{max} of 14.9 ± 14.5; 25.4 ± 17.0 for colon cancer, 6.1 ± 2.4 for gastric cancer and 6.8 ± 3.3 for pancreatic cancer. Of 10 [¹⁸F]DCFPyL PET/CT scans, 6 (60%) demonstrated positive expression with a mean SUV_{max} of 3.6 ± 2.5; 4.2 ± 3.9 for colon cancer, 2.7 ± 0.7 for gastric cancer and 3.6 ± 1.4 for pancreatic cancer. Examples of colon, gastric and pancreatic cancer scans are displayed in **Figures 1, 2 and 3**, respectively. The primary tumor was detectable (TBR ≥ 2) on 6 out of 9 (67%) [¹⁸F]FDG PET/CT scans (3/4 colon, 1/2 gastric, 2/3 pancreatic tumors) and on 7 out of 10 (70%) [¹⁸F]DCFPyL PET/CT scans (3/4 colon, 1/3 gastric, 3/3 pancreatic tumors). The mean TBR on [¹⁸F]FDG PET/CT was 13.0 ± 8.0 for colon cancer, 2.3 ± 0.9 for gastric cancer and 3.2 ± 1.6 for pancreatic cancer.

The mean TBR on [¹⁸F]DCFPyL was 3.3 ± 2.7 for colon cancer, 1.9 ± 0.5 for gastric cancer and 2.3 ± 0.5 for pancreatic cancer. For all patients except one (patient 1), volumetric PET/CT derived parameters could not be extracted due to the relatively low tumor uptake of [¹⁸F]DCFPyL and high uptake in surrounding tissue. The SUV_{max} and TBR on [¹⁸F]FDG were significantly higher compared to [¹⁸F]DCFPyL (p=0.028 and p=0.049, respectively). Although the primary metastatic sites were included in the field of view of the scans, no previously unknown lesions were found on [¹⁸F]DCFPyL or [¹⁸F]FDG PET/CT. **Figure 4** shows maximal intensity projections of both [¹⁸F]FDG and [¹⁸F]DCFPyL PET/CT scans, indicating much more intense uptake of [¹⁸F]FDG compared to [¹⁸F]DCFPyL. In one patient (patient 1) additional parameters could be extracted from both [¹⁸F]DCFPyL and [¹⁸F]FDG PET/CT. When comparing the [¹⁸F]DCFPyL to [¹⁸F]FDG PET/CT for this patient, the SUV_{max} was 9.9 versus 45.5, SUV_{mean} 6.4 versus 28.4, SUV_{min} 4.5 versus 22.8, SUV_{peak} 8.4 versus 41.0, TBR 7.3 versus 20.4, TV_{DCFPyL} 13.6 cm³ versus MTV 59.4 cm³, and TL_{DCFPyL} 87.6 versus TLG 1686.1, as displayed in **Table 2**.

TABLE 1. Overview of patient characteristics.

No figure	Age	Tumor location	Tumor differentiation	cTNM stage*	pTNM stage	Max diameter (mm)**	SUV _{max} [¹⁸ F] DCFPyL	SUV _{max} [¹⁸ F] FDG	TBR [¹⁸ F] DCFPyL	TBR [¹⁸ F] FDG	H-score
1	72	Colon adenocarcinoma	Well/moderate	cT3/4N1M0	pT3N0M0	180	9.9	45.5	7.3	20.4	120
2	68	Colon adenocarcinoma	Well/moderate	cT4N2M0	pT4N0M0	80	1.9	29.1	2.3	15.6	225
3	73	Colon adenocarcinoma	Poor	cT4N0M0	pT4N0M0	50	3.3	22.5	2.4	14.1	60
4	58	Colon adenocarcinoma	Well/moderate	cT3N0M0	pT4N0M0	15	1.5	4.5	1.2	1.7	80
5	38	Signet ring cell gastric carcinoma	Poor	cT2-3N0M0	ypT3N0M0	42	3.5	n.a.	1.9	n.a.	0
6	71	Tubular gastric adenocarcinoma	Moderate	cT4N1M0	ypT3N1M0	25	2.5	7.8	2.3	2.9	150
7	50	Tubular gastric adenocarcinoma	Poor	cT3N0M0	ypT4N1M0	45	2.1	4.4	1.4	1.6	0
8	70	PDAC	Well	cT3N0M0	pT2N1M0	22	3.3	3.6	2.0	1.3	150
9	76	PDAC	Moderate	cT3N0M0	pT2N1M0	28	2.4	6.8	2.0	4.3	30
10	63	PDAC	Well	cT3N2M0	pT2N2M0	35	5.1	10.1	2.8	3.9	0

Abbreviations: TNM stage, tumor, nodal and metastatic status; SUV, standardized uptake value; n.a., not available; H-score, immunohistochemical staining score; PDAC, pancreatic ductal adenocarcinoma. *Pathological TNM stage for colon and pancreatic cancer patients, initial clinical TNM stage for gastric cancer patients (as neoadjuvant therapy was given after [¹⁸F]DCFPyL PET/CT). **Diameter measured at pathological examination.

Immunohistochemical analysis

Immunohistochemistry resulted in a general mean H-score of 81.5 ± 77.8 , 121.3 ± 73.5 for colon cancer, 50.0 ± 86.6 for gastric cancer, and 60.0 ± 79.4 for pancreatic cancer. [¹⁸F]DCFPyL SUV_{max} was not correlated to the PSMA H-score (R^2 0.0001, $p=0.997$; **Figure 5**). **Figure 6** shows examples of immunohistochemical staining for PSMA of the patients displayed in **Figures 1, 2 and 3**.

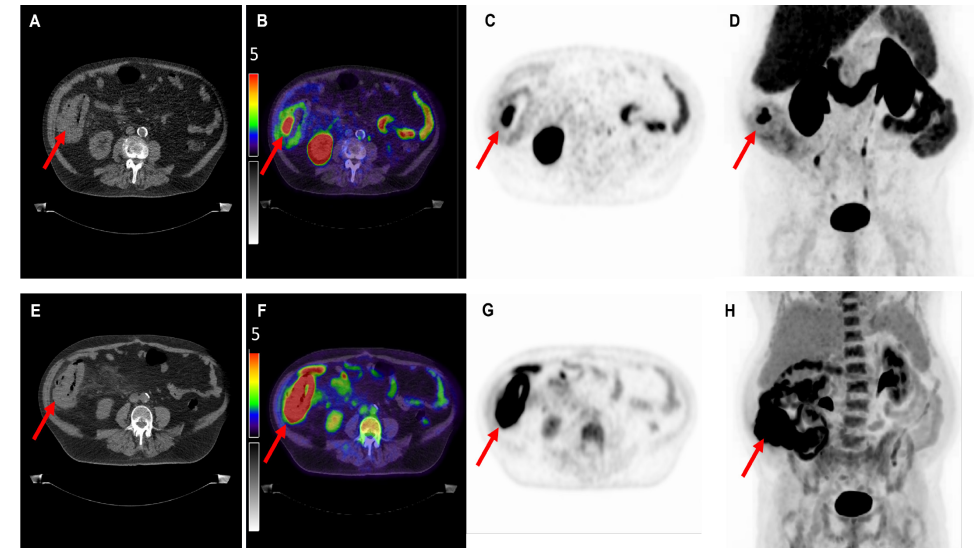


FIGURE 1. Overview of imaging modalities of a patient with pT3N0M0 colon carcinoma (patient 1). The arrows indicate (upper row) a lesion with intense [¹⁸F]DCFPyL expression with a SUV_{max} of 9.9 and (bottom row) a lesion with [¹⁸F]FDG uptake with a SUV_{max} of 45.5. From left to right: low dose CT (A and E), fused PET/CT (B and F), PET (C and G), and the maximal intensity projection (MIP, D and H). Image scale SUV 0-5.

TABLE 2. Overview of extended imaging parameters patient 1.

	[¹⁸ F]DCFPyL	[¹⁸ F]FDG
SUV _{max}	9.9	45.5
SUV _{mean}	6.4	28.4
SUV _{min}	4.5	22.8
SUV _{peak}	8.4	41.0
TBR	7.3	20.4
TV _{DCFPyL} / MTV (cm ³)	13.6	59.4
TL _{DCFPyL} / TLG	87.6	1686.1

Abbreviations: SUV, standardized uptake value; TBR, tumor to bloodpool ratio; TV_{DCFPyL}, tumor volume on [¹⁸F]DCFPyL PET/CT; MTV, metabolic tumor volume; TL_{DCFPyL}, total lesion uptake on [¹⁸F]DCFPyL PET/CT; TLG, total lesion glycolysis.

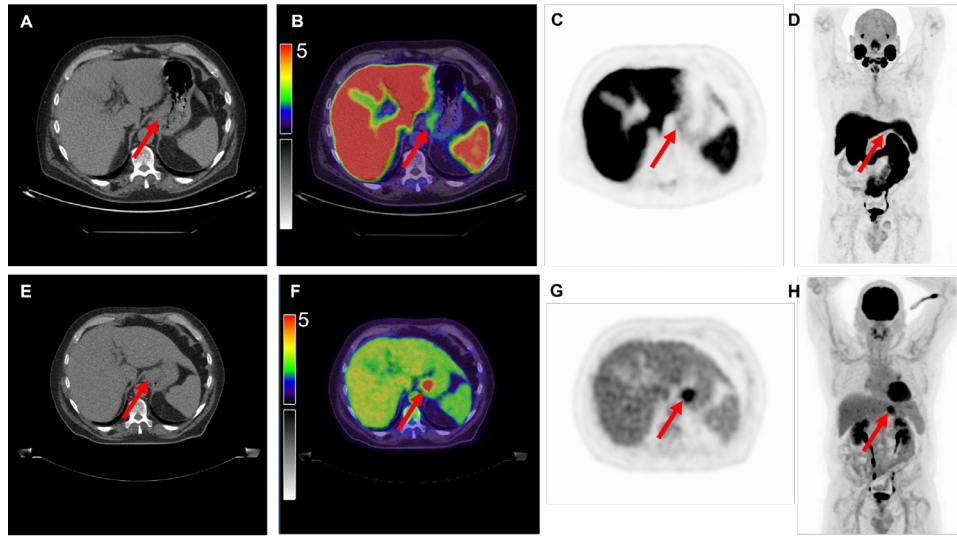


FIGURE 2. Overview of imaging modalities of a patient with cT4N1M0 tubular gastric carcinoma (patient 6). The arrows indicate (upper row) a lesion with light [¹⁸F]DCFPyL expression with a SUV_{max} of 2.5 and (bottom row) a lesion with [¹⁸F]FDG uptake with a SUV_{max} of 7.8. From left to right: low dose CT (A and E), fused PET/CT (B and F), PET (C and G), and the maximal intensity projection (MIP, D and H). Image scale SUV 0-5.

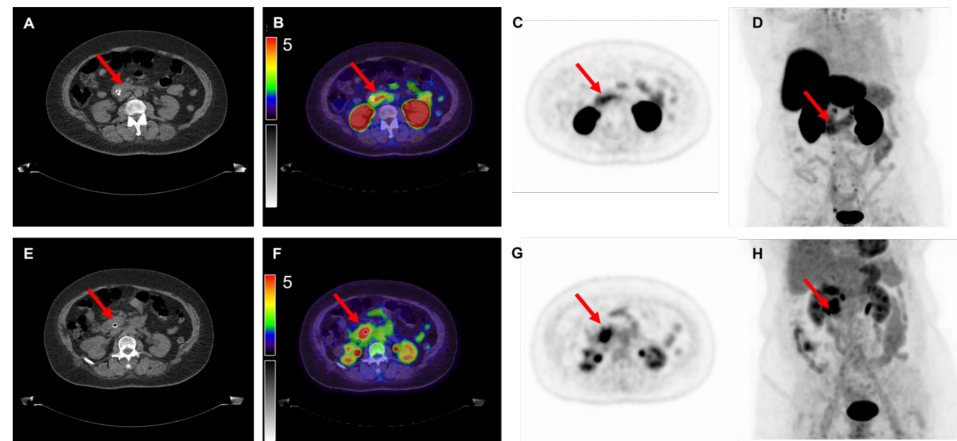


FIGURE 3. Overview of imaging modalities of a patient with pT2N2M0 pancreatic ductal adenocarcinoma (patient 10). The arrows indicate (upper row) a lesion with moderate to intense [¹⁸F]DCFPyL expression with a SUV_{max} of 5.1 and (bottom row) a lesion with [¹⁸F]FDG uptake with a SUV_{max} of 10.1. From left to right: low dose CT (A and E), fused PET/CT (B and F), PET (C and G), and the maximal intensity projection (MIP, D and H). Image scale SUV 0-5.

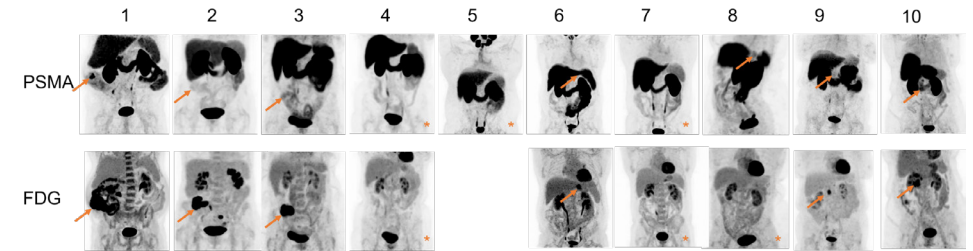


FIGURE 4. Maximum Intensity Projection (MIP) PET images of all included patients. The arrows indicate the location of the primary tumor. In the MIP PET images with an asterisk the primary tumor was not visible. [¹⁸F]FDG PET/CT of patient 5 was not performed as this was not standard of care due to his cT2-3 gastric tumor.

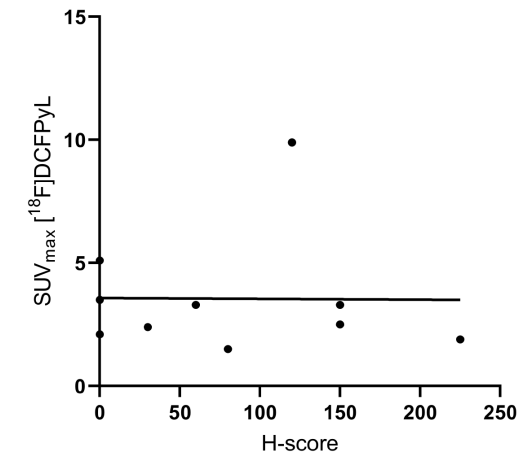


FIGURE 5. Scatterplot of [¹⁸F]DCFPyL SUV_{max} values with associated H scores. Abbreviations: SUV_{max}, maximal standardized uptake value.

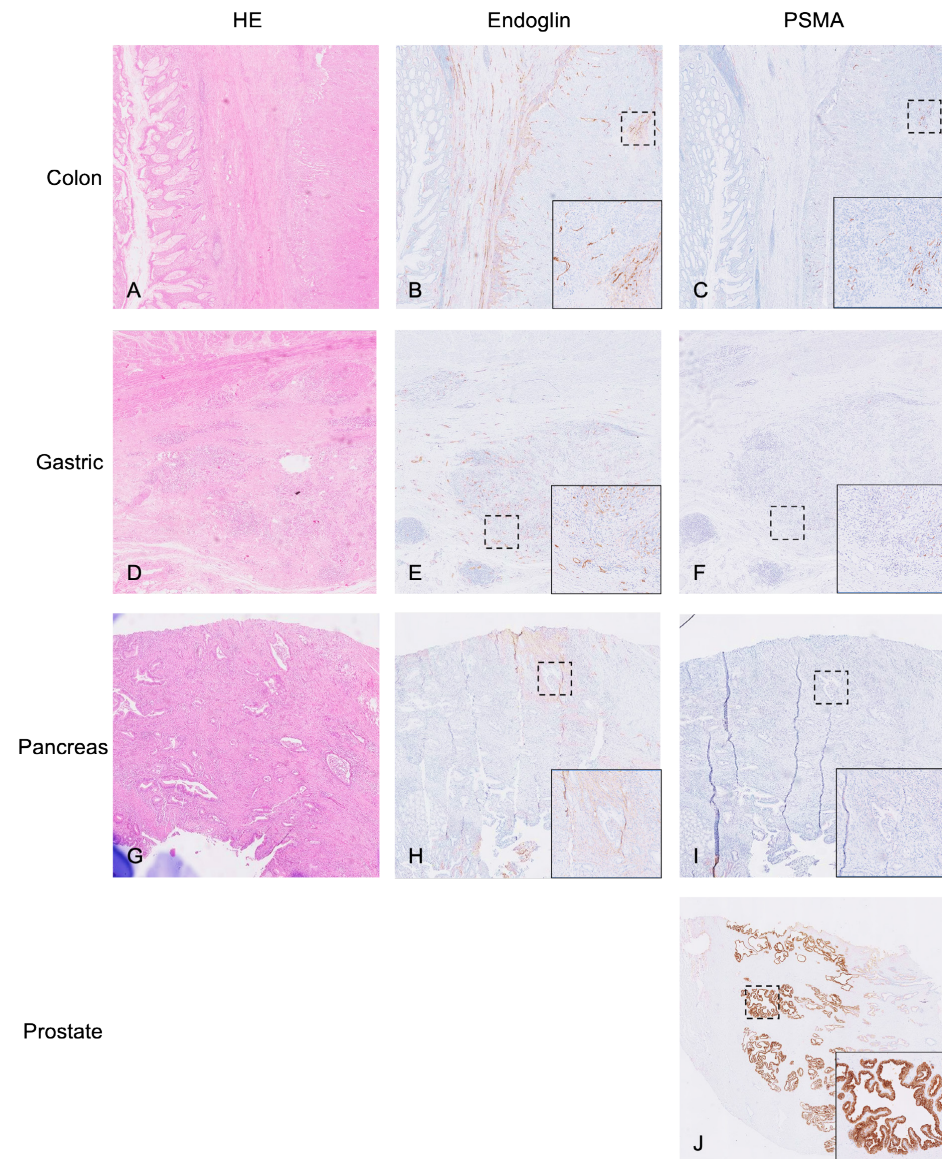


FIGURE 6. Overview of immunohistochemical stainings. This figure displays Haematoxylin and Eosin (HE), endoglin and PSMA staining of, respectively, colon (A, B, C, H-score 120), gastric (D, E, F, H-score 150) and pancreatic cancer (G, H, I, H-score 0). As a positive control the PSMA staining was performed on prostate cancer tissue (J, H-score 300). Overview images were made at 1-2x magnification, zoom images at 10x magnification.

DISCUSSION

Results from this study demonstrate the detection of the primary tumor by [^{18}F]DCFPyL PET/CT in 7 out of 10 patients (3/4 colon, 1/3 gastric, 3/3 pancreatic cancers), with a mean TBR of 3.3 and mean SUV_{max} of 3.6. However, due to the low contrast and high level of uptake of surrounding tissue, the visual distinction of these tumors was difficult, and the SUV_{max} and TBR on [^{18}F]DCFPyL PET/CT were significantly lower compared to [^{18}F]FDG PET/CT. In addition, no correlation between PSMA expression in the tumor bed in the resected specimen and SUV_{max} on [^{18}F]DCFPyL PET/CT was found.

Previous literature has reported on PSMA targeted PET tracers to detect gastrointestinal tumors. This includes incidental findings and studies with a large number of patients. In four (suspected) prostate cancer patients, colorectal cancer was unexpectedly found, with a SUV_{max} varying from 7.4 to 19.6^{13-15,27}. A second study, including metastatic colorectal cancer patients, found a mean SUV_{max} in three patients for the primary tumor of 7.9 ± 2.5 (using [^{68}Ga]Ga-PSMA-11)²⁸. This was higher when compared to our found mean SUV_{max} of 4.2 ± 3.9 in three colon cancer patients. As in our study, the SUV_{max} on [^{18}F]FDG PET/CT was significantly higher than on PSMA PET/CT (23.7-43.7, $n=2$). Unfortunately, as these patients did not undergo surgery, no correlation to PSMA expression in the resection specimen was available. Most recently, a larger study by Krishnaraju *et al.* including 40 patients with pancreatic lesions was conducted (21 benign (wide variety of lesions) and 19 malignant)¹⁶. The [^{68}Ga]Ga-PSMA PET/CT was positive in 18 out of 19 pancreatic cancers, and the median SUV_{max} of malignant lesions was significantly higher compared to benign lesions (SUV_{max} 7.4 (IQR 4.5) versus 3.5 (IQR 1.6), $p<0.001$). The sensitivity and specificity of visual assessment of [^{68}Ga]Ga-PSMA in detecting malignant pancreatic lesions were 94.7% and 90.5%, respectively. Using a quantitative SUV_{max} cut-off value of 4.8, [^{68}Ga]Ga-PSMA detected malignant disease with a sensitivity of 84.2% and specificity of 90.5%). The study by Krishnaraju *et al.* found a considerably higher PSMA uptake in pancreatic cancers compared to our study (median SUV_{max} 7.4 versus median SUV_{max} of 3.3 in our study). Interestingly, the study by Krishnaraju *et al.* also performed [^{18}F]FDG PET/CT in each patient, however, the median SUV_{max} of both PET tracers were similar ([^{18}F]FDG 7.6, [^{68}Ga]Ga-PSMA 7.4) and SUV_{max} values of [^{18}F]FDG PET/CT were comparable to our study (mean SUV_{max} [^{18}F]FDG 6.8). The difference in PSMA uptake between these studies currently remains unexplained, but could be influenced by the differences in pharmacokinetic properties and targeting characteristics (e.g. affinity, binding site) between [^{18}F]DCFPyL and [^{68}Ga]Ga-PSMA^{29,30}. In addition, no proper pharmacokinetics studies with [^{68}Ga]Ga-PSMA were performed as have been performed for [^{18}F]DCFPyL (including arterial and venous sampling).

The relatively low uptake of [^{18}F]DCFPyL in this study is probably due to low PSMA expression on the tumors. As is visualized in **Figure 6**, PSMA expression in the tumor

bed of these cancers is significantly lower compared to prostate cancer. Although endothelial expression of PSMA was visually intense, it was only seen in a low number of angiogenic endothelial cells. However, IHC results for colon cancer for example were in line with previous literature, as all four patients expressed PSMA at varying levels. The physiological uptake of [¹⁸F]DCFPyL in the target organs has previously been described by Giesel *et al.*, who found a median SUV_{max} of 2.95 in the pancreas, but did not find any notable uptake in the stomach or colon (n=12)³¹. [¹⁸F]DCFPyL is, however, the most suitable tracer for the detection of gastrointestinal cancers due to its favorable renal clearance, as its alternative, [¹⁸F]PSMA-1007, shows predominant hepatobiliary excretion leading to an even higher background signal in both liver and intestines, which interferes with potentially pathological tracer accumulation especially in these cancers³¹. A reason for the low uptake of [¹⁸F]DCFPyL in patients with a high H-score could indicate the tracer was not able to penetrate into the tumor core enough. In general, it might be possible that higher grade tumors (such as included in the study by Cuda *et al.*²⁸) express higher degrees of PSMA. In addition, it is unclear which effect neoadjuvant therapy in gastric cancer patients could have had on the immunohistochemical staining of PSMA.

Possible limitations of this study include the limited sample size, which is due to the premature termination of the trial. However, results from the included 10 patients demonstrate a clear pattern of high background- and low tumor uptake, hampering clear tumor identification. As these results appear to be valid for most patients, we believe these results are representative of a larger population of the selected cancer types and thereby provide relevant information. To the best of our knowledge, this is one of the first prospective studies to include patients with gastrointestinal cancers and perform both [¹⁸F]DCFPyL as well as [¹⁸F]FDG PET/CT, and provide correlation to immunohistochemical expression of PSMA.

CONCLUSIONS

In conclusion, the detection of colon, gastric and pancreatic cancer using [¹⁸F]DCFPyL PET/CT imaging is feasible. However, low tumor uptake and high uptake in other organs hamper clear distinction of tumor mass. In this study, [¹⁸F]FDG PET/CT was found to be superior in detecting colon, gastric and pancreatic cancers. These results do not encourage further investigation into the application of [¹⁸F]DCFPyL PET/CT imaging in these cancers. However, this may be different for other PSMA targeted tracers.

REFERENCES

1. Ferlay J, Ervik M, Lam F, et al. Global cancer observatory: cancer today. Lyon, France: International Agency for Research on Cancer. 2020. Available from: <https://gco.iarc.fr.today>. Accessed February 9, 2022.
2. Cunningham D, Allum WH, Stenning SP, et al. Perioperative chemotherapy versus surgery alone for resectable gastroesophageal cancer. *N Engl J Med*. 2006;355:11–20.
3. Choi JY, Shim KN, Kim SE, et al. The clinical value of 18F-fluorodeoxyglucose uptake on positron emission tomography/computed tomography for predicting regional lymph node metastasis and non-curative surgery in primary gastric carcinoma. *Korean J Gastroenterol Taehan Sohwagi Hakhoe Chi*. 2014;64:340–347.
4. Seevaratnam R, Cardoso R, McGregor C, et al. How useful is preoperative imaging for tumor, node, metastasis (TNM) staging of gastric cancer? A meta-analysis. *Gastric Cancer Off J Int Gastric Cancer Assoc Jpn Gastric Cancer Assoc*. 2012;15 Suppl 1:S3-18.
5. Wang Z, Chen J-Q. Imaging in assessing hepatic and peritoneal metastases of gastric cancer: a systematic review. *BMC Gastroenterol*. 2011;11:19.
6. Gertsen EC, Brenkman HJF, van Hillegersberg R, et al. 18F-Fluorodeoxyglucose-Positron Emission Tomography/Computed Tomography and Laparoscopy for Staging of Locally Advanced Gastric Cancer: A Multicenter Prospective Dutch Cohort Study (PLASTIC). *JAMA Surg*. 2021;156:e215340.
7. Smyth E, Schöder H, Strong VE, et al. A prospective evaluation of the utility of 2-deoxy-2-[(18) F]fluoro-D-glucose positron emission tomography and computed tomography in staging locally advanced gastric cancer. *Cancer*. 2012;118:5481–5488.
8. Gerritsen A, Molenaar IQ, Bollen TL, et al. Preoperative characteristics of patients with presumed pancreatic cancer but ultimately benign disease: a multicenter series of 344 pancreatoduodenectomies. *Ann Surg Oncol*. 2014;21:3999–4006.
9. Tummers WS, Groen JV, Sibinga Mulder BG, et al. Impact of resection margin status on recurrence and survival in pancreatic cancer surgery. *Br J Surg*. . Epub ahead of print March 18, 2019. DOI: 10.1002/bjs.11115.
10. Haffner MC, Kronberger IE, Ross JS, et al. Prostate-specific membrane antigen expression in the neovasculature of gastric and colorectal cancers. *Hum Pathol*. 2009;40:1754–1761.
11. Ren H, Zhang H, Wang X, et al. Prostate-specific membrane antigen as a marker of pancreatic cancer cells. *Med Oncol Northwood Lond Engl*. 2014;31:857.
12. Vuijk FA, de Muynck LD a. N, Franken LC, et al. Molecular targets for diagnostic and intraoperative imaging of pancreatic ductal adenocarcinoma after neoadjuvant FOLFIRINOX treatment. *Sci Rep*. 2020;10:16211.
13. Huang Y-TT, Fong W, Thomas P. Rectal Carcinoma on 68Ga-PSMA PET/CT. *Clin Nucl Med*. 2016;41:e167-168.
14. Hangaard L, Jochumsen MR, Vendelbo MH, et al. Metastases From Colorectal Cancer Avid on 68Ga-PSMA PET/CT. *Clin Nucl Med*. 2017;42:532–533.
15. Stoykow C, Huber-Schumacher S, Almasreh N, et al. Strong PSMA Radioligand Uptake by Rectal Carcinoma: Who Put the “S” in PSMA? *Clin Nucl Med*. 2017;42:225–226.
16. Krishnaraju VS, Kumar R, Mittal BR, et al. Differentiating benign and malignant pancreatic masses: Ga-68

- PSMA PET/CT as a new diagnostic avenue. *Eur Radiol.* 2021;31:2199–2208.
17. Sartor O, de Bono J, Chi KN, et al. Lutetium-177-PSMA-617 for Metastatic Castration-Resistant Prostate Cancer. *N Engl J Med.* 2021;385:1091–1103.
 18. Jansen BHE, Yaqub M, Voortman J, et al. Simplified Methods for Quantification of 18F-DCFPyL Uptake in Patients with Prostate Cancer. *J Nucl Med.* 2019;60:1730–1735.
 19. Wondergem M, Zant FM van der, Knol RJJ, et al. 18F-DCFPyL PET/CT in the Detection of Prostate Cancer at 60 and 120 Minutes: Detection Rate, Image Quality, Activity Kinetics, and Biodistribution. *J Nucl Med.* 2017;58:1797–1804.
 20. Boellaard R, Delgado-Bolton R, Oyen WJG, et al. FDG PET/CT: EANM procedure guidelines for tumour imaging: version 2.0. *Eur J Nucl Med Mol Imaging.* 2015;42:328–354.
 21. Nioche C, Orhac F, Boughdad S, et al. LIFEx: A Freeware for Radiomic Feature Calculation in Multimodality Imaging to Accelerate Advances in the Characterization of Tumor Heterogeneity. *Cancer Res.* 2018;78:4786–4789.
 22. Schmuck S, von Klot CA, Henkenberens C, et al. Initial Experience with Volumetric 68Ga-PSMA I&T PET/CT for Assessment of Whole-Body Tumor Burden as a Quantitative Imaging Biomarker in Patients with Prostate Cancer. *J Nucl Med Off Publ Soc Nucl Med.* 2017;58:1962–1968.
 23. Jansen BHE, Cysouw MCF, Vis AN, et al. Repeatability of Quantitative 18F-DCFPyL PET/CT Measurements in Metastatic Prostate Cancer. *J Nucl Med.* 2020;61:1320–1325.
 24. Jung I, Gurzu S, Raica M, et al. The differences between the endothelial area marked with CD31 and CD105 in colorectal carcinomas by computer-assisted morphometrical analysis. *Romanian J Morphol Embryol Rev Roum Morphol Embryol.* 2009;50:239–243.
 25. Hirsch FR, Varella-Garcia M, Bunn PA, et al. Epidermal growth factor receptor in non-small-cell lung carcinomas: correlation between gene copy number and protein expression and impact on prognosis. *J Clin Oncol Off J Am Soc Clin Oncol.* 2003;21:3798–3807.
 26. John T, Liu G, Tsao M-S. Overview of molecular testing in non-small-cell lung cancer: mutational analysis, gene copy number, protein expression and other biomarkers of EGFR for the prediction of response to tyrosine kinase inhibitors. *Oncogene.* 2009;28 Suppl 1:S14-23.
 27. Arçay A, Eiber M, Langbein T. Incidental Finding of Colon Carcinoma Related to High Uptake in 18F-PSMA-1007 PET. *Clin Nucl Med.* 2020;45:561–562.
 28. Cuda TJ, Riddell AD, Liu C, et al. PET Imaging Quantifying 68Ga-PSMA-11 Uptake in Metastatic Colorectal Cancer. *J Nucl Med Off Publ Soc Nucl Med.* 2020;61:1576–1579.
 29. Ferreira G, Iravani A, Hofman MS, et al. Intra-individual comparison of 68Ga-PSMA-11 and 18F-DCFPyL normal-organ biodistribution. *Cancer Imaging.* 2019;19:23.
 30. Man KD, Laeken NV, Schelfhout V, et al. 18F-PSMA-11 Versus 68Ga-PSMA-11 Positron Emission Tomography/Computed Tomography for Staging and Biochemical Recurrence of Prostate Cancer: A Prospective Double-blind Randomised Cross-over Trial. *Eur Urol.* 2022;82:501–509.
 31. Giesel FL, Will L, Lawal I, et al. Intraindividual Comparison of 18F-PSMA-1007 and 18F-DCFPyL PET/CT in the Prospective Evaluation of Patients with Newly Diagnosed Prostate Carcinoma: A Pilot Study. *J Nucl Med Off Publ Soc Nucl Med.* 2018;59:1076–1080.

SECTION II

Rectal cancer



Accuracy of magnetic resonance imaging in
primary staging and restaging after neoadjuvant
therapy in rectal cancer patients

F.A. Vuijk, A.A. Lemij, S.J.D. Temmink, A.P. Zeilstra, K.A. Chotkan, M.A. Frouws,
A.W.K.S. Marinelli, P.A. Neijenhuis, R. Schmitz, F.A. Holman, A.S.L.P. Crobach,
A.L. Vahrmeijer, L.F. de Geus-Oei, S. Feshtali Shahbazi, K.C.M.J. Peeters and D.E. Hilling.

Submitted

6

ABSTRACT

Introduction

Local staging of rectal cancer is currently performed using multiparametric magnetic resonance imaging (MRI). Unfortunately, the accuracy of MRI is not always sufficient to determine disease stage. As a result, over- and undertreatment may occur, and chances for organ preservation are being missed. This study aims to confirm the diagnostic accuracy of MRI in (re)staging of rectal cancer and analyze the treatment consequences of incorrect staging.

Methods

This is a multicenter, retrospective cohort study including rectal cancer patients from four hospitals in The Netherlands. Data was acquired from the Dutch Cancer Registry, and stratified based on received treatment: surgery without neoadjuvant treatment, short course radiotherapy (SCRT), SCRT with a prolonged waiting period and chemoradiotherapy (CRT).

Results

This study demonstrates a low sensitivity of MRI for determining T stage (47.5%) and N stage (59.7%). As a result, 20.7-69.4% of patients received treatment that was not in line with national guidelines. This included 16.7% of CRT patients who were not offered the option of organ preservation, as their complete response was not detected on MRI. Incorrect N staging was the predominant factor in incorrect staging.

Conclusion

This report adds to the evidence of MRI having a low sensitivity for both T and N stage in rectal cancer patients. A trend was observed towards more overstaging in lower T stages, understaging in higher T stages, and general overstaging for N stage. New imaging techniques or algorithms for current imaging modalities should be explored to increase the accuracy of staging and subsequent treatment in rectal cancer patients.

INTRODUCTION

Primary local staging and restaging after neoadjuvant therapy of rectal cancer is currently performed using multiparametric magnetic resonance imaging (MRI). This generally includes T2-weighted, as well as diffusion-weighted scanning sequences. Computed tomography (CT) is used to identify possible distant metastases. Based on several MRI and patient related features, one of the following treatment options is chosen for patients with non-metastatic disease; upfront surgical resection, neoadjuvant short course radiotherapy (SCRT) followed by surgery (with or without prolonged waiting period), or neoadjuvant chemoradiotherapy (CRT) followed by surgical resection. These MRI features include the TNM stage, involvement of the mesorectal fascia (MRF), and the presence of extramural vascular invasion (EMVI), as described and advised by the European Society of Gastrointestinal and Abdominal Radiology (ESGAR)¹.

As with all imaging modalities, there are certain pitfalls inherent to MR imaging with regard to (re)staging rectal cancer. Among these are the differentiation between EMVI and desmoplastic reaction as well as the determination of small nodal involvement (i.e. lymph node metastasis). In addition, determining the TNM stage accurately after neoadjuvant therapy (due to the presence of therapy induced fibrosis, inflammation, and edema) and follow up of patients with a clinical complete response (complete regression of all tumor and lymph node tissue) remains challenging^{2,3}.

In the primary staging of rectal cancers using MRI, both over- and underestimation of the tumor and nodal stage can have significant influence on the choice of treatment. A recent analysis of data from the Dutch ColoRectal Audit reported overstaging by MRI of pT1 tumors in 55%, and of pN0 in 17% of patients⁴. As concluded from this data, 58% of pT1N0 tumors were overstaged and might have missed the opportunity of local treatment strategies. In addition to this, a report by Dahlbäck et al. found a sensitivity and specificity of 69% and 77% respectively for differentiating T1-2 tumors from T3-4 on MRI⁵. Moreover, sensitivity for detecting N1-2 disease was only 42%. Likewise, it is known that over- and understaging are common in restaging after neoadjuvant therapy. A previous report demonstrated correct T staging by three radiologists (joint reading) in only 47-68%, and correct N staging in 68-70%⁶. Other reports also described the lack of correlation between the tumor regression grade (TRG) as determined on MRI (mrTRG) and the histopathological regression grade (pTRG)⁷. In addition, Memon *et al.*, described an average accuracy of MRI for determining T stage after neoadjuvant chemoradiotherapy of 52% (ranging from 34-82%)⁸.

With recent studies such as the RAPIDO study investigating novel treatment regimens for neoadjuvant therapy resulting in even more downstaging and higher rates of complete

response, the importance of accurate staging and restaging is emphasized⁹. This study aims to confirm the diagnostic accuracy of MRI in (re)staging of rectal cancer patients in our region and analyze the subsequent treatment consequences of incorrect staging in these patients.

METHODS

Patients

This study is a Dutch multicenter, retrospective cohort study including rectal cancer patients treated at Leiden University Medical Center, Leiden (LUMC), Haaglanden Medical Center, The Hague (HMC), Groene Hart Hospital, Gouda (GHZ), and Alrijne Hospital, Leiderdorp between 2014 and 2018. The data was acquired from the Netherlands Cancer Registry (NCR or IKNL), the Dutch oncological quality institute which assembles data from all cancer patients in the Netherlands. If available in the electronic patient file from the originating hospital, missing data was added to the dataset manually. Afterwards, patients were excluded for the following reasons: no restaging TNM stage was available, type of neoadjuvant therapy was unknown, both clinical or pathological T and N stage were missing, no surgery was performed (and thus no pathological TNM was available). The study was conducted in concordance with the Declaration of Helsinki, and the laws and regulations of the Netherlands. The study was approved by the certified medical ethics review board (ethics committee Leiden, Den Haag, Delft) and the local review boards of the participating centers.

Data handling

Patients were categorized into 4 groups based on their treatment according to the Dutch Guideline for Colorectal Cancer (version update 2014)¹⁰: 1. immediate surgery without neoadjuvant treatment (cT1-2N0 or cT3N0 ≤5mm EMVI + distance to MRF >1mm), 2. SCRT followed by immediate surgical resection (cT1-3N1 or cT3N0 with >5mm EMVI + distance to MRF >1mm), 3. SCRT followed by prolonged waiting period after which restaging and surgical resection (SCRT+W) and 4. long-course neoadjuvant CRT followed by surgical resection (cT4 or cT3 + distance tot MRF ≤1mm or cN2). The SCRT+W group was defined by selecting patients who received SCRT after which a minimal waiting period of 1 week (7 days) was followed by surgical resection. For the SCRT+W and CRT group, a re-staging MRI had to be available. Both EMVI and MRF were not available in the IKNL dataset and were thus not considered in the analyses. The pathological TNM stage was used as golden standard for staging. To compare clinical staging (on MRI) with the pathological staging after resection, in the immediate surgery and SCRT groups the primary MRI was used, and in the SCRT+W and CRT groups the restaging MRI. As there is a waiting period between restaging MRI and surgery in the SCRT+W and CRT groups,

the comparison between TNM stage on MRI and pathological assessment in these groups, can be hampered by further downstaging of the tumor and/or lymph nodes in the waiting period (leading to overstaging of MRI in these groups). Because patients who receive SCRT (without prolonged waiting) undergo surgery within a week after radiotherapy, no downstaging of tumor and/or lymph nodes is expected in this group. For these reasons, we investigated treatment accuracy and consequence of incorrect staging in all groups, and accuracy of (re)staging on MRI only in the immediate surgery and SCRT group (not in the SCRT+W and CRT group). Pathological tumor regression grade (pTRG) was performed according to Mandard's previous report¹¹.

Statistical analysis

Statistical analyses were performed using SPSS version 25 (IBM SPSS Inc., Chicago, IL). Categorical variables were presented as frequencies and percentages, numerical variables as mean and standard deviation or median and interquartile range (IQR) based on the distribution. Differences in baseline characteristics between patients were tested with Pearson's Chi-Square test for categorical data and Kruskal-Wallis test for continuous data after testing for normal distribution. For the immediate surgery and SCRT group, primary staging based on MRI was compared to final pathological TNM stage by Chi-square tests. In the group SCRT+W and CRT group, the re-evaluation MRI (γTNM) was compared to the pathological TNM stage by Chi-square tests. Sensitivity of MRI was defined as the percentage of correctly staged tumors according to pathological stage for individual T and N stage. For all analyses, a p-value <0.05 was considered statistically significant.

RESULTS

Data of 1046 patients was acquired from the IKNL (332 from LUMC, 318 from HMC, 63 from GHZ Hospital, 371 from Alrijne Hospital). From these, 766 patients met the inclusion criteria and were included in further analyses. Of these 766 patients, 376 (49.1%) underwent immediate surgery, 138 (18.0%) SCRT, 58 (7.6%) SCRT+W, and 194 (25.3%) CRT **Figure 1**. Patient characteristics at baseline are summarized in **Table 1**. The groups are not equal at baseline with regards to age, T and N stage. Since the treatment of rectal cancer patients, in accordance with the Dutch guidelines, is determined by TNM classification amongst others, the difference in T and N stage was expected. The age difference might indicate that younger and more fit patients more frequently receive strenuous CRT, whereas older (more frail) patients were offered SCRT+W to increase their chance for organ sparing treatment. Results from the immediate surgery and SCRT are discussed below.

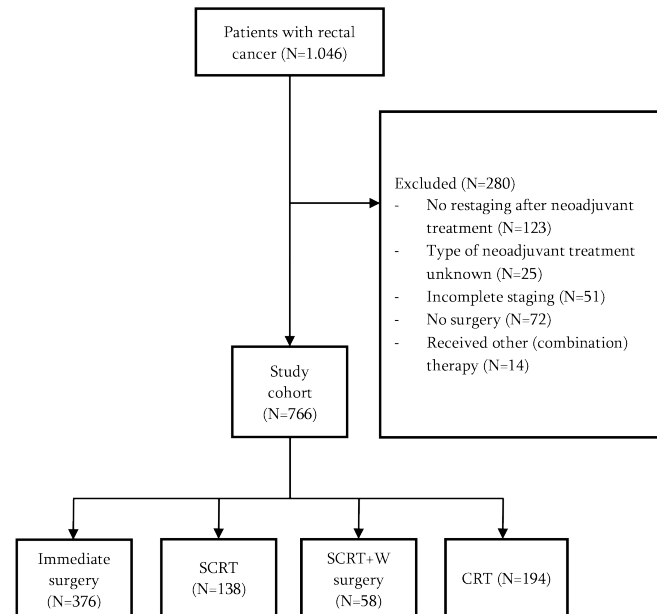


FIGURE 1. Flowchart inclusion and exclusion criteria.

TABLE 1. Patient- and tumor characteristics at baseline in three treatment groups.

	Immediate surgery	Short course radiotherapy with immediate surgery	Short course radiotherapy with delayed surgery	Neoadjuvant chemoradiotherapy	p-value
Patients (n(%))	376 (49.1)	138 (18.0)	58 (7.6)	194 (25.3)	na
Age (median (IQR))	68 (62-75)	66 (59-73)	74.5 (66-82)	64.5 (57-70)	<0.001
Gender (n(%))					0.924
Male	248 (66.0)	87 (63.0)	39 (67.2)	127 (65.5)	
Female	128 (34.0)	51 (37.0)	19 (32.8)	67 (34.5)	
Clinical TNM stage					
Tumor (n(%))					<0.001
T1	55 (14.6)	3 (2.2)	0 (0.0)	0 (0.0)	
T2	152 (40.4)	29 (21.0)	5 (8.6)	10 (5.2)	
T3	120 (31.9)	100 (72.5)	42 (72.4)	129 (66.5)	
T4	10 (2.7)	2 (1.4)	10 (17.3)	54 (27.8)	
Unknown	39 (10.4)	4 (2.9)	1 (1.7)	1 (0.5)	
Node (n(%))					<0.001
N0	331 (88.0)	17 (12.3)	13 (22.4)	32 (16.5)	
N1	29 (7.7)	114 (82.6)	33 (56.9)	57 (29.4)	
N2	9 (2.4)	4 (2.9)	12 (20.7)	105 (54.1)	
Unknown	7 (1.9)	3 (2.2)	0 (0.0)	0 (0.0)	
Metastasis (n(%))					0.191
M0	367 (97.6)	136 (98.6)	56 (96.6)	184 (94.8)	
M1	9 (2.4)	2 (1.4)	2 (3.4)	10 (5.2)	

Abbreviations: IQR, interquartile range; n, number; na, not applicable. Median age with Kruskal-Wallis and all others with chi-square test

Accuracy of MR imaging in T stage

In the immediate surgery group the T stage of 48.4% of patients was staged correctly, 14.4% of patients was understaged and 26.1% was overstaged (11.1% unknown). In the SCRT group, 58.0% of patients was staged correctly, 8.0% of patients was understaged, and 31.2% of patients was overstaged (2.8% unknown). The accuracy of MRI for T staging is visualized in **Figure 2A**, cross tables of T and N stages of the 4 groups are visualized in **Supplementary Table 1**, percentages of over- and understaging per T stage are visualized in **Table 2**.

Accuracy of MR imaging in N stage

In the immediate surgery, the N stage was correctly identified in 65.2% of patients, 16.2% of patients was understaged and 6.4% was overstaged (12.2% unknown). In the SCRT group, 35.5% of patients was staged correctly, 11.6% of patients was understaged, and 50.7% of patients was overstaged (2.2% unknown). The accuracy of MRI for N staging is visualized in **Figure 2B**, cross tables of the T and N stages of the 4 groups are visualized in **Supplementary Table 1**, percentages of over- and understaging per N stage are visualized in **Table 2**.

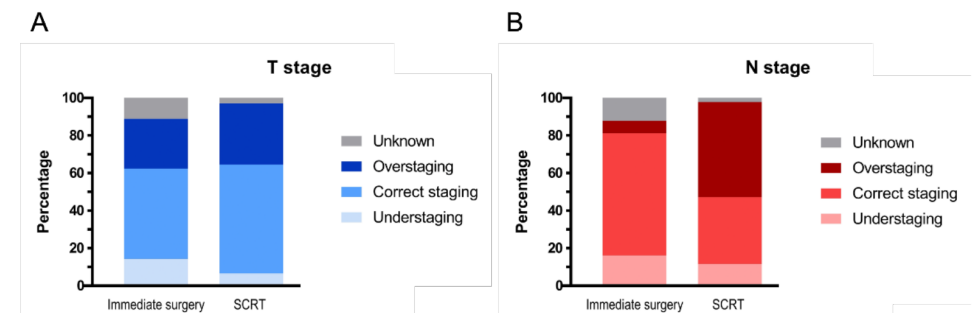


FIGURE 2. Visualization of MRI accuracy in rectal cancer staging. Figure 2A represents accuracy of T staging, Figure 2B represents accuracy of N staging. In the immediate surgery and SCRT group, the pathological T and N stage are compared to the primary clinical diagnostic staging from MRI. Abbreviations: T stage, tumor stage; SCRT, short course radiotherapy. Unknown: either clinical or pathological stage was missing.

Clinical consequence of incorrect staging

For these analyses, only non-metastatic patients with complete clinical and pathological data were included (n=629). To exclude patients who were not treated according to the national guideline based on other factors than incorrect T or N stage on MRI (e.g. age, comorbidity), only patients who were treated correctly in accordance with the clinical TNM stage were included in this subanalysis (n=470). In addition, the SCRT+W and CRT

group were excluded because of the expected further downstaging in the waiting period as mentioned before. Of 250 patients who underwent immediate surgery without neoadjuvant treatment, 197 patients (78.8%) were correctly treated according to the pathological TNM stage, 42 patients (16.8%) should have had SCRT and 11 patients (4.4%) should have had CRT respectively, based on the guideline. In almost all patients this was solely due to incorrect N staging (in 2 patients both iT and iN caused incorrect staging and treatment allocation). Of the 109 patients in the SCRT group 34 (31.2%) were treated correctly, 63 patients (57.8%) should have had immediate surgery, and 12 patients (11.0%) should have had CRT. This is shown in more detail in **Supplementary Table 1E**. In all patients, this was due to incorrect N staging.

TABLE 2. Over- and understaging per T and N stage. Data is divided per treatment group and shows the correctness of staging per T and N stage.

Pathological stage	Patients (n)	Understaged	Correct	Overstaged	Unknown
Immediate resection					
pT0	1	-	0 (0%)	1 (100%)	0
pT1	105	0 (0%)	45 (43%)	39 (37%)	21 (20%)
pT2	147	7 (5%)	78 (53%)	54 (37%)	8 (5%)
pT3	110	43 (39%)	55 (50%)	4 (4%)	8 (7%)
pT4	8	4 (50%)	4 (50%)	-	0
Unknown	5				
pN0	259	-	234 (90%)	22 (9%)	3 (1%)
pN1	62	50 (81%)	8 (13%)	2 (3%)	2 (3%)
pN2	15	11 (73%)	3 (20%)	-	1 (7%)
Unknown	40				
SCRT					
pT1	11	0 (0%)	3 (27%)	8 (73%)	0 (0%)
pT2	49	0 (0%)	15 (31%)	33 (67%)	1 (2%)
pT3	75	8 (11%)	62 (82%)	2 (3%)	3 (4%)
pT4	3	3 (100%)	0 (0%)	0 (0%)	0 (0%)
Unknown	4				
pN0	86	-	14 (16%)	70 (82%)	2 (2%)
pN1	36	1 (3%)	34 (94%)	0 (0%)	1 (3%)
pN2	16	15 (94%)	1 (6%)	-	0 (0%)
SCRT+W					
pT0	6	-	3 (50%)	3 (50%)	0 (0%)
pT1	7	0 (0%)	0 (0%)	6 (86%)	1 (14%)
pT2	16	3 (19%)	3 (19%)	9 (56%)	1 (6%)
pT3	25	8 (32%)	13 (52%)	4 (16%)	0 (0%)
pT4	4	1 (25%)	3 (75%)	-	0 (0%)
pN0	36	-	27 (75%)	9 (25%)	0 (0%)
pN1	15	9 (60%)	5 (33%)	1 (7%)	0 (0%)
pN2	4	3 (75%)	1 (25%)	-	0 (0%)
Unknown	3				

TABLE 2. Continued.

Pathological stage	Patients (n)	Understaged	Correct	Overstaged	Unknown
CRT					
pT0	44	-	8 (18%)	31 (71%)	5 (11%)
pT1	14	1 (7%)	0 (0%)	13 (93%)	0 (0%)
pT2	46	3 (7%)	16 (35%)	26 (56%)	1 (2%)
pT3	76	10 (13%)	46 (61%)	19 (25%)	1 (1%)
pT4	12	2 (17%)	10 (83%)	-	0 (0%)
Unknown	2				
pN0	138	-	101 (73%)	35 (25%)	2 (2%)
pN1	45	12 (27%)	26 (58%)	6 (13%)	1 (2%)
pN2	9	6 (67%)	3 (33%)	-	0 (0%)
Unknown	2				

Abbreviations: SCRT, short course radiotherapy; SCRT+W, short course radiotherapy with prolonged waiting period before surgery; CRT, chemoradiotherapy.

Identification of complete response

For this analysis, only patients with known complete pathological and clinical T and N stage who were treated according to national treatment guidelines were included (n=470). In total, 19 out of 114 (16.7%) patients who received CRT had a pathological complete response (ypT0N0) tumor at histopathological examination. Of these 19 patients with a ypT0N0 tumor, 3 patients were also staged as clinical complete responders (yiT0N0) at the restaging MRI but underwent surgery anyway. The other ypT0N0 patients were staged on MRI as yiT0N1 (n=1), yiT1N0 (n=1), yiT2N0 (n=2), yiT2N1 (n=1), yiT3N0 (n=6), yiT3N1 (n=1), yiT3N2 (n=2), yiT4N0 (n=2). Of the 58 patients in the SCRT+W group, 4 had a ypT0N0. Of these, only 1 was staged correctly on MRI. The others were yiT0N1, yiT3N0, and yiT3N2.

Including the 3 patients mentioned above, 5 patients who underwent CRT were restaged on MRI as clinical complete responders (yiT0N0), but underwent surgery resection anyway for which the reason is unknown. On histopathological examination, these patients had an ypT0N0 tumor (n=3), ypT1N1 tumor (n=1), and an ypT2N0 tumor (n=1).

DISCUSSION

Results from this retrospective regional study demonstrate a low sensitivity of MRI for determining T stage (47.5%) and N stage (59.7%). As a result, a significant number of patients received "incorrect" treatment due to over- or understaging (21.2-68.8% depending on the treatment group). This included 19 out of 114 (16.7%) patients who underwent CRT followed by futile surgical resection as the complete response to CRT

insufficiently recognized on MRI. Sporadically missing a cCR is inevitable, however, 16.7% of cCRs missed is too frequent. In all cases this was due to incorrect N staging (in two patients due to both T and N staging), as can be expected since the decision for neoadjuvant treatment is most frequently based on N stage. This study is the first to investigate what influence incorrect staging of rectal cancer has on treatment choice in all rectal cancer stages except metastatic patients.

Sensitivity of MRI for determining T and N stage varies greatly between treatment groups and T stages. In patients undergoing immediate surgery without prior neoadjuvant treatment, previous reports and meta-analysis describe a sensitivity for T and N stage of 53-87% and 28-77% respectively^{4,12-15}. Compared to these results, we found a lower sensitivity for T stage in this group (47.5%), but similar sensitivity for N stage (59.7%). Lower sensitivity of MRI for T stage is generally found in patients after neoadjuvant therapy. Various systematic reviews report a sensitivity for T-stage of 50-52% and a sensitivity for N-stage of 62-76.5% in patients after neoadjuvant therapy^{8,16,17}. Similar to the immediate surgery group, our results demonstrate lower sensitivity in the CRT group for T stage (40.2%), but similar for N stage (67%). Our results show a trend towards more overstaging in lower T stages, understaging in higher T stages, and general overstaging for N stage. This seems to be in line with previous reports^{4,8,15}, however more understaging of N stage has been described. In addition, this trend holds true for all treatment groups except SCRT, in which 67-79% of patients was overstaged in this study depending on T stage.

In this study, 21.2% of patients in the immediate surgery group and 68.8% in the SCRT group were not treated according to the guidelines due to incorrect MRI staging. In all cases, this was mostly due to incorrect N staging. Moreover, 16.7% of patients in the CRT group missed a chance at organ preservation due to an unrecognized pathological complete response (pT0N0). This data suggests that although sensitivity of MRI for determining T stage is low, the found low sensitivity for N stage has most clinical impact on treatment choice. As is known from previous reports, lymph node involvement is common even in small nodes. Perez *et al.* previously demonstrated that 95% of lymph node metastases were smaller than 5mm, and 50% was even smaller than 3mm¹⁸. This could largely explain why MRI is inaccurate at N staging as size in combination with various morphological features are considered when determining N stage. In addition to this, pathological assessment of lymph nodes is also not always completely reliable, and might depend on the amount of lymph nodes assessed. In current practice, pathologists search for lymph nodes in the resected specimen, and as a result can only determine the nodal stage based on these specific lymph nodes. No correlation of suspect lymph nodes on MRI to these lymph nodes in the resected specimen is performed, and tumor positive lymph nodes might be missed. Better correlation of

these could aid in finding and sampling the right lymph nodes during pathological assessment to improve pathological staging. Various other factors might improve the accuracy of staging using MRI. As demonstrated by van der Paardt *et al.*, the use of DW imaging sequences, and double or joint reading leads to a significantly higher sensitivity for determining T stage after neoadjuvant treatment¹⁶. In this study, double reading was performed (second reading before multidisciplinary meeting), however quality could be increased by selecting dedicated colorectal radiologists to increase their skill at rectal cancer MRI assessment (now frequently general abdominal radiologists in the period of investigation). Overstaging in the SCRT and CRT group might be due to the ongoing effect of neoadjuvant therapy after the restaging MRI. Interestingly, this report also indicates that lower section thickness (≤ 3 mm vs > 3 mm), rectal distention, and exclusively considering nodes > 5 mm as malignant did not result in increased performance. In addition, Detering *et al.* suggest the use of double reading, addition of endorectal ultrasound, and increased MRI field strength to increase sensitivity for T staging⁴. Other factors such as investigating different criteria for nodal involvement or the use of (lymph node specific) contrast agents might increase the sensitivity of MRI for N stage.

This study has various limitations. First, as data was retrieved from the Dutch Cancer Registry, errors could have been made during data entry. However, as received data was checked, missing data was added by a local researcher and patients were excluded in case of missing data, the influence of this is deemed minimal. Second, no information was available on the subcategory of both imaging and pathological T stage such as T3ab or T3cd, the exact tumor location (i.e. proximal or distal), and the status of mesorectal fascia involvement and EMVI. As the current guidelines consider these factors, these could have influenced the actual choice of treatment and thus our results. However, we tried to minimize this problem by only including patients that were in principal correctly treated according to the available clinical TNM stage in the 'clinical consequence of incorrect staging' analysis. In addition, all incorrect treatment based on over- or understaging was due to incorrect N staging (not T stage), for which all information was available (thus no influence of T subcategories).

In conclusion, this report adds to the evidence of MRI having a low sensitivity for both T and N stage in rectal cancer patients. Both over and understaging is common in the immediate surgery and SCRT group, but incorrect treatment decisions were almost always based on incorrect N staging. New imaging techniques or algorithms for current imaging modalities should be explored to increase the accuracy of staging (in general, but mostly N stage as this has most clinical consequence) and subsequent treatment in rectal cancer patients.

REFERENCES

1. Beets-Tan, R. G. H. *et al.* Magnetic resonance imaging for clinical management of rectal cancer: Updated recommendations from the 2016 European Society of Gastrointestinal and Abdominal Radiology (ESGAR) consensus meeting. *Eur. Radiol.* **28**, 1465–1475 (2018).
2. Nougaret, S., Jhaveri, K., Kassam, Z., Lall, C. & Kim, D. H. Rectal cancer MR staging: pearls and pitfalls at baseline examination. *Abdom. Radiol. N. Y.* **44**, 3536–3548 (2019).
3. Lambregts, D. M. J., Boellaard, T. N. & Beets-Tan, R. G. H. Response evaluation after neoadjuvant treatment for rectal cancer using modern MR imaging: a pictorial review. *Insights Imaging* **10**, 15 (2019).
4. Detering, R. *et al.* MRI cT1–2 rectal cancer staging accuracy: a population-based study. *BJS Br. J. Surg.* **n/a**.
5. Dahlbäck, C. *et al.* Accuracy of magnetic resonance imaging staging of tumour and nodal stage in rectal cancer treated by primary surgery: a population-based study. *Colorectal Dis. Off. J. Assoc. Coloproctology G. B. Irel.* **24**, 1047–1053 (2022).
6. van den Broek, J. J. *et al.* Accuracy of MRI in Restaging Locally Advanced Rectal Cancer After Preoperative Chemoradiation. *Dis. Colon Rectum* **60**, 274–283 (2017).
7. Sclafani, F. *et al.* Comparison between MRI and pathology in the assessment of tumour regression grade in rectal cancer. *Br. J. Cancer* **117**, 1478–1485 (2017).
8. Memon, S., Lynch, A. C., Bressel, M., Wise, A. G. & Heriot, A. G. Systematic review and meta-analysis of the accuracy of MRI and endorectal ultrasound in the restaging and response assessment of rectal cancer following neoadjuvant therapy. *Colorectal Dis. Off. J. Assoc. Coloproctology G. B. Irel.* **17**, 748–761 (2015).
9. Bahadoer, R. R. *et al.* Short-course radiotherapy followed by chemotherapy before total mesorectal excision (TME) versus preoperative chemoradiotherapy, TME, and optional adjuvant chemotherapy in locally advanced rectal cancer (RAPIDO): a randomised, open-label, phase 3 trial. *Lancet Oncol.* **22**, 29–42 (2021).
10. *Dutch Guideline Colorectal Cancer.* (Federation Medical Specialists, 2014).
11. Mandard, A. M. *et al.* Pathologic assessment of tumor regression after preoperative chemoradiotherapy of esophageal carcinoma. Clinicopathologic correlations. *Cancer* **73**, 2680–2686 (1994).
12. Al-Sukhni, E. *et al.* Diagnostic accuracy of MRI for assessment of T category, lymph node metastases, and circumferential resection margin involvement in patients with rectal cancer: a systematic review and meta-analysis. *Ann. Surg. Oncol.* **19**, 2212–2223 (2012).
13. Bipat, S. *et al.* Rectal cancer: local staging and assessment of lymph node involvement with endoluminal US, CT, and MR imaging—a meta-analysis. *Radiology* **232**, 773–783 (2004).
14. Zhang, G., Cai, Y.-Z. & Xu, G.-H. Diagnostic Accuracy of MRI for Assessment of T Category and Circumferential Resection Margin Involvement in Patients With Rectal Cancer: A Meta-Analysis. *Dis. Colon Rectum* **59**, 789–799 (2016).
15. Rosén, R., Nilsson, E., Rahman, M. & Rönnow, C.-F. Accuracy of MRI in early rectal cancer: national cohort study. *Br. J. Surg.* **109**, 570–572 (2022).
16. van der Paardt, M. P., Zagers, M. B., Beets-Tan, R. G. H., Stoker, J. & Bipat, S. Patients who undergo preoperative chemoradiotherapy for locally advanced rectal cancer restaged by using diagnostic MR imaging: a systematic review and meta-analysis. *Radiology* **269**, 101–112 (2013).
17. Zhao, R.-S., Wang, H., Zhou, Z.-Y., Zhou, Q. & Mulholland, M. W. Restaging of locally advanced rectal cancer with magnetic resonance imaging and endoluminal ultrasound after preoperative chemoradiotherapy: a systemic review and meta-analysis. *Dis. Colon Rectum* **57**, 388–395 (2014).
18. Perez, R. O. *et al.* Lymph node size in rectal cancer following neoadjuvant chemoradiation—can we rely on radiologic nodal staging after chemoradiation? *Dis. Colon Rectum* **52**, 1278–1284 (2009).

SUPPLEMENTARY

SUPPLEMENTARY TABLE 1. Cross tables of tumor and lymph node staging.

Immediate resection		pT					Total	
	T0	T1	T2	T3	T4	Unknown		
A cT	T1	0	45	7	2	0	1	55
	T2	0	30	78	41	2	1	152
	T3	0	9	54	55	2	0	120
	T4	1	0	0	4	4	1	10
	Unknown	0	21	8	8	0	2	39
Total	1	105	147	110	8	5	376	

SCRT		pT				Total	
	T1	T2	T3	T4			
B cT	T1	3	0	0	0	3	3
	T2	6	15	8	0	29	29
	T3	2	33	62	3	100	100
	T4	0	0	2	3	2	2
	Unknown	0	1	3	0	4	4
Total	11	49	75	3	138	138	

SCRT+W		pT				Total	
	T0	T1	T2	T3	T4		
C cT	T2	1	0	2	2	0	5
	T3	4	7	14	16	1	42
	T4	0	0	0	7	3	10
	Unknown	1	0	0	0	0	1
	Total	6	7	16	25	4	58

CRT		pT					Total	
	T0	T1	T2	T3	T4	Unknown		
D cT	T2	3	2	3	2	0	0	10
	T3	31	10	34	49	3	2	129
	T4	10	2	8	25	9	0	54
	Unknown	0	0	1	0	0	0	1
	Total	44	14	46	76	12	2	194

Treatment choice		Based on pathological stage				
	Immediate surgery	SCRT	CRT		Total	
E Based on clinical stage	Immediate surgery	197	42	11		250
	SCRT	63	34	12		109
	Total	260	76	23		359

Immediate resection		pN				Total
	N0	N1	N2	Unknown		
F cN	N0	234	50	8	39	331
	N1	18	8	3	0	29
	N2	4	2	3	0	9
	Unknown	3	2	1	1	7
	Total	259	62	15	40	376

SCRT		pN			Total
	N0	N1	N2		
G cN	N0	14	1	2	17
	N1	67	34	13	114
	N2	3	0	1	4
	Unknown	2	1	0	3
	Total	86	36	16	138

SCRT+W		pN				Total
	N0	N1	N2	Unknown		
H cN	N0	27	9	1	3	40
	N1	8	5	2	0	15
	N2	1	1	1	0	3
	Unknown	1	1	1	0	3
	Total	36	15	4	3	58

CRT		pN				Total
	N0	N1	N2	Unknown		
I cN	N0	101	12	3	2	118
	N1	22	26	3	0	51
	N2	13	6	3	0	22
	Unknown	2	1	0	0	3
	Total	138	45	9	2	194

Abbreviations: pT, pathological tumor stage; cT clinical tumor stage; SCRT, short course radiotherapy; SCRT+W, short course radiotherapy with prolonged waiting period; CRT, chemoradiotherapy.

[¹⁸F]FDG PET/CT in Treatment Response Evaluation: Colorectal Cancer

F.A. Vuijk, L. Heijmen, M.J. Roef, A.I.J. Arens, A.L. Vahrmeijer, E.L. van Persijn van Meerten,
D.E. Hilling and L.F. de Geus-Oei.

Atlas of Clinical PET-CT in Treatment Response Evaluation in Oncology (2021)



INTRODUCTION

With an incidence of 1.8 million and nearly 900 thousand deaths in 2018, colorectal cancer has the third highest cancer incidence, and ranks second amongst common causes of cancer death worldwide¹. As (neo)adjuvant treatment regimens have been adopted into treatment guidelines for both colon and rectal cancer (neoadjuvant short course radiotherapy and long course chemoradiotherapy for rectal cancer, adjuvant chemotherapy for colon cancer), treatment response monitoring has become of evident importance.

Currently, response monitoring is performed using computed tomography (CT) imaging combined with colonoscopy and magnetic resonance (MR) and digital rectal examination in rectal cancer patients. Up to now, the use of positron emission tomography (PET) has not been adopted into colorectal guidelines for response monitoring purposes yet.

[¹⁸F]Fluorodeoxyglucose (FDG) PET has the potential to provide metabolic information on tumor cells as indicated by the increased uptake and metabolism of glucose. This provides additional information compared to conventional CT or MR imaging alone. While hybrid PET/CT is a common and widely available technique, developments towards optimizing combined PET/MR scanners are still ongoing but show great promise.

In addition to the combination of PET with CT and MR, much progress is also being made in optimizing PET scanner hardware and software. Most recently, the introduction of the digital PET scanner shows promise to further increase the diagnostic abilities of PET. Previous research and concurrent clinical experience have reported additional value of the use of FDG PET in initial staging of recurrent colorectal cancer and metastases, localizing recurrent disease in patients with unexplained elevation of serum CEA and in the assessment of residual cancerous masses after treatment. However, the use of FDG PET for response monitoring of colorectal cancer is still cumbersome. As this technique provides metabolic data, FDG PET can detect intra-tumoral changes preceding anatomical alterations. The technique shows promise in monitoring, but also in predicting response to given therapy, thereby creating options to establish personalized patient treatment. As PET can not only provide qualitative data, but also quantitative data on multiple lesions simultaneously, monitoring lesions can be performed quantitatively over time.

As (neo)adjuvant therapies thrive and become adopted into standard care, the need for accurate response monitoring increases. This is clearly demonstrated by a subgroup of locally advanced rectal cancer patients, who receive neoadjuvant chemoradiation. A proportion of these patients show a complete remission of tumor and/or pathological lymph nodes after treatment. By accurately selecting these patients, surgery can be

omitted, and its associated morbidity and mortality avoided. Current imaging modalities including endoscopy and MR imaging provide reasonable evaluation of residual tumor and/or lymph nodes. However, not all patients with a complete response can be detected. In addition, early detection of non-responders could prevent futile treatment (and its associated side effects) and unnecessary postponing of inevitable surgical resection.

This chapter regarding response monitoring of colorectal cancer using FDG PET/CT, illustrates potential clinical examples in which FDG PET/CT might complement conventional diagnostic imaging modalities in time to come. Further research is however warranted to define the exact situations in which FDG PET/CT can be of additional value. The following clinical cases include response monitoring during neoadjuvant chemoradiation, local treatment of liver metastases, neoadjuvant treatment of recurrent rectal cancer and palliative systemic treatment of hepatic and extrahepatic disease.

CLINICAL CASE 1 - COLORECTAL LIVER METASTASIS

Clinical details: A 55-year-old male with a history of a sigmoid resection for a pT2N0M0 sigmoid carcinoma and metastasectomy for a metachronous liver lesion in segment Iva three years later. Three months after the metastasectomy, radiofrequency ablation (RFA) was performed on a second lesion in segment III. Now, six years after resection of the primary tumor, serum CEA is elevated, and no metastases were detected prospectively on CT imaging of the chest and abdomen.

Scan findings: A solitary FDG avid lesion is detected in the caudate liver lobe. Also, a photopenic area from the metastasectomy is observed in segment IVa. No evidence of disease recurrence is seen at the anastomosis site.

Interpretation: Suspected solitary liver metastasis in the caudate liver lobe.

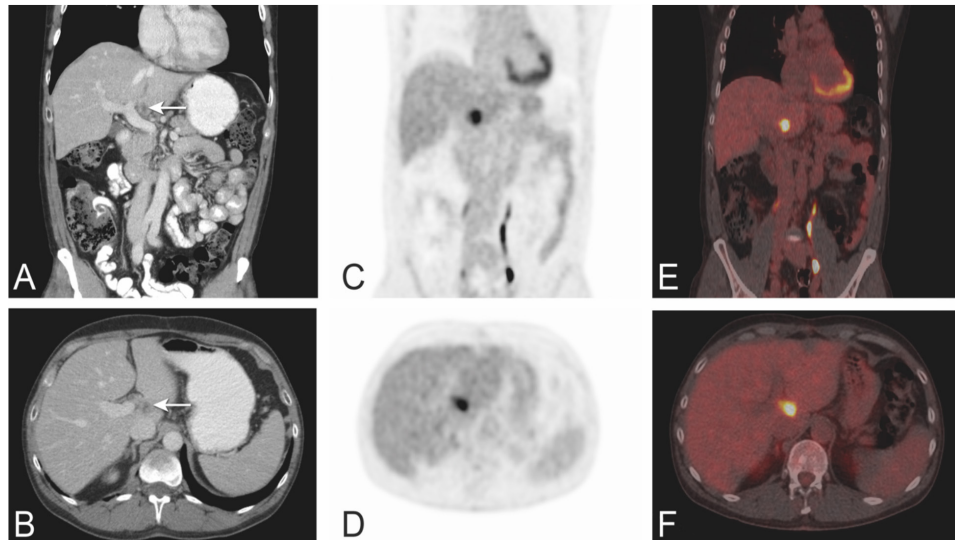


FIGURE 1. Solitary liver metastasis. Coronal (A, C, E) and axial (B, D, F) images of a solitary liver metastasis in the caudate liver lobe (segment I). Representative images of CT (A, B), PET (C, D) and PET/CT (E, F).

Teaching points:

- FDG PET/CT has a higher sensitivity for detecting colorectal liver metastases compared to contrast enhanced CT².
- FDG PET/CT can be helpful to localize recurrent disease in case of elevated CEA and undetectable disease on CT³.

CLINICAL CASE 2 - COLORECTAL LIVER METASTASIS

Clinical details: A 55-year-old male with a history of a coecum carcinoma for which a right hemicolectomy was performed, developed multiple metachronous liver metastases six years later. Left hemi hepatectomy and multiple metastasectomies were performed. One year later, RFA was performed on a recurrent liver metastasis. One year after the RFA, thus 8 years after primary diagnosis, at least 3 suspicious new liver lesions were found on FDG PET/CT (Fig. 2A-B) and deemed unresectable. Systemic treatment consisting of capecitabine, oxaliplatin and bevacizumab was initiated.

Scan findings: Complete remission of the liver metastases (Fig. 2C-D). No evidence of other (extra) hepatic metastases.

Interpretation: Complete response of liver metastasis after therapy.

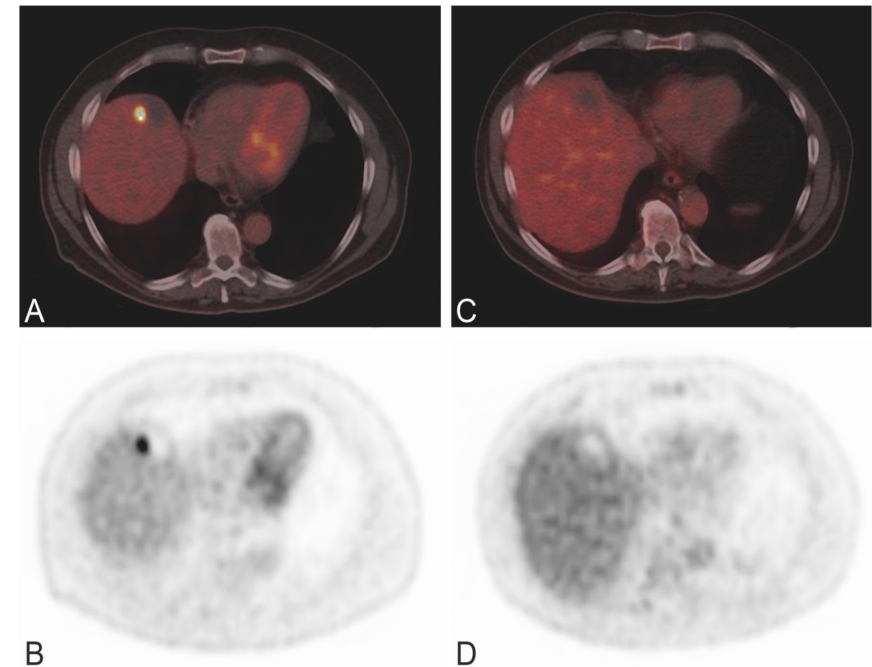


FIGURE 2. Response monitoring liver metastasis. Images of PET/CT (A, C) and PET (B, D) before (A, B) and after six cycles of therapy (C, D).

Teaching point:

- FDG PET/CT can reliably monitor response of liver metastases to systemic treatment.

CLINICAL CASE 3 - SEQUEL TO CASE 2

Clinical details: Four years after therapy, recurrent liver metastases were detected. Capecitabine monotherapy was restarted, and FDG PET/CT was used for response monitoring.

Scan findings: A persistent strong FDG avid metastasis is seen in segment 6/7 (Fig. 3A, E, I), SUV_{max} remains unchanged, however metabolic volume increases. FDG PET/CT shows no changes in the highly active lesion in segment 8 (Fig. 3C, G, K).

Interpretation: Stable disease in liver segment 8, slight increase in metabolic volume in segment 6/7. As previous experience in this patient showed stabilizing and eventually decreasing disease with continuous capecitabine treatment, treatment is continued, and evaluation is scheduled after 3 cycles.

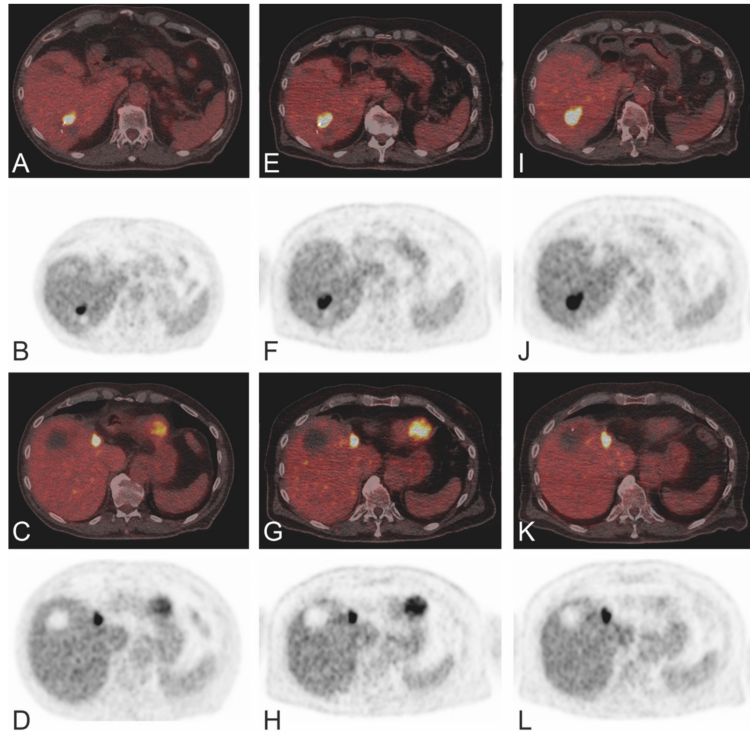


FIGURE 3. Response monitoring liver metastases. PET/CT (A, C, E, G, I, K) and PET (B, D, F, H, J, L) images before (A-D), after 3 cycles (E-H) and after 6 cycles (I-L) of capecitabine treatment.

Teaching point:

- Serial SUV_{max} measurements can monitor therapy response of liver metastases to chemotherapy.

CLINICAL CASE 4 - RESPONSE MONITORING OF LIVER METASTASES

Clinical details: A 74-year-old female with colon cancer and multiple synchronous liver metastases was treated with combination therapy consisting of capecitabine and bevacizumab. Treatment was terminated after 2 cycles due to liver failure, likely due to progressive liver metastases. Four weeks after termination of the treatment, the patient passed away.

The patients participated in a clinical trial, during which PET/CT imaging was performed. The research objective was to evaluate the predictive value of pretreatment PET/CT measurements and early changes one week after the start of therapy ⁴.

Scan findings: Mean SUV_{max} (of 5 lesions) was 15 before treatment, and 13 after 1 week of treatment. Total lesion glycolysis (TLG) in the same five lesions increased slightly from 3450 to 3565.

Interpretation: Progressive disease is observed as metabolic volume has increased.

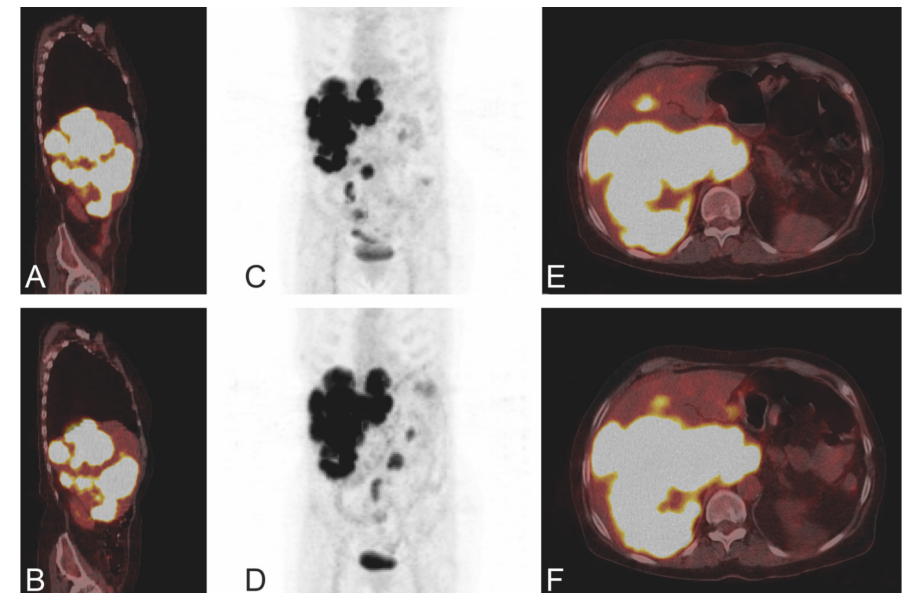


FIGURE 4. Response monitoring of liver metastases. Images of PET/CT (A, B, E, F) and the maximum intensity projection (C, D) before (A, C, E) and after (B, D, F) treatment.

Teaching points:

- FDG PET can identify patients not responding to therapy, thereby aiding in the decision to terminate treatment when no benefit is expected. Early response monitoring is challenging using CT, and only useful 8 weeks after start of treatment.

CLINICAL CASE 5 - RESPONSE MONITORING OF LIVER METASTASES

Clinical details: A 56-year-old male with colon cancer and synchronous liver metastases is treated with systemic therapy, a combination of capecitabine, oxaliplatin (CAPOX) and bevacizumab.

Scan findings: Mean SUV_{max} (of five lesions) was 7.0 before treatment, 7.0 one week into treatment and 6.8 after three cycles. TLG decreased from 320 before treatment to 230 after one week, and further to 100 after three cycles.

Interpretation: Partial response after three cycles of anti-tumor treatment.

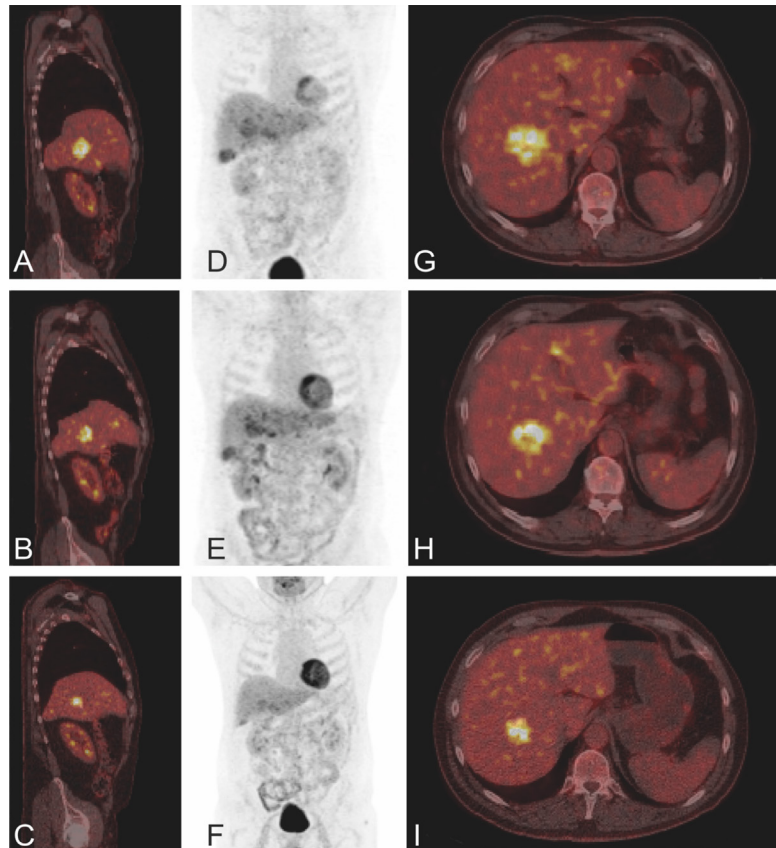


FIGURE 5. Response monitoring of liver metastases. PET/CT (A, B, C, G, H, I) and maximum intensity images (MIP)(D, E, F) before (A, D, G), after one week of therapy (B, E, H) and after 3 cycles (C, F, I).

Teaching points:

- Serial FDG PET/CT measurements can monitor therapy response of liver metastases to combination therapy (chemotherapy and anti-angiogenic treatment).

CLINICAL CASE 6 - RESPONSE MONITORING OF LIVER AND OTHER METASTASES

Clinical details: A 65-year-old male with colon cancer and synchronous liver and lung metastases was treated with neoadjuvant therapy, a combination of CAPOX and bevacizumab.

Scan findings: Mean SUV_{max} of the three liver lesions was 8.4 before treatment, 7.4 after one week and 4.2 after three cycles. TLG of the liver lesions was 950 before treatment, 680 after one week and 95 after three cycles.

Interpretation: Partial response to chemotherapy of the primary tumor, liver metastases and lung metastases.

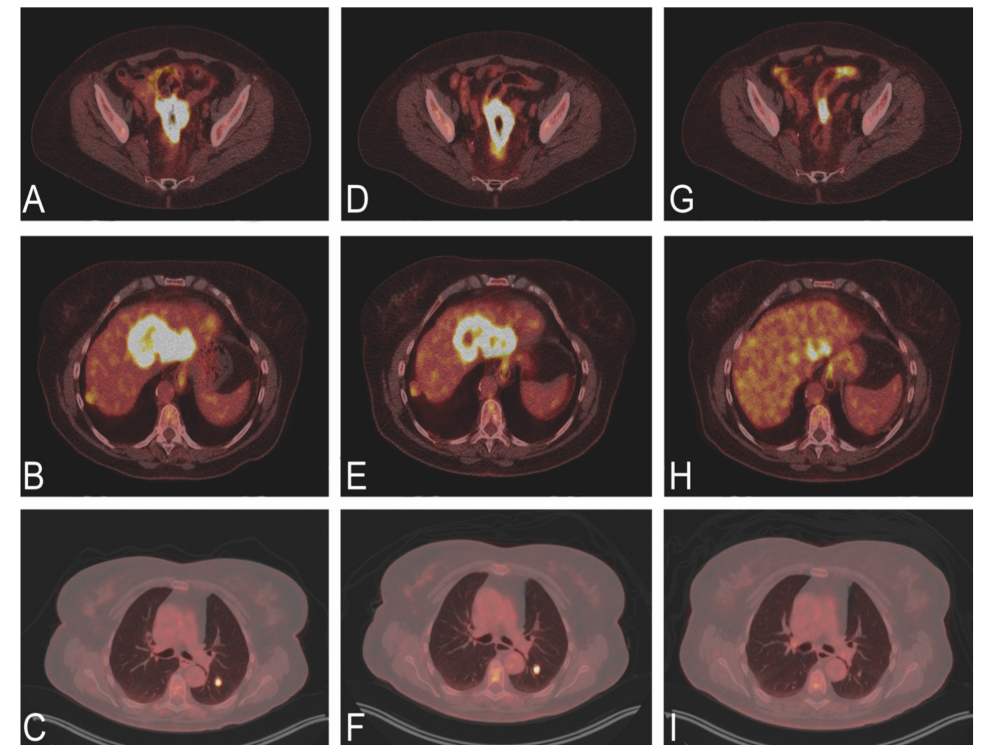


FIGURE 6. Response monitoring of liver metastases. PET/CT images before treatment (A-C), one week into treatment (D-F) and after three cycles (G-I) of respectively the primary tumor, liver metastases and lung metastases.

Teaching points:

- Early response monitoring is feasible using FDG PET/CT.

CLINICAL CASE 7 - RESPONSE MONITORING OF LIVER METASTASES

Clinical details: A 75-year-old male with colon cancer and synchronous liver metastases was treated with a combination of neoadjuvant CAPOX and bevacizumab to increase the chance of resectability of the liver metastases.

Scan findings: As the first three scans were part of research, SUV_{max} and TLG analysis was performed. SUV_{max} was 11 before treatment, 9 after one week of treatment and 7 after three cycles (nine weeks). Total lesion glycolysis decreased from 1200 before start of treatment to 500 after one week of therapy and decreased further to 220 after three cycles.

Interpretation: Partial response of liver lesions after three cycles, as well as after six cycles. Hereafter, the patient underwent metastasectomy. After this, no evidence of residual or recurrent disease was observed during 24 months of follow-up.

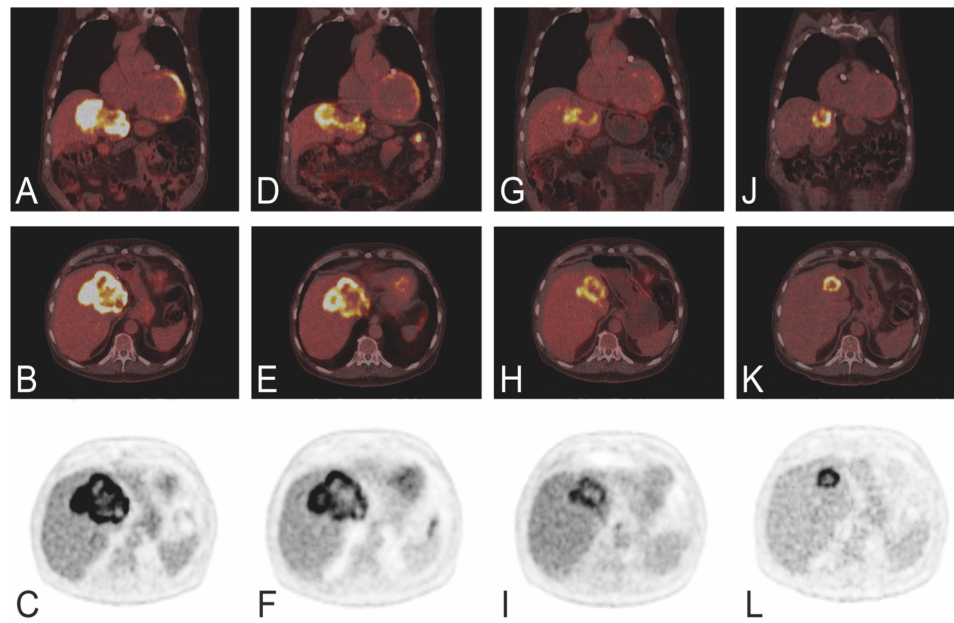


FIGURE 7. Response monitoring of liver metastases. PET/CT (A, B, D, E, G, H, J, K) and PET (C, F, I, L), before treatment (A-C), one week into treatment (D-F), after three cycles (G-I) and after six cycles (J-L).

Teaching point:

- Current response monitoring is performed using the RECIST criteria by evaluating the size of lesions 8-9 weeks after treatment. Metabolic response to anti-tumor treatment can be visualized earlier.

CLINICAL CASE 8 - RESIDUAL DISEASE AFTER LIVER METASTASECTOMY?

Clinical details: A 60-year-old male with rectal cancer and a solitary metachronous liver metastasis for which neoadjuvant short-course radiotherapy was administered and resection was performed. No previous systemic treatment has been given. PET/CT is performed before and four days after surgical metastasectomy.

Scan findings: SUV_{max} prior to resection is 7. After resection, slight diffuse uptake is seen along the edge of the resection cavity.

Interpretation: No evidence of residual disease. Postoperative changes are appreciated at the edge of the resection cavity.

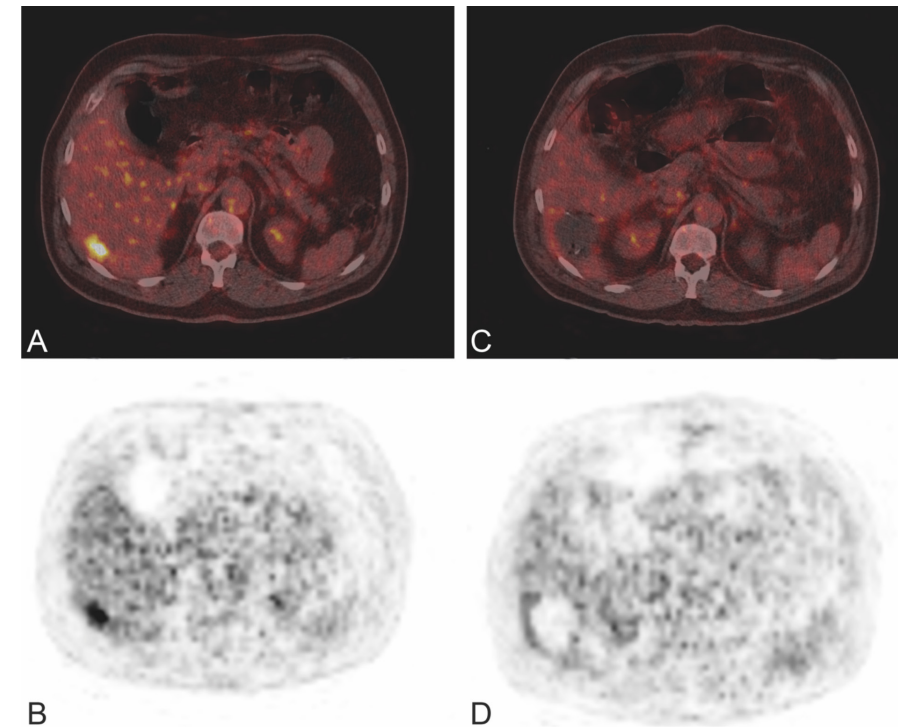


FIGURE 8. Evaluation after liver metastasectomy. PET/CT (A, C) and PET (B, D) images before (A-B) and 4 days after metastasectomy (C-D).

Teaching point:

- Physiologic mild diffuse uptake along the edge of metastasectomy can be seen in the first days to weeks after metastasectomy.

CLINICAL CASE 9 - PALLIATIVE TREATMENT OF LIVER METASTASES OF RECTAL CANCER

Clinical details: A 63-year-old male with rectal cancer in whom two synchronous liver metastases were detected. The patient was treated with palliative chemotherapy consisting of tegafur and uracil, as no curative options were available. CT imaging showed stable disease after 3 cycles according to RECIST.

Scan findings: Mean SUV_{max} of the two liver lesions was 8.0 before treatment, 9.0 after one week (+13%) and 9.4 after three cycles of treatment (+18%). Total lesion glycolysis was 34 before treatment, 46 after one week (+35%) and 40 (+18%) after three cycles.

Interpretation: Stable disease on PET/CT (PERCIST).

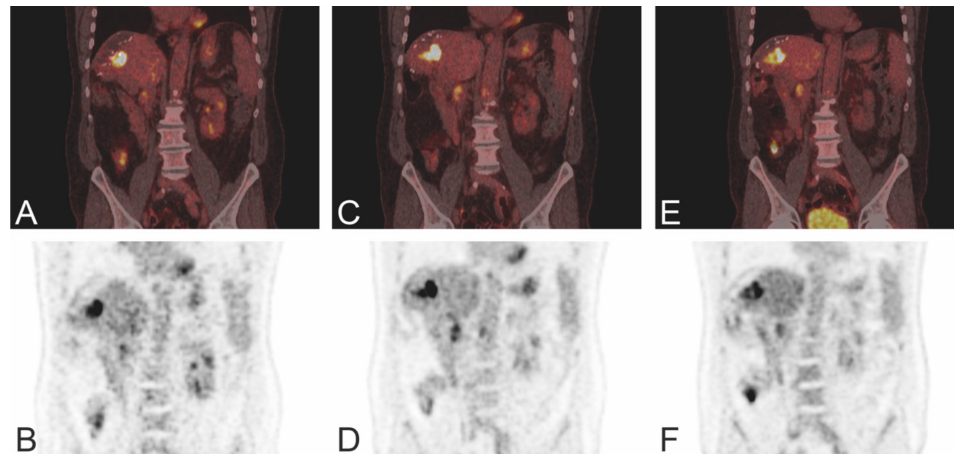


FIGURE 9. Response monitoring palliative rectal cancer. Representative PET/CT (A, C, E) and PET (B, D, F) images before treatment (A, B), one week into treatment (C, D) and after 3 cycles of treatment are depicted (E, F).

Teaching point:

- Fractional changes in tumor glucose metabolism on FDG PET/CT can stratify patients into groups with different survival probabilities⁵.

CLINICAL CASE 10 - RECURRENT DISEASE AFTER LIVER MICROWAVE ABLATION (MWA)

Clinical details: A 75-year-old male with a history of pT3N0M0 sigmoid cancer which was laparoscopically resected. Four years later, CEA was elevated, and a liver metastasis was detected in segment VIII on CT, which was treated with MWA (5 min, 100W). Routine follow up CT imaging 3 months after MWA showed no evidence of residual or recurrent disease. Five months later, CEA is again elevated and a lesion suspicious for recurrent metastasis was observed on FDG PET/CT (Fig. 10D). Subsequent MR imaging (one week later) confirmed a solitary recurrent liver metastasis (Fig. 10C).

Scan findings: A high metabolically active focus is located mediodorsal of the MWA area, cranial in segment VIII. The focus corresponds to the hypodense lesion as seen on CT and MRI.

Interpretation: Images suspicious for local recurrence after MWA of a liver metastasis in segment eight.

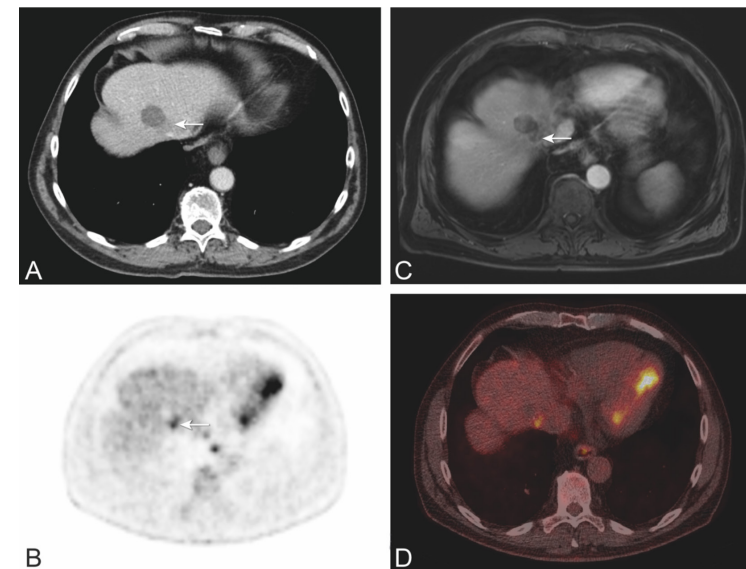


FIGURE 10. Recurrent disease after liver MWA. Images of contrast enhanced CT (A), PET (B), contrast enhanced MRI (C) and PET/CT (D) are depicted.

Teaching points:

- FDG PET/CT is accurate in detecting residual or recurrent disease immediately after local ablative therapy⁶.
- Focal and multifocal uptake is suspicious for recurrent disease already in the first months after local therapy.

CLINICAL CASE 11 - RECURRENT DISEASE AFTER LIVER RFA

Clinical details: A 75-year-old male with cT3N2M1 sigmoid carcinoma with multiple synchronous liver metastases in segment VII and VIII. Induction combination chemotherapy consisting of folinic acid, fluorouracil and oxaliplatin (FOLFOX) was given. Following systemic therapy, the liver lesions decreased in size but were still present. Both the primary tumor and liver metastases were resected or ablated using radiofrequency. Eighteen months later, serum CEA was rising, however, recurrent disease could not be localized on CT of the chest and abdomen.

Scan findings: Status after sigmoid resection, segment resection of segment 8 and RFA in segment 8/5. Focal FDG avidity is seen along the medial edge of the RFA area. No evidence of other metastases.

Interpretation: The FDG avidity in the liver lesion is suspect for a recurrent liver metastasis along the edge of the previous RFA cavity.

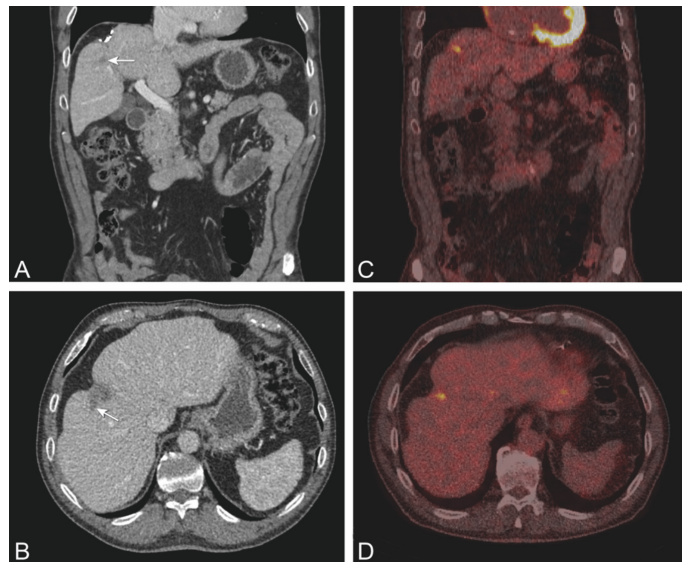


FIGURE 11. Recurrent disease after liver RFA. Images of CT (A, B) and PET/CT (C, D).

Teaching points:

- FDG PET/CT is more accurate during surveillance after RFA compared to contrast enhanced CT and MRI^{7,8}.
- Response evaluation after RFA can be performed by FDG PET/CT, as responding lesions become photopenic immediately following RFA⁹.
- Focal and multifocal uptake is suspicious for recurrent disease following local therapy.

CLINICAL CASE 12 - RECURRENT DISEASE AFTER LIVER RFA

Clinical details: A 60-year-old male with pT1N1M1 colon carcinoma with a synchronous liver metastasis. The colon carcinoma was resected, after which the solitary liver metastasis in segment seven was ablated using radiofrequency (RFA). Eight months later, a recurrent liver lesion is seen along the ablated site in segment VII on FDG PET/CT (Fig. 12D). Subsequent MR imaging confirmed a solitary liver metastasis in segment VII.

Scan findings: High FDG avidity is seen cranially in segment 7/8, corresponding to the lesion as seen on MRI located dorsolateral on the right side adjacent to the RFA cavity. No other FDG accumulation is observed in the liver parenchyma.

Interpretation: FDG uptake highly suspicious for local recurrent disease dorsolateral along the RFA cavity, corresponding to the lesion observed on MRI. No other metastases are detected.

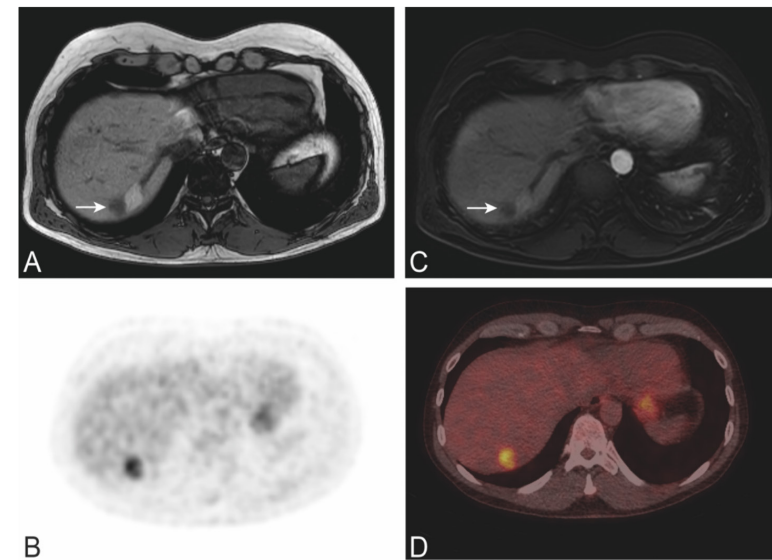


FIGURE 12. Recurrent disease after liver RFA. Images of T1 weighted MRI before contrast (A), PET (B), contrast enhanced MRI (C) and PET/CT (D).

Teaching points:

- FDG PET/CT is more accurate during surveillance after RFA compared to contrast enhanced CT or MRI^{7,8}.
- FDG PET shows promise in identifying very early response after local ablative treatment (within 24 hours post ablation)⁹.
- Focal and multifocal uptake is suspicious for recurrent disease following local therapy.

CLINICAL CASE 13 - PULMONARY METASTASES

Clinical details: An 80-year-old woman underwent laparoscopic sigmoid resection seven years ago for a pT3N0M0 sigmoid carcinoma. Three years after resection, local recurrence and multiple liver and lung metastases were detected and treated in the following years. Three lung metastases were treated with stereotactic radiotherapy. Five months later, CT imaging reveals progression of the known apical consolidation after radiotherapy in the left lower lobe and progression of a lung nodule in the right upper lobe. FDG PET/CT also shows moderate uptake in the progressive area, however uptake may be due to post radiation inflammation. Now, 18 months after stereotactic radiotherapy (STRT), another FDG PET/CT is performed.

Scan findings: Diffuse mild FDG uptake is observed in the area in the right upper lobe after STRT. However, avid FDG uptake is seen in three lung nodules 18 months after STRT. Two of these nodules are in the right upper lobe (one in and the other located dorsally from the radiation area, Fig. 13C-D), and one nodule in the left lower lobe.

Interpretation: Status after stereotactic radiotherapy of two pulmonary metastases. However, three new lung metastases are seen 18 months after STRT. Two in the right lung, 1 in the left. No evidence of other metastases or local recurrence.

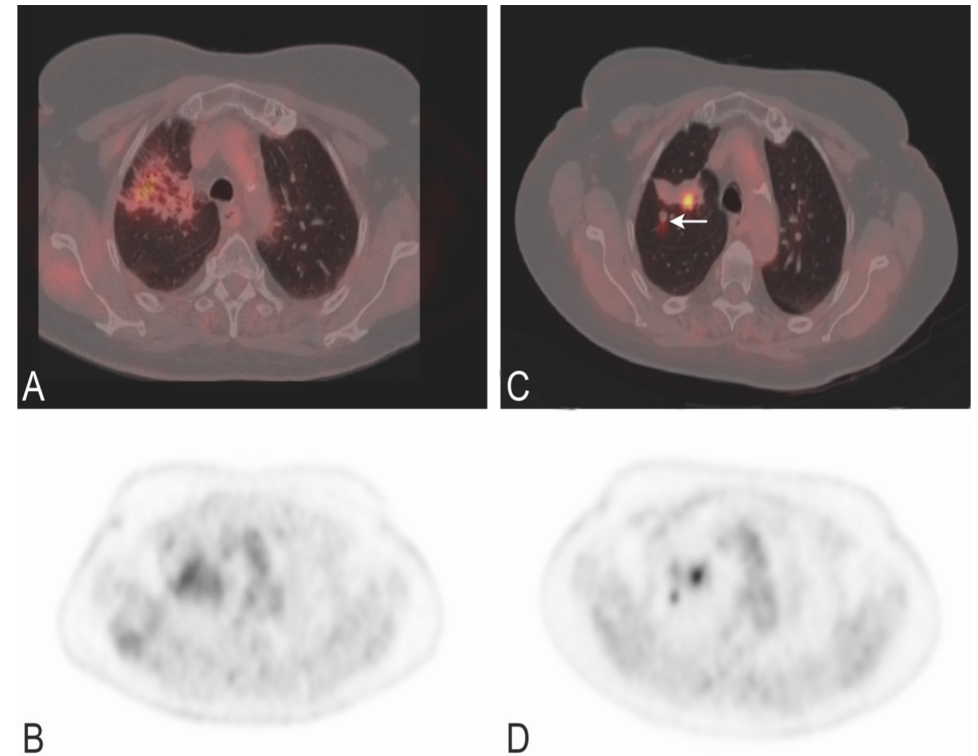


FIGURE 13. Lung metastasis. Images of PET/CT (A, C) and PET (B, D) 11 months after STRT (A, B) compared to 18 months after STRT (C, D). Note a location mismatch between PET and CT imaging is visible in the smaller nodule, as indicated by the arrow due to differences in respiration.

Teaching points:

- As few patients with pulmonary oligometastases from colorectal origin are eligible for local therapy, early detection is crucial.
- The sensitivity and specificity of FDG PET/CT for detecting pulmonary metastases from colorectal cancer are respectively 57.1 and 99.1%¹⁰. This is mainly due to the small size and partial volume effect.
- Although CT has higher sensitivity compared to FDG PET/CT in detecting lung nodules (90 vs. 57-76%), FDG PET/CT provides higher specificity (75-99 vs. 50%)^{10,11}. However, serial CT imaging probably provides high specificity as well, as is seen in common practice. Such approach, however, is not useful when early specific diagnosis is crucial.

CLINICAL CASE 14 - LYMPH NODE METASTASES

Clinical details: A 65-year-old woman with a history of breast cancer, to whom after resection, adjuvant chemo- and radiotherapy was given. Six years later, the patient presents with cT3N2M0 sigmoid carcinoma for which sigmoid resection was performed, followed by adjuvant chemotherapy (three cycles of capecitabine). Ten months later, two liver metastases from the sigmoid carcinoma (segment VI and VIII) were resected. In the same period, two para-aortal lymph nodes were resected. Now, three years after liver metastasectomy, new enlarged lymph nodes are detected. The patient is treated with three cycles of capecitabine.

Scan findings: As compared to the first scan, no significant change in size and metabolic activity of the left para-aortal and mediastinal lymph node metastasis is measured. Note that the hypermetabolic mediastinal lymph node is not enlarged.

Interpretation: Stable disease of both lymph node metastases is seen after 3 cycles.

Teaching points:

- As treatment decisions depend on presence of hepatic and extrahepatic metastases, FDG PET/CT can aid in providing accurate staging, leading to more effective patient management decisions¹².
- FDG PET/CT can alter staging for assessing extrahepatic disease in up to 20% of patients¹².
- FDG PET/CT can identify additional metastatic lymph nodes that are missed on CT imaging.
- Caution is warranted in SUV quantification of lymph nodes because of the possible partial volume effect.

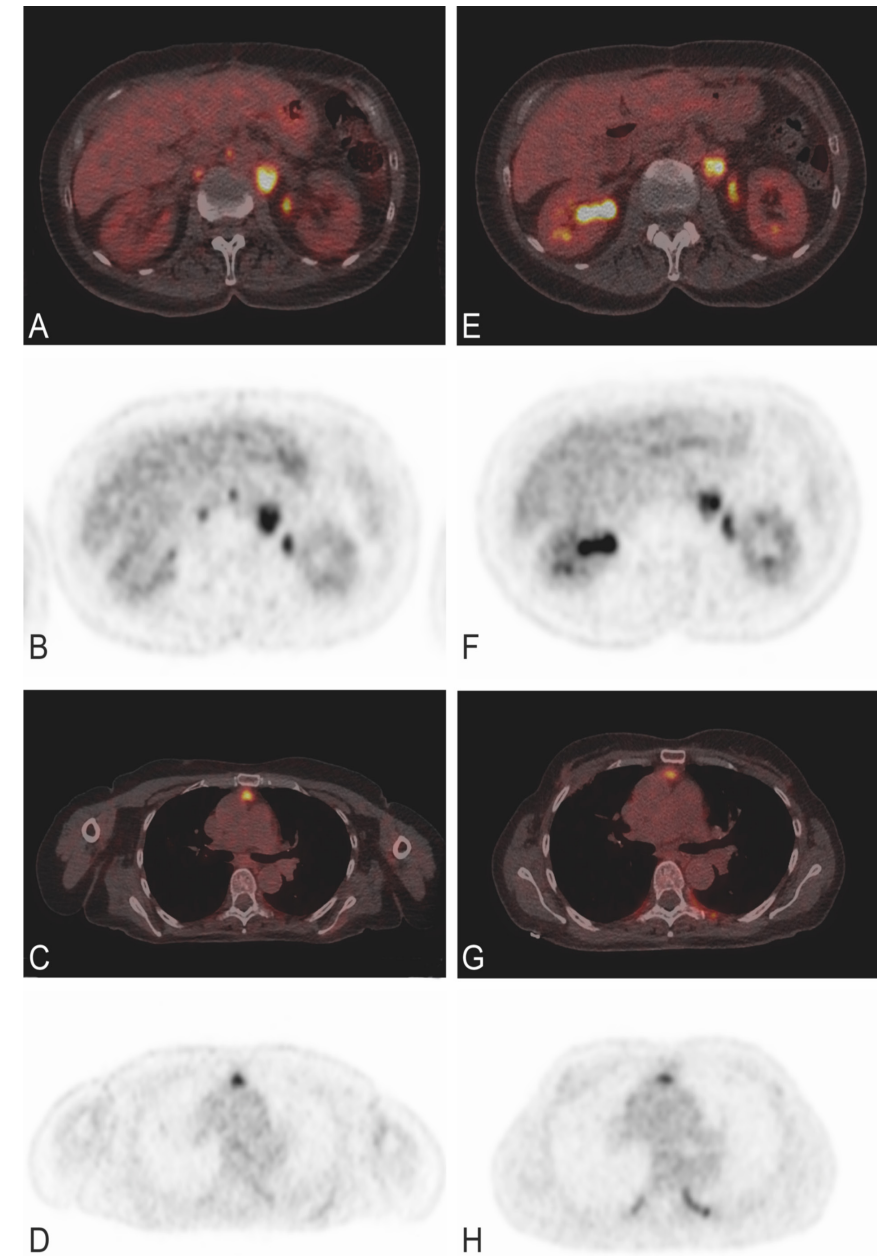


FIGURE 14. Response monitoring lymph node and pulmonary metastases. PET/CT (A, C, E, G) and PET (B, D, F, H) images before (A-D) and after (E-H) three cycles of capecitabine.

CLINICAL CASE 15 - RESPONSE MONITORING TO NEOADJUVANT CHEMORADIO THERAPY

Clinical details: A 60-year-old male with cT3N2M0 locally advanced rectal carcinoma for which neoadjuvant chemoradiation (25x2 Gy and concurrent capecitabine) was given. After neoadjuvant therapy, abdominoperineal resection was performed. The resection specimen showed ypT1N0 rectal adenocarcinoma on pathological examination. Response monitoring was performed using FDG PET/CT.

Scan findings: FDG accumulation in the primary rectal carcinoma decreased during neoadjuvant therapy. SUV_{max} at staging was 27, decreased to 21 two weeks into treatment and to 8.5 eight weeks after neoadjuvant treatment. No enlarged or avid lymph nodes were visible.

Interpretation: Partial response of the primary tumor.

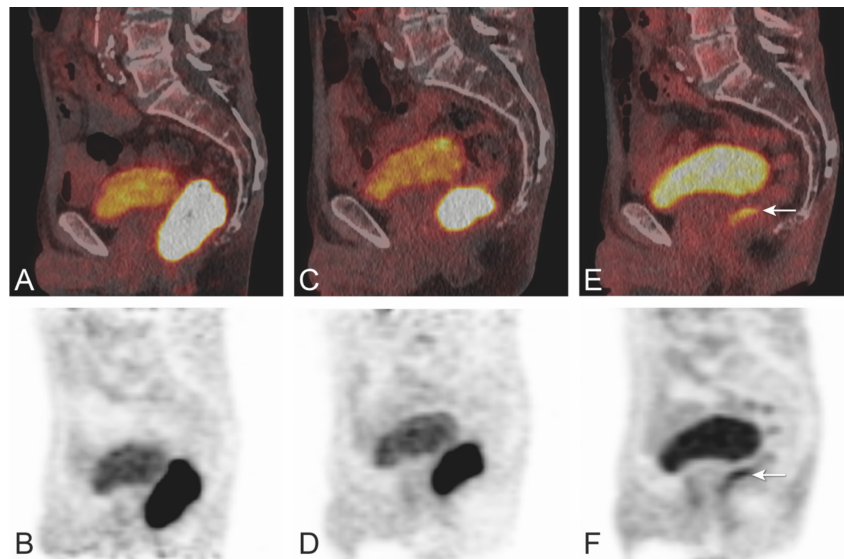


FIGURE 15. Response monitoring locally advanced rectal cancer. Images show PET/CT (A, C, E) and PET (B, D, F) images before (A, B), two weeks into treatment (C, D) and 6-8 weeks after neoadjuvant treatment (E, F).

Teaching points:

- FDG PET/CT can predict (early) tumor response to therapy. However, thresholds derived from large clinical trials are still lacking¹³.
- In the future, by monitoring early tumor response, neoadjuvant treatment can be adjusted and/or futile chemo(radio)therapy can be avoided in non-responding patients.

CLINICAL CASE 16 - MONITORING RESPONSE TO NEOADJUVANT CHEMORADIO THERAPY

Clinical details: A 60-year-old male with cT3N2M0 locally advanced rectal carcinoma for which neoadjuvant chemoradiotherapy (25x2 Gy and concurrent capecitabine) was started, followed by total mesorectal excision (TME) resection. The resection specimen showed ypT3N1 rectal adenocarcinoma. Response monitoring was performed using FDG PET/CT.

Scan findings: SUV_{max} at baseline was 26, it decreased to 12 two weeks into treatment and eight weeks after neoadjuvant treatment SUV_{max} further decreased to five.

Interpretation: A strong metabolic response is observed.

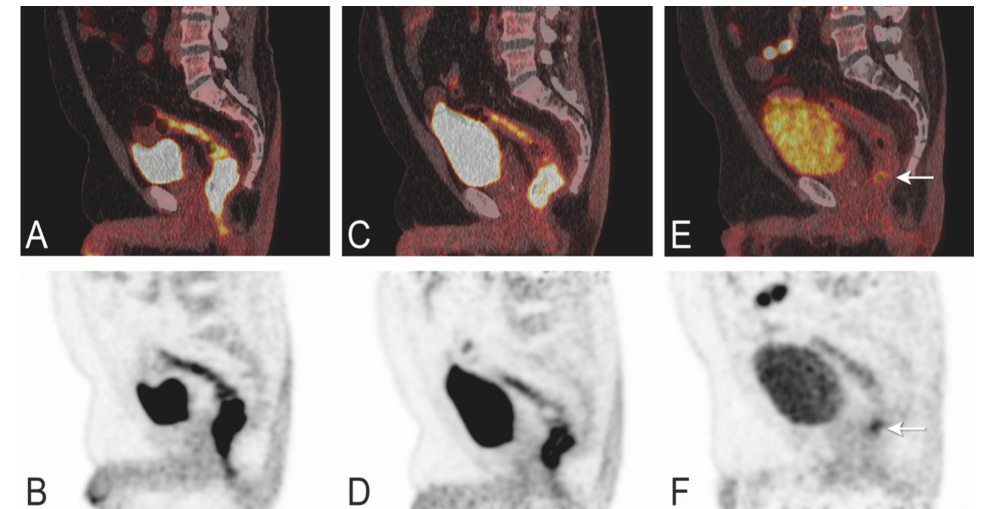


FIGURE 16. Response monitoring rectal cancer. Images show PET/CT (A, C, E) and PET (B, D, F) images before (A, B), two weeks into treatment (C, D) and 6-8 weeks after neoadjuvant treatment (E, F).

Teaching points:

- FDG PET/CT can predict (early) tumor response to therapy. However, thresholds derived from large clinical trials are still lacking¹³.
- In the future, by monitoring early tumor response, neoadjuvant treatment can be adjusted and/or futile chemo(radio)therapy can be avoided in non-responding patients.

CLINICAL CASE 17 - RECURRENT COLORECTAL CANCER

Clinical details: A 60-year-old male with cT3N0M0 proximal rectal cancer for which neoadjuvant chemoradiotherapy was given, followed by TME resection. Nine months later, recurrent rectal cancer was diagnosed, and the patient was treated with one cycle CAPOX followed by re-chemoradiation (15x2Gy in combination with capecitabine) and three additional cycles of CAPOX, followed by resection. Two FDG PET scans were performed, one during the first cycle of CAPOX, the second during the last cycle of CAPOX, 2 months later.

	During first cycle	During third cycle
SUV _{max}	11.6	11.2
Metabolic volume	77.3	67.8

Scan findings: No change in the intense FDG accumulation in the dorsal rectal wall above the anastomosis is seen. A large tumor strand is observed right cranially along the mesorectum.

Interpretation: Unchanged recurrent rectal tumor in the presacral area with strand cranial along the mesorectum. No signs of lymph node metastases. Subsequently, pelvic exenteration was performed. Three months after resection, recurrent disease was diagnosed, and palliative chemotherapy was initiated.

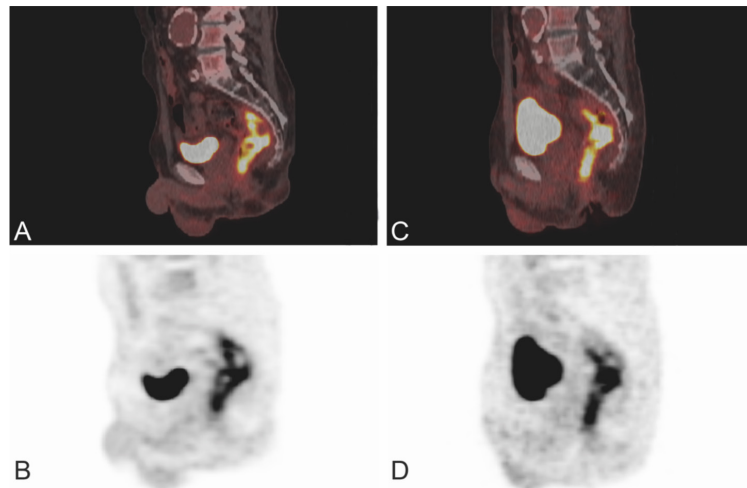


FIGURE 17. Response monitoring recurrent rectal cancer. Representative images of PET/CT (A, C) and PET (B, D) one week into treatment (A, B) and during the third cycle of treatment (C, D).

Teaching point:

- FDG PET/CT might aid in detecting recurrent rectal cancer patients not responding to therapy.

CLINICAL CASE 18 - RECURRENT COLORECTAL CANCER

Clinical details: A 65-year-old male with pT3N2M0 sigmoid tumor who underwent sigmoid resection. The patient received eight cycles of adjuvant CAPOX, oxaliplatin was terminated after the fourth cycle due to toxicity. Two months after the last cycle, serum CEA was elevated.

Scan findings: High FDG uptake is seen at the anastomosis site (Fig. 18E). Also, high uptake is observed in a possible peritoneal metastasis more proximal along the sigmoid (Fig. 18F). High uptake is appreciated in a left parailiacal lymph node (dotted white arrow, Fig. 18A). FDG avid foci are seen in the pararenal fascia (black arrow Fig. 18A) and peritoneum (white arrows Fig. 18A).

Interpretation: Images are suspicious for recurrent disease at the anastomosis site with metastases to the peritoneum, lymph nodes, omentum and right pararenal fascia.

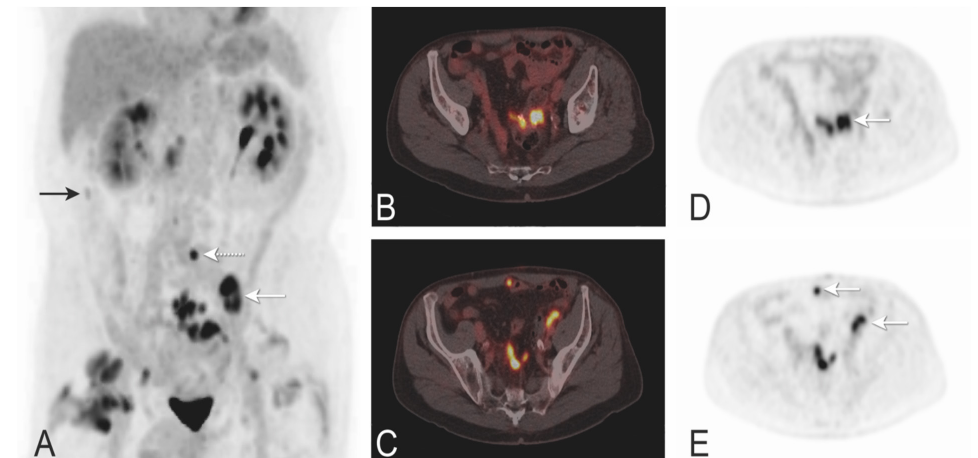


FIGURE 18. Local recurrence sigmoid tumor. Images of the maximum intensity projection (MIP, A), CT (B), PET/CT (C, D) and PET (E, F) are depicted. The recurrent tumor is indicated by the arrow in D, whereas the peritoneal metastases are indicated by the arrows in E.

Teaching points:

- Detection of local recurrence on CT and MRI can be challenging due to altered anatomy after oncologic resection.
- FDG PET/CT has a high sensitivity (84-100%), specificity (80-100%) and accuracy (74-94%) in detecting local recurrence of colorectal cancer¹⁴. Therefore, PET/CT has been adopted into colorectal guidelines for detection of local recurrence.

CLINICAL CASE 19 - RESPONSE MONITORING OF NEOADJUVANT TREATMENT OF LOCAL RECURRENT RECTAL CANCER

Clinical details: A 70-year-old male with pT3N2M1 rectal carcinoma and a synchronous solitary liver metastasis. The liver metastasis was treated with 3 neoadjuvant courses of CAPOX, after which RFA was performed. Following this, abdominoperineal resection of the primary rectal cancer was performed. Two years after resection, local recurrent disease was detected in a lymph node and was treated with 4 courses of induction chemotherapy (FOLFIRI) followed by chemoradiotherapy (capecitabine in combination with 15 x 2 Gy). FDG PET/CT was performed to monitor response.

Scan findings: Partial metabolic response was visualized on the interim scan after neoadjuvant chemotherapy (2 months later). A complete metabolic response was observed right after neoadjuvant chemoradiotherapy (5 months later).

Interpretation: A complete metabolic response is seen on the last scan, as was confirmed by the resection specimen showing a pathological complete response. Following neoadjuvant treatment, debulking surgery and intraoperative radiotherapy was performed. The resection specimen showed a pathological complete response to neoadjuvant therapy.

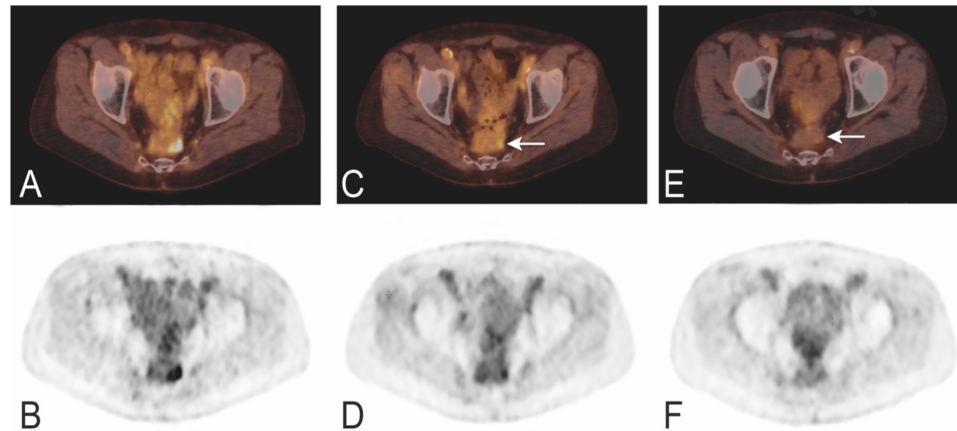


FIGURE 19. Response monitoring neoadjuvant treatment local recurrence. Representative PET/CT and PET images before treatment (A, B), after neoadjuvant chemotherapy (C, D) and after neoadjuvant chemoradiation (E, F) are depicted.

Teaching points:

- FDG PET/CT can provide additional information on the decision to give consolidation therapy between neoadjuvant therapy and surgery.

CLINICAL CASE 20 - RESPONSE MONITORING OF NEOADJUVANT TREATMENT OF LOCAL RECURRENT RECTAL CANCER

Clinical details: A 60-year-old male with locally advanced rectal carcinoma was treated with neoadjuvant chemoradiotherapy, followed by TME resection. Eighteen months later, local recurrent disease was detected and treated with induction chemotherapy (1 course CAPOX, then switched to 3 courses FOLFIRI due to toxicity) followed by chemoradiotherapy (capecitabine in combination with 15 x 2 Gy). Response monitoring was performed by FDG PET/CT.

Scan findings: No changes in FDG avidity were observed after neoadjuvant chemotherapy or after neoadjuvant chemoradiotherapy.

Interpretation: Stable disease was observed after neoadjuvant chemotherapy (2 months later) and immediately after neoadjuvant chemoradiotherapy (4 months later). Following treatment, surgical resection was planned.

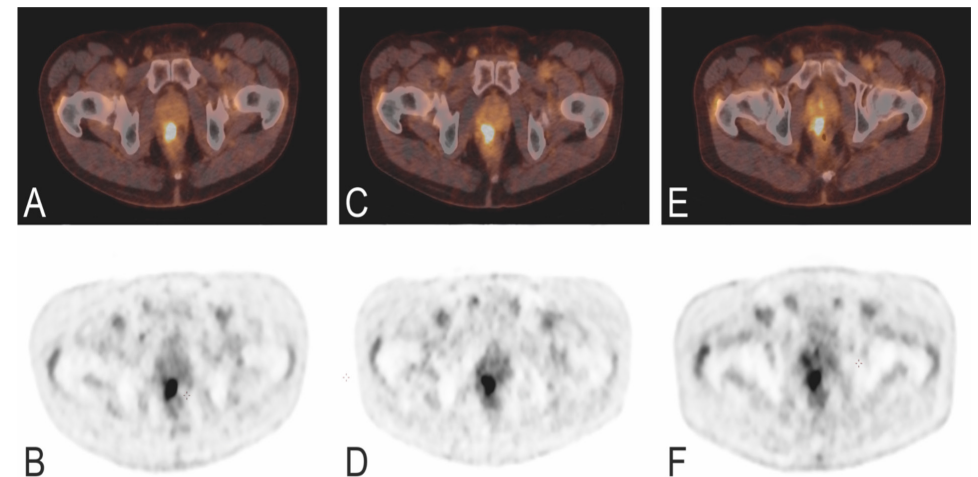


FIGURE 20. Response monitoring neoadjuvant treatment local recurrence. Representative PET/CT and PET images before treatment (A, B), after neoadjuvant chemotherapy (C, D) and after neoadjuvant chemoradiation (E, F) are depicted.

Teaching point:

- FDG PET/CT can provide additional information on the decision to give consolidation therapy between neoadjuvant therapy and surgery.

REFERENCES

1. Bray F, Ferlay J, Soerjomataram I, et al. Global cancer statistics 2018: GLOBOCAN estimates of incidence and mortality worldwide for 36 cancers in 185 countries. *CA Cancer J Clin*. 2018;68:394–424.
2. Sivesgaard K, Larsen LP, Sørensen M, et al. Diagnostic accuracy of CE-CT, MRI and FDG PET/CT for detecting colorectal cancer liver metastases in patients considered eligible for hepatic resection and/or local ablation. *Eur Radiol*. 2018;28:4735–4747.
3. Grassetto G, Fornasiero A, Bonciarelli G, et al. Additional value of FDG-PET/CT in management of “solitary” liver metastases: preliminary results of a prospective multicenter study. *Mol Imaging Biol MIB Off Publ Acad Mol Imaging*. 2010;12:139–144.
4. Heijmen L, ter Voert EEGW, Oyen WJG, et al. Multimodality Imaging to Predict Response to Systemic Treatment in Patients with Advanced Colorectal Cancer. *PLoS ONE*;10. Epub ahead of print April 1, 2015. DOI: 10.1371/journal.pone.0120823.
5. de Geus-Oei LF, van Laarhoven HWM, Visser EP, et al. Chemotherapy response evaluation with FDG–PET in patients with colorectal cancer. *Ann Oncol*. 2008;19:348–352.
6. Romanato J, Menezes MR, Santos A de O, et al. 18F-FDG PET/CT performed immediately after percutaneous ablation to evaluate outcomes of the procedure: preliminary results. *Radiol Bras*. 2019;52:24–32.
7. Veit P, Antoch G, Stergar H, et al. Detection of residual tumor after radiofrequency ablation of liver metastasis with dual-modality PET/CT: initial results. *Eur Radiol*. 2006;16:80–87.
8. Aarntzen EHJG, Heijmen L, Oyen WJG. 18F-FDG PET/CT in Local Ablative Therapies: A Systematic Review. *J Nucl Med*. 2018;59:551–556.
9. Liu Z-Y, Chang Z-H, Lu Z-M, et al. Early PET/CT after radiofrequency ablation in colorectal cancer liver metastases: is it useful? *Chin Med J (Engl)*. 2010;123:1690–1694.
10. Bamba Y, Itabashi M, Kameoka S. Value of PET/CT imaging for diagnosing pulmonary metastasis of colorectal cancer. *Hepatogastroenterology*. 2011;58:1972–1974.
11. Lopez-Lopez V, Robles R, Brusadin R, et al. Role of 18F-FDG PET/CT vs CT-scan in patients with pulmonary metastases previously operated on for colorectal liver metastases. *Br J Radiol*. 2017;91:20170216.
12. Lake E, Wadhvani S, Subar D, et al. The influence of FDG PET-CT on the detection of extrahepatic disease in patients being considered for resection of colorectal liver metastasis. *Ann R Coll Surg Engl*. 2014;96:211–215.
13. Maffione AM, Marzola MC, Capirci C, et al. Value of (18)F-FDG PET for Predicting Response to Neoadjuvant Therapy in Rectal Cancer: Systematic Review and Meta-Analysis. *AJR Am J Roentgenol*. 2015;204:1261–1268.
14. de Geus-Oei L-F, Vriens D, van Laarhoven HWM, et al. Monitoring and predicting response to therapy with 18F-FDG PET in colorectal cancer: a systematic review. *J Nucl Med Off Publ Soc Nucl Med*. 2009;50 Suppl 1:43S-54S.

Baseline and early digital [¹⁸F]FDG PET/CT and multiparametric MRI contain promising features to predict response to neoadjuvant therapy in locally advanced rectal cancer patients: a pilot study.

F.A. Vuijk, S. Feshtali Shahbazi, W.A. Noortman, F.H.P. van Velden, P. Dibbets-Schneider, A.W.K.S. Marinelli, P.A. Neijenhuis, R. Schmitz, E. Ghariq, L.A. Velema, F.P. Peters, F. Smit, K.C.M.J. Peeters, J.S.D. Temmink, A.S.L.P. Crobach, H. Putter, A.L. Vahrmeijer^a, D.E. Hilling and L.F. de Geus-Oei.

Nuclear Medicine Communications 2023



ABSTRACT

In this pilot study we investigated the feasibility of response prediction using digital [¹⁸F]FDG PET/CT and multiparametric MRI before, during and after neoadjuvant chemoradiation therapy in locally advanced rectal cancer patients, and aimed to select the most promising imaging modalities and timepoints for further investigation in a larger trial. Rectal cancer patients scheduled to undergo neoadjuvant chemoradiation therapy were prospectively included in this trial, and underwent multiparametric MRI and [¹⁸F]FDG PET/CT before-, 2 weeks into- and 6-8 weeks after chemoradiation therapy. Two groups were created based on pathological tumor regression grade, i.e. good responders (TRG1-2) and poor responders (TRG3-5). Using binary logistic regression analysis with a cut-off value of $p \leq 0.2$, promising predictive features for response were selected. Nineteen patients were included. Of these, 5 were good responders and 14 poor responders. Patient characteristics of these groups were similar at baseline. Fifty-seven features were extracted, of which 13 were found to be promising predictors of response. Baseline (T2: volume, DWI: ADC mean, DWI: difference entropy), early response (T2: volume change, DWI: ADC mean change) and end-of-treatment pre-surgical evaluation MRI (T2: grey level non-uniformity, DWI: inverse difference normalized, DWI: grey level non-uniformity normalized) as well as baseline (MTV, TLG) and early response PET/CT (ΔSUV_{max} , ΔSUL_{peak}) were promising features. Both multiparametric MRI and [¹⁸F]FDG PET/CT contain promising imaging features to predict response to nCRT in LARC patients. A future larger trial should investigate baseline, early response and end-of-treatment pre-surgical evaluation MRI and baseline and early response PET/CT.

INTRODUCTION

Patients diagnosed with locally advanced rectal cancer (LARC) are currently treated with neoadjuvant chemoradiotherapy (nCRT), prior to surgical resection. The goal of nCRT is to downsize and downstage the rectal cancer, thereby improving the rate of complete resections and lowering the risk of local recurrence¹. The majority of patients has a partial tumor response after nCRT¹, while in 15-20% this even results in a pathological complete response (pCR) of all tumor tissue^{1,2}. Most recently, results from the RAPIDO trial demonstrate even higher rates of pCR (28%) after neoadjuvant short course radiotherapy followed by chemotherapy³. Unfortunately, not all patients respond well to nCRT, but the exact number of non-responders is uncertain⁴.

According to current guidelines, treatment stratification and response assessment is performed using magnetic resonance imaging (MRI) and in selected cases, rectoscopy⁵. MRI features include the TNM stage, extramural vascular invasion (EMVI) and tumor distance to the mesorectal fascia⁶. Unfortunately, current imaging modalities are unable to predict response to nCRT accurately. In recent years, the Watch-and-Wait strategy has been implemented for patients with a clinical complete response (cCR) after neoadjuvant therapy, with excellent long-term outcome^{1,7}. By means of improved stratification before or early after onset of nCRT, precise selection of patients might be possible. In patients predicted to respond well, the (watchful) waiting period before surgery could be prolonged, possibly increasing the rate of cCR. Accurate identification of cCR patients can prevent futile surgery and its associated morbidity and mortality⁸. In patients with a predicted poor response, unbeneficial continuation of nCRT, therapy related toxicity and unwanted delay in initiation of a potentially effective treatment could be avoided.

Currently, 2-[¹⁸F]fluoro-2-deoxy-D-glucose ([¹⁸F]FDG) positron emission tomography combined with computed tomography (PET/CT) is advised in the national guideline for the detection of recurrence of rectal cancer in case of increased carcinoembryonic antigen (CEA) levels⁹. Many MRI and [¹⁸F]FDG PET/CT features have been investigated separately to predict response to nCRT before or early after onset of nCRT¹⁰⁻²¹. The combination of both modalities could possibly have complimentary value to predict response. Available data in the literature are insufficient to evaluate this approach, and no studies have investigated the application of digital PET/CT in this field^{13,16,19}. Owing to its increased energy resolution and time-of-flight performance, digital PET/CT has the potential to improve quantification of small or heterogeneous tumors and thereby provide more accurate metabolic information on tumor response, and might (in combination with multiparametric MRI) facilitate improved response prediction to nCRT.

In this pilot study we investigate the feasibility of response prediction using digital [¹⁸F]

FDG PET/CT and multiparametric MRI before, during and after nCRT in LARC patients, and aim to determine the most promising imaging modalities and timepoints for further investigation.

MATERIALS AND METHODS

Patient population

A multicenter, non-randomized prospective study was performed in patients admitted to the Leiden University Medical Center (LUMC, n=8), Haaglanden Medical Center (n=6), Alrijne Hospital Leiderdorp (n=4) and Groene Hart Hospital (n=1), diagnosed with (biopsy proven) LARC and treated according to national guidelines. Eligible patients were selected at multidisciplinary meetings, and asked for participation during their outpatient clinic visit. Treatment consisted of nCRT (25x2 Gy combined with 825 mg/m² bid capecitabine 5 days per week), followed by reevaluation after 6-8 weeks. Surgery followed within 4-6 weeks after reevaluation. In case of a near complete response, reevaluation was repeated after 6-8 weeks. In case of cCR, follow up was initiated according to the Watch-and-Wait protocol⁷. The study was conducted in concordance with the Declaration of Helsinki, and was approved by the Leiden-Den Haag-Delft medical ethics review board and the local boards of participating centers. All subjects provided written informed consent. The study was registered in the Netherlands Trial Register (identification number NL-756). Including standard of care imaging (rectoscopy, MRI scan of abdomen and CT scan of the chest and abdomen), all patients underwent [¹⁸F]FDG PET/CT and multiparametric MRI before nCRT, 10-14 days after nCRT onset (early response evaluation), and 6-8 weeks after the last treatment (end-of-treatment pre-surgical evaluation).

Data acquisition and image reconstruction

All digital [¹⁸F]FDG PET/CT scans of the lower abdomen were acquired on the same scanner, a Vereos PET/CT (Philips Healthcare, Best, the Netherlands). All acquisitions and reconstructions were in accordance with EANM guidelines for tumor PET imaging version 2.0²². Prior to PET/CT scanning, patients fasted for 6 hours and were prehydrated using 1 L of water. [¹⁸F]FDG was dosed using the quadratic formula: $379 \text{ (MBq}\cdot\text{min}\cdot\text{bed}^{-1}\cdot\text{kg}^{-2}) \times (\text{patient weight (kg)/75})^2 / \text{emission acquisition duration per bed position (min}\cdot\text{bed}^{-1})$ with a factor of $379 \text{ MBq}\cdot\text{min}\cdot\text{bed}^{-1}\cdot\text{kg}^{-2}$. Patients received 20 mg intravenous furosemide 15 min post injection. Patients underwent a low-dose CT scan for attenuation correction 60 (55-65) min post injection (120 kV, 35 mA_{eff}), followed by a PET scan of 5 minutes per bed position. Reconstructed PET images had a voxel size 4x4x4 mm. Multiparametric MRI of the lower abdomen was made on various systems, and included T2- and diffusion weighted imaging (DWI) sequences. Patients underwent bowel preparation using a 5 mL Microlax® enema three hours before imaging (Johnson and Johnson, New Brunswick,

New Jersey, United States). Further details are described in **Supplemental Table 1**.

Quantitative image analysis

MRI assessment was performed by a board-certified abdominal radiologist (S.F.S., 11 years of experience), using Sectra IDS7 software (version 21.2; Sectra AB, Linköping, Sweden). Apparent diffusion coefficient (ADC) values were calculated from the DWI image. Volumes of interest (VOIs) were drawn manually (F.V. under supervision of S.F.S.) to include the primary tumor on the DWI and T2 maps. Various quantitative features were extracted using 3DSlicer (version 4.11)²³ and PyRadiomics (version 3.0) that was running in Python (version 3.7; Python Software Foundation, Wilmington, Delaware)²⁴. First, following the methodology of Schurink *et al.*¹⁹, the following features were extracted from the VOIs: T2 mesh volume, T2 entropy, DWI mesh volume, mean ADC, ADC entropy, and their respective response indices (RI). Second, to allow full comparison to the results from Schurink *et al.*^{19,20} and following recent promising results from Delli Pizzi *et al.*²⁵, 105 radiomic features were extracted from the T2 baseline images for additional radiomic analysis: shape (14), first order (18), grey level cooccurrence matrix (22), grey level run length matrix (16), grey level size zone matrix (16), grey level dependence matrix (14) and neighboring grey tone difference matrix (5) features. Images were interpolated to isotropic voxels of 2.00x2.00x2.00 mm³ using B-spline interpolation, with grids aligned by the input origin and only covering the VOI. Both T2 and DWI images were normalized to a mean of 300 and a standard deviation of 100, allowing comparison of the relative gray values between patients²⁶. Features were extracted using a fixed bin size, which was determined in such a way that most VOIs contained between 30-130 bins. This resulted in a bin size of 5 and 15 for T2 and DWI images, respectively.

PET/CT assessment was performed by a board-certified nuclear medicine physician (L.G., 25 years of experience), using Sectra IDS7 software (version 21.2; Sectra AB, Linköping, Sweden). VOIs were automatically delineated with an isocontour threshold of 50% of the maximal standardized uptake value (SUV_{max}) using IntelliSpace Portal (version 9.0; Koninklijke Philips N.V., Amsterdam, the Netherlands). The following features were included in the analysis with their corresponding RI based on the following articles. Joye *et al.* pooled data from 25 studies investigating [¹⁸F]FDG PET/CT and found the following features to be promising predictors for response¹⁷: the SUV_{max} post therapy, RI of the SUV_{max}, the metabolic tumor volume (MTV, obtained using a SUL_{peak} threshold of 50%) and total lesion glycolysis (TLG, SUV_{mean} x MTV). All features were body weighted, except SUL_{peak} which was weighted using the lean body mass following the methodology described in PERCIST 1.0 and by O *et al.*²⁷. They advise the use of SUL_{peak} as exploratory data when the liver is not present in all scans. No radiomic feature analysis was performed on data from [¹⁸F]FDG PET/CT, as this has not been described in literature before.

Pathology

Pathological assessment of the resection specimen was performed according to the Dutch national guidelines⁹. In addition to this, the extent of tumor regression was evaluated according to Mandard's Tumor Regression Grade (TRG) by the local board certified pathologist²⁸. Mandard's TRG classifies response to given therapy in 5 classes based on the amount of vital tumor cells and extent of therapy induced fibrosis. When classified TRG 1, no residual tumor cells were seen, and the patient is considered to have a pathologic complete response (pCR). A regrowth free survival time of >6 months was considered a surrogate endpoint for TRG1 in patients with a cCR in Watch-and-Wait follow up.

Statistical analysis

Statistical analysis was performed using SPSS (version 25; IBM SPSS, Inc., Chicago, USA) and R (version 3.6.0; R Foundation for Statistical Computing, Vienna, Austria). For statistical analysis, patients were divided into two groups based on the pathological TRG or regrowth free follow up in case of Watch-and-Wait: good responders (TRG1-2) and poor responders (TRG 3-5). Descriptive data were displayed as mean \pm standard deviation or median (interquartile range), depending on the distribution of data. Non-parametric data were compared using the Mann Whitney U test, whereas parametric data were compared using a T-test. Results were considered significant when $p < 0.05$. Promising imaging features were selected using binary logistic regression, after dividing through their respective standard deviation. Due to the small sample size and large amount of tested features, MRI and PET/CT features were considered promising when a p -value ≤ 0.2 was reached.

Unsupervised radiomic feature selection using redundancy filtering and factor analysis was performed using FMradio (Factor Modeling for Radiomics Data, package version 1.1.1; Amsterdam UMC, Amsterdam, the Netherlands), developed for R (version 3.6.0; R Foundation for Statistical Computing, Vienna, Austria)²⁹. The large feature dimensionality compared to the small sample size might result in overfitting and deteriorates the generalizability of the radiomic model. Therefore, one feature was selected for every ten subjects³⁰. Features were scaled (centered around 0, variance of 1) to avoid that features with the largest value would dominate the analysis. Redundancy filtering on Pearson correlation matrix was performed with a threshold of $\tau = 0.95$ and from each group one feature was retained. Factor analysis of the redundancy filtered correlation matrix was performed and two factors (19 patients) were selected per sequence and time point. The sampling adequacy of the model was determined by the Kaiser-Meier-Olkin (KMO) measure, which had to be between 0.9 and 1.0. The features with the highest loading on the factors were selected.

RESULTS

Nineteen patients were included in the period between July 2018 and March 2020. All patients completed chemoradiotherapy, and all but one underwent surgery after an average of 14.1 ± 6.6 weeks (one cCR patient in Watch-and-Wait). All but one patient completed all 6 imaging studies: in one patient the final [¹⁸F]FDG PET/CT was not performed due to logistical problems. Sixteen men and three women were included in this study with a median age of 63.1 (56.3-67.0) years old. The median follow up time was 11.6 (9.0-17.1) months. No recurrent disease was found. One patient had a cCR without regrowth during follow up, four patients had a pTRG1, 9 pTRG3, 4 pTRG4 and 1 pTRG5. Based on the pTRG, 5 patients (26.3%) were good responders, 14 (73.7%) were poor responders. There were no significant differences at baseline between groups regarding age, sex, cT stage, cN stage, EMVI, and tumor differentiation, as summarized in **Table 1**.

TABLE 1. Patient and tumor characteristics at baseline. Table shows difference between the good and poor response group at baseline with corresponding p -value.

		Good response (n=5)	Poor response (n=14)	p-value
Age (years)	Mean \pm SD	63.6 \pm 11.08	62.9 \pm 6.12	0.273
Gender	Male	4	12	0.770
	Female	1	2	
cT	2	1	0	0.363
	3	3	10	
	4	1	4	
cN	0	1	2	1.00
	1	0	1	
	2	4	11	
EMVI	Yes	0	3	0.565
	No	5	11	
	Missing	0	0	
Differentiation (biopsy)	Well/moderate	3	13	0.071
	Poor	1	0	
	Missing	1	1	

Abbreviations: SD, standard deviation; cT, clinical tumor stage on routine staging MRI; cN, clinical nodal stage on routine staging MRI; EMVI, extramural vascular invasion; IQR, interquartile range. * Significant difference between groups ($p < 0.05$).

Quantitative features

A total of 57 quantitative features were extracted. Redundancy filtering and factor analysis of the radiomic feature sets was performed and KMOs were excellent (> 0.96). The features corresponding best with the two factors per sequence and timepoint were included in the analysis.

Using binary logistic regression analysis with predefined cut off value of $p \leq 0.2$, 13 features were found to be promising predictors of response. At baseline imaging, 3 MRI and 2 PET/CT features were found to be promising. At early response evaluation, no promising features were found. However, 2 MRI and 2 PET/CT early response evaluation to baseline response index features were found to be promising. At end-of-treatment pre-surgical evaluation, 3 MRI and 1 PET/CT feature were found to be promising, but no response index features were promising.

These results are shown in more detail in the forrest plot in **Figure 1**, which displays all features with their respective odds ratio and confidence interval. It shows numerous features to have preferable odds ratios. However, only 13 have a $p \leq 0.2$. Detailed results from binary logistic regression analysis are displayed in **Table 2**. **Figure 2 and 3** present examples of a good and poor responder on sequential multimodality imaging.

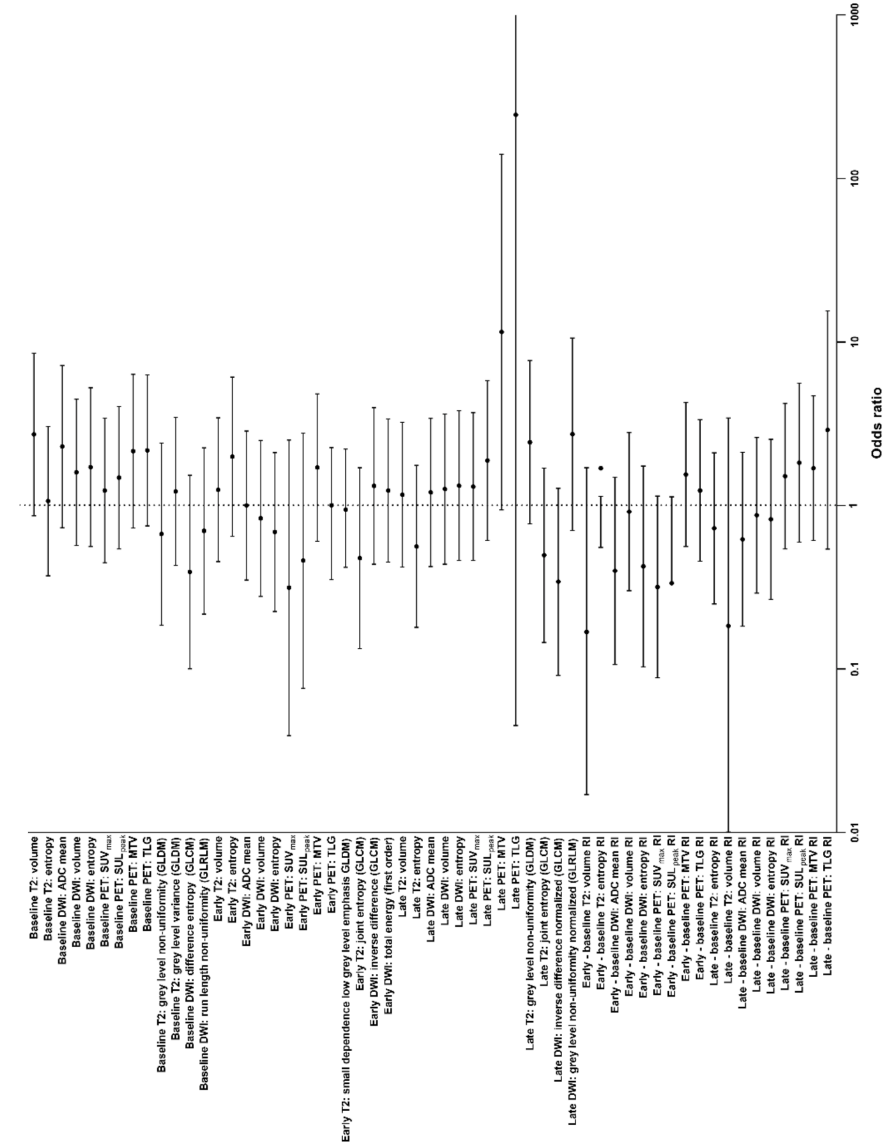


FIGURE 1. Forrest plot of investigated features. Figure shows odds ratio for TRG1-2 with 95% confidence intervals from binary logistical regression analyses on logarithmic scale (x-axis). Abbreviations: SUV_{max}: maximum standardized uptake value; SUV_{peak}: peak standardized uptake value corrected for lean body mass; MTV: metabolic tumor volume; TLG, total lesion glycolysis; T2 volume, tumor volume on T2 series; T2 entropy, tumor entropy on T2 series; DWI volume, tumor volume on diffusion weighted imaging series; ADC mean, mean apparent diffusion coefficient; DWI entropy, tumor entropy on diffusion weighted imaging series; GLCM: grey level cooccurrence matrix, GLDM: grey level dependence matrix, GLRLM: grey level run length matrix, RI, response index (change over time).

TABLE 2. Binary logistical regression analysis of MRI and PET/CT features for prediction of response.

Table shows regression coefficient, odds ratios with confidence intervals and p-values. Abbreviations: SUV_{max}, maximum standardized uptake value; SUL_{peak}, peak standardized uptake value corrected for lean body mass; MTV, metabolic tumor volume; TLG, total lesion glycolysis; T2 volume, tumor volume on T2 series; T2 entropy, tumor entropy on T2 series; DWI volume, tumor volume on diffusion weighted imaging series; ADC mean, mean apparent diffusion coefficient; DWI entropy, tumor entropy on diffusion weighted imaging series; GLCM: grey level cooccurrence matrix, GLDM: grey level dependence matrix, GLRLM: grey level run length matrix, RI, response index (change over time).

Feature	Regression coefficient	Odds ratio	Standard error	95% confidence interval		P value
				Lower limit	Upper limit	
Baseline T2: tumor volume	0.999	2.716	0.584	0.864	8.537	0.087
Baseline T2: entropy	0.06	1.062	0.536	0.371	3.037	0.911
Baseline DWI: mean ADC	0.827	2.287	0.583	0.730	7.168	0.156
Baseline DWI: tumor volume	0.464	1.591	0.525	0.568	4.456	0.377
Baseline DWI: entropy	0.537	1.711	0.570	0.559	5.231	0.347
Baseline T2: grey level non-uniformity (GLDM)	-0.405	0.667	0.655	0.185	2.408	0.536
Baseline T2: grey level variance (GLDM)	0.195	1.216	0.531	0.429	3.445	0.713
Baseline DWI: difference entropy (GLCM)	-0.940	0.391	0.695	0.100	1.527	0.177
Baseline DWI: run length non-uniformity (GLRLM)	-0.360	0.697	0.598	0.216	2.250	0.546
Baseline PET: SUV _{max}	0.210	1.233	0.520	0.445	3.418	0.687
Baseline PET: SUL _{peak}	0.388	1.475	0.511	0.541	4.016	0.447
Baseline PET: MTV	0.764	2.147	0.552	0.728	6.337	0.166
Baseline PET: TLG	0.773	2.166	0.543	0.748	6.276	0.154
Early T2: tumor volume	0.220	1.246	0.517	0.452	3.435	0.670
Early T2: entropy	0.686	1.986	0.571	0.648	6.084	0.230
Early DWI: ADC mean	-0.003	0.997	0.536	0.349	2.848	0.995
Early DWI: tumor volume	-0.184	0.832	0.561	0.277	2.497	0.743
Early DWI: entropy	-0.376	0.687	0.571	0.224	2.104	0.511
Early T2: small dependence low grey level emphasis (GLDM)	-0.061	0.941	0.414	0.418	2.120	0.883
Early T2: joint entropy (GLCM)	-0.745	0.475	0.651	0.133	1.699	0.252
Early DWI: inverse difference (GLCM)	0.273	1.314	0.563	0.436	3.957	0.628
Early DWI: total energy (first order)	0.208	1.231	0.515	0.449	3.376	0.686
Early PET: SUV _{max}	-1.159	0.314	1.061	0.039	2.508	0.274
Early PET: SUL _{peak}	-0.778	0.459	0.916	0.076	2.764	0.396
Early PET: MTV	0.532	1.702	0.529	0.603	4.803	0.315
Early PET: TLG	0.001	1.001	0.535	0.351	2.856	0.999
Late T2: tumor volume	0.150	1.161	0.520	0.419	3.221	0.774
Late T2: entropy	-0.579	0.560	0.583	0.179	1.755	0.320
Late DWI: ADC mean	0.181	1.199	0.533	0.422	3.407	0.734
Late DWI: tumor volume	0.228	1.256	0.540	0.436	3.616	0.673
Late DWI: entropy	0.276	1.318	0.539	0.459	3.788	0.608

TABLE 2. Continued.

Feature	Regression coefficient	Odds ratio	Standard error	95% confidence interval		P value
				Lower limit	Upper limit	
Late T2: grey level non-uniformity (GLDM)	0.889	2.432	0.587	0.770	7.687	0.130
Late T2: joint entropy (GLCM)	-0.703	0.495	0.626	0.145	1.688	0.261
Late DWI: inverse difference normalized (GLCM)	-1.077	0.341	0.672	0.091	1.271	0.109
Late DWI: grey level non-uniformity normalized (GLRLM)	1.001	2.722	0.692	0.702	10.558	0.148
Late PET: SUV _{max}	0.263	1.301	0.531	0.459	3.686	0.621
Late PET: SUL _{peak}	0.631	1.880	0.575	0.610	5.800	0.272
Late PET: MTV	2.441	11.480	1.278	0.937	140.578	0.056
Late PET: TLG	5.499	244.488	4.385	0.045	1320336.926	0.210
Early – baseline T2: tumor volume RI	-1.781	0.168	1.179	0.017	1.699	0.131
Early – baseline T2: entropy RI	0.522	1.685	0.568	0.553	5.134	0.359
Early – baseline DWI: ADC mean RI	-0.923	0.397	0.673	0.106	1.486	0.170
Early – baseline DWI: tumor volume RI	-0.089	0.915	0.569	0.300	2.789	0.875
Early – baseline DWI: entropy RI	-0.860	0.423	0.721	0.103	1.738	0.233
Early – baseline PET: SUV _{max} RI	-1.150	0.316	0.653	0.088	1.139	0.078
Early – baseline PET: SUL _{peak} RI	-1.096	0.334	0.621	0.099	1.129	0.078
Early – baseline PET: MTV RI	0.434	1.543	0.518	0.559	4.259	0.402
Early – baseline PET: TLG RI	0.210	1.233	0.509	0.455	3.347	0.680
Late – baseline T2: tumor volume RI	-1.700	0.183	1.496	0.010	3.427	0.256
Late – baseline T2: entropy RI	-0.325	0.723	0.544	0.249	2.098	0.550
Late – baseline DWI: ADC mean RI	-0.480	0.619	0.626	0.182	2.110	0.443
Late – baseline DWI: tumor volume RI	-0.141	0.869	0.560	0.290	2.603	0.801
Late – baseline DWI: entropy RI	-0.198	0.821	0.575	0.266	2.533	0.731
Late – baseline PET: SUV _{max} RI	0.410	1.507	0.522	0.541	4.197	0.432
Late – baseline PET: SUL _{peak} RI	0.600	1.823	0.571	0.595	5.582	0.293
Late – baseline PET: MTV RI	0.523	1.687	0.520	0.609	4.676	0.315
Late – baseline PET: TLG RI	1.062	2.892	0.856	0.540	15.482	0.215

Abbreviations: SUV_{max}, maximum standardized uptake value; SUL_{peak}, peak standardized uptake value corrected for lean body mass; MTV, metabolic tumor volume; TLG, total lesion glycolysis; T2 volume, tumor volume on T2 series; T2 entropy, tumor entropy on T2 series; DWI volume, tumor volume on diffusion weighted imaging series; ADC mean, mean apparent diffusion coefficient; DWI entropy, tumor entropy on diffusion weighted imaging series; GLCM: grey level cooccurrence matrix, GLDM: grey level dependence matrix, GLRLM: grey level run length matrix, RI, response index (change over time).

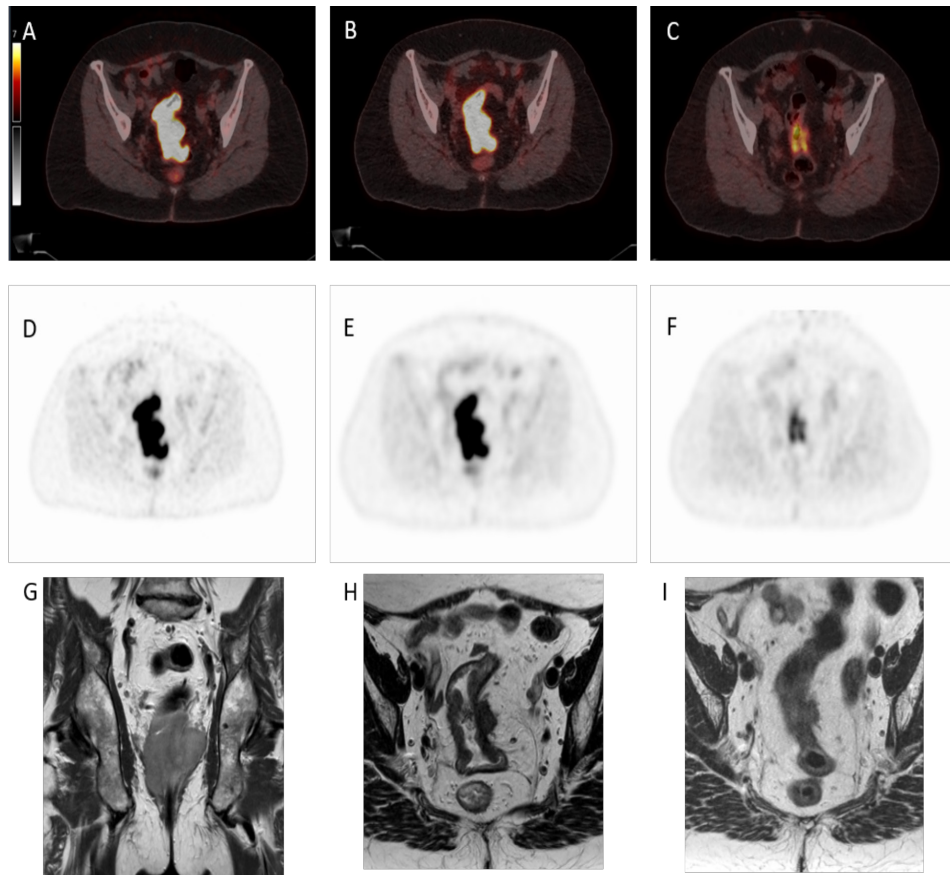


FIGURE 2. [¹⁸F]FDG PET/CT and T2 weighted MRI images of a poor responder before, during and after neoadjuvant chemoradiotherapy. Fifty-eight year old woman with cT4aN2M0 rectal cancer had a partial response to chemoradiotherapy to a yiT3N1M0. Pathological examination showed a ypT3N0M0 tumor and pTRG of 4. SUV_{max} was 17.8 at baseline, 17.8 at interim assessment, and 6.5 at re-evaluation. Figure shows [¹⁸F]FDG PET/CT fusion (A, B, C) and PET-only (D, E, F) images as well as T2 weighted MRI (G, H, I) images before (A, D, G), during (B, E, H) and after (C, F, I) neoadjuvant chemoradiotherapy.

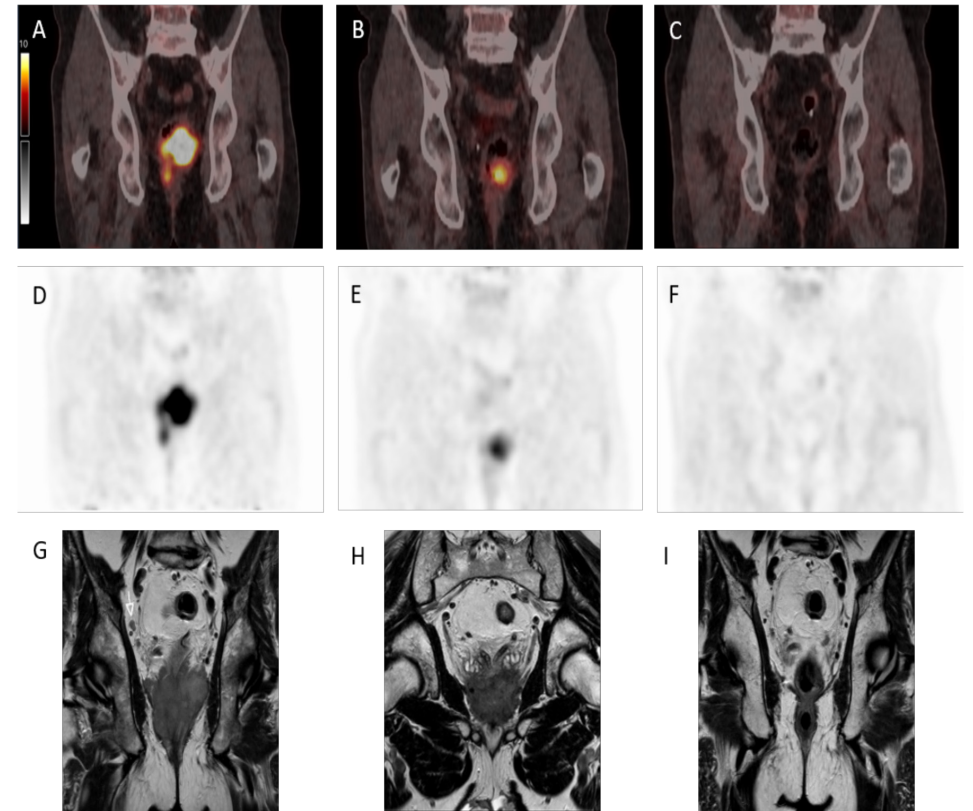


FIGURE 3. [¹⁸F]FDG PET/CT and T2 weighted MRI images before, during and after neoadjuvant therapy of a patient with a clinical complete response. Sixty-two year old man with cT4bN2M0 rectal cancer had a good response to a yiT1-2N0M0 which further regressed to a yiT0N0M0 six months after chemoradiotherapy, and is currently still followed in the Watch-and-Wait after 12 months of recurrence free follow up. SUV_{max} was 18.1 at baseline, 10.4 at interim assessment, and too low to measure at re-evaluation. Figure shows [¹⁸F]FDG PET/CT fusion (A, B, C) and PET-only (D, E, F) images as well as T2 weighted MRI (G, H, I) images before (A, D, G), during (B, E, H) and after (C, F, I) neoadjuvant chemoradiotherapy.

DISCUSSION

Results from this pilot study indicate that 13 out of 57 features are promising predictors of response, with baseline and early change showing the most clinically relevant features. As deduced from these results, end-of-treatment pre-surgical evaluation digital PET/CT was least probable to provide predictive (and clinically relevant) features. As far as we know, this is the first prospective study in LARC patients investigating the predictive value of multiparametric MRI and digital [¹⁸F]FDG PET/CT, at 3 set time points during neoadjuvant chemoradiation.

The results from this study confirm the feasibility of response prediction using digital [¹⁸F]FDG PET/CT and multiparametric MRI. These results are in line with previous reports from various small trials demonstrating the predictive value of various T2- and DW MRI and [¹⁸F]FDG PET/CT features, which have up until now not resulted in clinically usable prediction models^{14,17}. In contrast to our results, a recent study in 19 LARC patients found only baseline MTV and no early response evaluation features (2 weeks into nCRT) to be possible predictors of response³¹. In our study we also found baseline MTV to be a promising feature. However, we also found 4 other baseline features (3 MRI, 1 PET) and 4 early response evaluation RI features (2 MRI, 2 PET). Interestingly, they found more predicting features at end-of-treatment pre-surgical evaluation [¹⁸F]FDG PET/CT (SUV_{max}, SUV_{peak}, MTV, SUL_{peak}, TLG), whereas our study only found MTV to be a promising feature (note that the exact timing of the late evaluation [¹⁸F]FDG PET/CT in their study is unclear). As a next step towards clinical implementation, Schurink *et al.* developed prediction models including features from MRI and [¹⁸F]FDG PET/CT that were also used in the current study. The first study found an area under the curve (AUC) of 0.83 for response prediction at baseline using MRI derived T-stage, T2 entropy and T2 volume¹⁹. The second study found an AUC of 0.83 using clinical (T-stage, N-stage, age, gender, interval between nCRT and end-of-treatment pre-surgical evaluation) and baseline features (T2 entropy, ADC entropy and SUV_{mean})²⁰. Interestingly, models including radiomic features did not outperform the simpler model²⁰. Moreover, radiomic analysis of PET/CT images (AUC 0.78) did outperform simpler features (SUV_{mean}, TLG and mean Hounsfield unit, AUC 0.50)²⁰. However, PET/CT radiomic analyses were performed on the CT-only images, thus questioning the added value of PET. In comparison to our study, in which MRI-based radiomic features were analysed, we found 4 out of 12 radiomic features to be promising predictors of response (1 baseline and 3 end-of-treatment pre-surgical evaluation features). Unfortunately, no AUC values were available due to the limited number of patients. Interestingly, the end-of-treatment pre-surgical evaluation [¹⁸F]FDG PET/CT was least promising in this dataset. This might be due to the occurrence of radiation induced proctitis interfering with end-of-treatment pre-surgical evaluation PET/CT, since inflammation results in increased uptake of [¹⁸F]FDG and is not present at early response evaluation yet.

Although accurate response prediction is currently challenging, the significant number of unidentified complete responders who undergo surgical resection stresses the importance of accurate response assessment and prediction. Following our results, a future trial should include multiparametric MRI at all three timepoints, and [¹⁸F]FDG PET/CT at baseline and early response evaluation. Furthermore, the sample size should be sufficient to define cut-off values and develop accurate prediction models. While this study focused primarily on predicting response using imaging modalities, the (combined) use of readily available predictive features such as metabolomics and analysis of biopsy

material, and the integration of these in prediction models might further increase the accuracy of response prediction.

As inherent to any pilot study, this trial has various limitations. Due to the inclusion of only 19 patients and analysis of 57 features, no definite conclusions can be drawn from the data but only suggestions can be given towards design of future clinical trials. Due to the multicentric execution of this study various MRI scanners, with varying field strength, from various vendors and with varying scanning protocols were used. This introduces heterogeneity in the quantitative MRI features. Nevertheless, this reflects the clinical routine as the acquisition of a larger dataset of LARC patients requires inclusion from multiple hospitals. Preferably quantitative parameters would be compared from the various MRI scanners, protocols and field strengths. However, such a dataset is currently unavailable. A previous study by Mes *et al.*, however, found minimal influence of varying signal intensities from various MRI scanners on the outcome of radiomics analysis, thus suggesting the influence of this heterogeneity to be limited (high concordance (mean 0.82 ± 0.19) for 89 radiomics features before and after grey level normalization)³². Most recently, Schurink *et al.* investigated the influence of multiple MRI vendors and acquisition protocols on radiomic analysis in 649 rectal cancer patients³³. They found significant differences in image features between 9 centres, with more differences found in ADC/DWI imaging compared to T2 weighted MRI. Last, inter observer variability has been introduced as the TRG was determined by various local pathologists. However, as the data were divided into only two groups, the influence of this was deemed minimal. Future studies should take these issues into account, and either further investigate the possible influence of various scanner types and acquisition protocols, perform the study on one MRI scanner within the same institute, or develop methods to harmonize the data. Also, a future study should consider the possible shift towards the use of more short course radiotherapy combined with systemic chemotherapy following results from the RAPIDO trial, as opposed to CRT as described by current guidelines³. This issue is less relevant for pooling data from [¹⁸F]FDG PET/CT, since data are (largely) harmonized by following the EANM guidelines and only one single PET/CT scanner was used in this study²².

In conclusion, results from this study suggest that baseline, early response and end-of-treatment pre-surgical evaluation MRI and baseline and early response evaluation PET/CT features are promising to predict response to neoadjuvant therapy in rectal cancer patients. These results, in combination with the clinical need for improved treatment stratification, encourage further research into response prediction using [¹⁸F]FDG PET/CT and multiparametric MRI.

REFERENCES

1. Maas M, Nelemans PJ, Valentini V, et al. Long-term outcome in patients with a pathological complete response after chemoradiation for rectal cancer: a pooled analysis of individual patient data. *Lancet Oncol*. 2010;11:835–844.
2. Al-Sukhni E, Attwood K, Mattson DM, et al. Predictors of Pathologic Complete Response Following Neoadjuvant Chemoradiotherapy for Rectal Cancer. *Ann Surg Oncol*. 2016;23:1177–1186.
3. Bahadoer RR, Dijkstra EA, van Etten B, et al. Short-course radiotherapy followed by chemotherapy before total mesorectal excision (TME) versus preoperative chemoradiotherapy, TME, and optional adjuvant chemotherapy in locally advanced rectal cancer (RAPIDO): a randomised, open-label, phase 3 trial. *Lancet Oncol*. 2021;22:29–42.
4. Park J-S, Baek J-H, Lee W-S, et al. Long-term oncologic outcomes in pathologic tumor response after neoadjuvant chemoradiation for locally advanced rectal cancer. *Korean J Clin Oncol*. 2018;14:37–42.
5. Beets-Tan RGH, Lambregts DMJ, Maas M, et al. Magnetic resonance imaging for clinical management of rectal cancer: Updated recommendations from the 2016 European Society of Gastrointestinal and Abdominal Radiology (ESGAR) consensus meeting. *Eur Radiol*. 2018;28:1465–1475.
6. Landelijke Werkgroep Gastro Intestinale Tumoren. Oncoline Available from: <https://www.oncoline.nl/colorectaalcarcinoom>. Accessed November 6, 2019.
7. van der Valk MJM, Hilling DE, Bastiaannet E, et al. Long-term outcomes of clinical complete responders after neoadjuvant treatment for rectal cancer in the International Watch & Wait Database (IWWD): an international multicentre registry study. *Lancet Lond Engl*. 2018;391:2537–2545.
8. Hendren SK, O'Connor BI, Liu M, et al. Prevalence of male and female sexual dysfunction is high following surgery for rectal cancer. *Ann Surg*. 2005;242:212–223.
9. Dutch Guideline Colorectal Cancer. Federation Medical Specialists Available from: https://richtlijnendatabase.nl/richtlijn/colorectaal_carcinoom_crc. 2019. Accessed December 25, 2021.
10. van Stiphout RGPM, Valentini V, Buijssen J, et al. Nomogram predicting response after chemoradiotherapy in rectal cancer using sequential PETCT imaging: a multicentric prospective study with external validation. *Radiother Oncol J Eur Soc Ther Radiol Oncol*. 2014;113:215–222.
11. Janssen MHM, Öllers MC, van Stiphout RGPM, et al. PET-based treatment response evaluation in rectal cancer: prediction and validation. *Int J Radiat Oncol Biol Phys*. 2012;82:871–876.
12. Cliffe H, Patel C, Prestwich R, et al. Radiotherapy response evaluation using FDG PET-CT—established and emerging applications. *Br J Radiol*.;90 . DOI: 10.1259/bjr.20160764.
13. Joye I, Debuquoy A, Deroose CM, et al. Quantitative imaging outperforms molecular markers when predicting response to chemoradiotherapy for rectal cancer. *Radiother Oncol J Eur Soc Ther Radiol Oncol*. 2017;124:104–109.
14. Mahadevan LS, Zhong J, Venkatesulu B, et al. Imaging predictors of treatment outcomes in rectal cancer: An overview. *Crit Rev Oncol Hematol*. 2018;129:153–162.
15. Meng X, Huang Z, Wang R, et al. Prediction of response to preoperative chemoradiotherapy in patients with locally advanced rectal cancer. *Biosci Trends*. 2014;8:11–23.
16. Giannini V, Mazzetti S, Bertotto I, et al. Predicting locally advanced rectal cancer response to neoadjuvant therapy with 18F-FDG PET and MRI radiomics features. *Eur J Nucl Med Mol Imaging*. 2019;46:878–888.
17. Joye I, Deroose CM, Vandecaveye V, et al. The role of diffusion-weighted MRI and (18)F-FDG PET/CT in the prediction of pathologic complete response after radiochemotherapy for rectal cancer: a systematic review. *Radiother Oncol J Eur Soc Ther Radiol Oncol*. 2014;113:158–165.
18. Avallone A, Aloj L, Pecori B, et al. 18F-FDG PET/CT Is an Early Predictor of Pathologic Tumor Response and Survival After Preoperative Radiochemotherapy with Bevacizumab in High-Risk Locally Advanced Rectal Cancer. *J Nucl Med Off Publ Soc Nucl Med*. 2019;60:1560–1568.
19. Schurink NW, Min LA, Berbee M, et al. Value of combined multiparametric MRI and FDG-PET/CT to identify well-responding rectal cancer patients before the start of neoadjuvant chemoradiation. *Eur Radiol*. 2020;30:2945–2954.
20. Schurink NW, van Kranen SR, Berbee M, et al. Studying local tumour heterogeneity on MRI and FDG-PET/CT to predict response to neoadjuvant chemoradiotherapy in rectal cancer. *Eur Radiol*. . Epub ahead of print February 10, 2021. DOI: 10.1007/s00330-021-07724-0.
21. Maffione AM, Marzola MC, Capirci C, et al. Value of (18)F-FDG PET for Predicting Response to Neoadjuvant Therapy in Rectal Cancer: Systematic Review and Meta-Analysis. *AJR Am J Roentgenol*. 2015;204:1261–1268.
22. Boellaard R, Delgado-Bolton R, Oyen WJG, et al. FDG PET/CT: EANM procedure guidelines for tumour imaging: version 2.0. *Eur J Nucl Med Mol Imaging*. 2015;42:328–354.
23. Kikinis R, Pieper SD, Vosburgh KG. 3D Slicer: A Platform for Subject-Specific Image Analysis, Visualization, and Clinical Support. In: Jolesz FA, ed. *Intraoperative Imaging and Image-Guided Therapy*. New York, NY: Springer;277–289.
24. van Griethuysen JJ, Fedorov A, Parmar C, et al. Computational Radiomics System to Decode the Radiographic Phenotype. *Cancer Res*. 2017;77:e104–e107.
25. Delli Pizzi A, Chiarelli AM, Chiacchiaretta P, et al. MRI-based clinical-radiomics model predicts tumor response before treatment in locally advanced rectal cancer. *Sci Rep*. 2021;11:5379.
26. van Timmeren JE, Cester D, Tanadini-Lang S, et al. Radiomics in medical imaging—“how-to” guide and critical reflection. *Insights Imaging*. 2020;11:91.
27. O JH, Lodge MA, Wahl RL. Practical PERCIST: A Simplified Guide to PET Response Criteria in Solid Tumors 1.0. *Radiology*. 2016;280:576–584.
28. Mandard AM, Dalibard F, Mandard JC, et al. Pathologic assessment of tumor regression after preoperative chemoradiotherapy of esophageal carcinoma. Clinicopathologic correlations. *Cancer*. 1994;73:2680–2686.
29. Peeters C, Übelhör C, Mes S, et al. Stable prediction with radiomics data. 2019.
30. Gillies RJ, Kinahan PE, Hricak H. Radiomics: Images Are More than Pictures, They Are Data. *Radiology*. 2016;278:563–577.
31. Uslu-Besli L, Mermut Ö, Yardimci AH, et al. Comparison of 18F-FDG PET/CT and DW-MRI in assessment of neoadjuvant radiochemotherapy response in locally advanced rectal cancer patients. *Rev Espanola Med Nucl E Imagen Mol*. 2021;40:19–29.
32. Mes SW, van Velden FHP, Peltenburg B, et al. Outcome prediction of head and neck squamous cell carcinoma by MRI radiomic signatures. *Eur Radiol*. 2020;30:6311–6321.

33. Schurink NW, van Kranen SR, Roberti S, et al. Sources of variation in multicenter rectal MRI data and their effect on radiomics feature reproducibility. *Eur Radiol.* 2022;32:1506–1516.

SUPPLEMENTARY

SUPPLEMENTAL TABLE 1. Specifications of MRI scanners. Table shows specifications of various MRI scanners used in this study.

Vendor	Field strength (Tesla)	Number of scans	Acquisition voxel size (mm)
Philips Ingenia	1.5	6	0.62 x 0.81
Philips Ingenia	1.5	2	1.49 x 2.00
Philips Ingenia	1.5	15	0.49 x 0.64
Philips Ingenia	3	1	0.94 x 1.25
Philips Ingenia	3	1	0.49 x 0.62
Philips Ingenia	3	7	0.49 x 0.62
Philips Ingenia Elition X	3	9	0.70 x 0.79
Philips Ingenia Elition X	3	1	0.70 x 0.53
Philips Ingenia Elition X	3	1	0.89 x 1.56
Siemens Avanto	1.5	1	0.69 x 0.80
Siemens Avanto	1.5	1	0.63 x 0.73
Siemens Avanto	1.5	1	0.59 x 0.78
Siemens Avanto	1.5	1	0.47 x 0.67
Siemens Avanto	1.5	1	0.51 x 0.72
Siemens Avanto	1.5	1	0.63 x 0.79
Siemens Aera	1.5	2	0.47 x 0.59
Siemens Aera	1.5	6	0.63 x 0.78

MRI sequences included T2 weighted sequences in sagittal, oblique axial and oblique coronal direction and an orthogonal diffusion weighted imaging (DWI) sequence (*b*-values 0, 200, and 800/1000, identical direction of T2 oblique axial). Oblique axial scans were perpendicular to the long axis of the rectal wall.

Intra-tumoral genomic heterogeneity in rectal cancer: mutational status is dependent on preoperative biopsy depth and location.

F.A. Vuijk, C. van de Water, S. Lent – van Vliet, M.J.M. van der Valk, F. Simmer, C.J.H. van de Velde, A.L. Vahrmeijer, I.D. Nagtegaal and D.E. Hilling.

Cancers (Basel) 2021

9

ABSTRACT

Neoadjuvant therapy before surgical resection is indicated for patients with locally advanced rectal cancer. However, a significant number of patients show minimal or no response to neoadjuvant therapy. Unfortunately, we are currently unable to predict response and identify non-responding patients before neoadjuvant treatment is given. Genomic mutational status might provide valuable prognostic information. However, it is unclear whether predictions based on genomic mutational status in single preoperative biopsies are reliable due to intra-tumoral heterogeneity. In this study we aim to investigate the reliability of genomic mutations found in single pre-operative biopsies by comparing genomic mutations to 4 other locations within the same tumor using next generation sequencing. Rectal cancer patients undergoing primary resection without neoadjuvant therapy were included. Of all patients, one biopsy, two deep and two superficial samples were obtained and sequenced using a targeted next generation sequencing gene panel. Concordance between these 5 samples was assessed. In this feasibility study we included 11 patients. In 7 out of 11 (64%) patients, all 5 samples showed concordant mutations. In 4 out of 11 patients (36%) discordant mutations were observed. In conclusion, assessment of mutational status on a single pre-operative biopsy shows discordance with tumor tissue from other locations in 36% of cases. These results warrant careful interpretation of biopsy material analysis, as these might be influenced by tumor heterogeneity.

INTRODUCTION

Locally advanced rectal cancer (LARC) patients are currently treated with neoadjuvant (chemo)radiotherapy followed by surgical resection¹. In clinical practice, the observed response to neoadjuvant therapy is heterogeneous. A pathological complete response (complete regression of tumor and/or pathological lymph nodes) is seen in 15-20% of patients, whereas in the vast majority of patients (54-75%) neoadjuvant therapy results in a partial response^{2,3}. Unfortunately, a subset of 10-50% of LARC patients receives futile neoadjuvant treatment when minimal or no response is observed^{2,4}. Currently, treatment stratification and prognosis is based on clinical TNM stage, tumor distance to the mesorectal fascia and the presence of extramural vascular invasion⁵. Response prediction based on parameters readily available before neoadjuvant treatment might provide a means to ensure patient-tailored treatment, and reduce unnecessary waiting periods and therapy related toxicity in non-responders.

Tumor associated immune response and intra-tumoral heterogeneity might be involved in causing therapeutic resistance of the tumor to neoadjuvant therapy⁶. Intra-tumoral genomic heterogeneity refers to the presence of genetically distinct sub clones within cancer lesions, and is developed by tumors in reaction to a diversity of microenvironmental factors including hypoxia, tissue stiffness, immune response and chronic inflammation or can be caused by the polyclonal origin of these tumors^{7,8}. Intra-tumoral genomic heterogeneity is particularly significant in colorectal cancer, and is attributed to the presence of both microsatellite- and chromosomal instability⁹⁻¹¹.

In previous studies, the value of several clinical, pathological and radiological parameters in predicting response to (neoadjuvant) therapy has been assessed¹²⁻²⁰. Unfortunately, these studies so far have not resulted in clinically used prediction models. The predictive value of genomic mutations in colorectal cancer has previously been investigated, concluding that *KRAS*, as well as *RAS*, *BRAF* and *PIK3CA* mutations, are predictive of tumor response to anti-EGFR therapy^{17,18,21-25}. Furthermore, a high degree of intra-tumoral genomic heterogeneity has been associated with worse disease-free survival and was correlated with a higher rate of liver metastases²⁶. So far, no specific genomic mutations have been found to accurately predict response to neoadjuvant therapy in LARC patients¹⁹.

A combination of genomic mutations might provide valuable prognostic information. However, the reliability of next generation sequencing performed on routinely obtained single preoperative biopsies has yet to be established. Intra-tumoral heterogeneity has been shown to be significant in rectal tumors and their associated lymph nodes and metastases^{27,28}. Therefore, genomic mutations found in single preoperative biopsies

might vary within individual patients, depending on the biopsy location and depth.

In this study we aim to investigate the reliability of genomic mutations found in a single preoperative biopsy by comparing these mutations to 4 other locations within the same tumor using next generation sequencing for genes frequently mutated in colorectal cancer.

MATERIALS AND METHODS

Patients

Rectal cancer patients from the Radboud University Medical Center, Nijmegen, the Netherlands and diagnosed between 2010 and 2012 with a biopsy confirmed rectal adenocarcinoma were retrospectively included in this study. To exclude any influence of neoadjuvant therapy on the results, only patients undergoing direct surgical resection of the primary tumor (without neoadjuvant chemo- and/or radiotherapy) were included. Patient characteristics were obtained from medical records, including age, gender, clinical- and pathological characteristics. This project was conducted in accordance with the Declaration of Helsinki, and did not require approval of the local IRB according to local WMO regulations.

Tumor identification and DNA isolation

For each patient, five tissue samples were obtained from representative formalin-fixed paraffin-embedded (FFPE) tumor blocks containing material of 1 preoperative diagnostic biopsy, 2 superficial tumor tissue samples and 2 deep (central) tumor tissues samples of the resected specimen. Optimal FFPE blocks (with adequate tumor cellularity of $\geq 20\%$ from full samples, and $>10\%$ in biopsy samples) for smMIP analysis were identified and marked by an expert pathologist (I.N.) on representative hematoxylin and eosin (H&E) stained slides. To obtain sufficient genomic DNA, marked tumor areas were cut out from 10 sequential (non-stained) slides (each 6 μm thick). DNA was isolated at 56 °C for 1 hour using TET-lysis buffer with 5% Chelex-100 (Bio-Rad, Hercules, USA) and 400 μg proteinase K (Qiagen, Valencia, USA), followed by inactivation at 95°C during 10 minutes²⁹. The DNA concentration was determined using the Qubit High Sensitivity Kit (Invitrogen, Carlsbad, USA) per manufacturer's protocol.

smMIP sequencing

A panel of 911 smMIPs was used to detect variants in 31 cancer-related genes, as displayed in **Table 1**. To provide gender control, smMIPs targeting AMELX and AMELY were included. The smMIP sequencing protocol has previously been clinically validated and used in the Radboud University Medical Center²⁹. One hundred nanogram of isolated

DNA was included per sample. After sample preparation, manual library preparation was performed²⁹. The purified libraries were diluted. Sequencing was performed using the NextSeq500 (Illumina, San Diego, USA) per manufacturer's protocol (300 cycles High Output sequencing Kit, Illumina, San Diego, USA), resulting in 2 x 150 bp paired end reads.

Sequence data analysis

Sequence data was generated from the NextSeq500, after which Bcl to FASTQ conversion and demultiplexing of barcoded reads was automatically performed. Sequence Pilot software (JSI Medical Systems GmbH, Ettenheim, Germany) was used for generating consensus reads and variant identification, with settings as previously described²⁹. Variants found in samples passing gender control and exceeding an average minimum reading depth of 180 were automatically filtered with an in-house Python script, as depicted in **Figure 1**. This threshold excludes, with a certainty of $>95\%$, the presence of a mutation at minimally 10% mutant allele frequency within covered regions. As SOX9 and SEC63 have many pseudogenes resulting in uncertainty about found mutations, we have excluded these from further analysis. Due to a technical sequencing artifact (in all samples), PTEN mutation c.407G>A was excluded from the analysis.

Statistical analysis

Statistical analysis was performed using SPSS version 23 (SPSS, Inc., Chicago, USA). Numerical data is presented as mean (standard deviation) or median (interquartile range) based on distribution. Categorical data is presented as frequencies and percentages. In order to quantify tumor heterogeneity, differences in mutational status between biopsy, deep and superficial tumor samples were analyzed by calculating the percentages of concordance and discordance. Concordance was defined as all five samples (1 biopsy, 2 deep samples, and 2 superficial samples) showing identical (or no) mutations. Discordance was defined as ≥ 1 mutation(s) in either of the 5 samples, which was not found in (one of) the other samples. For all tests performed, $P < 0.05$ was considered statistically significant.

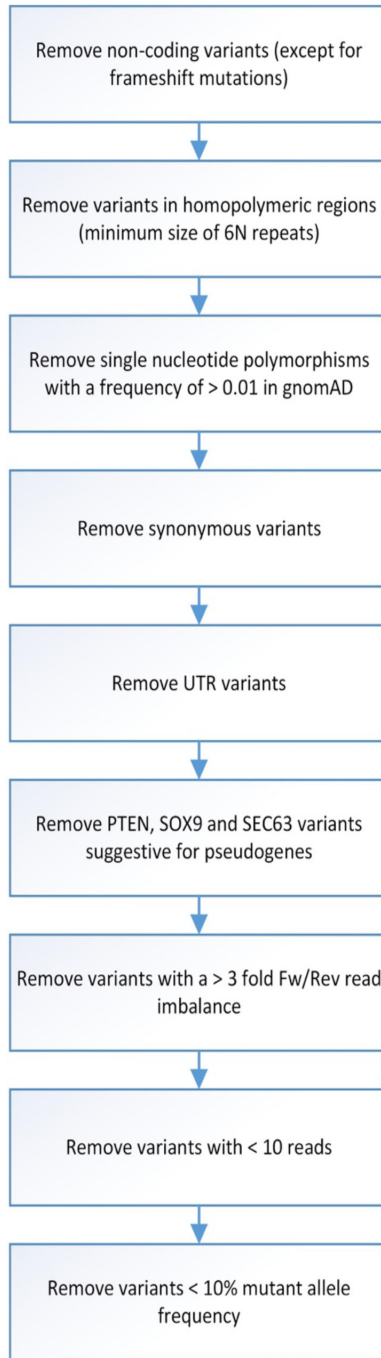


FIGURE 1. Flowchart of smMIP analysis data filtering.
Overview of steps involved in data filtering before smMIP data analysis was performed.

TABLE 1. Overview of regions targeted by Transcan smMIP panel.

Gene	Transcript ID (RefSeq)	Transcript ID (Ensembl)	Exon number	Targeted regions	Positions analyzed for variants
<i>ACVR1B</i>	ENST00000257963	NM_004302	02	Activin types I and II receptor domain	c.92-5 to c.331+5
<i>ACVR2A</i>	ENST00000241416	NM_001616	03-09	Transforming growth factor beta type I GS-motif	c.556 to c.1518+5
<i>AMER1</i>	ENST00000330258	NM_152424	06-11	Protein kinase domain	c.673-5 to c.1542+5
<i>APC</i>	ENST00000257430	NM_000038	02	WTX Protein	c.639 to c.1629
<i>ARID1A</i>	ENST00000324856	NM_006015	01-16	Whole gene	c1-5 to c.8532+5
			11-12	ARID DNA-binding domain	c.2989 to c.3397
			20	SWI/SNF-like complex subunit BAF250/Osa	c.5820 to c.6777
<i>B2M</i>	ENST00000558401	NM_004048	02	Immunoglobulin C1-set domain	c.68-5 to c.346+5
<i>BRAF</i>	ENST00000288602	NM_004333	15	Codon D594-K601	c.1742-5 to 1860+5
<i>CASP5</i>	ENST00000393141	NM_004347	02-03	CARD domain	c.8 to 433+5
<i>CASP8</i>	ENST00000358485	NM_001080125	07-09	Caspase domain	c.838 to 1617+5
<i>CTNNB1</i>	ENST00000349496	NM_001904	03	Codon D32-S45	c.36 to c.163
			08	Codon W383-N387	c.1082-5 to c.1185+5
<i>EGFR</i>	ENST00000275493	NM_005228	12	Receptor L domain	c.1391 to c.1498+5
			18-21	Protein tyrosine kinase	c.2062-5 to 2625+5
<i>ERBB2</i>	ENST00000269571	NM_004448	18-24	Protein tyrosine kinase	c.2101 to c.2970+5
<i>FBXW7</i>	ENST00000281708	NM_033632	07-12	WD domain, G-beta repeat	c.1035 to c.2124+5
<i>GNAS</i>	ENST00000371085	NM_000516	08-09	Codon R201 and Q227	c.586-5 to c.718+5
<i>IDH2</i>	ENST00000330062	NM_002168	04	Codon R140 and R172	c.374-5 to c.534+5
<i>KRAS</i>	ENST00000311936	NM_004985	02	Codon G12, and G13	c.1-5 to c.111+5
			03	Codon A59 and Q61	c.112-5 to c.232
			04	Codon K117 and A146	c.291-5 to c.385 and c.402 to c.450+5
<i>MET</i>	ENST00000318493	NM_001127500	15-21	Protein tyrosine kinase	c.3140 to c.4227+5
<i>NRAS</i>	ENST00000369535	NM_002524	02	Codon G12 and G13	c.1-5 to c.99
			03	Codon A59 and Q61	c.135 to c.272
<i>PIK3CA</i>	ENST00000263967	NM_006218	10	Codon E542 to Q546	c.1557 to c.1664+5
			21	Codon M1043 to G1049	c.3041 to c.3207+5

TABLE 1. Continued.

Gene	Transcript ID (RefSeq)	Transcript ID (Ensembl)	Exon number	Targeted regions	Positions analyzed for variants
<i>POLE</i>	ENST00000320574	NM_006231	03-13	DNA-directed DNA polymerase, exonuclease domain	B, c.205-5 to c.1301
<i>PTEN</i>	ENST00000371953	NM_000314	05-08	Dual specificity phosphatase, catalytic domain, C2 domain of PTEN tumor-suppressor protein	c.310 to c.1026+5
<i>RNF43</i>	ENST00000407977	NM_017763	02-10	Whole CDS	c.1-5 to c.2352+5
<i>SMAD2</i>	ENST00000262160	NM_005901	02-11	Whole CDS	c.1-5 to c.1404+5
<i>SMAD4</i>	ENST00000342988	NM_005359	03-04	MH1 domain	c.250-5 to c.454+5
			09-12	MH2 domain	c.956-5 to c.1659+5
<i>SMARCA2</i>	ENST00000349721	NM_003070	15-21	SNF2-related, N-terminal domain	c.2185-5 to 3078+5
			23-25	Helicase, C-terminal	c.3136 to c.3684+5
<i>SMARCA4</i>	ENST00000450717	NM_001128846	15-21	SNF2-related, N-terminal domain	c.2275-5 to c.3168+5
			23-25	Helicase, C-terminal	c.3324 to c.3374+5
<i>SMARCB1</i>	ENST00000263121	NM_003073	05-09	SNF5/SMARCB1/INI1	c.501-5 to c.1158+5
<i>SOX9</i>	ENST00000245479	NM_000346	01-03	Whole CDS	c.1-5 to c.1530+5
<i>TCF7L2</i>	ENST00000369397	NM_030756	01-06	CTNNB1 binding, N-terminal	c.1-5 to c.719+5
			09-10	High mobility group box domain	c.933-5 to c.1200+5
<i>TGFBR2</i>	ENST00000359013	NM_001024847	04	Codon E125	c.339-5 to c.529+5
<i>TP53</i>	ENST00000269305	NM_000546	03-08	P53 DNA-binding domain	c.83 to c.919+5

RESULTS

Patients

Data and tissue of 11 patients were included in this study. Patients were on average 72 ± 27.4 years old, and consisted of 6 men and 5 females. Of these, 9 had a pT3 tumor and 2 a pT4 tumor. All patients were diagnosed with a UICC stage 2 or 3 tumor (Table 2). All patients were treated with immediate resection of the rectal tumor, without prior chemo- and/or radiotherapy. The rectal tumor was on average located 57.8 ± 46.3 mm from the anal verge, and measured 53.5 ± 21.6 mm in diameter. Patient 7 had a poorly differentiated tumor (UICC grade 3), whereas all the other patients had a moderately/well differentiated tumor (UICC grade 1-2). All tumors were microsatellite stable. Detailed clinicopathological features are summarized in Table 2.

TABLE 2. Patient characteristics.

Variables		N=11
Age (years)	Mean (SD)	72.2 (27.4)
Gender	Male	6 (55%)
	Female	5 (45%)
pT	3	9 (82%)
	4	2 (18%)
pN	0	6 (55%)
	1	3 (27%)
	2	2 (18%)
UICC stage	2A	6
	3A	4
	3C	1
EMVI	Yes	4 (36%)
	No	6 (55%)
	Missing	1 (9%)
Differentiation (UICC grade)	Well/moderate (UICC grade 1-2)	9 (82%)
	Poor (UICC grade 3)	1 (9%)
	Missing	1 (9%)
Distance to CRM (mm)	Mean (SD)	14.1 (7.7)
Diameter tumor (mm)	Mean (SD)	53.5 (21.6)
Total number of lymph nodes	Median (IQR)	15 (12-19)
Number of tumor positive lymph nodes	Median (IQR)	0 (0-3)
Distance from anal verge (mm)	Mean (SD)	57.8 (46.3)

Abbreviations: UICC grade, Union for International Cancer Control pathological differentiation grade; SD, standard deviation; pT, clinical tumor stage; pN, clinical nodal stage; EMVI, extramural vascular invasion; CRM, circumferential resection margin; IQR, interquartile range.

Mutation concordance

Twenty-eight genomic mutations were found in the following 8 genes: *APC* (9/11), *BRAF* (1/11), *FBXW7* (2/11), *KRAS* (7/11), *PIK3CA* (1/11), *PTEN* (1/11), *SMAD4* (1/11) and

TP53 (6/11). Insufficient (partial) read depth was found in biopsy samples of 3 patients (patient 5, 8 and 9). In 7 out of 11 (64%) patients, all 5 samples showed concordant mutations. In 4 out of 11 patients (36%) a discordance in mutations was observed within the 5 samples. In patient 2 a discordance in *KRAS* (2 different mutations), *SMAD4* and *TP53* mutations was found between the superficial sample and the biopsy as well as both deep samples. Patient 4 showed discordance as the *TP53* mutation was only found in the biopsy and one of two superficial samples. Patient 5 showed discordance for one of the two *APC* mutations. This *APC* mutation was only found in the superficial samples compared to the deep samples (biopsy results were not available). In patient 8 discordance was found as different *TP53* mutations were found in the biopsy compared to the deep and superficial samples. These results are depicted in **Figure 2** and **3**.

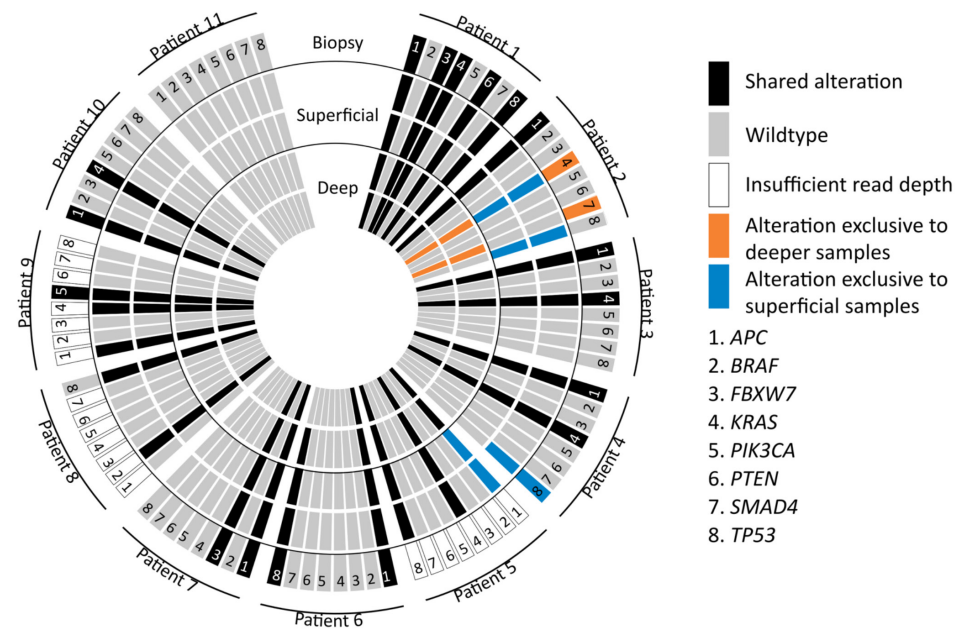


FIGURE 2. Graphical display of mutations in all samples. Representation of *APC*, *BRAF*, *FBXW7*, *KRAS*, *PIK3CA*, *PTEN*, *SMAD4*, *TP53* mutations found in deep, superficial and biopsy samples. The blue, orange and black colors represent the location of found mutations, and possible relation to specifically the deep, superficial or biopsy specimen.

Interestingly, patient 4, 5 and 8 have one discordant mutation, whereas patient 2 has five. No differences in differentiation grade, microsatellite status, tumor stage were found to explain this difference. However, patient 2 was the only patient with a mucinous tumor at pathological examination, whereas the other patients all had not otherwise specified adenocarcinomas.

In this study, 13 *APC* mutations were found, of which 11 most likely result in loss of function (5 non-sense and 6 frameshift mutations). Regarding *TP53* mutations, 5 missense mutations have been found which are non-functional according to the TP53-IACR database³⁰. Furthermore, the effect of the other two *TP53* mutations (one frameshift and one frame deletion) is unclear. All but one *KRAS* mutations are activating hotspot mutations, and the *BRAF* mutation was found in very close proximity to the real hotspot and most likely also results in increased *BRAF* activity³¹⁻³³. When compared to previous results from the TCGA study in rectal cancers, the percentage of found mutation frequencies is similar³⁴.

When putting these found mutations into a clinical perspective, only *KRAS* mutations are currently primarily of influence in colorectal cancer patients, as these are predictive for cetuximab and panitumumab therapy success. Interestingly, two *KRAS* hotspot mutations (*KRAS* c.35G>A and *KRAS* c1.83A>T) were discordant.

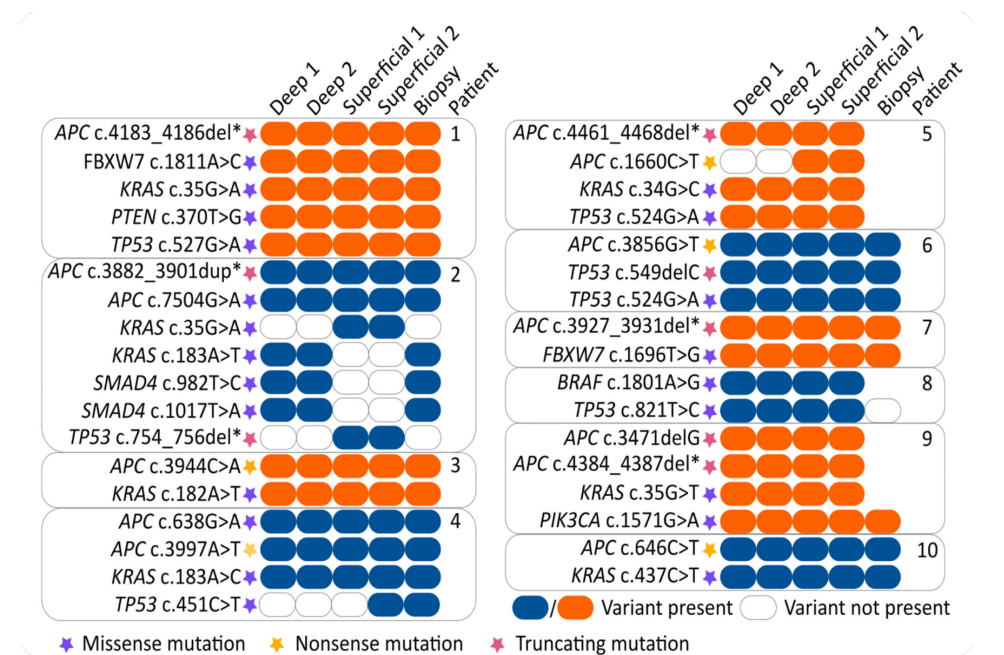


FIGURE 3. Overview of specific mutations. Overview of specific mutations found in all samples. The various mutations are represented by orange and blue colored boxes (blue/orange box = mutation variant is present and clear box = mutation variant is absent). Purple, yellow and red stars indicate the function of the found mutation (purple = missense mutation, yellow = nonsense mutation and red = truncating mutation). The location of the tumor sample is indicated at the top of the boxes.

DISCUSSION

Response to neoadjuvant therapy is heterogeneous in LARC patients^{2,4}. Adequate stratification based on parameters available before treatment might enable better use of neoadjuvant therapy. In this light, genomic mutational status might provide valuable prognostic information.

In this study, genomic mutations in pre-operative biopsies were compared to 4 other locations within the same tumor using next generations sequencing. In 36% of the patients, evaluation of genomic mutational status on a single pre-operative biopsy has shown discordance between the various tumor samples. This illustrates the genomic variability in rectal cancer and could explain the so-far experienced difficulties in obtaining reliable biomarkers. These results are in line with previous evidence supporting the presence of intra-tumoral genomic heterogeneity in a considerable proportion of rectal cancers³⁵. Three previous studies have compared genomic mutations in up to 3 intra tumoral locations. Hardiman *et al.* reported up to 10 coding variants uniquely corresponding to one of 3 of the tumor locations in their study of 6 patients³⁵. In the study of Bettoni *et al.*, only 27% of the observed mutations corresponded to all three samples of a single rectal adenocarcinoma in one patient³⁶. On the other hand, Dijkstra *et al.* reported no differences in mutational status between deep and superficial colorectal cancer tissue in 30 patients³⁷. However, the spacial distance between compared tumor samples in this study was limited, as samples were taken from serial sectioning of FFPE blocks three times every 1.2 mm. This might have resulted in serial sectioning of one tumor clone (and thus no difference in found mutations), whereas our study (and others) used tumor samples with a higher spatial distance recovered from various tumor locations.

This study has several limitations. First of all, the small sample size. Moreover, insufficient read depth was achieved in biopsy material from 3 patients. Therefore, we could not call variants at all target regions for these samples. Also, the limited targeted next generation sequencing panel might have influenced the interpretation of our results. The number of discordant cases might actually be higher, as this targeted gene panel only provides information on a selected number of mutations. Furthermore, the tumor cell percentage in several samples was low, which may have resulted in mutant allele frequencies below the calling threshold. Lastly, there is no 100% certainty the found mutations were not germ-line mutations, however considering the observed allelic frequency this is very unlikely.

To increase the reliability of the biopsy analysis, the use of multiple and possibly even deeper/larger preoperative biopsies might provide a better representation of intra-tumoral heterogeneity. However, this might also increase the risk of procedure related

complications. A second possibility might be the application of whole exome sequencing or larger targeted gene panels (such as the TSO500, Illumina, San Diego, USA), as this possibly provides a more elaborate analysis of genomic mutations, as compared to next generation sequencing using a limited targeted gene panel. Using these techniques, the mutant-allele heterogeneity (MATH) score was developed to quantitatively assess the spread of allele frequencies, and has been correlated to response^{19,38}. However, as sampling errors are innate to the biopsy technique, parameters derived from full tumor imaging might be preferable to incorporate characteristics of all genetic sub clones present in these cancers. Following this, predicting algorithms should therefore include various clinical, radiological and pathological parameters to overcome the complexity of tumor heterogeneity.

CONCLUSION

In conclusion, assessment of mutational status on a single pre-operative biopsy shows discordance with tumor tissue from other locations in 36% of cases. These results warrant careful interpretation of biopsy material analysis, as these might be influenced by tumor heterogeneity.

REFERENCES

1. Beets-Tan RGH, Lambregts DMJ, Maas M, et al. Magnetic resonance imaging for clinical management of rectal cancer: Updated recommendations from the 2016 European Society of Gastrointestinal and Abdominal Radiology (ESGAR) consensus meeting. *Eur Radiol.* 2018;28:1465–1475.
2. Maas M, Nelemans PJ, Valentini V, et al. Long-term outcome in patients with a pathological complete response after chemoradiation for rectal cancer: a pooled analysis of individual patient data. *Lancet Oncol.* 2010;11:835–844.
3. Appelt AL, Pløen J, Harling H, et al. High-dose chemoradiotherapy and watchful waiting for distal rectal cancer: a prospective observational study. *Lancet Oncol.* 2015;16:919–927.
4. Park J-S, Baek J-H, Lee W-S, et al. Long-term oncologic outcomes in pathologic tumor response after neoadjuvant chemoradiation for locally advanced rectal cancer. *Korean J Clin Oncol.* 2018;14:37–42.
5. Landelijke Werkgroep Gastro Intestinale Tumoren. Oncoline Available from: <https://www.oncoline.nl/colorectaalcarcinoom>. Accessed November 6, 2019.
6. Frydrych LM, Ulintz P, Bankhead A, et al. Rectal cancer sub-clones respond differentially to neoadjuvant therapy. *Neoplasia.* 2019;21:1051–1062.
7. Hinohara K, Polyak K. Intratumoral Heterogeneity: More Than Just Mutations. *Trends in Cell Biology.* 2019;29:569–579.
8. Parsons BL. Many different tumor types have polyclonal tumor origin: evidence and implications. *Mutat Res.* 2008;659:232–247.
9. Molinari C, Marisi G, Passardi A, et al. Heterogeneity in Colorectal Cancer: A Challenge for Personalized Medicine? *Int J Mol Sci.*;19 . Epub ahead of print November 23, 2018. DOI: 10.3390/ijms19123733.
10. Grady WM, Carethers JM. Genomic and epigenetic instability in colorectal cancer pathogenesis. *Gastroenterology.* 2008;135:1079–1099.
11. Vogelstein B, Papadopoulos N, Velculescu VE, et al. Cancer genome landscapes. *Science.* 2013;339:1546–1558.
12. Habr-Gama A, São Julião GP, Gama-Rodrigues J, et al. Baseline T Classification Predicts Early Tumor Regrowth After Nonoperative Management in Distal Rectal Cancer After Extended Neoadjuvant Chemoradiation and Initial Complete Clinical Response. *Dis Colon Rectum.* 2017;60:586–594.
13. Joye I, Deroose CM, Vandecaveye V, et al. The role of diffusion-weighted MRI and (18)F-FDG PET/CT in the prediction of pathologic complete response after radiochemotherapy for rectal cancer: a systematic review. *Radiother Oncol.* 2014;113:158–165.
14. Giralt J, Eraso A, Armengol M, et al. Epidermal growth factor receptor is a predictor of tumor response in locally advanced rectal cancer patients treated with preoperative radiotherapy. *International Journal of Radiation Oncology*Biophysics*Physics.* 2002;54:1460–1465.
15. Reerink O, Karrenbeld A, Plukker JTM, et al. Molecular Prognostic Factors in Locally Irresectable Rectal Cancer Treated Preoperatively by Chemo-radiotherapy. *Anticancer Res.* 2004;24:1217–1222.
16. Tsang JS, Vencken S, Sharaf O, et al. Global DNA methylation is altered by neoadjuvant chemoradiotherapy in rectal cancer and may predict response to treatment – A pilot study. *European Journal of Surgical Oncology (EJSO).* 2014;40:1459–1466.
17. Lièvre A, Bachet J-B, Le Corre D, et al. KRAS mutation status is predictive of response to cetuximab therapy in colorectal cancer. *Cancer Res.* 2006;66:3992–3995.
18. Linardou H, Dahabreh IJ, Kanaloupiti D, et al. Assessment of somatic k-RAS mutations as a mechanism associated with resistance to EGFR-targeted agents: a systematic review and meta-analysis of studies in advanced non-small-cell lung cancer and metastatic colorectal cancer. *Lancet Oncol.* 2008;9:962–972.
19. Greenbaum A, Martin DR, Bocklage T, et al. Tumor Heterogeneity as a Predictor of Response to Neoadjuvant Chemotherapy in Locally Advanced Rectal Cancer. *Clin Colorectal Cancer.* 2019;18:102–109.
20. Oh BY, Shin H-T, Yun JW, et al. Intratumor heterogeneity inferred from targeted deep sequencing as a prognostic indicator. *Sci Rep.* 2019;9:1–8.
21. De Roock W, Claes B, Bernasconi D, et al. Effects of KRAS, BRAF, NRAS, and PIK3CA mutations on the efficacy of cetuximab plus chemotherapy in chemotherapy-refractory metastatic colorectal cancer: a retrospective consortium analysis. *Lancet Oncol.* 2010;11:753–762.
22. Jhawer M, Goel S, Wilson AJ, et al. PIK3CA mutation/PTEN expression status predicts response of colon cancer cells to the epidermal growth factor receptor inhibitor cetuximab. *Cancer Res.* 2008;68:1953–1961.
23. Tian S, Simon I, Moreno V, et al. A combined oncogenic pathway signature of BRAF, KRAS and PI3KCA mutation improves colorectal cancer classification and cetuximab treatment prediction. *Gut.* 2013;62:540–549.
24. Sartore-Bianchi A, Martini M, Molinari F, et al. PIK3CA mutations in colorectal cancer are associated with clinical resistance to EGFR-targeted monoclonal antibodies. *Cancer Res.* 2009;69:1851–1857.
25. Douillard J-Y, Oliner KS, Siena S, et al. Panitumumab-FOLFOX4 treatment and RAS mutations in colorectal cancer. *N Engl J Med.* 2013;369:1023–1034.
26. Joung J-G, Oh BY, Hong HK, et al. Tumor Heterogeneity Predicts Metastatic Potential in Colorectal Cancer. *Clin Cancer Res.* 2017;23:7209–7216.
27. Baldus SE, Schaefer K-L, Engers R, et al. Prevalence and heterogeneity of KRAS, BRAF, and PIK3CA mutations in primary colorectal adenocarcinomas and their corresponding metastases. *Clin Cancer Res.* 2010;16:790–799.
28. Losi L, Baisse B, Bouzourene H, et al. Evolution of intratumoral genetic heterogeneity during colorectal cancer progression. *Carcinogenesis.* 2005;26:916–922.
29. Eijkelenboom A, Kamping EJ, Kastner-van Raaij AW, et al. Reliable Next-Generation Sequencing of Formalin-Fixed, Paraffin-Embedded Tissue Using Single Molecule Tags. *The Journal of Molecular Diagnostics.* 2016;18:851–863.
30. Bouaoun L, Sonkin D, Ardin M, et al. TP53 Variations in Human Cancers: New Lessons from the IARC TP53 Database and Genomics Data. *Human Mutation.* 2016;37:865–876.
31. Dahlman KB, Xia J, Hutchinson K, et al. BRAF(L597) mutations in melanoma are associated with sensitivity to MEK inhibitors. *Cancer Discovery.* 2012;2:791–797.
32. Yao Z, Yaeger R, Rodrik-Outmezguine VS, et al. Tumours with class 3 BRAF mutants are sensitive to the inhibition of activated RAS. *Nature.* 2017;548:234–238.
33. Acquaviva G, de Biase D, Diquigiovanni C, et al. BRAF Exon 15 Mutations in Papillary Carcinoma and

Adjacent Thyroid Parenchyma: A Search for the Early Molecular Events Associated with Tumor Development. *Cancers*;12 . Epub ahead of print February 12, 2020. DOI: 10.3390/cancers12020430.

34. Cancer Genome Atlas Network. Comprehensive molecular characterization of human colon and rectal cancer. *Nature*. 2012;487:330–337.
35. Hardiman KM, Ulintz PJ, Kuick RD, et al. Intra-tumor genetic heterogeneity in rectal cancer. *Laboratory Investigation*. 2016;96:4–15.
36. Bettoni F, Masotti C, Habr-Gama A, et al. Intratumoral Genetic Heterogeneity in Rectal Cancer: Are Single Biopsies representative of the entirety of the tumor? *Ann Surg*. 2017;265:e4–e6.
37. Dijkstra JR, Tops BBJ, Nagtegaal ID, et al. The homogeneous mutation status of a 22 gene panel justifies the use of serial sections of colorectal cancer tissue for external quality assessment. *Virchows Arch*. 2015;467:273–278.
38. Mroz EA, Rocco JW. MATH, a novel measure of intratumor genetic heterogeneity, is high in poor-outcome classes of head and neck squamous cell carcinoma. *Oral Oncol*. 2013;49:211–215.

SECTION III

Conclusions



Summary, discussion and
future perspectives

10

SUMMARY

In this thesis, two large oncological entities are discussed: pancreatic and (colo)rectal cancer. In **Section 1**, research on pancreatic cancer is discussed. As overall survival rates of pancreatic cancer patients are currently very low, there are still major steps to be taken to increase patient outcome. One of the contributing factors to the low survival rate is the delayed detection of the disease, typically occurring in its advanced stages when symptoms become apparent. Additionally, unfavorable biological characteristics such as a high presence of stroma and increased resistance to therapy also play a role. The research in this thesis as described in **Section 1**, has focused on improving detection and therapy response evaluation of pancreatic cancer by investigating novel targets for diagnostic targeted molecular imaging and to help differentiate between therapy induced fibrosis and remaining vital tumor cells after neoadjuvant therapy. Colorectal cancer patients on the other hand have a much better prognosis. Improving quality of life is currently a major focus in this field, for example by improving neoadjuvant treatment regimens for the treatment of rectal cancer. When the number of rectal cancer patients with a complete response of all tumor tissue after neoadjuvant therapy increases, the need for drastic operative treatment with its associated risk of complications can be avoided. The research in this thesis as described in **Section 2**, has focused on exploring novel techniques to predict and monitor response to neoadjuvant therapy to optimize treatment regimens possibly resulting in better patient outcomes.

Pancreatic cancer

Current available imaging techniques are unreliable in assessing response to given therapies. In addition, they are unable to accurately differentiate between (vital) tumor tissue and therapy induced fibrosis and inflammation in pancreatic cancer patients after neoadjuvant therapy. Targeted molecular imaging (e.g. tumor targeted PET/CT) might provide a solution to this problem. **Chapter 2** provides a narrative review of the available scientific evidence on clinically tested tumor targeted PET/CT tracers for the detection of pancreatic cancer. The sensitivity of FDG-PET/CT for detecting pancreatic carcinoma varies, but it is generally reported to be moderate to high (70-90%). However, it is difficult to differentiate pancreatic carcinoma from pancreatitis, which also shows a high [¹⁸F]FDG uptake. To overcome this problem, researchers have explored the use of dual-phase PET/CT imaging and various non-FDG imaging tracers to distinguish tumor cells from pancreatitis, therapy-induced fibrosis, necrosis, and inflammation. [¹⁸F]FLT, as well as various tracers targeting fibroblast activating protein (FAP), integrin $\alpha_v\beta_6$, and prostate specific membrane antigen (PSMA) showed promise in detecting pancreatic cancer and providing diagnostic aid in distinguishing vital tumor cells from inflammation. The second part of this review describes the current status of targeted radionuclide therapy in pancreatic cancer. These include ⁹⁰Y, ¹³¹I, and ¹⁷⁷Lu labeled tracers targeting

carcinoembryonic antigen (CEA) and MUC1. Unfortunately, clinical trials have shown conflicting results regarding their effectivity.

As previously mentioned, the treatment of pancreatic cancer is very challenging. This is partly due to the presence of abundant stromal cells, which create physical barriers and prevent systemic treatment from adequately reaching the tumor cells. Stromal cells are part of the tumor microenvironment (TME), which is the environment surrounding tumor cells. The TME includes for example blood vessels, immune cells, stromal cells, and fibroblasts. To illustrate the importance of the TME, malignant cells only account for approximately 30% of tumor mass (depending on cancer type). The rest of the tumor mass consists of e.g. fibroblasts (25%), immune cells (20%), endothelial cells (5%) and macrophages (5%)¹⁻⁴. In recent years, the role and influence of the TME on tumor development and metastases has been studied extensively for both imaging as well as therapeutic purposes. **Chapter 3** provides an extensive overview of the various TME components that can be targeted for imaging purposes, i.e. tumor associated vasculature, immune cells such as macrophages and T-lymphocytes, cancer-associated fibroblasts, and the extracellular matrix. As described in this chapter, a lot of clinical data is available on the use of tumor vasculature targeting agents (e.g. targeting the RGD sequence) for use in various imaging modalities such as PET/CT or NIR fluorescent imaging. In addition, with increasing use of immunotherapy for many indications, there is a lot of interest in immune cell imaging in order to predict response to immunotherapy (e.g. PD-1, PD-L1). Finally, FAP targeted imaging has revealed to be very promising recently, being subject of multiple studies. As FAP shows promise to be a pan-cancer target for imaging and therapeutics, various PET and radionuclide therapy tracers have been developed and are currently tested in clinical trials all over the world. In the future, visualization of the TME might provide extra information about the potential aggressiveness of the tumor or the potential therapeutic efficacy of targeted therapies.

Chapter 4 displays the results from a preclinical study investigating novel targets for molecular imaging of pancreatic cancer, more specifically after neoadjuvant FOLFIRINOX therapy, to aid in the beforementioned diagnostic challenges. Expression of integrin $\alpha_v\beta_6$, carcinoembryonic antigen cell adhesion molecule 5 (CEACAM5), mesothelin, PSMA, urokinase-type plasminogen activator receptor (uPAR), FAP, integrin α_5 and epidermal growth factor receptor (EGFR) were evaluated using immunohistochemistry on tissue slides. Integrin $\alpha_v\beta_6$, CEACAM5, mesothelin and PSMA immunohistochemistry stainings showed significantly higher expression in pancreatic cancer compared to tumor associated pancreatitis and pre-existing normal pancreatic parenchyma. No expression of $\alpha_v\beta_6$, CEACAM5 and mesothelin was observed in therapy induced fibrosis. Integrin $\alpha_v\beta_6$ and CEACAM5 allowed for metastatic lymph node detection with a sensitivity and specificity of 83-100% and 100% respectively. In conclusion, targeting integrin $\alpha_v\beta_6$, CEA,

and mesothelin has the potential to distinguish vital pancreatic cancer cells from fibrotic tissue after neoadjuvant FOLFIRINOX treatment. Integrin $\alpha_v\beta_6$ and CEACAM5 detect both primary tumors and tumor positive lymph nodes.

In **Chapter 5**, the next step is taken towards clinical use of a targeted PET/CT tracer in pancreatic cancer. A PSMA targeted tracer, [^{18}F]DCFPyL, which is normally used for the imaging of prostate cancer, was repurposed and its potential to detect primary colon-, gastric- and pancreatic cancer was investigated. A total of 11 patients was included in this clinical pilot study, and all underwent preoperative [^{18}F]DCFPyL and [^{18}F]FDG PET/CT and imaging results were compared. The detection of colon-, gastric- and pancreatic cancers using [^{18}F]DCFPyL PET/CT was feasible, as the primary tumor was detected in 7 out of 10 patients using [^{18}F]DCFPyL. However, relatively low [^{18}F]DCFPyL uptake in the tumor and high physiological uptake in both organs and background hampered clear distinction of the tumor in most patients. As a result, [^{18}F]FDG PET/CT was superior in detecting colon-, gastric and pancreatic cancers. Following these results, no further research is warranted into the use of [^{18}F]DCFPyL in these cancer types without prior selection. Such a selection process could for instance consist of PSMA specific immunohistochemistry staining of pre-operative biopsy material, which may possibly be able to detect tumors with high PSMA expression in patients who could benefit from [^{18}F]DCFPyL PET/CT imaging.

(Colo)rectal cancer

Currently, primary staging and restaging of rectal cancer is performed using multiparametric MRI and endoscopy. Unfortunately, previous studies have demonstrated varying and low sensitivity and specificity most evidently seen at restaging after neoadjuvant therapy. In **Chapter 6**, a regional retrospective study in rectal cancer patients demonstrated a low sensitivity of MRI for determining T stage (48.4-58.0%) and N stage (35.5-65.2%). As a result, a significant number of patients received incorrect treatment due to over- or understaging (22.2% in immediate surgery group, 68.8% in short course radiotherapy group). Interestingly, in all cases this was due to incorrect N staging. These results showed a trend towards more overstaging in lower T stages, understaging in higher T stages, and general understaging for N stage. This research adds to the evidence demonstrating low accuracy of MRI for both T and N staging in rectal cancer, and warrants future research to ensure accurate staging, enabling correct treatment decision making.

In **Chapter 7**, an overview is provided on the potential use of [^{18}F]FDG PET/CT for treatment response evaluation in colorectal cancer. This overview was written for educational purposes. Twenty clinical cases with corresponding radiological images are displayed, and teaching points for each case were discussed. Cases discussed in this chapter included response monitoring during and after neoadjuvant chemoradiation,

local treatment of liver metastases, neoadjuvant treatment of recurrent rectal cancer and palliative systemic treatment of hepatic and extrahepatic disease.

In **Chapter 8** the feasibility of response prediction using digital [^{18}F]FDG PET/CT and multiparametric MRI before, during and after neoadjuvant chemoradiation therapy in locally advanced rectal cancer patients was investigated. In addition to the anatomical information MRI provides, digital [^{18}F]FDG PET/CT can provide metabolic information on the tumor over time. Moreover, digital PET/CT provides higher resolution over conventional PET/CT scanners, potentially enabling the detection of smaller tumor nodules or metastatic lymph nodes. In this clinical pilot study, 19 rectal cancer patients were included and underwent both digital [^{18}F]FDG PET/CT and multiparametric MRI before, during and after neoadjuvant chemoradiation therapy. From these imaging studies, 57 imaging features were extracted based on their ability to distinguish between good and poor response to neoadjuvant therapy. Twelve features from both imaging modalities were selected to be promising, but should be subject to further investigation in a larger prospective trial.

As we know from colorectal cancer, analysis of specific mutations in tumor cells can guide and predict cancer treatment (e.g. *KRAS* mutation predicts efficacy of EGFR targeted therapies). Likewise, analysis of mutations in preoperative biopsy samples might predict efficacy of (neo)adjuvant therapy in rectal cancer patients. With this purpose in mind, the research described in **Chapter 9** was set up. As a step towards predicting response based on mutational analysis of biopsy samples, the accuracy (i.e. repeatability) of this method had to be established. As we know, tumor heterogeneity results in various clones/populations of tumor cells spread throughout one tumor. With this in mind, analyzing one single biopsy sample taken from only the luminal side of a tumor (as this is the only side accessible by endoscopy) might not be representative for all tumor cell populations in the tumor. This study aimed to investigate the influence of this tumor heterogeneity on the results from mutational analysis from biopsy material. Results from mutational analysis of biopsy material were compared to tissue from 4 other locations within the same tumor using next generation sequencing. Results from this study showed that different mutations were found in various samples from one tumor in 36% of 11 included patients. This resulted in the conclusion that assessment of mutational status on a single pre-operative biopsy sample was inadequate in a substantial proportion of patients, and its use warrants careful interpretation.

GENERAL DISCUSSION

Although various questions have been answered by the work in this thesis, many more questions and data gaps have been brought to light. More than anything, the work in this thesis once again underlines the complexity of processes involved in cancer treatment. It highlights the fact that using our current “simplistic” approaches (searching for one all-encompassing predicting parameter) is challenging to accurately predict response to therapy.

This challenge in predicting response to therapy is demonstrated by various studies in this thesis. In **Chapter 4**, immunohistochemistry experiments were employed to identify potential targets that could serve as imaging targets (i.e. to predict which imaging targets/ tracers could be successful in the clinic). The degree of expression of a certain biomarker is hypothesized to correlate with tracer uptake during e.g. PET/CT or NIR fluorescent imaging. Although there are certainly many different applications in which this approach has been successful, the immunohistochemical experiments described in this chapter followed by the unsatisfactory results from the clinical implementation in **Chapter 5** demonstrate an example of how difficult it can be to predict clinical imaging results based on immunohistochemistry experiments. Several critical questions regarding the method of using immunohistochemistry to predict clinical imaging results can be posed. First, how accurate and quantifiable is this assessment of the degree of expression? As in this thesis the rating was performed visually by the pathologist, we can at best get an estimate of the percentage of cells staining and the corresponding intensity. As a pathologist is not able to count and assess all cells separately, no exact measurement can be performed using this method. In recent years, (semi)automated software such as QuPath⁵ has been developed to more accurately quantify immunohistochemical stainings. After training the software to identify certain cell types (e.g. tumor cells, stromal cells), it can provide detailed information on the percentage and intensity of cells stained. Unfortunately, this software was not yet readily available at the time of the experiments in this thesis.

Next, as only one tissue slide from each tumor was assessed, it could be difficult to make an overall assessment of the ‘total available binding sites’ that are available in the tumor for imaging agents to bind to. Although one could assume that you can deduct the total biomarker expression in a tumor from a sample tissue slide, various factors can influence this estimation. For example, expression of certain biomarkers can vary throughout the tumor due to e.g. tumor heterogeneity or increased expression in for example the invasive front of the tumor. Such differences in expression pattern can possibly result in an incorrect estimate on overall biomarker expression in a certain tumor. As demonstrated in **Chapter 9**, tumor heterogeneity in for example rectal

cancer can significantly influence results from such sample testing approaches. As the assessment of various tissue slides per tumor is very time consuming for the pathologist, the use of software such as QuPath could enable research groups to assess multiple slides per tumor, and improve their estimate of biomarker expression throughout the whole tumor. A third question regarding this approach refers to what degree of biomarker expression is sufficient to enable *in vivo* imaging of this target with satisfactory contrast to physiological uptake in adjacent organs. Intense physiological expression of the target biomarker in adjacent tissue can hamper tumor detection, as experienced in **Chapter 5**. More specific to this study; significant tracer uptake in the gastric wall, pancreas, liver, gallbladder, spleen and small intestines hampered clear identification of pancreatic, colon and gastric tumors. In the search for imaging targets, not only uptake in the target organ itself should be considered, but also uptake in the surrounding organs as this can hamper tumor identification. Depending on the tumor type and location, different background organs should be considered. Finally, in addition to the percentage of cells stained and the intensity of this staining, the cellular location of the found expression should be taken into account. Previously, mostly tumor cells were targeted directly for imaging and treatment purposes. More recently, stromal cells (surrounding the tumor cells) are also being targeted, as these represent a significant part of tumor content as well. To illustrate, stromal cells can account for up to 90% of tumor mass in pancreatic cancer⁶. Neovascularity is part of this stroma, and consists of endothelial cells. As described in **Chapter 4**, moderate PSMA expression was found in the endothelial cells in pancreatic cancer. As endothelial cells only account for a few percent of total tumor mass, this resulted in a relatively low ‘total’ expression in terms of available binding sites for imaging tracer (a few percent of the tumor mass x moderate staining = low number of total binding sites). This has possibly contributed to the unsatisfactory results in **Chapter 5**.

A second lesson that can be learned from the work in this thesis, is how difficult it is to find a (combination of) parameter(s) for prediction of clinical results (e.g. response to therapy). Not only the predictive ability of such parameters is important, but also whether they are representative for the whole tumor (in case samples are taken) and whether these samples or measurements are repeatable and result in similar results. A first example of such a challenge regarding representation of the whole tumor and consequent repetition of measurements is found in the work performed in **Chapter 9**. In this study, different mutation profiles were found within various samples from the same tumor in 36% of patients. These results demonstrate how tumor heterogeneity influences the results of mutational analysis when using biopsy material versus using the whole tumor specimen, and thus question the suitability of mutational analysis from biopsy material for response prediction. Unfortunately, only the luminal side of the tumor is accessible for biopsy during endoscopy, thus no data can be acquired on the

non-luminal tumor parts using this method. Of note, this problem is only relevant for heterogeneous tumors, as in completely homogeneous tumors the results will be identical regardless of the biopsy location. In contrast to using biopsy material and extrapolate results derived from a sample, the use of imaging methods such as PET/CT provide a method to acquire data on the full tumor including all its heterogeneous cell populations. A second example of this challenge to find suitable predicting parameters is found in the work described in **Chapter 8**, where not only the type of scan (MRI or [¹⁸F]FDG PET/CT) but also the timing of the scan in the treatment period and the use of different scanners and scanning protocols is of great importance when trying to predict response. Following this second example, a very strict and consequent study protocol is required to be able to investigate such multimodal approaches. On the other hand, results derived from studies performed in such highly controlled environments might be difficult to translate and apply to the clinical setting as this setting is not as controlled. This results in the following paradox that complex prediction models including data from various different modalities might be able to predict response with sufficient accuracy, but could be difficult to implement in the daily clinical setting. One opportunity to decrease variability in scanning results, could be the use of combined PET-MRI scans, instead of the two separately. One of the many advantages of combined PET-MRI could be increased delineation of the tumor and/or (metastatic) lymph nodes (as you can now reference to MRI instead of CT images).

This paradox should stimulate us as researchers and clinicians to search for ways in which we can use the already available information to support informed clinical decision making. This is more relevant than ever, as there is a vast amount of information gathered in the standard diagnostic work up of every single patient, and tools for analysis and subsequent prediction model development of such large quantities of data improve by the day.

FUTURE PERSPECTIVES

There is a great number of promising developments in the field of molecular imaging. Many new targeted imaging tracers are being developed, scanner technology is constantly improving, and guidelines are being developed to advise on the best (evidence based) way to use these newly available technologies. The use of successfully translated PET/CT tracers such as [¹⁸F]FDG have been implemented in national guidelines, as for example to detect recurrent disease (indicated by increase CEA levels) in the follow up after surgical resection of colorectal cancer⁷.

Various research groups are currently investigating the further application of [¹⁸F]FDG

in diagnosis and treatment response monitoring of both rectal and pancreatic cancer. A recent example of this is found in the publication of the PandigPET study⁸. In this trial, the additional value of digital [¹⁸F]FDG PET/CT in primary staging and restaging after neoadjuvant therapy in pancreatic cancer was investigated. Results from this trial demonstrated a strong positive correlation between change in [¹⁸F]FDG uptake and change in CT tumor diameter and change in CA19-9. In addition, the application of digital [¹⁸F]FDG PET/CT resulted in detection of previously unknown small liver metastases in 5 out of 35 patients. These results warrant further exploration of the additional value of digital [¹⁸F]FDG PET/CT in pancreatic cancer, as it could possibly improve both initial staging and response monitoring. Currently, a similar study (IMAGE-PET trial) is being conducted by our colleagues at the Amsterdam UMC to investigate whether a decline in [¹⁸F]FDG uptake correlates to surgical resectability, biological tumor marker response and pathological response.

In addition to [¹⁸F]FDG, other PET/CT tracers are being developed and tested in clinical trials. In our own research group, we are currently working on the clinical implementation of various novel PET/CT tracers for the detection and response monitoring of pancreatic cancer. These include [¹⁸F]Fluciclatide (NL7605), [¹⁸F]FP-R₀1-MG-F2⁹ and [⁶⁸Ga]Ga-FAPI-46¹⁰, targeting a combination of integrins, integrin $\alpha_v\beta_6$ and the fibroblast activation protein (FAP), respectively. Focusing on the latter one, FAP is expressed by cancer associated fibroblasts in most cancer types. Since its first introduction into human clinical trials in 2019, interest in this tracer has spiked as this may prove to be a novel pan-cancer imaging tracer with great diagnostic and therapeutic potential. As investigated in **Chapter 2** of this thesis in a preclinical setting, and later confirmed by results from various clinical trials, targeting FAP indeed has great potential in diagnosis and treatment of pancreatic cancer¹¹⁻¹³. A recent systematic review and meta-analysis by our group on the diagnostic test accuracy of FAPI PET/CT in hepato-pancreato-biliary (HPB) tumors (Henrar *et al.*, to be published) concluded that FAPI PET/CT demonstrated higher uptake (mean SUV_{max} 15.6, 95% CI 12.4-18.9) compared to [¹⁸F]FDG PET/CT (mean SUV_{max} 6.5, 95% CI 4.4-8.5) in 242 pancreatic cancer patients. In addition, the detection rate of FAPI PET/CT was significantly higher in hepatocellular carcinoma, biliary tract cancers and lymph node-, liver- or distant metastases from all HPB tumors compared to [¹⁸F]FDG PET/CT. In addition to its diagnostic potential, it could serve as a theranostic agent, and thus also be used for e.g. radionuclide therapy. A recent review by colleagues from the Radboud Medical Center (Nijmegen, The Netherlands) concluded that FAP targeted radionuclide therapy using tracers such as [⁹⁰Y]-FAPI-46 and [¹⁷⁷Lu]-FAPI-46 has already been tested in various limited case series in more than 100 cancer patients¹⁴. Early results encourage further investigation, with therapy responses observed in difficult to treat end stage cancer patients and manageable adverse events. The first results from prospective clinical basket trials are expected in the upcoming year (e.g. NCT04939610, NCT05723640).

Next to diagnosing cancer, much effort is currently put into developing reliable methods to predict and monitor response to cancer therapy^{15–18}. With increasing use of neoadjuvant therapy to enhance both surgical and survival outcomes, many new neoadjuvant treatment regimens are currently under investigation. To illustrate this, both the Dutch Pancreatic Cancer Group (DPCG) and the Dutch Colorectal Cancer Group (DCCG) have conducted various clinical trials over the last years investigating novel combinations for neoadjuvant therapy. These include for example the PREOPANC-1 and -2 trials (and currently ongoing PREOPANC-3 and -4) in pancreatic cancer and the RAPIDO trial in rectal cancer^{19–23}. Accurate prediction of response to a certain anti-cancer therapy could be used to choose the most effective treatment regimen at an individual patient level. Inefficient treatment with often serious risk of complications and adverse events could be avoided, and possibly patient outcomes could be improved. An example of this is seen in patients with advanced pancreatic cancer, who according to the local guideline are treated with FOLFIRINOX. Although many patients benefit from this therapy, there is also a subset of patients who are unresponsive to this therapy but do experience severe toxicity (including e.g. neutropenia, thrombocytopenia and diarrhea). The PANCAKE study, another initiative of the DPCG, currently investigates whether certain biomarkers such as ctDNA, microRNA, or SNPs might be able to predict response to FOLFIRINOX therapy²⁴.

As it is difficult to find one single parameter from clinical, imaging, or pathological data that has enough accuracy to predict response at an individual patient level, much effort is put into the development of prediction models in which multiple of these parameters are combined. As neoadjuvant therapy for rectal cancer patients has been implemented for several years now with great success (pCR rate ~10-30%^{25–29}), there is a vast amount of data available to develop such models. To illustrate, a recent publication in the *Lancet* by Feng *et al.*, describes the development and validation of the RAPIDS prediction model³⁰. This model was constructed by machine learning based on both MRI radiomics and histological pathomics pre-treatment data. The final model (after training and validating in 3 data sets with over 900 patients) was able to predict pCR with a sensitivity of 89% and specificity of 74%.

In the future, I foresee a significant role for molecular imaging using PET/CT to enable more accurate diagnosis and guide individualized patient treatment. Together with prediction models such as the ones mentioned before in this thesis, I hope this will further increase our ability to select the optimal treatment for the individual patient. By doing so, we might be able to select the most effective anti-cancer treatment and avoid unnecessary adverse events from ineffective treatment regimens.

REFERENCES

1. Puram SV, Tirosh I, Parikh AS, et al. Single-cell transcriptomic analysis of primary and metastatic tumor ecosystems in head and neck cancer. *Cell*. 2017;171:1611–1624.e24.
2. Yu X, Chen YA, Conejo-Garcia JR, et al. Estimation of immune cell content in tumor using single-cell RNA-seq reference data. *BMC Cancer*. 2019;19:715.
3. Smits AJJ, Kummer JA, de Bruin PC, et al. The estimation of tumor cell percentage for molecular testing by pathologists is not accurate. *Mod Pathol Off J U S Can Acad Pathol Inc*. 2014;27:168–174.
4. Lambrechts D, Wauters E, Boeckx B, et al. Phenotype molding of stromal cells in the lung tumor microenvironment. *Nat Med*. 2018;24:1277–1289.
5. QuPath: Open source software for digital pathology image analysis - PubMed Available from: <https://pubmed.ncbi.nlm.nih.gov/29203879/>. Accessed June 19, 2023.
6. Leppänen J, Lindholm V, Isohookana J, et al. Tenascin C, Fibronectin, and Tumor-Stroma Ratio in Pancreatic Ductal Adenocarcinoma. *Pancreas*. 2019;48:43–48.
7. Startpagina - Colorectaal carcinoom (CRC) - Richtlijn - Richtlijndatabase Available from: https://richtlijndatabase.nl/richtlijn/colorectaal_carcinoom_crc/startpagina_-_cnc.html. Accessed June 19, 2023.
8. de Jong TL, Koopman D, van der Worp CAJ, et al. Added value of digital FDG-PET/CT in disease staging and restaging in patients with resectable or borderline resectable pancreatic cancer. *Surg Oncol*. 2023;47:101909.
9. Nakamoto R, Ferri V, Duan H, et al. Pilot-phase PET/CT study targeting integrin $\alpha\beta 6$ in pancreatic cancer patients using the cystine-knot peptide-based 18F-FP-R01-MG-F2. *Eur J Nucl Med Mol Imaging*. 2022;50:184–193.
10. PANSCAN-1 - studie (Alvleesklierkanker, Galwegkanker) - Onderzoekbijkanker.nl Available from: <https://www.onderzoekbijkanker.nl/trials-zoeken/trial/1367/panscan-1-studie-alvleesklierkanker-galwegkanker.html>. Accessed June 18, 2023.
11. Evangelista L, Frantellizzi V, Schillaci O, et al. Radiolabeled FAPI in pancreatic cancer: can it be an additional value in the management of patients? *Expert Rev Anticancer Ther*. 2023;23:745–752.
12. Veldhuijzen van Zanten SEM, Pieterman KJ, Wijnhoven BPL, et al. FAPI PET versus FDG PET, CT or MRI for Staging Pancreatic-, Gastric- and Cholangiocarcinoma: Systematic Review and Head-to-Head Comparisons of Diagnostic Performances. *Diagn Basel Switz*. 2022;12:1958.
13. Kratochwil C, Flechsig P, Lindner T, et al. 68Ga-FAPI PET/CT: Tracer Uptake in 28 Different Kinds of Cancer. *J Nucl Med Off Publ Soc Nucl Med*. 2019;60:801–805.
14. Privé BM, Boussihmad MA, Timmermans B, et al. Fibroblast activation protein-targeted radionuclide therapy: background, opportunities, and challenges of first (pre)clinical studies. *Eur J Nucl Med Mol Imaging*. 2023;50:1906–1918.
15. Maffione AM, Marzola MC, Capirci C, et al. Value of (18)F-FDG PET for Predicting Response to Neoadjuvant Therapy in Rectal Cancer: Systematic Review and Meta-Analysis. *AJR Am J Roentgenol*. 2015;204:1261–1268.
16. Koo PJ, Kim S-J, Chang S, et al. Interim Fluorine-18 Fluorodeoxyglucose Positron Emission Tomography/Computed Tomography to Predict Pathologic Response to Preoperative Chemoradiotherapy and

- Prognosis in Patients With Locally Advanced Rectal Cancer. *Clin Colorectal Cancer*. 2016;15:e213–e219.
17. Joye I, Deroose CM, Vandecaveye V, et al. The role of diffusion-weighted MRI and (18)F-FDG PET/CT in the prediction of pathologic complete response after radiochemotherapy for rectal cancer: a systematic review. *Radiother Oncol J Eur Soc Ther Radiol Oncol*. 2014;113:158–165.
 18. van Stiphout RGPM, Valentini V, Buijsen J, et al. Nomogram predicting response after chemoradiotherapy in rectal cancer using sequential PETCT imaging: a multicentric prospective study with external validation. *Radiother Oncol J Eur Soc Ther Radiol Oncol*. 2014;113:215–222.
 19. Versteijne E, van Dam JL, Suker M, et al. Neoadjuvant Chemoradiotherapy Versus Upfront Surgery for Resectable and Borderline Resectable Pancreatic Cancer: Long-Term Results of the Dutch Randomized PREOPANC Trial. *J Clin Oncol Off J Am Soc Clin Oncol*. 2022;40:1220–1230.
 20. Janssen QP, van Dam JL, Bonsing BA, et al. Total neoadjuvant FOLFIRINOX versus neoadjuvant gemcitabine-based chemoradiotherapy and adjuvant gemcitabine for resectable and borderline resectable pancreatic cancer (PREOPANC-2 trial): study protocol for a nationwide multicenter randomized controlled trial. *BMC Cancer*. 2021;21:300.
 21. PREOPANC-3 studie (Alveesklierkanker) | Kanker.nl Available from: <https://www.kanker.nl/trials/1229-preopanc-3-studie-alveesklierkanker>. Accessed June 18, 2023.
 22. PREOPANC-4 - studie (Alveesklierkanker) | Kanker.nl Available from: <https://www.kanker.nl/trials/1303-preopanc-4---studie-alveesklierkanker>. Accessed June 18, 2023.
 23. Dijkstra EA, Nilsson PJ, Hospers GAP, et al. Locoregional Failure During and After Short-course Radiotherapy followed by Chemotherapy and Surgery Compared to Long-course Chemoradiotherapy and Surgery - A Five-year Follow-up of the RAPIDO Trial. *Ann Surg*. . Epub ahead of print January 20, 2023. DOI: 10.1097/SLA.0000000000005799.
 24. PANCAKE - studie (Alveesklierkanker) - Onderzoekbijkanker.nl Available from: <https://www.onderzoekbijkanker.nl/trials-zoeken/trial/1218/pancake-studie-alveesklierkanker.html>. Accessed June 18, 2023.
 25. Maas M, Beets-Tan RGH, Lambregts DMJ, et al. Wait-and-see policy for clinical complete responders after chemoradiation for rectal cancer. *J Clin Oncol Off J Am Soc Clin Oncol*. 2011;29:4633–4640.
 26. Maas M, Nelemans PJ, Valentini V, et al. Long-term outcome in patients with a pathological complete response after chemoradiation for rectal cancer: a pooled analysis of individual patient data. *Lancet Oncol*. 2010;11:835–844.
 27. Rödel C, Martus P, Papadopoulos T, et al. Prognostic significance of tumor regression after preoperative chemoradiotherapy for rectal cancer. *J Clin Oncol Off J Am Soc Clin Oncol*. 2005;23:8688–8696.
 28. de Campos-Lobato LF, Stocchi L, da Luz Moreira A, et al. Pathologic complete response after neoadjuvant treatment for rectal cancer decreases distant recurrence and could eradicate local recurrence. *Ann Surg Oncol*. 2011;18:1590–1598.
 29. Shin JK, Huh JW, Lee WY, et al. Clinical prediction model of pathological response following neoadjuvant chemoradiotherapy for rectal cancer. *Sci Rep*. 2022;12:7145.
 30. Feng L, Liu Z, Li C, et al. Development and validation of a radiopathomics model to predict pathological complete response to neoadjuvant chemoradiotherapy in locally advanced rectal cancer: a multicentre observational study. *Lancet Digit Health*. 2022;4:e8–e17.

Nederlandse samenvatting

11

NEDERLANSE SAMENVATTING

In dit proefschrift worden twee oncologische entiteiten besproken: alveesklier- en (colo)rectaalkanker. In **Sectie 1** wordt onderzoek naar alveesklierkanker besproken. Aangezien de overlevingskansen van patiënten met alveesklierkanker momenteel erg laag zijn, moeten er nog grote stappen worden gezet om de uitkomst voor patiënten te verbeteren. Een van de oorzaken van dit lage overlevingspercentage is de late detectie van de ziekte, doordat pas laat in het ziekteproces klachten tot uiting komen. Daarnaast spelen ongunstige biologische kenmerken zoals de hoge hoeveelheid stroma en hoge resistentie tegen therapie ook een rol. Het onderzoek in deze scriptie, zoals beschreven in **Sectie 1**, heeft zich gericht op het verbeteren van de detectie en evaluatie van therapierespons van alveesklierkanker door het onderzoeken van nieuwe targets voor moleculaire beeldvorming en om bijvoorbeeld onderscheid te kunnen maken tussen door therapie veroorzaakte fibrose en resterende vitale tumorcellen na neoadjuvante therapie. Aan de andere kant hebben patiënten met colorectale kanker een veel betere prognose. Het verbeteren van de kwaliteit van leven is momenteel een belangrijke focus op dit gebied, bijvoorbeeld door verbeterde neoadjuvante behandelingsregimes in de behandeling van rectumkanker. Wanneer het aantal patiënten met rectumkanker met een volledige respons van al het tumorweefsel na neoadjuvante therapie toeneemt, kan de noodzaak voor ingrijpende operatieve behandeling met het bijbehorende risico op complicaties worden vermeden. Het onderzoek in deze scriptie, zoals beschreven in **Sectie 2**, heeft zich gericht op het verkennen van nieuwe technieken om respons op neoadjuvante therapie te voorspellen en te monitoren om behandelingschema's te optimaliseren, wat mogelijk kan resulteren in betere uitkomsten voor patiënten.

Alveesklierkanker

Huidige beschikbare beeldvormingstechnieken zijn onvoldoende betrouwbaar bij het beoordelen van de respons op gegeven therapieën. Bovendien kunnen ze geen accuraat onderscheid maken tussen (vitale) tumorcellen en door therapie veroorzaakte fibrose en ontsteking bij patiënten met alveesklierkanker na neoadjuvante therapie. Gerichte moleculaire beeldvorming (bijv. tumorgerichte PET/CT) zou een oplossing kunnen bieden voor dit probleem. **Hoofdstuk 2** biedt een beschrijvend overzicht van het beschikbare wetenschappelijke bewijs over klinisch geteste tumorgerichte PET/CT-tracers voor de detectie van alveesklierkanker. De gevoeligheid van FDG-PET/CT voor het detecteren van alveesklierkanker varieert, maar wordt over het algemeen ervaren als matig tot hoog (70-90%). Het is echter moeilijk om alveesklierkanker te onderscheiden van pancreatitis, dat ook een hoge [¹⁸F]FDG-opname laat zien. Om dit probleem te overwinnen, hebben onderzoekers het gebruik van dual-fase PET/CT-beeldvorming en verschillende niet-FDG-tracers onderzocht om tumorcellen te onderscheiden van pancreatitis, door therapie veroorzaakte fibrose, necrose en ontsteking. [¹⁸F]FLT,

evenals verschillende tracers die fibroblast activerend eiwit (FAP), integrine $\alpha\beta 6$ en prostaatspecifiek membraanantigeen (PSMA) targeten, leken veelbelovend voor het detecteren van alveesklierkanker en als diagnostische hulp bij het onderscheiden van vitale tumorcellen van ontsteking. Het tweede deel van dit overzicht beschrijft de huidige status van radio-isotooptherapie bij alveesklierkanker. Deze omvatten ⁹⁰Y, ¹³¹I en ¹⁷⁷Lu gelabelde tracers gericht op het carcino-embryonaal antigeen (CEA) en MUC1. Helaas hebben klinische onderzoeken tot nu toe tegenstrijdige resultaten laten zien over hun effectiviteit.

Zoals eerder vermeld is de behandeling van alveesklierkanker zeer uitdagend. Dit komt deels door de aanwezigheid van veel stromacellen, die fysieke barrières creëren en voorkomen dat systemische behandeling de tumorcellen adequaat bereikt. Stromacellen maken deel uit van de tumor microenvironment (TME), wat de omgeving rondom tumorcellen beslaat. De TME omvat bijvoorbeeld bloedvaten, immuuncellen, stromacellen en fibroblasten. Om het belang van de TME te illustreren, vertegenwoordigen kwaadaardige cellen slechts ongeveer 30% van de totale tumormassa (afhankelijk van het type kanker). De rest van de tumormassa bestaat bijvoorbeeld uit fibroblasten (25%), immuuncellen (20%), endotheelcellen (5%) en macrofagen (5%)¹⁻⁴. De rol en invloed van de TME op tumorgroei en uitzaaiingen zijn de afgelopen jaren uitgebreid bestudeerd, zowel voor beeldvormings- als therapeutische doeleinden. **Hoofdstuk 3** biedt een uitgebreid overzicht van de verschillende componenten van de TME die kunnen worden gebruikt voor beeldvormingsdoeleinden, zoals vasculatuur geassocieerd met tumoren, immuuncellen zoals macrofagen en T-lymfocyten, kankergerelateerde fibroblasten en de extracellulaire matrix. Zoals beschreven in dit hoofdstuk is er veel klinische data beschikbaar over het gebruik van middelen die gericht zijn op de tumorvasculatuur (bijv. gericht op de RGD-sequentie) voor gebruik in verschillende beeldvormingstechnieken zoals PET/CT of NIR-fluorescentiebeeldvorming. Bovendien is er met toenemend gebruik van immunotherapie voor veel indicaties veel interesse in het afbeelden van immuuncellen om reacties op immunotherapie te voorspellen (bijv. PD-1, PD-L1). Ten slotte is het gerichte FAP-beeldvorming onlangs zeer veelbelovend gebleken en is het onderwerp geweest van meerdere studies. Aangezien FAP veelbelovend lijkt als een target voor veel/alle kankers voor beeldvorming en therapie, zijn verschillende PET- en radio-isotooptherapietracers ontwikkeld en worden deze momenteel getest in klinische onderzoeken over de hele wereld. In de toekomst kan visualisatie van de TME extra informatie opleveren over de potentiële agressiviteit van de tumor of de potentiële therapeutische werkzaamheid van gerichte therapieën.

Hoofdstuk 4 toont de resultaten van een preklinische studie die nieuwe targets onderzoekt voor moleculaire beeldvorming van alveesklierkanker, specifiek na neoadjuvante FOLFIRINOX-therapie, om te helpen bij de eerder genoemde diagnostische uitdagingen.

Expressie van integrine $\alpha\beta 6$, carcino-embryonaal antigeen celadhesiemolecuul 5 (CEACAM5), mesotheline, PSMA, urokinase-type plasmine activator receptor (uPAR), FAP, integrine $\alpha 5$ en epidermale groeifactorreceptor (EGFR) werden geëvalueerd met behulp van immunohistochemie op weefselcoupes. Immunohistochemische-kleuringen van integrine $\alpha\beta 6$, CEACAM5, mesotheline en PSMA vertoonden aanzienlijk hogere expressie bij alveesklierkanker in vergelijking met tumor geassocieerde pancreatitis en het onaangetaste pre-existente pancreasweefsel. Er werd geen expressie van $\alpha\beta 6$, CEACAM5 en mesotheline waargenomen bij door therapie veroorzaakte fibrose. Integrine $\alpha\beta 6$ en CEACAM5 maakten detectie van gemetastaseerde lymfeklieren mogelijk met een gevoeligheid en specificiteit van respectievelijk 83-100% en 100%. Concluderend hebben beeldvorming gericht op integrine $\alpha\beta 6$, CEA en mesotheline potentie om vitale alveesklierkankercellen te onderscheiden van fibrotisch weefsel na neoadjuvante FOLFIRINOX-behandeling. Integrine $\alpha\beta 6$ en CEACAM5 detecteren zowel primaire tumoren als tumor positieve lymfeklieren.

In **Hoofdstuk 5** wordt de volgende stap gezet naar het klinische gebruik van een gerichte PET/CT-tracer bij alveesklierkanker. Een op PSMA gerichte tracer, [^{18}F]DCFPyL, die normaal gesproken wordt gebruikt voor de beeldvorming van prostaatkanker, werd gebruikt en zijn potentie om primaire colon-, maag- en alveesklierkanker te detecteren werd onderzocht. In totaal namen 11 patiënten deel aan deze klinische pilotstudie, en allen ondergingen preoperatieve [^{18}F]DCFPyL en [^{18}F]FDG PET/CT en de beeldvormingsresultaten werden vergeleken. De detectie van colon-, maag- en alveesklierkanker met behulp van [^{18}F]DCFPyL PET/CT was mogelijk, aangezien de primaire tumor werd gedetecteerd bij 7 van de 10 patiënten met [^{18}F]DCFPyL. Echter, een relatief lage opname van [^{18}F]DCFPyL in de tumor en een hoge fysiologische opname in zowel organen als achtergrond bemoeilijkten een duidelijk onderscheid van de tumor bij de meeste patiënten. Als gevolg hiervan was [^{18}F]FDG PET/CT superieur in het detecteren van colon-, maag- en alveesklierkanker. Naar aanleiding van deze resultaten is verder onderzoek naar het gebruik van [^{18}F]DCFPyL bij deze soorten kanker niet gerechtvaardigd zonder voorafgaande selectie. Een dergelijk selectieproces kan bijvoorbeeld bestaan uit PSMA-specifieke immunohistochemiekleuring van preoperatief biopsiemateriaal, wat mogelijk tumoren met een hoge PSMA-expressie kan detecteren bij patiënten die baat zouden kunnen hebben bij [^{18}F]DCFPyL PET/CT-beeldvorming.

(Colo)rectumkanker

Momenteel wordt de primaire stadiering en restadiering van rectumkanker uitgevoerd met behulp van multiparametrische MRI en endoscopie. Helaas hebben eerdere studies variabele en lage gevoeligheid en specificiteit aangetoond, vooral bij restadiering na neoadjuvante therapie. In **Hoofdstuk 6** toonde een regionale retrospectieve studie bij patiënten met rectumkanker een lage gevoeligheid van MRI aan voor het bepalen

van het T-stadium (48.4-58.0%) en N-stadium (35.5-65.2%). Als gevolg van onjuiste stadiering kreeg een aanzienlijk aantal patiënten onjuiste behandeling vanwege over- of onderschatting (22.2% in de groep met directe chirurgie, 68.8% in de groep met kortdurende radiotherapie). Interessant genoeg was dit in alle gevallen te wijten aan onjuiste N-stadiering. Deze resultaten toonden een trend naar meer overschatting bij lagere T-stadia, onderschatting bij hogere T-stadia, en over het algemeen onderschatting voor N-stadium. Dit onderzoek draagt bij aan het bewijs dat MRI een lage nauwkeurigheid heeft voor zowel T- als N-stadiering bij rectumkanker, en pleit voor toekomstig onderzoek om nauwkeurige stadiering te garanderen, wat beter geïnformeerde behandelbeslissingen mogelijk maakt.

In **Hoofdstuk 7** wordt een overzicht gegeven van het mogelijke gebruik van [^{18}F]FDG PET/CT voor de evaluatie van de behandelingsrespons bij colorectale kanker. Dit overzicht is geschreven voor educatieve doeleinden. Er worden twintig klinische casus met bijbehorende radiologische beelden getoond, en er worden leerpunten besproken voor elke casus. De casus die in dit hoofdstuk worden besproken, omvatten monitoring van respons tijdens en na neoadjuvante chemoradiatie, lokale behandeling van levermetastasen, neoadjuvante behandeling van recidief rectumkanker en palliatieve systemische behandeling van lever- en extrahepatische aandoeningen.

In **Hoofdstuk 8** is de haalbaarheid van voorspelling van respons onderzocht met behulp van digitale [^{18}F]FDG PET/CT en multiparametrische MRI vóór, tijdens en na neoadjuvante chemoradiatiebehandeling bij patiënten met lokaal gevorderde rectumkanker. Naast de anatomische informatie die MRI biedt, kan digitale [^{18}F]FDG PET/CT in de loop van de tijd metabole informatie over de tumor verstrekken. Bovendien biedt digitale PET/CT een hogere resolutie dan conventionele PET/CT-scanners, wat mogelijk de detectie van kleinere tumorknobbels of gemetastaseerde lymfeklieren mogelijk maakt. In deze klinische pilotstudie werden 19 patiënten met rectumkanker opgenomen en ondergingen zowel digitale [^{18}F]FDG PET/CT als multiparametrische MRI vóór, tijdens en na neoadjuvante chemoradiatiebehandeling. Uit deze beeldvormingsstudies werden 57 beeldvormingskenmerken geëxtraheerd op basis van hun vermogen om onderscheid te maken tussen een goede en slechte respons op neoadjuvante therapie. Twaalf kenmerken van beide beeldvormingsmodaliteiten werden als veelbelovend geselecteerd, maar moeten worden onderworpen aan verder onderzoek in een grotere prospectieve proef.

Zoals we weten bij darmkanker kan de analyse van specifieke mutaties in tumorcellen de behandeling van kanker sturen en voorspellen (bijv. voorspelt de KRAS-mutatie de effectiviteit van EGFR-gerichte therapieën). Evenzo zou de analyse van mutaties in preoperatieve biopsie weefsels de potentie kunnen voorspellen van (neo)adjuvante therapie bij patiënten met rectumkanker. Met dit doel voor ogen is het onderzoek

dat beschreven wordt in **Hoofdstuk 9** opgezet. Als een stap naar het voorspellen van respons op basis van mutatieanalyse van biopsie weefsel, moest de herhaalbaarheid van deze methode worden vastgesteld. Zoals we weten leidt tumorheterogeniteit tot verschillende populaties van tumorcellen die zich door de hele tumor verspreiden. Met dit in gedachten, kan het analyseren van slechts één biopsie weefsel dat slechts van de luminale zijde van een tumor is genomen (aangezien dit de enige zijde is die toegankelijk is via endoscopie) mogelijk niet representatief zijn voor alle tumorcelpopulaties in de tumor. Deze studie had tot doel de invloed van deze tumorheterogeniteit op de resultaten van mutatieanalyse van biologisch materiaal te onderzoeken. Resultaten van mutatieanalyse van biopsiemateriaal werden vergeleken met weefsel van 4 andere locaties binnen dezelfde tumor met behulp van next-generation sequencing. Resultaten van deze studie toonden aan dat verschillende mutaties werden gevonden in diverse monsters van één tumor bij 36% van de 11 patiënten. Dit leidde tot de conclusie dat de beoordeling van de mutatiestatus op een enkel preoperatief biopsiemonster onvoldoende accuraat was bij een aanzienlijk aantal patiënten, en het gebruik ervan vereist zorgvuldige interpretatie.

References

1. Puram SV, Tirosh I, Parikh AS, et al. Single-cell transcriptomic analysis of primary and metastatic tumor ecosystems in head and neck cancer. *Cell*. 2017;171:1611-1624.e24.
2. Yu X, Chen YA, Conejo-Garcia JR, et al. Estimation of immune cell content in tumor using single-cell RNA-seq reference data. *BMC Cancer*. 2019;19:715.
3. Smits AJJ, Kummer JA, de Bruin PC, et al. The estimation of tumor cell percentage for molecular testing by pathologists is not accurate. *Mod Pathol Off J U S Can Acad Pathol Inc*. 2014;27:168–174.
4. Lambrechts D, Wauters E, Boeckx B, et al. Phenotype molding of stromal cells in the lung tumor microenvironment. *Nat Med*. 2018;24:1277–1289.

List of publications
Curriculum Vitae
Dankwoord



LIST OF PUBLICATIONS

Vuijk FA, Feshtali Shahbazi S, Noortman WA, van Velden FHP, Dibbets-Schneider P, Marinelli AWKS, Neijenhuis PA, Schmitz R, Ghariq E, Velema LA, Peters FP, Smit F, Peeters KCMJ, Temmink SJD, Crobach SALP, Putter H, Vahrmeijer AL, Hilling DE, de Geus-Oei LF. Baseline and early digital [18F]FDG PET/CT and multiparametric MRI contain promising features to predict response to neoadjuvant therapy in locally advanced rectal cancer patients: a pilot study. *Nucl Med Commun*. 2023 Jul 1;44(7):613-621. PMID: 37132268.

De Jong TL, Koopman D, van der Worp CAJ, Stevens H, **Vuijk FA**, Vahrmeijer AL, Mieog JSD, de Groot JB, Meijssen MAC, Nieuwenhuijs VB, de Geus-Oei LF, Jager PL, Patijn GA. Added value of digital FDG-PET/CT in disease staging and restaging in patients with resectable or borderline resectable pancreatic cancer. *Surg Oncol*. 2023 Apr;47:101909. PMID: 36739788.

Vuijk FA, Kleiburg F, Noortman WA, Heijmen L, Feshtali Shahbazi S, van Velden FHP, Baart VM, Bhairosingh SS, Windhorst AD, Hawinkels LJAC, Dibbets-Schneider P, Bouwman N, Crobach ASLP, Fariña-Sarasqueta A, Marinelli AWKS, Oprea-Lager DE, Swijnenburg RJ, Smit f, Vahrmeijer AL, de Geus-Oei LF, Hilling DE, Slingerland M. Prostate-specific membrane antigen targeted PET/CT imaging in patients with colon, gastric and pancreatic cancer. *Cancers (Basel)*. 2022 Dec 15;14(24):6209. doi: 10.3390/cancers14246209. PMID: 36551695; PMCID: PMC9777210.

Vuijk FA, de Bruin C, Peeters-Schote MPCD, Notting IC. Recurrent intracranial hypertension in a toddler with Graves' disease. *Horm Res Paediatr*, Feb 2021. PMID: 35168232

Poels TT, **Vuijk FA**, de Geus-Oei LF, Vahrmeijer AL, Oprea-Lager DE, Swijnenburg RJ. Molecular Targeted Positron Emission Tomography Imaging and Radionuclide Therapy of Pancreatic Ductal Adenocarcinoma. *Cancers (Basel)*. 2021 Dec 7;13(24):6164. PMID: 34944781;.

van Dam MA, **Vuijk FA**, Stibbe JA, Houvast RD, Luelmo SAC, Crobach S, Shahbazi Feshtali S, de Geus-Oei LF, Bonsing BA, Sier CFM, Kuppen PJK, Swijnenburg RJ, Windhorst AD, Burggraaf J, Vahrmeijer AL, Mieog JSD. Overview and Future Perspectives on Tumor-Targeted Positron Emission Tomography and Fluorescence Imaging of Pancreatic Cancer in the Era of Neoadjuvant Therapy. *Cancers (Basel)*. 2021 Dec 2;13(23):6088. PMID: 34885196.

Baart VM, van Manen L, Bhairosingh SS, **Vuijk FA**, lamele L, de Jonge H, Scotti C, Resnati M, Cordfunke RA, Kuppen PJK, Mazar AP, Burggraaf J, Vahrmeijer AL, Sier CFM. Side-by-Side Comparison of uPAR-Targeting Optical Imaging Antibodies and Antibody Fragments for Fluorescence-Guided Surgery of Solid Tumors. *Mol Imaging Biol*. 2021 Oct 12. PMID: 34642899.

Buntinx M, **Vuijk FA**, Verburgh C. Exacerbatie van psoriasis guttata na COVID-19. *Nederlands Tijdschrift voor Dermatologie en Venereologie*, Aug 2021.

Vuijk FA, Houvast R, Baart VM, van de Velde CJH, Vahrmeijer AL, Hilling DE, Mieog JSD, Slingerland M, de Geus-Oei LF, Hawinkels LJAC, Sier CFM. Molecular imaging of the tumor stroma and beyond. *The Tumor Stroma, Jenny Stanford Publishing 2021*, ISBN 9789814968065.

Vuijk FA, Heijmen L, Roef MJ, Arens AIJ, Vahrmeijer AL, van Persijn van Meerten EL, Hilling DE, de Geus-Oei LF. [18F]FDG PET/CT in Treatment Response Monitoring: Colorectal Cancer. Clinical Atlas of PET-CT in Treatment Response Evaluation, *Springer July 2021*, ISBN 978-3-030-68858-5.

Vuijk FA, van de Water C, Lent-van Vliet S, van der Valk MJM, Simmer F, van de Velde CJH, Vahrmeijer AL, Nagtegaal ID, Hilling DE. Intra-Tumoral Genomic Heterogeneity in Rectal Cancer: Mutational Status Is Dependent on Preoperative Biopsy Depth and Location. *Cancers (Basel)*. 2021 May 9;13(9):2271. PMID: 34065112.

Franken LC, **Vuijk FA**, Soer EC, Roos E, Erdmann JI, Hooijer GKJ, Vahrmeijer AL, Gambhir SS, van Gulik TM, Sarasqueta AF, Verheij J, Swijnenburg RJ. Expression of integrin $\alpha\beta 6$ differentiates perihilar cholangiocarcinoma (PHC) from benign disease mimicking PHC. *Eur J Surg Oncol*. 2021 Mar;47(3 Pt B):628-634. PMID: 33069505.

Vuijk FA, de Muynck LDAN, Franken LC, Busch OR, Wilmink JW, Besselink MG, Bonsing BA, Bhairosingh SS, Kuppen PJK, Mieog JSD, Sier CFM, Vahrmeijer AL, Verheij J, Fariña-Sarasqueta A, Swijnenburg RJ. Molecular targets for diagnostic and intraoperative imaging of pancreatic ductal adenocarcinoma after neoadjuvant FOLFIRINOX treatment. *Sci Rep*. 2020 Oct 1;10(1):16211. PMID: 33004930.

van der Valk MJM, **Vuijk FA**, Putter H, van de Velde CJH, Beets GL, Hilling DE. Disqualification of Neoadjuvant Rectal Score Based on Data of 6596 Patients From the Netherlands Cancer Registry. *Clin Colorectal Cancer*. 2019 Jun;18(2):e231-e236. PMID: 30772135.

Vuijk FA, Hilling DE, Mieog JSD, Vahrmeijer AL. Response to the Letter to the Editor. *J Surg Oncol*. 2019 Mar;119(3):399. 2018 Dec 3. PMID: 30508288.

Vuijk FA, Hilling DE, Mieog JSD, Vahrmeijer AL. Fluorescent-guided surgery for sentinel lymph node detection in gastric cancer and carcinoembryonic antigen targeted fluorescent-guided surgery in colorectal and pancreatic cancer. *J Surg Oncol*. 2018 Aug;118(2):315-323. 2018 Sep 14. PMID: 30216455.

Boogerd LSF, **Vuijk FA**, Hoogstins CES, Handgraaf HJM, van der Valk MJM, Kuppen PJK, Sier CFM, van de Velde CJH, Burggraaf J, Fariña-Sarasqueta A, Vahrmeijer AL. Correlation Between Preoperative Serum Carcinoembryonic Antigen Levels and Expression on Pancreatic and Rectal Cancer Tissue. *Biomark Cancer*. 2017 May. PMID: 28579847.

CURRICULUM VITAE

Floris Vuijk was born on the 23rd of February 1996 in the city of The Hague. After graduating from the Christian Gymnasium Sorghvliet (The Hague) in 2014, he continued his studies at the Faculty of Medicine of the Leiden University. In 2016, he became involved as a student in the lab of dr. Alexander Vahrmeijer, which resulted in a research internship at Stanford University (Palo Alto, USA), in the lab of dr. Eben Rosenthal focused on fluorescent guided surgery. Upon return he started his PhD research in the lab of dr. Alexander Vahrmeijer at the Leiden University Medical Center under shared supervision of prof. dr. Lioe-Fee de Geus-Oei and dr. Denise Hilling, which is described in this thesis. In 2022 he graduated from the Leiden University, and is currently working as a medical advisor for MSD, The Netherlands.

DANKWOORD

Dit proefschrift is het resultaat van intensieve samenwerking over de afgelopen jaren, en was niet mogelijk geweest zonder alle betrokken collega's en patiënten die deelnamen aan de studies in dit proefschrift. Daarnaast zijn er een aantal mensen die ik graag in het bijzonder zou willen bedanken voor hun betrokkenheid in de afgelopen jaren.

Prof. dr. de Geus-Oei, beste Lioe-Fee, als onderzoeker vanuit de Heelkunde heb ik mij gewaagd op het terrein van radiologisch en nucleair geneeskundig onderzoek, en heb ik gelukkig jou hierin gevonden als expert op dit gebied. Ik heb jouw begeleiding en betrokkenheid over de afgelopen jaren erg gewaardeerd, en veel geleerd van onze samenwerking.

Dr. Vahrmeijer, beste Lex, heel veel dank voor het vertrouwen wat je had toen je mij als tweedejaars student opnam in jouw onderzoeksgroep en uiteindelijk liet afreizen naar Stanford. In de jaren die hierop volgde heb ik het vertrouwen wat je mij hebt gegeven altijd erg gewaardeerd, en bewonder ik hoe je ons allen de ruimte geeft om ons te ontwikkelen.

Dr. Hilling, beste Denise, als copromotor stond jij altijd klaar voor mijn vragen en waardeer ik dat jij, net als Lex, mij altijd erg vrij hebt gelaten om mijn promotie zelf in te vullen. Zonder jouw begeleiding was dit proefschrift niet zo tot stand gekomen. Jouw communicatieve kwaliteiten en vermogen om altijd de juiste mensen bij elkaar te krijgen en te enthousiasmeren zijn voor mij een voorbeeld.

Dr. Swijnenburg, beste Rutger-Jan, eerst vanuit het LUMC en later vanuit Amsterdam was jij betrokken bij meerdere projecten die we samen hebben gedaan. Dank dat je mij deze mogelijkheden hebt geboden, en dank voor je begeleiding en vertrouwen in deze projecten.

Dr. Sier, beste Kees, ondanks dat dit proefschrift voornamelijk klinisch georiënteerd onderzoek bevat, heb ik dankzij jouw betrokkenheid toch ook kunnen meekijken in de keuken van het preklinische onderzoek. Ik heb onze gesprekken en jouw uitgebreide uitleg en enthousiasme voor de wetenschap altijd erg gewaardeerd en veel van geleerd.

Alle collega's van de afdeling Heelkunde, Radiologie en Nucleaire Geneeskunde wil ik bedanken voor hun hulp en betrokkenheid bij de studies in dit proefschrift. In het bijzonder Floris, Shirin, Wyanne, Linda, Petra, Demi, en Fleur; dank voor jullie betrokkenheid! Daarnaast natuurlijk alle verdere collega's en kamergenoten van de C7, dank voor jullie hulp en gezelligheid in en buiten het ziekenhuis.

Paranimfen Victor en Labrinus, dank dat jullie hier vandaag met mij staan. Een mooie afsluiting van de afgelopen jaren.

Lieve pap, mam, dat we hier vandaag samen zijn is in de basis aan jullie te danken. Dank voor jullie voorbeeld en alle mogelijkheden die jullie ons allemaal altijd hebben geboden. Marie, Maus en Piet, met de paplepel werd ons de geneeskunde vanaf de geboorte ingegoten, en zelfs Maus die een ander pad in leek te slaan heeft de weg naar de medische wereld teruggevonden. Ik ben blij dat we hier vandaag allemaal samen zijn, en dank aan jullie allemaal voor de input voor de titel en kaft van dit proefschrift. Lieve oma, met 102 jaar oud ben jij vanaf de zijlijn mijn aller oudste en wijste steun en toeverlaat. Wat ben ik trots op jou en wat een geweldig voorbeeld ben je voor ons allen.

Geachte dokter van Henten, mijn liefste Tessa en sinds kort eigenlijk mevrouw Vuijk, iedere dag opnieuw ben ik ontzettend blij en dankbaar dat we na al die jaren nog steeds gelukkig samen zijn. Ik ben je ontzettend dankbaar voor je onvoorwaardelijke steun ook in dit traject.